

**EVOLUTION OF MICROSTRUCTURE AND CRYSTALLOGRAPHIC
TEXTURE DURING THERMO-MECHANICAL PROCESSING BY WARM-
ROLLING IN A DUPLEX STAINLESS STEEL**

Mohammed Zaid Ahmed

A Dissertation Submitted to
Indian Institute of Technology Hyderabad
In Partial Fulfillment of the Requirements for the Degree
of Doctor of Philosophy

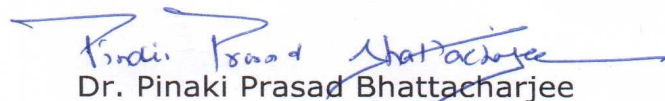


Department of Materials Science and Metallurgical Engineering

September, 2014

Certificate

I hereby certify that the matter embodied in this thesis entitled **"EVOLUTION OF MICROSTRUCTURE AND CRYSTALLOGRAPHIC TEXTURE DURING THERMO-MECHANICAL PROCESSING BY WARM-ROLLING IN A DUPLEX STAINLESS STEEL"** has been carried out by **Mohammed Zaid Ahmed** at the Department of Materials Science and Metallurgical Engineering, Indian Institute of Technology Hyderabad, India under my supervision and that it has not been submitted elsewhere for the award of any degree or diploma.



Dr. Pinaki Prasad Bhattacharjee

Department of Materials Science
and Metallurgical Engineering
Indian Institute of Technology

Hyderabad

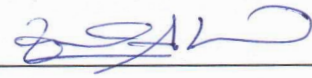
502205

INDIA

Dr. PINAKI PRASAD BHATTACHARJEE
Associate Professor & Head
Department of Material Science &
Metallurgical Engineering
Indian Institute of Technology Hyderabad
Yeddumailaram-502 205, Telangana, India

Declaration

I declare that this written submission represents my ideas in my own words, and where others' ideas or words have been included, I have adequately cited and referenced the original sources. I also declare that I have adhered to all principles of academic honesty and integrity and have not misrepresented or fabricated or falsified any idea/data/fact/source in my submission. I understand that any violation of the above will be a cause for disciplinary action by the Institute and can also evoke penal action from the sources that have thus not been properly cited, or from whom proper permission has not been taken when needed.

A handwritten signature in blue ink, appearing to read 'Mohammed Zaid Ahmed', is written over a horizontal line.

(Mohammed Zaid Ahmed)

(MS11P008)

Approval Sheet

This thesis entitled **Evolution of microstructure and crystallographic texture during thermo-mechanical processing by warm-rolling in a duplex stainless steel** by **Mohammed Zaid Ahmed** is approved for the degree of Doctor of Philosophy from IIT Hyderabad.

I. Samajdar

Prof. I. Samajdar

-Name and affiliation-

Examiner

Saswata Bhattacharyya

Dr. Saswata

-Name and affiliation-

Examiner

Pinaki Prasad Bhattacharjee
Dr. Pinaki Prasad Bhattacharjee

-Name and affiliation-

Adviser

- NA -

-Name and affiliation-

Co-Adviser

Amir Khan Rajagopal
Dr. Amir Khan Rajagopal

-Name and affiliation-

Chairman

Acknowledgements

It is hard for me to express my feelings in words here, even though I try my best to do that.

I am thankful to Almighty Allah who has shown me the right path, guided and helped me to achieve whatever in my life. It also gives me an immense pleasure to start with my family here. I gratefully acknowledge the great support of every member of my family when I finally decided to pursue research career. Their unconditional support and motivation throughout this journey helped me in completing my PhD work successfully.

I express my deepest gratitude to my supervisor Dr. Pinaki Prasad Bhattacharjee for constantly providing me motivation and suggestions throughout my PhD work. I would like to thank him for helping me developing self-learning ability and for the excellent scientific discussions which helped me in understanding the intricacies of the research topic that I have pursued. Apart from this, I would also like to express my sincere thanks to him in understanding my strength and weakness. His great patience helped me to overcome many of the difficulties that I have encountered during this work.

I would like to thank Dr. Malakondaiah (former director of DMRL, Hyderabad), Dr. T. Raghu (Scientist "G") and Mr. S.S.Satheesh (Scientist 'D') for providing the starting material used in this research work.

I would also like to thank Prof. Peter Hodgson (Director, Institute for Frontier Materials, Deakin University Australia) for kindly hosting me at Deakin University. This greatly helped me in improving my understanding of many aspects of steels research.

Thanks to all the faculty members of Material Science and Metallurgical Engineering (MSME) Department who has helped and supported me by their valuable suggestions throughout my PhD work.

I would like to express thanks to all my colleges and friends of MSME department, especially to Jagga, Bhadak, Dan, Elango, Nida, Palli Srinivas, Karthik, Akki Bhaskar, Venkateshwar, and Sushmita, for their valuable suggestions and support.

I would like to express my thanks to my friend Dr. Kashfuddoja of Department of Mechanical and Aerospace Engineering for his support and motivation.

I would like to express my thanks to all my friends at IIT Hyderabad who helped me in maintaining a social life even in the most difficult periods in course of this research work.

I would like to express my thanks to all non-teaching staffs who have helped me in establishing the lab and also in conducting the day to day research work without which I would have succeeded in this research work.

Thanks to all.

- Mohammed Zaid Ahmed -

Contents

List of Figures	VI
List of Tables	XVII
List of Abbreviations	XVII
Synopsis	XIX
Chapter 1 Introduction	1
Chapter 2 Literature Review	4
2.1 Duplex Materials	5
2.2 Evolution of Texture During Deformation and Recrystallization of Single phase FCC materials	12
2.2.1 Representation of Texture	12
2.2.2 Deformation Texture of FCC Materials	20
2.2.3 Annealing Texture of FCC Materials	22
2.3 Deformation and Annealing Texture of Single Phase BCC Materials	28
2.3.1 Deformation Texture of BCC Materials	28
2.3.2 Annealing Texture of BCC Materials	30
2.4 Evolution of Microstructure and Texture in DSS During Deformation and Annealing of DSS	34
2.4.1 Evolution of Microstructure and Texture During Deformation	34
2.4.2 Evolution of Microstructure and Texture During Annealing	39
2.5 Objectives and Scope of the Present Work	43
Chapter 3 Experimental	46
3.1 Alloy Preparation	46
3.2 Preparation of Starting Material for Deformation Processing	46
3.3 Deformation Processing	51
3.4 Warm-Rolling	52

3.4.1 Unidirectional or Straight Warm-Rolling	52
3.4.2 Cross Warm-Rolling (CWR)	52
3.5 Annealing	53
3.5.1 Annealing of UWR Processed Material	53
3.5.2 Annealing of CWR Processed Material	53
3.6 Chemical Composition, Microstructural and Texture Characterization	55
3.6.1 Measurement of Microtexture Using EBSD	56
3.6.2 Experimental Details of EBSD Analysis	64
3.7 Mechanical Characterization	65
Chapter4 Effect of Processing Temperature on Microstructure And Texture During Warm Rolling And Recrystallization	67
4.1 Microstructure and Texture of the Homogenized Starting Material	68
4.2 Evolution of Microstructure and Texture During Warm-Rolling at 498K (225°C)	72
4.2.1 Evolution of Microstructure	72
4.2.2 Evolution of Texture	77
4.3 Evolution of Microstructure and Texture During Warm-Rolling at 698K (425°C)	82
4.3.1 Evolution of Microstructure	82
4.3.2 Evolution of Texture	87
4.4 Evolution of Microstructure and Texture During Warm-Rolling at 898K (625°C)	91
4.4.1 Evolution of Microstructure	91
4.4.2 Evolution of Texture	94
4.5 Evolution of Microstructure and Texture During Subsequent recrystallization	98

4.6 Evolution of Microstructure and Texture During Annealing of 90% Warm-Rolled DSS at 498K (225°C)	100
4.6.1 Evolution of Microstructure During Annealing	100
4.6.2 Evolution of Texture During Annealing	102
4.7 Evolution of Microstructure and Texture During Annealing of 90% Warm-Rolled DSS at 698K (425°C)	109
4.7.1 Evolution of Microstructure During Annealing	109
4.7.2 Evolution of Texture During Annealing	114
4.8 Evolution of Microstructure and Texture During Annealing of 90% Warm-Rolled DSS at 898K (625°C)	114
4.8.1 Evolution of Microstructure During Annealing	121
4.8.2 Evolution of Texture During Annealing	125
4.9 Discussion	125
4.9.1 Evolution of Microstructure and Texture During Warm-Rolling	132
4.9.2 Evolution of Microstructure and Texture During Isothermal Annealing	142
Chapter 5 Effect of Severe Deformation on the Microstructure And Texture During Warm-Rolling and Recrystallization	150
5.1 Severe Warm-Rolling of DSS	151

5.2 Evolution of Microstructure and Texture During Severe Warm-Rolling of DSS at 898K (625°)	154
5.2.1 Evolution of Microstructure	154
5.2.2 Evolution of Texture	157
5.3 Evolution of Microstructure and Texture During Annealing	163
5.3.1 Evolution of Microstructure During Annealing	163
5.3.2 Evolution of Texture During Annealing	171
5.4 Evolution of Mechanical Properties During Warm-Rolling and Isothermal Annealing	181
5.5 Discussion	183
5.5.1 Evolution of Microstructure and Texture During Severe Warm-Rolling	183
5.5.2 Evolution of Microstructure and Texture During Annealing	191
5.6 Evolution of Mechanical Properties during Severe Warm-Rolling and Annealing	194
Chapter 6 Effect of Change in Strain Path on the Microstructure and Texture During Warm-Rolling and Recrystallization	196
6.1 Cross Warm-Rolling (CWR)	197
6.2 Evolution of Microstructure and Texture During Cross Warm-Rolling (CWR) of Duplex Stainless Steel	198
6.2.1 Evolution of Microstructure	198
6.2.2 Evolution of Texture	203
6.3 Evolution of Microstructure and Texture During Annealing Of CWR Material	206

6.3.1 Evolution of Microstructure During Annealing	206
6.3.2 Evolution of Texture During Annealing	210
6.4 Discussion	219
6.4.1 Texture Evolution During Processing By CWR	219
6.4.2 Texture Evolution During Annealing	223
Chapter 7 Summary and Conclusions	227
References	232

List of Figures

Figure No.	Title	Page No.
------------	-------	----------

-: Chapter 2:-

2.1	Section of the ternary Fe-Cr-Ni phase diagram[4].	6
2.2	Summary of the effects of alloying elements on the formation of various precipitates [6].	11
2.3	The unit sphere showing the position of the (0001) pole with regard to an external reference frame which is described by the two angles α and β [9].	13
2.4	Representation of the $\{100\}$ poles of a cubic crystal in the stereographic projection. (a) Crystal in the unit sphere; (b) projection of the $\{100\}$ poles onto the equator plane; (c) $\{100\}$ pole figure and definition of the pole figure angles α and β for the (100) pole [9].	15
2.5	Schematic illustration of (a) reference system and (b) Euler angles [10].	16
2.6	Schematic representation of the three dimensional Euler space[11].	17
2.7	Three dimensional view of Euler space with locations of some important ideal orientations and fibres of FCC metals [16].	19
2.8	Ideal orientations of FCC materials shown in the ϕ_2 sections of Euler space [16].	19
2.9	(111) pole figure of 95% cold rolled (a) copper and (b) Aluminium [7].	21
2.10	ODF of 90% cold rolled aluminium with positions of deformation texture components indicated [7].	21
2.11	(111) pole figure of 95% cold rolled 70:30 brass [16].	23
2.12	ODF of 95% cold rolled 70:30 brass [16].	23

2.13 Schematic illustration of ((a,b)) continuous and ((c,d)) discontinuous annealing processes [7].	25
2.14 Three dimensional view of Euler space with locations of some important ideal orientations and fibers of BCC metals [43].	29
2.15 Typical $\phi_2 = 45^\circ$ section of ODF of BCC materials showing the locations of individual texture components along the two fibers [9].	29
2.16 $\phi_2 = 45^\circ$ sections of ODFs of ELC IF steel after cold reductions of (a) 70% and (b) 85% [43].	31
2.17 (a) $\phi_2 = 45^\circ$ section of the ODF of 90% cold-rolled Ti+Nb microalloyed interstitial-free steel, (b) $\phi_2 = 45^\circ$ section of ODF of 90% cold rolled and annealed (1hr at 700°C) Ti-alloyed interstitial-free steel [9].	33
2.18 ODFs of (a) austenite and (b) ferrite in hot-rolled DSS [65].	36
2.19 The formation of banded morphology in DSS cold-rolled to (a) 60% and (b) 90% reduction in thickness [69].	36
2.20 Schematic of the microstructural arrangement in cold-rolled DSS (rolling direction horizontal) [69].	38
2.21 (a) $\phi_2 = 45^\circ$ section of ODF of ferrite phase and (b) ODF of austenite phase in 90% cold-rolled DSS [69].	38
2.22 (a) $\phi_2 = 45^\circ$ section of ODF of ferrite and (b) ODF of austenite in DSS cold-rolled to 90% reduction in thickness and annealed for 2000s at 1100°C [69].	42

-: Chapter 3:-

3.1 As cast ingot of DSS used in the present research.	48
3.2 DSS billet in the hot forged condition.	49

3.3	Flow diagram showing the preparation of the homogenized starting material.	50
3.4	Schematic illustration of the CWR route. The RD of the current pass, thickness of the sheet at every pass, % reduction in thickness and corresponding equivalent strain are indicated.	54
3.5	Origin of Kikuchi lines from the EBSD perspective [1].	57
3.6	Components of a commercial EBSD system [1].	59
3.7	Schematic representation of the Hough transformation; (a) two bands in the original space, (b) the bands in the transformed Hough space [1].	61
3.8	Schematic representation of the geometry of (a) diffraction and (b) EBSD [2].	62
3.9	Schematic of the tensile test specimens. All dimensions shown are in mm.	66

-: Chapter 4:-

4.1	Phase map showing the distribution of ferrite and austenite in the homogenized DSS used as the starting material for subsequent warm-rolling.	70
4.2	$\phi_2 = 45^\circ$ section of the ODF of ferrite in starting homogenized DSS. The ideal locations of the texture components are shown in the ODF section.	71
4.3	(a) shows the (111) PF of austenite in homogenized DSS, (b) shows the ideal locations of individual texture components in (111) PF. (c) shows the $\phi_2 = 0^\circ, 45^\circ$ and 65° sections of the ODF of austenite in homogenized DSS along with the ideal locations of individual texture components.	73
4.4	Phase maps of the DSS warm-rolled at 498K (225°C) to (a) 20%, (b) 40%, (c) 70% and (d) 90% reduction in thickness. (e) shows a region of interest cropped from the phase map of 90% warm-rolled material shown in (d).	74

- 4.5** Schematic diagram showing (a) misorientation between a grain at the center and all other points at the perimeter of the kernel and (b) misorientation between a grain at the center and all points in the kernel [1]. **78**
- 4.6** (a) shows the $\phi_2=45^\circ$ section of the ODF and (b) shows the orientation map of ferrite (austenite regions are masked) in DSS warm-rolled to 90% reduction in thickness at 498K (225°C). **79**
- 4.7** (a) shows the (111) PF, (b) shows the $\phi_2 = 0^\circ, 45^\circ$ and 65° sections of the ODF and (c) shows the orientation map of austenite (ferrite regions are masked) in DSS 90% warm-rolled at 498K (225°C). **81**
- 4.8** Phase maps of DSS warm-rolled at 698K (425°C) to (a) 20%, (b) 40%, (c) 70% and (d) 90% reduction in thickness. (e) shows a region of interest cropped from the map shown in (d). **83**
- 4.9** (a) shows the phase map obtained from another region of interest in DSS 90% warm-rolled to 90% reduction in thickness at 698K (425°C). (b) shows the $\phi_2 = 45^\circ$ section of ODF and (c) shows the orientation map of ferrite (austenite regions are masked). **85**
- 4.10** (a) shows the $\phi_2=45^\circ$ section of the ODF and (b) shows the orientation map of ferrite (austenite regions are masked) in DSS warm-rolled to 90% reduction in thickness at 698K (425°C). **88**
- 4.11** (a) shows the (111) PF, (b) shows the $\phi_2 = 0^\circ, 45^\circ$ and 65° sections of the ODF and (c) shows the orientation map of austenite (ferrite regions are masked) in DSS warm-rolled to 90% reduction in thickness at 698K (425°C). **90**
- 4.12** Phase maps of DSS warm-rolled at 898K (625°C) to (a) 20%, (b) 40%, (c) 70% and (d) 90% reduction in thickness. (e) shows a region of interest cropped from the phase map of 90% warm-rolled DSS shown in (d). **92**

- 4.13** (a) shows the $\phi_2=45^\circ$ section of the ODF and (b) shows the orientation map of ferrite (austenite regions are masked) in DSS warm-rolled to 90% reduction in thickness at 898K (625°C). **95**
- 4.14** (a) shows the (111) PF and (b) shows the $\phi_2 = 0^\circ, 45^\circ$ and 65° sections of the ODF, (c) shows the orientation map of austenite (ferrite regions are masked) in DSS warm-rolled to 90% reduction in thickness at 898K (625°C). **97**
- 4.15** Phase maps of the (a) A2, (b) A20, (c) A30 and (d) A120 DSS specimens. **101**
- 4.16** Evolution of (a) ferrite fraction, (b) grain thickness (measured along the ND) and (c) aspect ratio of the two phases in isothermally annealed A series DSS specimens. **103**
- 4.17** $\phi_2=45^\circ$ section of the ODF of ferrite in isothermally annealed (a) A2, (b) A20, (c) A30, (d) A120 DSS specimens. **104**
- 4.18** Variation of RD and ND-fiber fractions in ferrite in isothermally annealed A series DSS specimens. **106**
- 4.19** (111) PF of austenite in isothermally annealed (a) A2, (b) A20, (c) A30, (d) A120 DSS specimens. **107**
- 4.20** $\phi_2 = 0^\circ, 45^\circ, 65^\circ$ sections of the ODFs of austenite in isothermally annealed (a) A2, (b) A20, (c) A30, (d) A120 DSS specimens. **108**
- 4.21** Evolution of texture components in austenite in isothermally annealed A series DSS specimens. **110**
- 4.22** Phase maps of the (a) B2, (b) B20, (c) B30,(d) B120 DSS specimens. **111**
- 4.23** Variation of (a) ferrite fraction, (b) grain thickness (measured along the ND) and (c) aspect ratio of the two phases in isothermally annealed B series DSS specimens. **113**
- 4.24** $\phi_2=45^\circ$ section of the ODF of ferrite in (a) B2, (b) B20, (c) B30, (d) B120 DSS specimens. **115**
- 4.25** Evolution of texture components during isothermal annealing in ferrite in isothermally annealed B series DSS specimens. **117**

- 4.26** (111) PFs of austenite in isothermally annealed (a) B0, (b) B2, (c) B20, (d) B30, (e) B120 specimens. **118**
- 4.27** $\phi_2 = 0^\circ, 45^\circ, 65^\circ$ sections of the ODFs of austenite in isothermally annealed (a) B2, (b) B20, (c) B30, (d) B120 specimens. **119**
- 4.28** Evolution of texture components during isothermal annealing in austenite in B series DSS specimens. C(T) and G^T are twin components of C and G, respectively. **120**
- 4.29** Phase maps of isothermally annealed (a) C2, (b) C20, (c) C30 and (d) C120 specimens. **122**
- 4.30** Variation of (a) ferrite fraction, (b) grain thickness (measured along the ND) and (c) aspect ratio of the two phases in isothermally annealed C series DSS specimens. **124**
- 4.31** $\phi_2=45^\circ$ section of the ODF of ferrite in (a) C2, (b) C20, (c) C30, (d) C120 DSS specimens. **126**
- 4.32** Variation of RD and ND-fiber fractions in ferrite in isothermally annealed C series DSS specimens. **127**
- 4.33** (111) PF of austenite in 90% warm-rolled and isothermally annealed (a) C2, (b) C20, (c) C30, (d) C120 DSS specimens. **129**
- 4.34** $\phi_2 = 0^\circ, 45^\circ, 65^\circ$ ODF sections of austenite in (a) C2, (b) C20, (c) C30, (d) C120 DSS specimens. **130**
- 4.35** Evolution of texture components during isothermal annealing in austenite in C series DSS specimens. **131**
- 4.36** (a) shows austenite fraction, (b) shows thickness of the phase bands, (c) and (d) show HAGB fraction and HAGB spacing of the two phases, respectively after 90% warm-rolling at different temperatures. (e) shows area fraction having $KAM \leq 1$ in the two phases in DSS 90% warm-rolled at different temperatures. The abbreviation WR is used for "Warm-Rolling" for convenience. **133**
- 4.37** Volume percentages of different texture components in austenite in DSS warm-rolled to 90% reduction in thickness at different temperatures. **137**

- 4.38** (111) pole figure of austenite in (a) 40%, (b) 70%, and (c) 90% cold-rolled DSS. **138**
- 4.39** $\phi_2=0^\circ, 45^\circ, 65^\circ$ sections of the ODFs of austenite in (a) 40%, (b) 70%, and (c) 90% cold-rolled DSS. **139**
- 4.40** Texture components in ferrite in DSS warm-rolled to 90% reduction in thickness at different temperatures. **141**
- 4.41** Schematic showing mutual interpretation of two phases at triple points during breakdown of the lamellar structure. **143**
- 4.42** (a) and (b) show the phase maps of DSS warm-rolled to 90% reduction in thickness at 698K (425°C) and 898K (625°C) (i.e. B0 and C0 specimens), respectively. (c) shows the point to origin misorientation along the arrows inside ferrite bands in specimens B0 and C0 shown in (a) and (b), respectively. **145**

-: Chapter 5:-

- 5.1** Phase maps of DSS warm-rolled to ((a),(b)) 95% and ((c),(d)) 98% reduction in thickness at ((a),(c)) 498K (225°C) and ((b),(d)) 698K (425°C). **152**
- 5.2** Variation of austenite fraction in DSS during warm-rolling at different temperatures. **153**
- 5.3** Phase maps of DSS warm-rolled at 898K (625°C) to (a) 70%, (b) 90%, (c) 95% and (d) 98% reduction in thickness. **155**
- 5.4** Variation of HAGB spacing along ND in the two phases of DSS warm-rolled to different reduction in thickness at 898K (625°C). **156**
- 5.5** $\phi_2 = 45^\circ$ section of ODF of ferrite in DSS warm-rolled at 898K (625°C) to (a) 70%, (b) 90%, (c) 95%, (d) 98% reduction in thickness. **158**
- 5.6** Volume fractions of RD and ND-fibers in ferrite in DSS warm-rolled at 898K (625°C) to different reduction in thickness. SM is used as abbreviation for the homogenized starting material. **159**

- 5.7** (111) PFs of austenite in DSS warm-rolled at 898K (625°C) to (a) 70%, (b) 90%, (c) 95%, (d) 98% reduction in thickness. **161**
- 5.8** $\phi_2=0^\circ, 45^\circ, 65^\circ$ sections of the ODFs of austenite in DSS warm-rolled at 898K (625°C) to (a) 70%, (b) 90%, (c) 95% and (d) 98% reduction in thickness. **162**
- 5.9** Volume fraction of texture components in austenite in DSS warm-rolled to different reduction in thickness at 898K (625°C). **164**
- 5.10** Phase maps of 70% warm-rolled DSS after isothermal annealing 1448K (1175°C) for (a) 2, (b) 30 and (c) 120 minutes. **165**
- 5.11** Phase maps of 95% warm-rolled DSS after isothermal annealing at 1448K (1175°C) for (a) 2, (b) 30 and (c) 120 minutes. **167**
- 5.12** Phase maps of 98% warm-rolled DSS after isothermal annealing 1448K (1175°C) for (a) 2, (b) 30 and (c) 120 minutes. **168**
- 5.13** Variation of HAGB spacing in (a) austenite and (b) ferrite in DSS warm-rolled to different reduction in thickness and isothermally annealed at 1448K (1175°C). (c) shows the aspect ratio of the two phases in DSS warm-rolled to different reduction in thickness and annealed at 1448K (1175°C) for 2 minutes DSS. **170**
- 5.14** $\phi_2 = 45^\circ$ section of ODF of ferrite in DSS warm-rolled to ((a)-(d)) 70%, ((e)-(h)) 90% and ((i)-(l)) 95% and ((m)-(p)) 98% reduction in thickness and isothermally annealed at 1498K (1175°C) for 2, 30, 60 and 120 minutes. **172**
- 5.15** Variation in the volume fraction of RD and ND-fibers in ferrite in (a) 70%, (b) 90%, (c) 95% and (d) 98% warm-rolled DSS during isothermal annealing at 1448K (1175°C). **173**
- 5.16** (111) PFs of austenite in DSS ((a)-(d)) 70%, ((e)-(h)) 90%, ((i)-(l)) 95% and ((m)-(p)) 98% warm-rolled and isothermally

annealed at 1448K (1175°C) for 2, 30, 60 and 120 minutes.

175

5.17 $\phi_2 = 0^\circ$, 45° and 65° sections of ODFs of austenite in DSS 70% warm-rolled and then isothermally annealed at 1448K (1175°C) for (a) 2, (b) 30, (c) 60, and (d) 120 minutes.

176

5.18 Fig.5.17: $\phi_2 = 0^\circ$, 45° and 65° sections of ODFs of austenite in DSS 90% warm-rolled and then isothermally annealed at 1448K (1175°C) for (a) 2, (b) 30, (c) 60, and (d) 120 minutes.

177

5.19 $\phi_2 = 0^\circ$, 45° and 65° sections of ODFs of austenite in DSS 90% warm-rolled and then isothermally annealed at 1448K (1175°C) for (a) 2, (b) 30, (c) 60, and (d) 120 minutes.

178

5.20 $\phi_2 = 0^\circ$, 45° and 65° sections of ODFs of austenite in DSS 98% warm-rolled and then isothermally annealed at 1448K (1175°C) for (a) 2, (b) 30, (c) 60, and (d) 120 minutes.

179

5.21 Variation of individual texture components in austenite (a) 70%, (b) 90%, (c) 95% and (d) 98% warm-rolled DSS during isothermal annealing at 1448K (1175°C).

180

5.22 Comparison of engineering stress-strain plots of severely warm-rolled DSS.

182

5.23 Engineering stress-strain plots of 90% warm-rolled and isothermally annealed DSS.

185

5.24 Engineering stress-strain plots of 95% warm-rolled and isothermally annealed DSS.

186

5.25 Engineering stress-strain plots of 98% warm-rolled and isothermally annealed DSS.

187

-: Chapter 6:-

6.1 Phase maps of homogenized DSS processed by CWR at 898K (625°C) to (a) 18%, (b) 33%, (c) 45%, (d) 55%, (e) 63%, (f) 70% (g) 75%, (h) 80%, (i) 84%, (j) 86% and (k) 90% reduction in thickness.

189

6.2 (a) shows the phase map, (b) and (c) show the GB maps of ferrite (austenite regions are masked) and austenite (ferrite regions are masked), respectively in the 90% CWR processed DSS, (d) shows the accumulated misorientation inside the ferrite bands along the arrow marks shown in (b). **200**

6.3 Variation of (a) phase fraction, (b) HAGB fraction and (c) HAGB spacing in DSS during processing by CWR. **202**

6.4 (a) shows the $\phi_2 = 45^\circ$ section and (b) shows the orientation map of ferrite (austenite regions are masked) in 90% CWR processed DSS. **204**

6.5 (a) shows the (111) PF of austenite in 90% CWR processed DSS and (b) shows the ideal locations of the components in the (111) PF. (c) shows the $\phi_2 = 0^\circ$, 45° and 65° sections and (d) shows the orientation map of austenite (ferrite regions are masked) in the 90% CWR processed DSS. **205**

6.6 Phase maps of 90% CWR processed DSS isothermally annealed at 1448K (1175°C) for (a) 2 minutes, (b) 30 minutes, (c) 60 minutes and (d) 120 minutes. **207**

6.7 Variation of (a) grain thickness along ND and (b) aspect ratio of the two phases in 90% CWR processed DSS during isothermal annealing at 1448K (1175°C). **209**

6.8 $\phi_2 = 45^\circ$ sections of ODFs of ferrite in 90% CWR processed DSS isothermally annealed at 1448K (1175°C) for (a) 2 minutes, (b) 30 minutes, (c) 60 minutes and (d) 120 minutes. **211**

6.9 Orientation maps of ferrite (austenite regions are masked) in 90% CWR processed DSS isothermally annealed at 1448K (1175°C) for (a) 2 minutes, (b) 30 minutes, (c) 60 minutes and (d) 120 minutes. **212**

6.10 Variation of volume fraction of texture components in ferrite in 90% CWR processed DSS during isothermal annealing at 1448K (1175°C). **213**

6.11 (111) PFs of austenite in 90% CWR processed DSS isothermally annealed at 1448K (1175°C) for (a) 2 minutes, (b) 30 minutes, (c) 60 minutes and (d) 120 minutes. **215**

6.12 $\phi_2 = 0^\circ, 45^\circ$ and 65° sections of the ODFs of austenite in 90% CWR processed DSS isothermally annealed at 1448K (1175°C) for (a) 2 minutes, (b) 30 minutes, (c) 60 minutes and (d) 120 minutes. **216**

6.13 Orientation maps of austenite (ferrite regions are masked) in 90% CWR processed DSS isothermally annealed at 1448K (1175°C) for (a) 2 minutes, (b) 30 minutes, (c) 60 minutes and (d) 120 minutes. **217**

6.14 Variation of volume fraction of texture components in austenite in 90% CWR processed DSS during isothermal annealing. **218**

List of Tables

Figure No.	Title	Page No.
-: Chapter 2 :-		
Table 2.1:	Typical chemistry of DSS grades [3].	8
Table 2.2:	List of commercially available DSS grades with chemical composition [5].	9
-: Chapter 3 :-		
Table 3.1:	Chemical composition of the as-cast DSS used in the present research.	47
-: Chapter 4 :-		
Table 4.1:	Distribution of alloying elements in the two constituent phases in the starting homogenized DSS.	69
Table.4.2:	Evolution of key microstructural parameters in ferrite and austenite in DSS during warm-rolling at 498K (225°C).	76
Table.4.3:	Evolution of key microstructural parameters in ferrite and austenite in DSS during warm-rolling at 698K (425°C).	86
Table.4.4:	Evolution of key microstructural parameters in ferrite and austenite in DSS during warm-rolling at 898K (625°C).	93
Table 4.5:	Sample designation scheme used in the present work for different warm-rolled (90% reduction in thickness) and isothermally annealed DSS specimens.	99
-: Chapter 5 :-		
Table 5.1:	Summary of the mechanical properties of warm rolled and subsequently annealed material.	184

List of Abbreviations

BCC	–	Body Centred Cubic
CWR	–	Cross Warm-Rolling
DSS	–	Duplex Stainless Steel
EBSD	–	Electron Back Scattered Diffraction
ECAP	–	Equi Channel Angular Extrusion
EDS	–	Energy Dispersive Spectroscopy
FCC	–	Face Centred Cubic
FEG	–	Field Emission Gun
HAGB	–	High Angle Grain Boundary
HEA	—	High Entropy Alloys
HPT	-	High Pressure Torsion
LAGB	–	Low Angle Grain Boundary
ND	–	Normal Direction
ODF	–	Orientation Distribution Function
PFs	–	Pole Figures
RD	–	Rolling Direction
SCC	-	Stress Corrosion Cracking
SEM	–	Scanning Electron Microscope
SFE	–	Stacking Fault Energy
TBs	–	Twin Boundaries
TD	–	Transverse Direction
TWIP	–	Twin Induced Plasticity
UTS	–	Ultimate Tensile Strength
UWR	-	Unidirectional Warm Rolling
XRD	-	X-Ray Diffraction
YS	–	Yield Strength

Synopsis

Thermo-mechanical processing of materials involving heavy deformation and annealing results in the development of characteristic microstructure and crystallographic texture which greatly affect their properties. As a result, the development of microstructure and texture during thermo-mechanical processing has been intensely investigated in a range of materials including single phase metals and alloys, two phase materials and intermetallic alloys. However, the development of microstructure and texture in duplex alloys where both the phases have polycrystalline grain structure, such as, ($\alpha+\beta$) brass and (ferrite+austenite) duplex stainless steels (DSS) has received far less attention. Since these alloys constitute an important class of structural materials adequate understanding of microstructure and texture formation in these alloys will be key to enhance their properties for a wide range of applications.

The present work attempts to clarify the evolution of microstructure and texture in duplex alloys using DSS as a model system. In the present work warm-rolling (processing temperature is above room temperature, but below recrystallization temperature) is employed as the preferred thermo-mechanical processing route. Processing by warm-rolling is considered particularly important in the present research considering the fact that additional complexities due to deformation induced phase transformation can be avoided. It might be noted that previous investigations of microstructure and texture evolution in duplex alloys have pursued processing by either hot or cold-rolling. However, the effect of thermo-mechanical processing by warm-rolling has not been investigated so far. This constitutes a major novelty of the present work. The effect of three major processing

parameters, namely warm-rolling temperature, strain and change in strain path is systematically investigated in this work.

The DSS alloy with chemical composition 0.08wt.%C-24wt.%Cr-10.5wt.%Ni-3wt.%Mo is prepared by vacuum induction melting and casting. The as-cast DSS ingot is obtained in the form of a tapered cylinder with top diameter 72mm, bottom diameter 62mm and height 290mm. The ingot is progressively hot-forged or clogged at 1473K (1200°C) to dimensions of 60mm (Thickness)X(55mm (Width) X 300mm (Length). The hot-forged slab is subsequently hot-rolled at 1398K (1125°C) to ~82.5% reduction in thickness to a thickness of 10.5mm. This is followed by homogenization annealing at 1448K (1175°C) for 7200 seconds (120 minutes) to achieve nearly equal volume fraction of austenite and ferrite in the microstructure. These homogenization annealed materials are used for further thermo-mechanical processing by warm-rolling to study the effect of different processing parameters as already stated before.

In order to study the effect of warm-rolling temperature the homogenization annealed material is warm-rolled to 90% reduction in thickness at three different temperatures, namely, 498K (225°C), 698K (425°C) and 898K (625°C). The 90% warm-rolled materials are subsequently annealed at 1448K (1175°C) for time intervals ranging from 120 seconds (2 minutes) to 7200 seconds (120 minutes).

Development of an ultrafine lamellar deformation structure having an alternate arrangement of the two phase bands is observed during warm-rolling. The individual phase bands are further subdivided by high angle grain boundaries (HAGBs defined by misorientation angle (θ) $\geq 15^\circ$). However, in comparison to the two end temperatures of warm-rolling, the microstructure of the material warm-rolled at 698K (425°C) shows distinctly different behavior characterized by significant fragmentation of the ferrite

phase. The texture of ferrite is characterized by the presence of ND (ND//<111>) and RD (RD//<110>) fibers. However, as compared to ferrite in the DSS warm-rolled at 498K (225°C) and 898K (625°C), ferrite in the DSS warm-rolled at 698K (425°C) shows much stronger RD-fiber than ND-fiber. On the other hand, austenite shows the development of pure metal type (or copper type) deformation texture in different warm-rolled materials in contrast to the strong brass type texture in cold-rolled DSS. These observations indicate that the development of microstructure and texture is greatly influenced by the warm-rolling temperature.

The effect of warm-rolling temperature on the evolution of microstructure and texture could be explained based on the interaction of carbon atoms with dislocations (dynamic strain aging). At the warm-rolling temperature of 498K (225°C) the mobility of the carbon atoms may be insufficient to effectively lock dislocations. On the other hand, at the warm-rolling temperature of 898K (625°C) the mobility of the carbon atoms may be too high. At the intermediate temperature of 698K (425°C) the locking of dislocations by carbon atoms would be most effective. As a result the ferrite would be the harder phase showing evidently more mechanical fragmentation.

The microstructure evolution at different warm-rolling temperatures is amply corroborated by the pattern of texture evolution in ferrite in DSS. Slip on the $\{110\}<111>$ system is preferentially retarded by the interaction of the carbon atoms with dislocations. The slip retardation is particularly effective on the $\{110\}$ plane due to the greater number of available interstitial sites. As a result the $\{110\}<111>$ system is more work-hardened and slip takes place preferentially on the $\{112\}<111>$ system. The choice of slip systems leads to stronger RD-fiber as compared to the ND-fiber in ferrite in DSS warm-rolled at 498K (225°C) .

The development of pure metal type texture in austenite is understood from the increase in stacking fault energy (SFE) at the elevated temperatures of warm-rolling. The increase in SFE results in the suppression of formation of deformation twins in favor of dislocation slip. This results in the formation of pure metal type texture characterized by the presence of strong S ($\{123\}\langle 634\rangle$), brass or B_s ($\{110\}\langle 112\rangle$) and Cu ($\{112\}\langle 111\rangle$) components.

The annealing of different 90% warm-rolled materials is carried out only at the temperature of homogenization so that microstructure and texture evolution is not affected by phase transformation. Development of a lamellar bamboo type morphology with an alternate arrangement of bands of the two phases is observed in different warm-rolled DSS after isothermal annealing at 1448K (1175°C) for short duration. The interconnecting boundaries are mostly low angle grain boundaries ($2^\circ \leq \theta < 15^\circ$) in case of ferrite. In contrast, the interconnecting boundaries were mostly HAGBs in austenite. The microstructural evolution indicates that the primary softening mechanism in ferrite is recovery whereas in austenite it is discontinuous recrystallization. The breakdown of the bamboo structure with the concurrent evolution of globular morphology is observed with increasing isothermal annealing time and evidenced by an increase in the aspect ratio. The mechanism of this transformation is explained on the basis of mutual interpenetration of the two phases along the triple points. The grain growth process is greatly restricted in the two phases of the annealed DSS, which is attributed to resistance to grain growth exerted by one phase on the other.

Ferrite in different isothermally annealed DSS shows retention of the two characteristic texture fibers consistent with the recovery behavior of ferrite. However, RD-fiber is found to be much stronger than ND-fiber. The development of stronger RD-fiber components is attributed to recovery behavior of these components as opposed to

the recrystallization type behavior of the ND-fiber components. Warm-rolling of DSS results in diminished driving force for recrystallization and results in the formation of much stronger RD-fiber.

Retention of deformation texture components is observed in austenite in different warm-rolled and isothermally annealed DSS. This indicates discontinuous recrystallization but without any preferential orientation selection. The usual brass recrystallization component ($\{236\}<385>$) which is often found to be the dominant component in the recrystallization texture of low SFE materials is not found strong in austenite in different warm-rolled and annealed DSS.

The effect of imposed strain is investigated by warm-rolling the homogenized DSS at 898K (625°C) to 98% reduction in thickness. The microstructure and texture evolution of the 70%, 90%, 95% and 98% warm-rolled and annealed materials are compared to study the effect of imposed strain. The warm-rolling temperature is selected based on the fact that the austenite in DSS is found to be stable even up to the highest deformation level at this processing temperature only.

Evolution of ultrafine lamellar deformation structure with an alternate arrangement of the phase bands is observed with increasing strain. However, the microstructure shows significant fragmentation in the ferrite phase beyond 90% warm-rolling. Ferrite shows near saturation behavior in the HAGB spacing beyond 90% reduction in thickness. In contrast, the HAGB spacing in austenite continues to decrease with increasing deformation. Ultrafine microstructure with HAGB spacing of ~ 250 nm and ~ 390 nm in austenite and ferrite, respectively is obtained after 98% reduction. The finer HAGB spacing in austenite indicates that the austenite continues to be subdivided in a progressively finer scale with increasing deformation. In contrast, fragmented microstructure of

ferrite shows that ferrite undergoes deformation induced mechanical fragmentation which results in no significant reduction in HAGB spacing beyond 90% reduction in thickness.

The texture of ferrite in different warm-rolled DSS shows the presence of both RD and ND fibers. However, the strength of the RD-fiber is increased with increasing deformation while the strength of the ND-fiber is not changed significantly beyond 90% warm-rolling. On the other hand, the B_s component is strengthened with increasing deformation in austenite indicating a gradual transition from pure metal type texture to brass type texture. The crucial role of deformation twin formation during texture transition is indicated by the consistent increase of the volume fraction of twin of the copper orientation (Cu^T) ($\{552\}<115>$) with increasing deformation beyond 90% warm-rolling.

The microstructural evolution during annealing is found to be affected by imposed strain and appears to be different for austenite and ferrite. The transformation from lamellar bamboo type morphology to globular morphology is much faster in ferrite of 98% warm-rolled DSS as compared to ferrite in 70% warm-rolled DSS. However, after longer isothermal holding the aspect ratio of ferrite in different warm-rolled DSS are found to be similar. In case of austenite, the effect of imposed strain on the kinetics of transformation from lamellar bamboo type morphology to globular morphology is less pronounced as compared to ferrite. The effect of strain on the kinetics of microstructural transformation is explained on the basis of evolution of finer microstructure with increasing deformation, which provides faster diffusion paths accelerating the kinetics of transformation during recrystallization.

The texture of ferrite in DSS warm-rolled to different strain levels shows the presence of stronger RD-fiber components than ND-fiber components after annealing. This is explained from the recovery behavior in ferrite. The difference in strength of RD and ND fibers

after annealing increases with increasing strain. In case of ferrite in 98% warm-rolled and annealed DSS the RD and ND fibers are not continuous and the intensity maxima along the RD fiber is shifted from $\{001\}\langle 110 \rangle$ to $\{112\}\langle 110 \rangle$ with increasing isothermal holding time. Retention of deformation texture components is observed in austenite in different warm-rolled and annealed DSS. Stronger BS component is observed in austenite in 98% warm-rolled DSS after short isothermal annealing which is attributed to the presence of stronger BS component in the deformation texture of austenite in the 98% warm-rolled DSS prior to annealing. With increasing isothermal annealing time the strength of the brass component is decreased.

The effect of thermo-mechanical processing by warm-rolling on the evolution of mechanical properties is investigated by carrying out tensile test on DSS warm-rolled at 898K (625°C) to more than 90% reduction in thickness and after annealing for different time intervals, namely 120 seconds (2 minutes) and 1800 seconds (30 minutes) where major microstructural transformations are observed. The ultimate tensile strength (UTS) is increased with increasing strain. Ultra high strength (UTS >1.0 GPa) but limited ductility (elongation to fracture: 4-6%) is achieved in the as warm-rolled condition. However, the UTS is greatly diminished (~700 MPa), whereas the ductility is significantly improved (elongation to failure $\geq 20\%$) after annealing. The drastic loss in strength at the expense of increased ductility is attributed to faster removal of deformation structure inside the phase bands after annealing.

The effect of change in strain path is investigated using processing by multi-pass cross-rolling route. During cross-rolling the RD and TD are mutually interchanged in every pass by rotation around the ND by 90°. The cross-rolling process was carried out at up to 90% reduction in thickness at 898K (625°C) so that

microstructure and texture evolution is not affected by dynamic strain aging.

Structural rotation is observed during cross-rolling such that after every warm-rolling pass banded microstructure consisting of alternate arrangement of the two phases elongated along the RD of the current pass is developed. Development of ultrafine lamellar structure is evident after 90% deformation.

Strong brass and rotated brass components were observed in austenite in DSS after processing by cross warm-rolling in contrast to strong pure metal type texture in the straight rolled material. On the other hand, The ferrite in the cross warm-rolling processed steel showed remarkably strong RD-fiber (RD//<011>) component {001}<011>. The development of texture in the two phases after processing by cross warm-rolling is explained by the stability of the texture components.

During isothermal annealing of the 90% cross warm-rolling processed material, the development of lamellar bamboo type morphology is observed initially before the collapse of the lamellar structure due to the mutual interpenetration of the phase bands. Ferrite shows strong recovery behavior resulting in formation of annealing texture similar to the deformation texture. In contrast, the austenite shows primary recrystallization without preferential orientation selection leading to the retention of deformation texture. The evolution of deformation and annealing texture in the two phases of the DSS is found to be independent of one another.

The present work systematically illustrates that development of microstructure and texture in the two phases of the experimental DSS alloy during thermo-mechanical processing by warm-rolling is strongly affected by the processing parameters, namely, warm-rolling temperature, strain and change in strain path. However, the evolution of microstructure and texture in the two phases can be explained on the basis of the behavior of the respective single

phase materials. In other words, the microstructure and texture evolution in one phase is not significantly affected by the presence of the other phase. This phenomenon is explained on the basis of evolution of a lamellar deformation structure with an alternate arrangement of phase bands during warm-rolling. It is believed that the major strain accommodation should take place at the phase boundaries which separate the two phases along the RD or in other words phase boundaries which are perpendicular to the RD. Since these phase boundaries are much less than the phase boundaries which are parallel to the RD, the evolution of microstructure and texture of the two phases remains independent of one another.

-: CHAPTER 1 :- INTRODUCTION

Thermo-mechanical processing of materials involving heavy deformation and annealing results in changes in microstructure and crystallographic texture. The microstructure and texture greatly affect the mechanical properties of the processed materials. Notable examples where crystallographic texture can significantly influence the physical or mechanical properties of materials include aluminum alloys for beverage can applications, deep drawing quality of steels for automotive applications, aluminum for use as capacitor foils and nickel base substrate tapes for coated superconductor applications. As a consequence the origin of crystallographic texture during thermo-mechanical processing has been an area of active research interest.

The origin of deformation and recrystallization texture has been intensely investigated in a wide variety of materials, including single phase FCC and BCC metals and alloys, two phase materials with the second phase dispersed in the matrix as precipitates and intermetallic alloys. However, the microstructure and particularly texture evolution during thermo-mechanical processing of duplex alloys where both the phases have grain structure, such as, ($\alpha+\beta$) brass or ferritic-austenitic duplex stainless steels (DSS) have received far less attention.

A brief but critical literature review presented in Chapter 2 reveals that the majority of the earlier studies has focused on ($\alpha+\beta$) brass as a model material for understanding the deformation and recrystallization behavior of duplex alloys. The published results suggest that deformation and recrystallization behavior of duplex alloys may be significantly complex affected by factors including phase fraction, imposed strain, precipitation of phases due to difference in homogenization and annealing temperatures. Studies on DSS are rather limited and they have been mostly carried out to understand microstructure and texture evolution after processing in either the hot or cold-working regimes.

In the present research an attempt has been made to understand the evolution of microstructure and texture in duplex alloys during thermo-mechanical processing using a custom made DSS alloy as a model material. In the present study the thermo-mechanical processing of DSS alloy has been carried out using warm-rolling. It must be pointed out that warm-rolling behavior of DSS has not been investigated so far. However, warm-rolling of DSS is considered particularly important in the present research as the deformation induced martensitic transformation which can occur easily during cold-working can be avoided. This ensures that additional complexities arising out of deformation induced martensitic transformation can be avoided.

The effects of three parameters, namely, warm-rolling temperature (Chapter 4), severe deformation (Chapter 5) and strain path change (Chapter 6) on the evolution of microstructure and texture have been investigated in the present work. Electron Back Scatter Diffraction (EBSD) technique has been used as the main experimental technique (Chapter 3) for analyzing the microstructure and texture of individual phases. Tensile properties of selected DSS specimens have been evaluated in order to understand the evolution of mechanical properties and explore the potential of warm-rolling as a novel thermo-mechanical processing route for DSS alloys.

-: CHAPTER 2 :- LITERATURE REVIEW

2.1 Duplex materials

Many of the commercially available and widely used engineering alloys are characterized by the presence of more than one phase. The second phase may usually be present as precipitates or dispersions in the matrix of the major phase. Notable examples of these materials are precipitation strengthened aluminum alloys and dual phase steels in which ferrite is the continuous phase and martensite with plate-like structure is distributed within the matrix of ferrite [1]. In contrast, duplex alloys are two phase materials where both phases have a grain structure for e.g. ($\alpha+\beta$) brass, ($\alpha+\beta$) titanium alloys and (ferritic+austenitic) duplex stainless steels (DSS).

The DSS are widely used in marine, oil refineries, and in chemical processing industries. The wide range of applications of DSS stems out from the high corrosion resistance and excellent mechanical properties of DSS. Austenitic stainless steels have good weldability and toughness, whereas weak resistance to stress corrosion cracking (SCC)[2]. On the other hand, ferritic steels have good resistance to SCC but with poor toughness, especially in the welded condition [2]. A combination of both austenite and ferrite may yield optimized properties including strength, toughness and high corrosion resistance. Therefore, it is important to maintain approximately equal volume fractions of the two phases in order to achieve optimized properties.

DSS in general have base composition of Fe-Cr-Ni with different other alloying elements like Mn, N, Mo, W. Microstructural evolution in DSS can be understood by means of diagram developed by Welding Research Council (Fig.2.1) [3]. The effects of different alloying elements on stability of phases is summarized by the Cr_{eq}/Ni_{eq} ($Ni_{eq}=Ni\%+35.\%C+20.\%N+0.5.\%Mn+0.25.\%Cu$), (Cr_{eq}

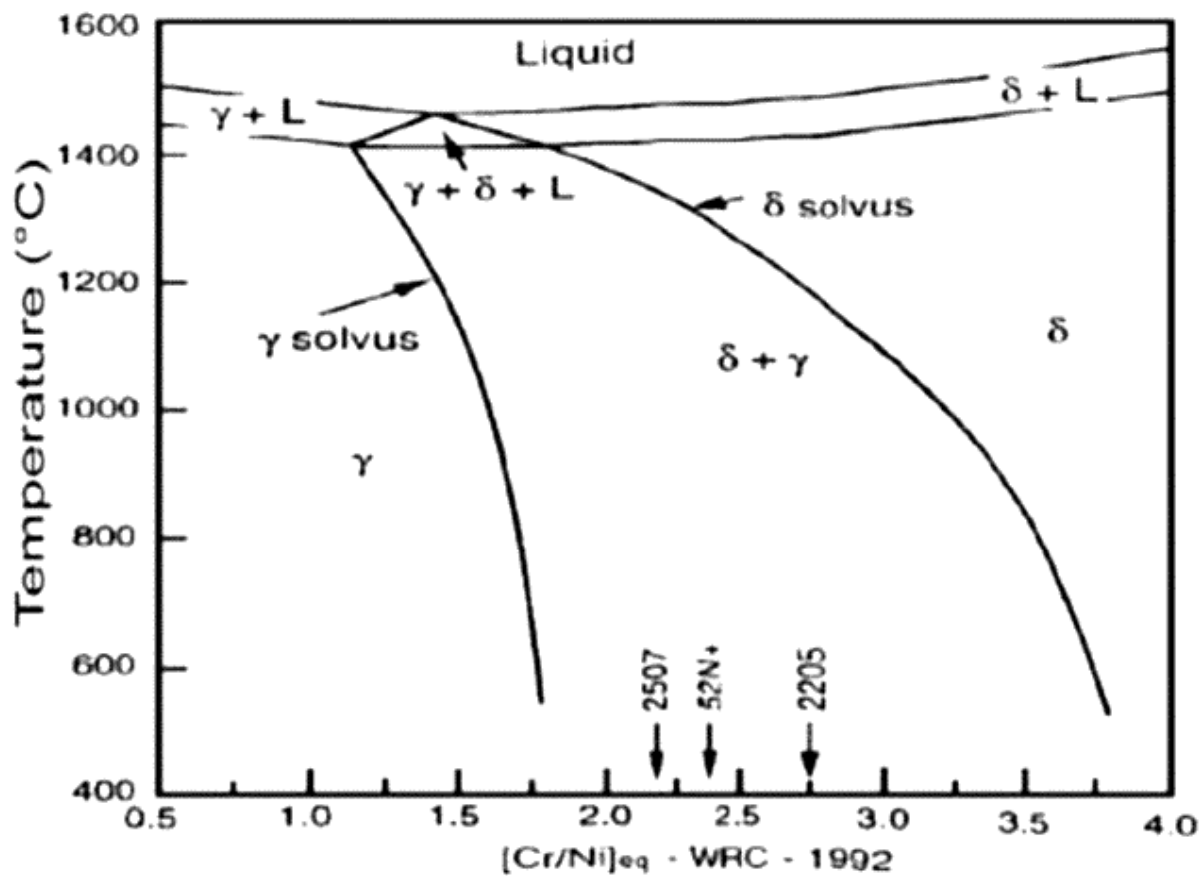


Fig.2.1: Section of the ternary Fe-Cr-Ni phase diagram [3].

$= \%Cr + \%Mo + 1.5\%Si + 0.7\%Nb$)) parameter. It may be observed from Fig.2.1 that such steels solidify as δ -ferrite. During cooling, below the δ -solvus temperature, the solid state transformation $\delta \rightarrow \gamma$ takes place. Table 2.1 shows the typical alloying elements and their contents in DSS [4]. Among these alloying elements Ni, Mn and N are austenite stabilizers, whereas, Cr, Mo, W are typical ferrite stabilizers. The three classical families of duplex grades are 2304 Mo free grades, the standard duplex type 2205 and the super-duplex grade 2507. The designation of alloys is given by the weight percentage of Cr and Ni (for example 2205 designation is for 22 wt.% of Cr and 05 wt.% of Ni). As the addition of Ni, Cr and Mo makes the alloy costlier, new generation of DSS were developed known as lean and hyper-DSS by substituting Ni by Mn and/or N [4]. The newly designed DSS are cost efficient without compromising the desired properties required for the intended applications. Table 2.2 shows a summary of various commercially available DSS grades along with their typical composition.

The main drawback of DSS is the formation of intermetallic phases which degrades mechanical properties. Figure 2.2 shows the effect of alloying elements on the formation of secondary phases below 1000°C. Such as σ -phase and α' . Other secondary phases are also observed to be stable with compositions such as Cr_2N , χ -phase and R phase. Due to the formation of secondary phases the working temperature of DSS is often limited to below 300°C or above 1000°C.

It may be noted that controlled thermo-mechanical processing of duplex steels can improve mechanical properties. However, this necessitates proper understanding the evolution of microstructure and texture during thermo-mechanical processing. Interestingly, while the deformation of single phase FCC or BCC metals and alloys, two phase alloys with second phase in the dispersed form has been

Table 2.1: Typical chemistry of Duplex stainless steel grades [4]

Family		Cr	Mo	Ni	Mn	Cu	N	Others
Standard Duplex	S32304	23	0	4	1		0.13	
	S32205	22	3	6	1		0.17	
	S32750	25	3.5	7	1		0.27	
	S32760	25	3.8	7	1	0.7	0.27	0.7
	S32520	25	3.5	7	1	1.5	0.25	
NEW-Duplex (EX)	S31500	18.5	2.7	5	1		0.1	
	S32101	21	0	1.5	5		0.2	
	S32001	20	0.3	1.7	5	0.3	0.15	
	S32003	20	1.7	3.5	2		0.15	
	S31260	27	3	7	1	0.5	0.16	0.3W
	S39274	25	3	7	1	0.6	0.27	2W
	S32906	29	2	6	1		0.4	
	S32707	27	5	6.5	1		0.4	

Table 2.2: List of commercially available DSS grades with chemical composition [5].

UNS No	C	Cr	Mo	Ni	N	Mn	Cu	W
Wrought duplex steel								
First generation duplex grade								
S32900	0.08	23-28	1-2	2.5-5	-	1		
S31500	0.03	28-29	2.5-3	4.3-5.2	0.05-0.1			
S32404	0.04	20.5-22.5	2-3	5.5-8.5	0.2	2	1-2	
Second generation duplex grade								
Lean								
S32001	0.03	19.5-21.5	0.6	1-3	0.05-0.17	4-6	1	
S32101	0.04	21-22	0.1-0.8	1.35-1.7	0.2-0.25	4-6	0.1-0.8	
S32202	0.03	21.5-24	0.45	1-2.8	0.18-0.26	2		
S82011	0.03	20.5-23.5	0.1-1	1-2	0.15-0.27	2-3	0.5	
S32304	0.03	21.5-24.5	0.05-0.6	3-5.5	0.05-0.2	2	0.5-0.6	
Standard								
S32003	0.03	19.5-22.5	1.5-2	3-4	0.14-0.2	2		
S31803	0.03	21-23	2.5-3.5	4.5-6.5	0.08-0.2	2		
S32205	0.03	22-23	3-3.5	4.5-6.5	0.14-0.2	2		
25Cr								
S31200	0.03	24-26	1.2-2	5.5-6.5	0.14-0.2	1		
S31260	0.03	24-26	2.5-3.5	5.5-7.5	0.1-0.3	1	0.2-0.8	0.1-0.5
S32506	0.03	24-26	3-3.5	5.5-7.2	0.08-0.2	1.5		0.05-0.3
S32520	0.03	24-26	3-4	5.5-8	0.2-0.3	1.5	0.5-2	
S32550	0.04	24-27	2.9-3.9	4.5-6.5	0.1-0.25	1.2	1.5-2.5	

Super duplex								
S32750	0.03	24-26	3-5	6-8	0.24-0.32	1	0.5	
S32760	0.03	24-26	3-4	6-8	0.2-0.3	1.1	0.5-1	0.5-1
S32808	0.03	26-29	0.8-1.2	7-8.2	0.3-0.4	0.8		2.1-2.5
S32906	0.03	24-26	1.5-2.6	5.8-7.5	0.3-0.4	1.5	0.8	
S32950	0.03	24-26	1-2.5	3.5-5.2	0.15-0.35	2		
S39274	0.03	28-30	2.5-3.5	6.8-8	0.24-0.32	1	0.2-0.8	1.5-2.5
S39277	0.025	26-29	3-4	6.5-8	0.23-0.33	0.8	1.2-2	0.8-1.2
Hyper duplex								
S32707	0.03	28-33	4-5	5.5-9.5	0.3-0.5	1.5	1	
S33207	0.03	24.5-26.5	3-5	6-9	0.4-0.6	1.5	1	
Cast duplex stainless steel								
J93370	0.04	24.5-26.5	1.75-2.25	4.75-6	-	1	2.75-3.25	
J93372	0.04	24-27	1.7-2.3	4.7-6	0.1-0.25	1	2.7-3.3	
J93373	0.03	22.5-24.5	2.9-3.8	5.6-6.7	0.22-0.33	1.2	1.4-1.9	
J93345	0.08	24-27	3-4.5	8-11	0.1-0.3	1		
J93371	0.06	21-23	1.75-2.5	4-6	0.15-0.25	1		
J92205	0.03	24-26	2.5-3.5	4.5-6.5	0.1-0.3	1.5		
J93404	0.03	24-26	4-5	6-8	0.1-0.3	1.5		
J93380	0.03	24-26	3-4	0	0.2-0.3	1	0.5-1	0.5-1

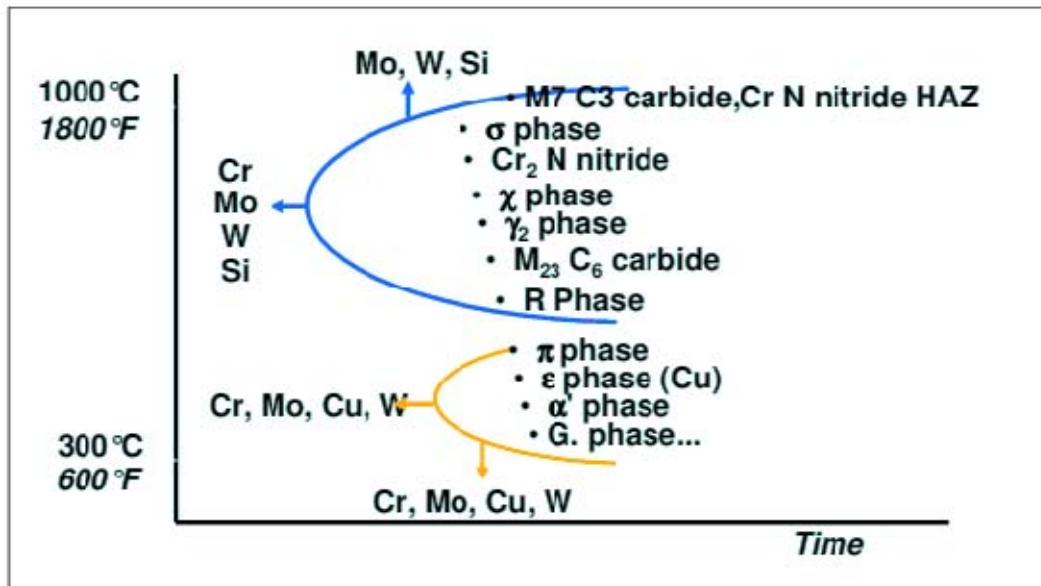


Fig.2.2: Summary of the effects of alloying elements on the formation of various precipitates [6].

extensively investigated, duplex alloys have attracted much lesser attention [7]. In the present study the focus is on understanding of the evolution of microstructure and texture during thermo-mechanical processing i.e. during deformation and recrystallization of DSS. As DSS consists of two phases (FCC+BCC), proper understanding of the evolution of microstructure and texture of the two phases during thermo-mechanical processing is of utmost importance.

In the following sections the microstructure and texture of the single phase FCC and BCC alloys will be critically reviewed which will be followed by an extensive review of the available literature on duplex alloys to place the present research in the most appropriate context.

2.2 Evolution of texture during deformation and recrystallization of single phase FCC materials

2.2.1 Representation of texture

Deformation processing of polycrystalline materials in general leads to preferred orientations or crystallographic texture with respect to a fixed reference system. The crystallographic texture can be conveniently represented by $\langle uvw \rangle$ where planes are parallel to the rolling plane (or $\langle hkl \rangle$ directions are parallel to the ND as in the cubic system plane and plane normals have the same indices) and $\langle uvw \rangle$ directions are parallel to the RD.

Amongst several methods of representing texture, pole figures (PFs) are simple yet effective. A PF is a stereographic projection, which is a two dimensional (2D) representation showing the distribution of poles (or plane normal) with respect to the sample reference system. Figure 2.3 shows the position of the (0001) pole on the unit sphere with regard to a sample reference frame. The position of a given pole on the sphere is commonly characterized in

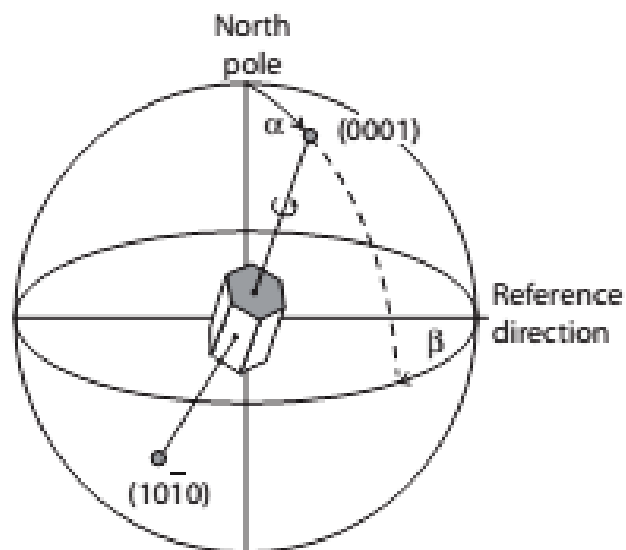


Fig.2.3: The unit sphere showing the position of the (0001) pole with regard to an external reference frame which is described by the two angles α and β [8].

terms of the two angles α and β . The angle α describes the azimuth of the pole, whereas the angle β denotes the rotation of the pole starting from a specified reference direction.

The principle of projection of a pole onto a 2D plane is shown in Fig.2.4 where the $\{100\}$ poles of a cubic crystal present in the stereographic projection with respect to the sample reference frame. Figure 2.4(a) shows the crystal in the unit sphere whose $\{100\}$ poles are projected onto the equatorial plane (Fig. 2.4(b)) and Fig.2.4(c) shows $\{100\}$ PF and definition of the PF angles α and β for the (100) pole with respect to the sample reference system.

Although, PF is one of the most effective ways of representing texture, however the information provided by PFs is mostly qualitative or semi-quantitative in nature [8]. Thus, analysis of PFs is rather difficult or ambiguous for complex texture where several components are present. In these cases analysis of orientation distribution functions (ODFs) yields much detailed information concerning texture.

ODF is a three dimensional representation of texture and gives the frequency of occurrence of any given orientation or texture component in Euler space. The Euler space is defined by three mutually orthogonal axes defined by a set of three Euler angles ϕ_1 , Φ , ϕ_2 . These set of Euler angles constitute a scheme of three consecutive rotations for transforming the sample frame (S) into crystal frame (C) as shown in Fig.2.5. Thus, each orientation given by $\langle uvw \rangle$ notation would correspond to a set of ϕ_1 , Φ , ϕ_2 and occupy a point in the three dimensional Euler space shown schematically in Fig.2.6.

ODFs are generated from several experimentally measured PFs using diverse mathematical methods. Most widely accepted methods are developed independently by Bunge [9] and Roe [10] who have used generalized spherical harmonic functions for this

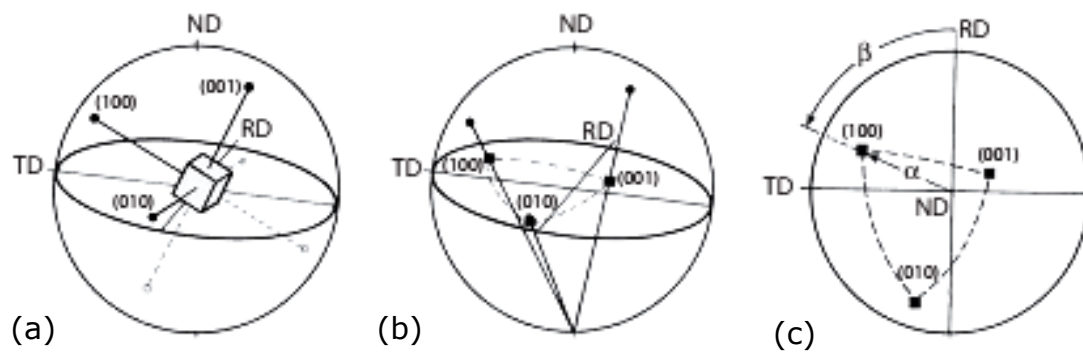


Fig.2.4: Representation of the $\{100\}$ poles of a cubic crystal in the stereographic projection. (a) Crystal in the unit sphere; (b) projection of the $\{100\}$ poles onto the equator plane; (c) $\{100\}$ pole figure and definition of the pole figure angles α and β for the (100) pole [8].

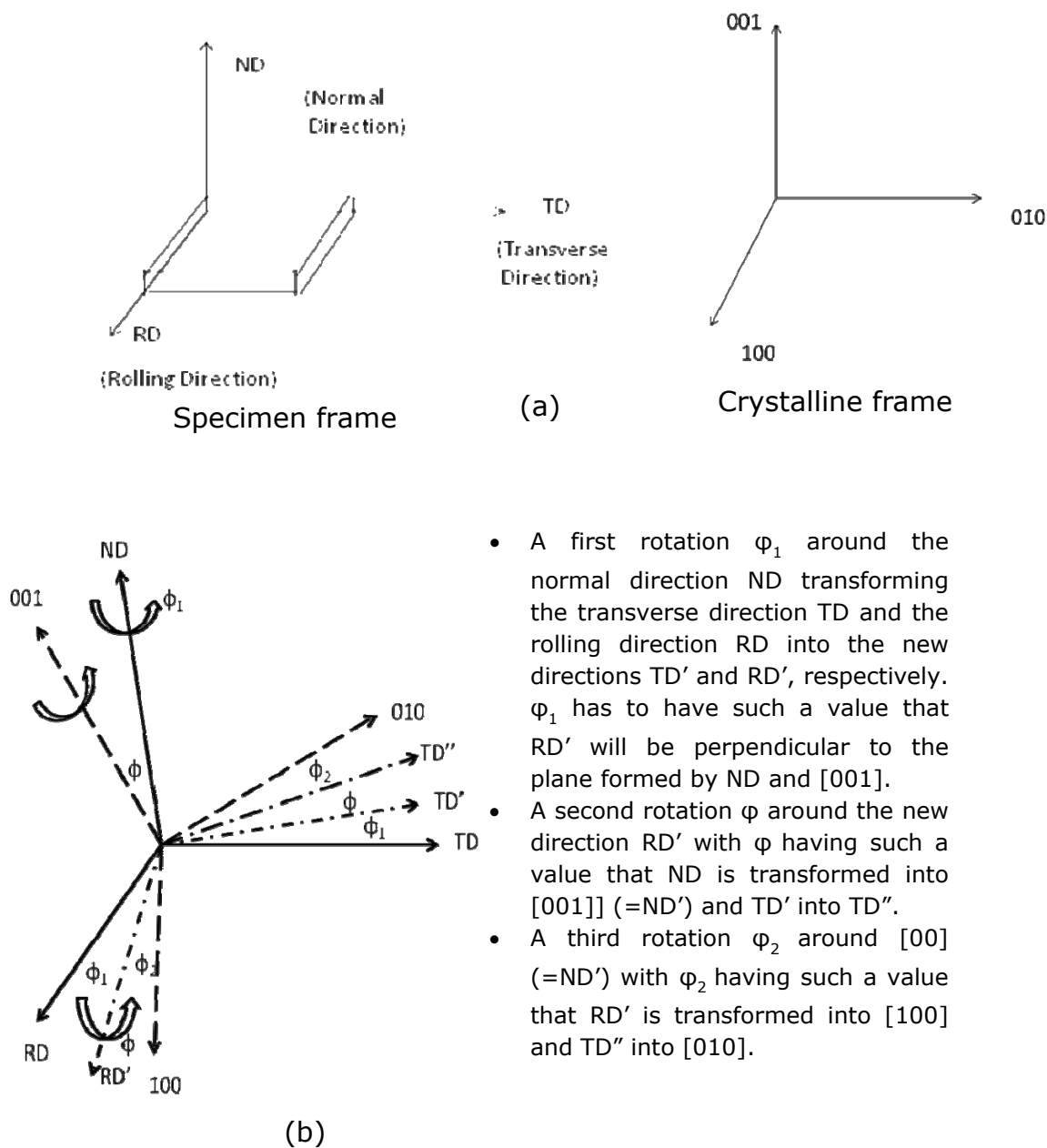


Fig. 2.5: Schematic illustration of (a) reference system and (b) Euler angles [11].

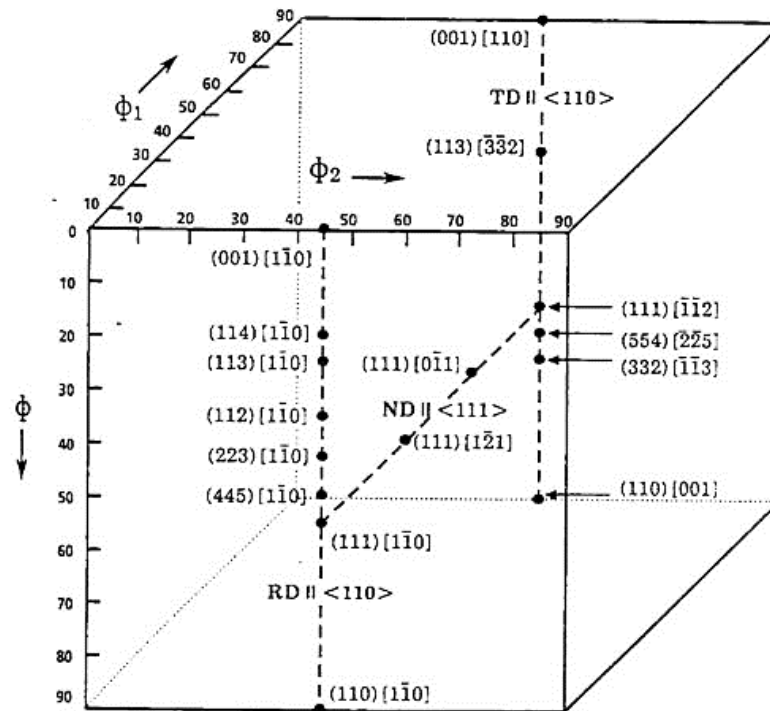


Fig.2.6: Schematic representation of the three dimensional Euler space [12].

purpose. A detailed analysis of the mathematical treatments for ODF calculation can be found elsewhere [13, 14].

Depending on the crystal and sample symmetries the Euler space can be reduced. For example the Euler space is reduced to $0^\circ \leq \phi_1 \leq 90^\circ$, $0^\circ \leq \Phi \leq 90^\circ$ and $0^\circ \leq \phi_2 \leq 90^\circ$ for cubic crystal structure and orthorhombic sample symmetry. However, the total Euler space can still be divided into three basic regions where each orientation appears only once.

The preferred orientation or texture would be expressed as the value of the orientation density at each point in Euler space in multiples of random. As it is difficult to interpret ODF in three dimensional space it is conveniently represented in two dimensional space using constant sections along one of the Euler angles in steps of 5° . For FCC materials ODF is represented in constant ϕ_2 sections [15] whereas for BCC materials constant ϕ_1 sections are used for representation of texture [16].

Texture can also be conveniently represented in certain cases by plotting orientation densities along certain characteristic paths or distinct crystallographic fibers. In heavily rolled FCC materials texture is characterized by two important fibers i.e. α and β fibers. The α fiber ($\{011\}$ //ND) extends from the Goss or G ($\{011\}<100>$) to the brass or B_s ($\{011\}<112>$) orientation while the β fiber runs from the copper or Cu ($\{112\}<111>$) to the brass or B_s ($\{011\}<112>$) through S ($\{123\}<634>$). Figure 2.7 illustrates the positions of the texture fibers along with the main rolling texture components of FCC materials in Euler space, whereas Fig.2.8 indicates their ideal locations in the constant ϕ_2 sections.

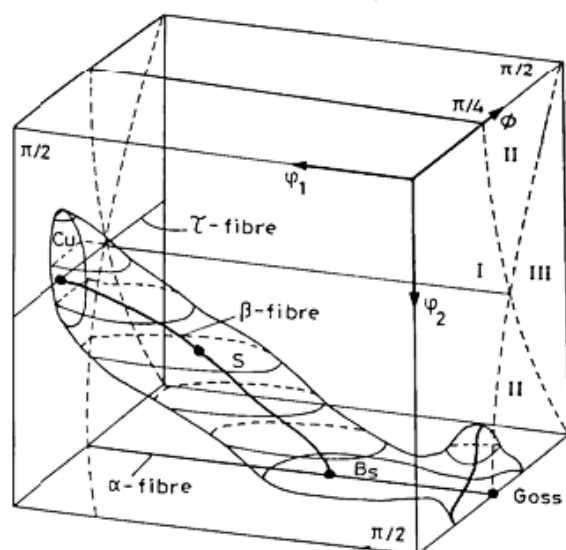


Fig.2.7: Three dimensional view of Euler space with locations of some important ideal orientations and fibers of FCC metals [15].

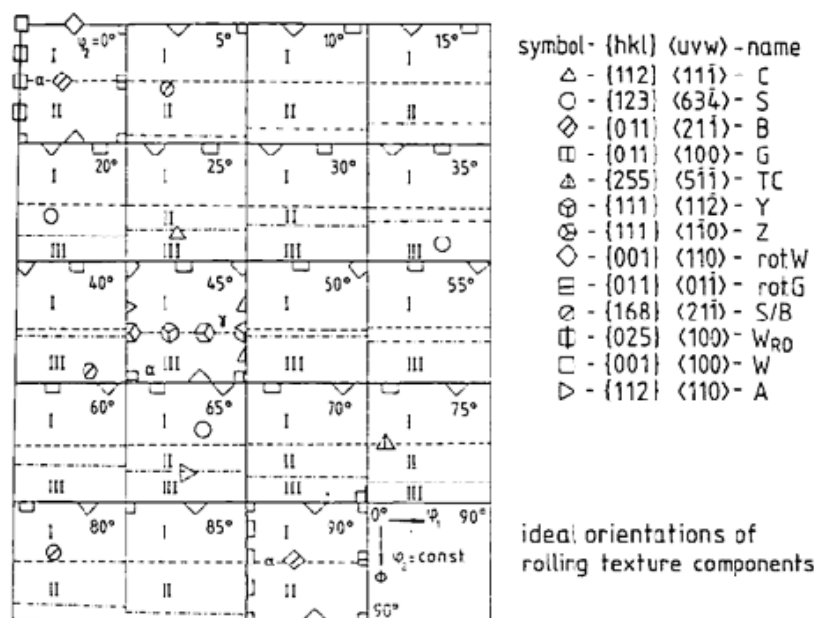


Fig.2.8: Ideal orientations of FCC materials shown in the ϕ_2 sections of Euler space [15].

2.2.2 Deformation texture of FCC materials

Microstructure and texture evolution of FCC materials during deformation depends significantly on their stacking fault energy (SFE). Therefore, medium to high SFE materials, such as, aluminum, nickel and copper show very different deformation texture as compared to low SFE FCC materials, such as, austenitic stainless steels and brass.

The rolling textures of high to medium SFE materials such as Al, Ni, and Cu are characterized by pure metal or copper type texture [7]. The copper type texture may be described by the strong presence of the ideal orientations Cu, S and B_s [17-19]. The name copper type texture is given as the texture developed is identical to the texture developed in pure copper which is shown in Fig.2.9. Figures 2.9(a) and 2.9(b) show the (111) PF of 95% cold rolled copper and aluminum, respectively which appear quite similar. This texture is developed in the form of a continuous tube running from B_s ($\phi_1=35^\circ$, $\Phi=45^\circ$, $\phi_2=0^\circ/90^\circ$) through S ($\phi_1=59^\circ$, $\Phi=37^\circ$, $\phi_2=63^\circ$) to Cu ($\phi_1=90^\circ$, $\Phi=34^\circ$, $\phi_2=45^\circ$). A schematic representation of the tube is given in Fig.2.7. The tube shown in Fig.2.7 [15] can also be described in terms of its axis or skeleton line. A better description of the texture in 90% rolled pure copper can be provided by the ODF shown in Fig.2.10 which shows strong intensities at the ideal locations of pure metal texture components.

The deformation textures of low SFE FCC metals and alloys such as austenitic stainless steel, α brass are known as brass or alloy type texture. Alloy type texture is described by the presence of the ideal orientations which include G ($\phi_1=0^\circ$, $\Phi=45^\circ$, $\phi_2=90^\circ$) and B_s orientation ($\phi_1=35^\circ$, $\Phi=45^\circ$, $\phi_2=90^\circ$). In low SFE alloys, with increasing strain, copper type texture is gradually transformed to brass type texture. Such transition is observed in Cu-Zn alloys [15]

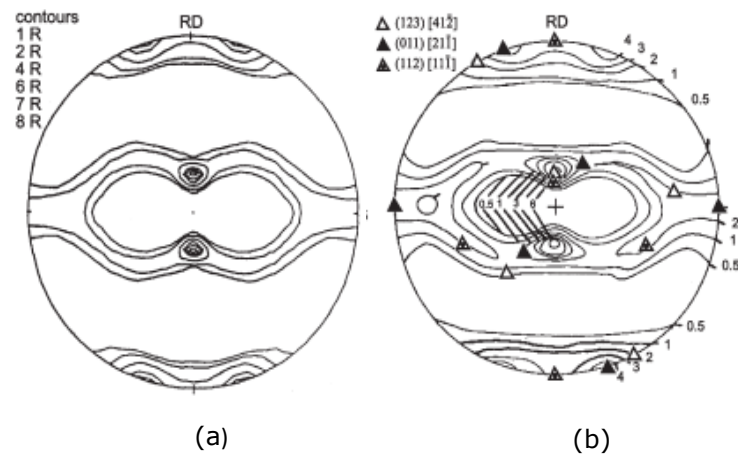


Fig.2.9: (111) pole figure of 95% cold rolled (a) copper and (b) aluminum [7].

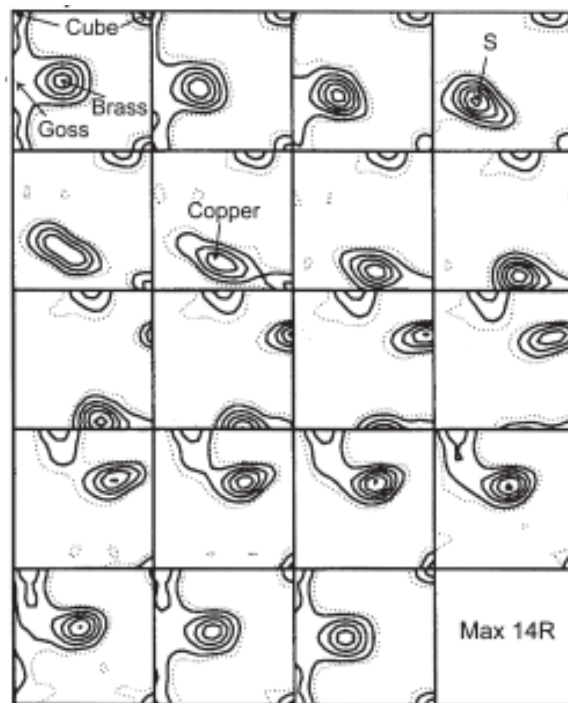


Fig.2.10: ODF of 90% cold rolled aluminum with positions of deformation texture components indicated [7].

which is attributed to decrease in SFE due to increasing solute content.

Development of alloy type texture is shown in Fig.2.11 by the (111) PFs of a series of Cu-Zn alloys having 0, 5, and 30% Zn rolled to 50%, 75% and 95% reduction in thickness [15]. Well-developed alloy type texture after 95% cold-rolling of 70:30 brass is shown in the ODF in Fig.2.12. Transition from copper type texture to brass type texture in low SFE alloys is explained on the basis of formation of deformation twins [19] [20-23].

2.2.3 Annealing textures of FCC materials

During deformation energy is stored in materials mainly in the form of dislocations. This energy is released by three main processes, namely, recovery, recrystallization, and grain growth. The driving force for both recovery and recrystallization processes is the reduction in the stored energy of the deformed materials. However, as recovery lowers the driving force for recrystallization, excessive recovery may retard recrystallization. Conversely, the extent of recovery is limited by the ease with which recrystallization can occur.

Recrystallization in which the nucleation and growth of strain free grains occurs by the formation and migration of high angle grain boundaries (HAGBs) which consumes the deformed microstructure is known as primary or discontinuous recrystallization. In contrast, the process by which deformation microstructure can be converted into a microstructure consisting of grains fully bounded by HAGBs without any nucleation and growth of strain free grains (which are characteristics of a discontinuous recrystallization process as already pointed out) is known as continuous recrystallization or extended recovery.

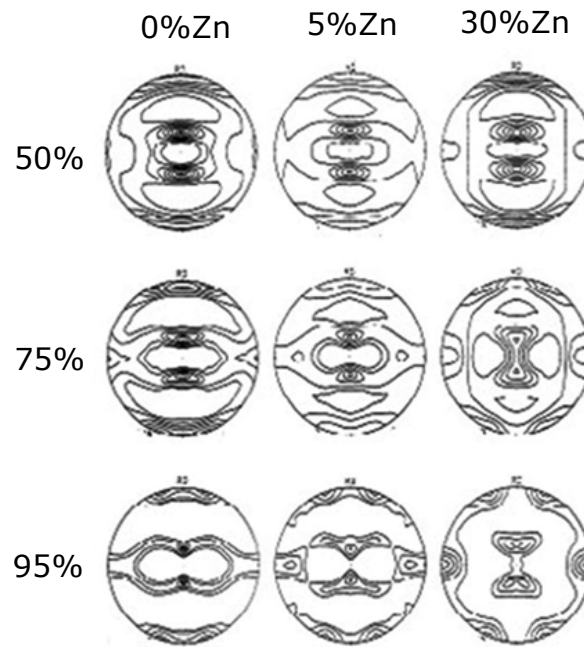


Fig.2.11: (111) pole figure of 95% cold rolled 70:30 brass [15].



Fig.2.12: ODF of 95% cold rolled 70:30 brass [15].

In the continuous recrystallization process the major mechanism of microstructural transformation is subgrain growth. Figure 2.13 schematically shows the major differences between the continuous (Fig.2.13((a)-(b)) and discontinuous recrystallization (Fig.2.13((c)-(d)) processes [24].

In general, during continuous recrystallization (extended recovery process) no perceptible change in annealing texture as compared to deformation texture is expected. This could be easily understood by the fact that this process does not involve nucleation and growth of strain free grains. In sharp contrast, the annealing textures of materials which show the discontinuous recrystallization behavior involving nucleation and growth of strain free grains, recrystallization textures may be significantly different as compared to their deformation textures.

Medium to high SFE FCC metals and alloys, such as, pure aluminum, nickel and copper show sharp cube texture ($\{001\}<100>$) following heavy deformation and annealing. The origin of the cube texture has been a subject of intense research for many years, presumably due to the importance of this texture component in controlling the physical and mechanical properties in many engineering applications including high voltage aluminum capacitor foil [25], nickel base superconducting substrate tapes [26] and deep-drawing properties of aluminum alloy beverage cans [27]. Understanding the origin of cube texture is also important for analyzing the two major but contrasting theories of formation of recrystallization texture, namely, oriented nucleation and oriented growth models.

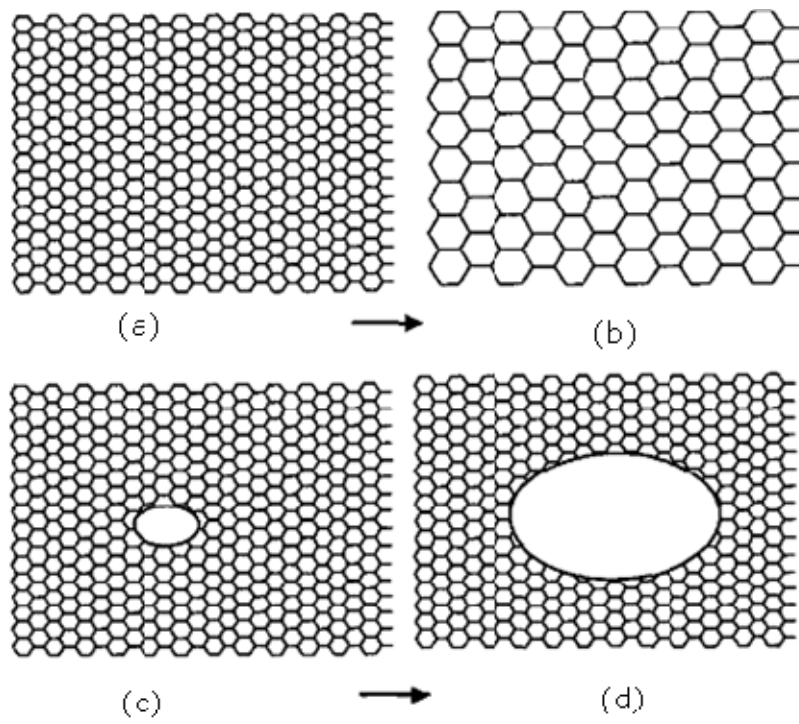


Fig.2.13: Schematic illustration of ((a,b)) continuous and ((c,d)) discontinuous annealing processes [7].

The basic premise of the oriented nucleation theory is the preferred nucleation of grains of certain orientations e.g. cube orientation from pre-existing regions in the deformation matrix (known as cube bands) [28]. It is also suggested that the preferential nucleation of cube grains would be aided by the lower stored energy of the cube regions due to their unique dislocation arrangement for ideal cube orientation involving interaction of dislocations with orthogonal burgers vector.

The development of sharp recrystallization texture, according to the oriented growth model, is attributed to the preferential growth of grains of specific orientations (e.g. cube grains) from a rather random assembly of orientations. The preferential growth of certain orientations is attributed to the presence of high mobility boundaries with special misorientation relationship e.g. $40^\circ <111>$ separating these grains from the deformed matrix.

In contrast to high to medium SFE FCC materials, the annealing textures of low SFE materials are far less investigated and understood. It must be pointed out that while the development of a brass-type texture during cold-rolling in low SFE alloys is widely reported [22, 29], there is much less clarity concerning the recrystallization texture of low SFE materials. This is compounded by the fact that the recrystallization texture of low SFE alloys is strongly influenced by the starting grain size, annealing temperatures and imposed strain. In addition, alloy composition also plays a crucial role.

In a more simplified manner, the annealing textures of low SFE FCC materials have been mostly studied using 70:30 brass as a model material. Low temperature annealing of heavily deformed 70:30 brass results in the formation of the well-known brass recrystallization component $\{236\} <385>$ component. The origin of brass recrystallization component is attributed to a sequential process involving nucleation at shear bands, formation of twins and

growth of this component due to the favorable misorientation relationship ($40^\circ < 111 \rangle$) with the major rolling texture component of the low SFE FCC materials i.e. the brass component [30]. However, the brass recrystallization component is weak after annealing at high temperatures and recrystallization texture is dominated by typical rolling texture components, such as B_s , S and ND-rotated cube [7].

In recent times, annealing textures of other low SFE materials, such as, austenitic steels, twinning induced plasticity (TWIP steels) and high entropy alloys (HEAs) have been reported. Bracke et al [31] have critically analyzed the effects of various processing and microstructural parameters on the formation of recrystallization textures in various TWIP and austenitic stainless steels having low SFE values (15-45 mJ/m²). Interestingly, the majority of the investigations reported retention of rolling texture components, particularly the B_s and G [31-33] and development of α -fiber in the [33, 34]. As already pointed out, continuous recrystallization or extended recovery can result in the retention of deformation texture, however, this possibility has been ruled out in favor of discontinuous recrystallization evidenced by the presence of clear recrystallization front [32]. The alternative but more acceptable explanation for the retention of deformation texture components after recrystallization is a consequence of nucleation of recrystallization without preferential orientation selection in an energetically homogeneous deformed matrix [31, 32]. Very similar observations have recently been reported in low SFE high entropy alloys [35]. In contrast, some researchers have also reported very weak or even randomized texture in TWIP steels after cold-rolling and annealing [36, 37]. The weak or randomized texture has been explained on the basis of nucleation at micro shear bands [36, 38], large starting grain size prior to cold-rolling [31] or profuse annealing twin formation due to low SFE of the alloys [39].

2.3 Deformation and annealing textures of single phase BCC materials

2.3.1 Deformation textures of BCC materials

The rolling textures of BCC materials are usually described by two crystallographic fibers, namely, the RD (or α) ($\langle 011 \rangle // \text{RD}$) and ND (or γ) ($\langle 111 \rangle // \text{ND}$). Figure 2.14 shows the two fibers together with the major orientations along these fibers [40]. Despite the fact that BCC rolling and recrystallization textures are usually shown in constant ϕ_1 sections, it is observed that the two most important texture fibers can be easily visualized in the $\phi_2=45^\circ$ section as shown in Fig.2.15 [8]. The characteristic changes in texture during rolling and recrystallization can thus be effectively compared by plotting the intensity along these fibers.

The rolling and recrystallization textures of different types of BCC steels show similarities, but also exhibit characteristic differences depending on starting texture, microstructure and presence of precipitates. However, review of texture development in low carbon, interstitial free (IF) and ferritic stainless steels will be most relevant for the present study.

The rolling texture evolution in low-carbon steels is independent of composition and processing [41]. During hot-rolling of these steels recrystallization and $\gamma \rightarrow \alpha$ phase transformation happens which leads to grain refinement and a randomization of texture [40]. During cold-rolling the texture is strengthened with increasing strain. At lower strain ($\leq 70\%$ reduction in thickness), strong RD-fiber with $\{001\}\langle 110 \rangle$ and $\{112\}\langle 110 \rangle$ as the dominating components could be observed. In contrast, weak presence of the ND-fiber component $\{111\}\langle 112 \rangle$ is reported. However, beyond

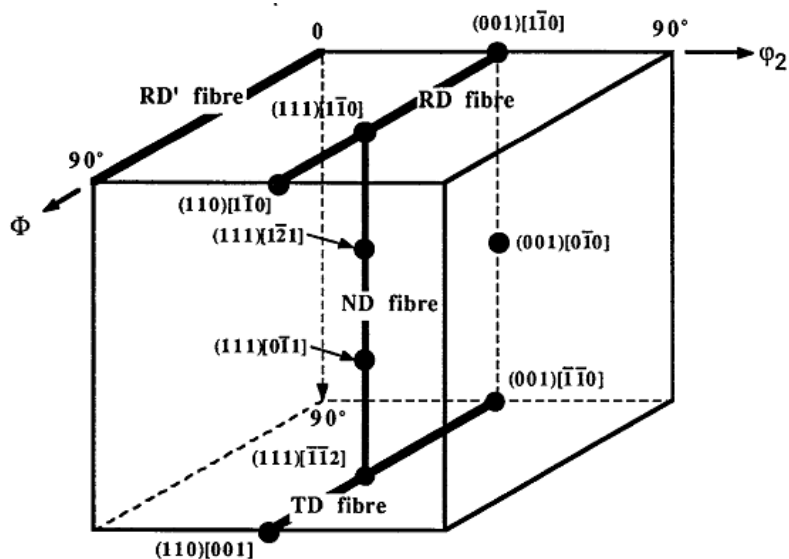


Fig.2.14: Three dimensional view of Euler space with locations of some important ideal orientations and fibers of BCC metals [40].

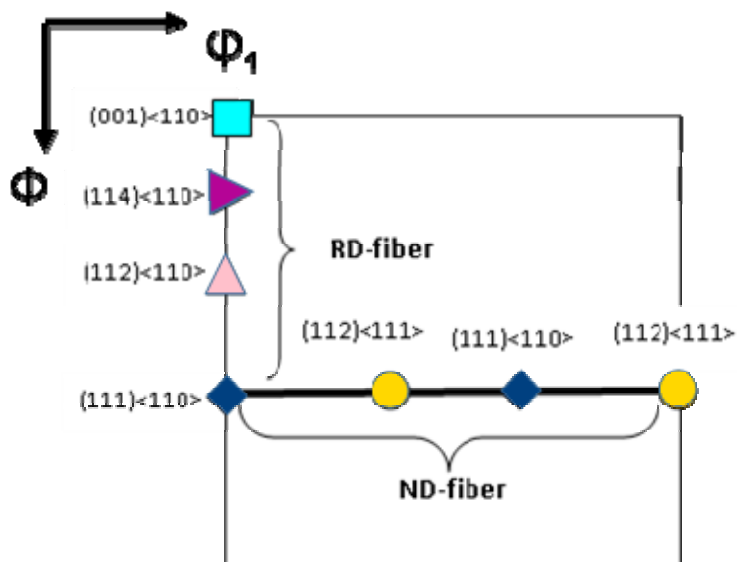


Fig.2.15: Typical $\phi_2 = 45^\circ$ section of ODF of BCC materials showing the locations of individual texture components along the two fibers [8].

this deformation level maximum of the RD-fiber is shifted to $\{112\}\langle 110 \rangle$ and that on the ND-fiber from $\{111\}\langle 112 \rangle$ to $\{111\}\langle 110 \rangle$ [16]. The ND-fiber usually shows uniform intensity upto 80% reduction, but during further deformation the $\{111\}\langle 110 \rangle$ emerge as the dominant texture component. This is understood from Fig.2.16 which show variation of texture components along RD and ND fibers with increasing reduction in an extra low carbon IF steel.

Ferritic stainless steel grades will not undergo $\gamma \rightarrow \alpha$ phase transformation during hot rolling, as a result, no randomization of texture takes place [42, 43]. Development of texture in these steels is dependent on the composition and processing history. The hot bands of ferritic stainless steels commonly display pronounced textures and strong through-thickness gradients. In the center layer a sharp RD-fiber [44] and close to the surface strong shear components such as G, $\{441\}\langle 1118 \rangle$, and B_s develop during hot-rolling [44]. However, after heavy cold-rolling, stronger RD-fiber than ND-fiber is observed. The sharpness of the α -fiber is increased at the center layer of the strip, whereas, in the surface layer shear components rotate towards the RD-fiber [44].

Other BCC materials, like tantalum, molybdenum, and niobium, show the presence of RD and ND-fibers in the cold-rolling textures. However, pronounced through-thickness texture gradient is reported in cold-rolled refractory metals [8].

2.3.2 Annealing textures of BCC materials

Annealing textures of BCC materials strongly depend on the previous hot and cold-rolling textures [45]. The main effect of recrystallization on the textures of BCC metals is the sharpening of the ND-fiber at the expense of the RD-fiber [46, 47]. This is clearly

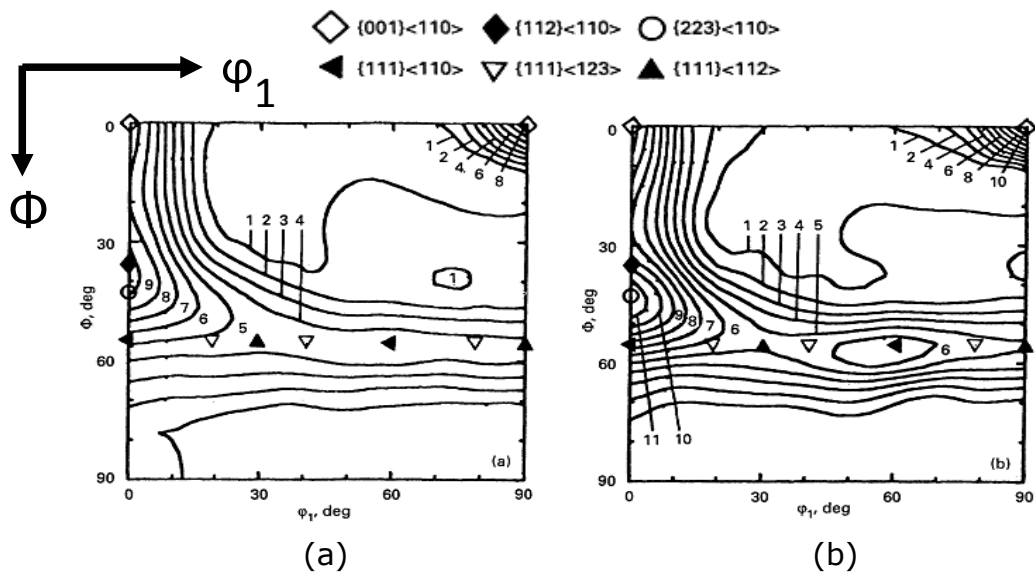


Fig.2.16: $\phi_2 = 45^\circ$ sections of ODFs of ELC IF steel after cold reductions of (a) 70% and (b) 85% [48].

understood from Fig.2.17 which shows the $\phi_2 = 45^\circ$ sections of the ODFs of 90% cold-rolled (Fig.2.17(a)) and annealed (Fig.2.17(b)) Ti and Nb added IF steel.

The typical ND-fiber recrystallization texture of BCC materials is attributed to the preferred nucleation at the pre-existing HAGBs favorable for easy nucleation [49]. The ND-fiber orientations $\{111\}\langle 110 \rangle$ and $\{111\}\langle 112 \rangle$ presumably have higher stored energy than other texture components [46]. Therefore, nuclei form preferentially in grains with ND-fiber orientations, which subsequently grow at the expense of other orientations, including the RD-fiber orientations. For ferritic stainless steels, however, different recrystallization textures are reported after annealing. The recrystallization textures are often quite weak, consisting of ND-fiber orientations with a fairly uneven intensity distribution [50]. This is attributed to the effect of the fine dispersions in the matrix which retard the migration of the grain boundaries [44].

Due to annealing after low deformation or at low temperatures (i.e. where the driving force for recrystallization is low), recovery becomes the primary softening mechanism in deformed BCC materials. The process of recovery is particularly important with regard to the development of RD-fiber component $\{001\}\langle 110 \rangle$. In comparison to other rolling texture components of the RD and ND fibers, $\{001\}\langle 110 \rangle$ is having the minimum stored energy resulting in preferential recovery [51]. As a result this component is retained in the annealing texture along with other ND-fiber orientations [40]. Specimens which are heavily deformed or annealed at higher temperatures, a pronounced ND-fiber texture is developed through usual discontinuous recrystallization process as already explained.

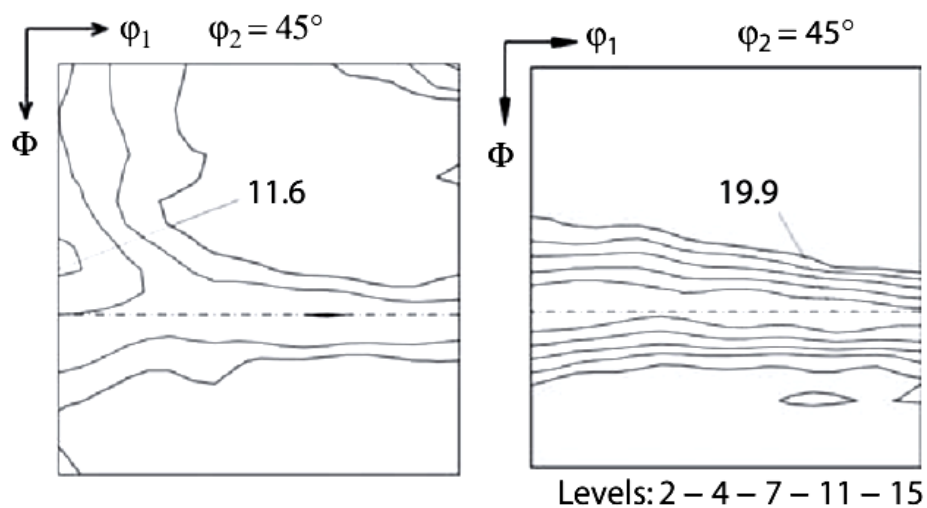


Fig.2.17: (a) $\phi_2 = 45^\circ$ section of the ODF of 90% cold-rolled Ti+Nb microalloyed interstitial-free steel, (b) $\phi_2 = 45^\circ$ section of ODF of 90% cold rolled and annealed (1hr at 700°C) Ti-alloyed interstitial-free steel [8].

2.4 Evolution of microstructure and texture in DSS during deformation and annealing of DSS

2.4.1 Evolution of microstructure and texture during deformation

Evolution of Microstructure and texture in DSS has been studied extensively during hot-working [52-62] and to a lesser extent during cold-rolling [63-72]. The purpose of this section is not to comprehensively cover the available literature on DSS, but to bring out the most salient observations pertaining to hot and cold-working of DSS in order to place the present research in the most appropriate context.

Hot deformation of DSS leads to dynamic restoration processes, such as dynamic recovery and dynamic recrystallization. Dynamic restoration processes in the two phases are very similar to those in the single phase materials. Single-phase austenitic steels usually show dynamic recrystallization behavior owing to their low SFE. It might be noted that although dynamic recrystallization has been reported in austenite of DSS [52] contradicting observations suggesting that this behavior is inhibited in two phase alloys is also reported [53]. In contrast to austenite, ferrite undergoes dynamic recovery [54, 55]. Softening mechanism in the ferritic phase has also been described as extended dynamic recovery [56] or continuous recrystallization. These two mechanisms are differentiated based on the relative proportion of low- and high-angle boundaries in the microstructure.

During hot-rolling, deformation behavior of the two phases in DSS is considerably affected by the presence of the other phase. In hot working range austenite is significantly stronger than ferrite which affects the strain partitioning [54, 57, 58]. At high temperatures i.e. above 1000°C, it is found that strain partitioning takes place at the early stages of deformation and the imposed strain is mostly accommodated by the ferrite phase [55]. At higher

strains, the load is transferred from ferrite to austenite resulting in an increase in the dislocation density in austenite till dynamic recrystallization is initiated [59].

Duprez et al [60] have reported that the texture development in the two phases of DSS during hot-rolling is similar to that in the respective rolled single phase materials. As a result the texture of austenite is found to consist of the β -fiber components and a weak cube component, whereas the ferrite texture exhibits presence of both RD and ND fibers [60, 61]. The microtexture of individual phases in hot-rolled DSS has been carried out by Herrera et al [62]. These authors have reported the presence of α and β fiber components along with the cube component in austenite (Fig.2.18 (a)) whereas the texture of ferrite is characterized by stronger RD-fiber and cube component (Fig.2.18(b)).

Cold-rolling behavior of DSS has been studied in the medium to heavy deformation regime [63-72]. The two phases show the development of lamellar banded morphology during cold working as shown in Fig.2.19 [66]. Figure 2.19(a) shows the development of banded morphology in DSS after 60% reduction in thickness while Fig.2.19(b) shows remarkable refinement of thick banded microstructure after 90% reduction.

Significant phase interaction during rolling has been reported by other researchers which strongly affect the microstructure and texture evolution [63, 64]. It is shown that austenite, being the softer phase in DSS, exhibits more strain-hardening than ferrite [65]. In sharp contrast, cold-rolling behavior of nitrogen alloyed DSS with nearly equal volume fraction of the two phases shows that the imposed strain is partitioned rather equally amongst the two constituent phases [66]. It has been reported that the deformation

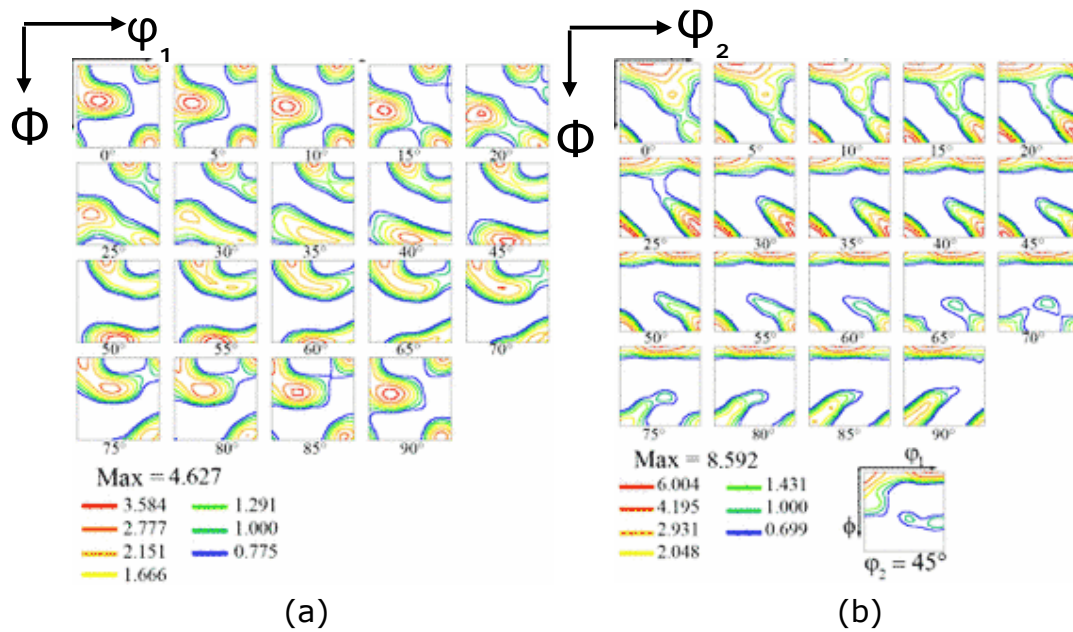


Fig.2.18: ODFs of (a) austenite and (b) ferrite in hot-rolled DSS [62].

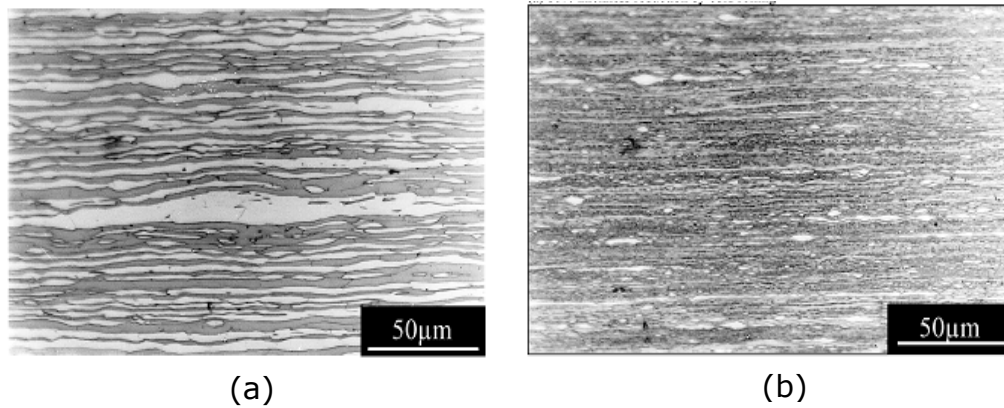
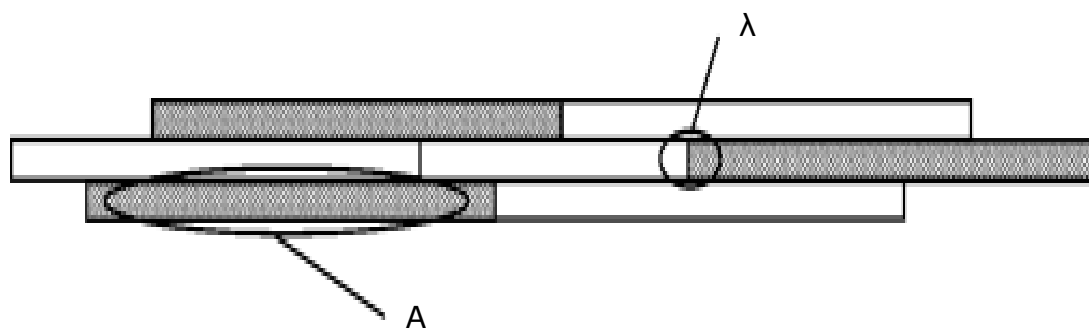


Fig.2.19: The formation of banded morphology in DSS cold-rolled to (a) 60% and (b) 90% reduction in thickness [66].

the behavior of one phase is not affected by the presence of the other phase. In other words the two phases show deformation behavior independent of one another. The observed behavior has been explained by Keichel et al [66] based on the lamellar deformation structure of heavily cold-rolled DSS. Keichel et al [66] have argued that the strain accommodation should take place at the phase boundaries which separate the two phases along the RD or in other words phase boundaries which are perpendicular to the RD as schematically shown in Fig.2.20. Since these phase boundaries have a much less presence than the phase boundaries which are parallel to the RD, the deformation behavior of the two phases should be independent of one another.

In contrast to the formation of microstructure during cold deformation, the evolution of texture has been studied to a rather limited extent. Ferrite in heavily cold-rolled DSS shows the presence of characteristic RD and ND fibers (Fig.2.21(a)), whereas austenite in DSS shows a predominantly brass type texture (Fig.2.21(b)). Thus, the deformation textures of the two phases of DSS resemble those of the respective single phase materials [67-69]. This is understood from the fact that the two phases of DSS undergo deformation independent of one another and as a result, they have finally developed texture characteristic of the respective single phase materials. However the initial texture is found to play an important role in the formation of deformation texture during cold-rolling [67]. It is reported that DSS with random starting texture show sluggish development of rolling textures in both the phases. In contrast, in case of presence of strong initial texture, evolution of stable rolling texture components with characteristic spread could be observed with increasing deformation.



λ = Area where phase boundary separating two phases
 A = phase boundary area.

Fig.2.20: Schematic of the microstructural arrangement in cold-rolled DSS (rolling direction horizontal) [66].

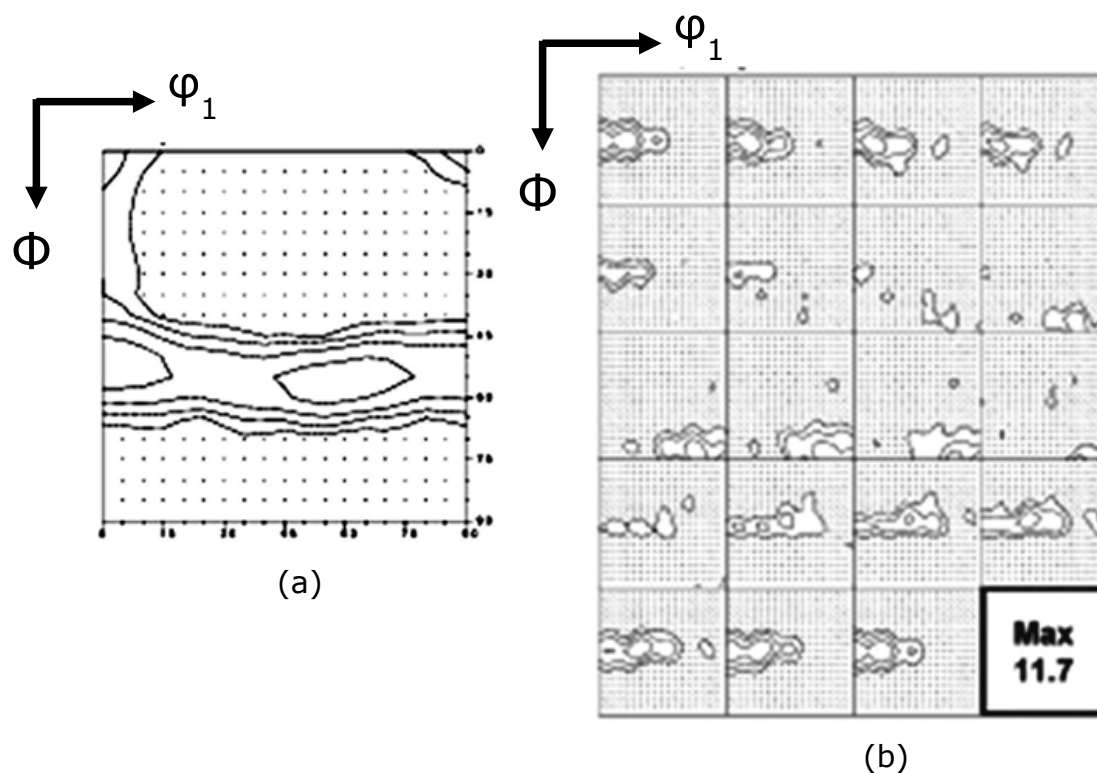


Fig.2.21: (a) $\phi_2 = 45^\circ$ section of ODF of ferrite phase and (b) ODF of austenite phase in 90% cold-rolled DSS.

The evolution of microstructure in DSS during severe plastic deformation (SPD) processing has been investigated more recently [70-72]. DSS processed by a combined rolling and swaging route to a strain of ~ 6.9 reveals the development of a fine lamellar structure in both austenite and ferrite phases with a high fraction of HAGBs [70]. The rapid grain subdivision is attributed to the formation of deformation twins in austenite at the early stages of deformation. In contrast, the microstructure in ferrite at early stages of deformation is characterized by the presence of dislocation cell walls and subgrain [70].

Similar mechanism of grain subdivision has also been reported in DSS processed by Equi Channel Angular Pressing (ECAP) up to 4 passes [71]. Deformation twins are observed at lower strains which reduce the grain size to submicron level. At higher strain regime twin-twin and twin-dislocation interactions play a crucial role in further grain size refinement leading to the formation of nanostructure. Beyond 4 ECAP passes, deformation induced phase transformation of austenite is observed. Microstructural evolution in DSS processed by High Pressure Torsion (HPT) has also been reported [72]. It is observed that grain refinement in austenite in the initial stages of deformation proceeds by the mechanism of twinning and de-twinning whereas grain refinement in ferrite proceeds via grain subdivision mechanism.

2.4.2 Evolution of microstructure and texture during Annealing

Humphreys et al [7] have observed that the choice of annealing temperature following deformation in duplex alloys may give rise to two conditions, namely, evolution of equilibrium or non-equilibrium microstructures. In the first case the annealing temperature is kept same as the homogenization temperature at which the two phases of the duplex alloys are stabilized before deformation. In the second

case the annealing temperature is different than that of the homogenization treatment. It may be apparent that no phase transformation is involved in the first case. However, in the second case phase transformation and recrystallization occur concurrently.

The effect of various factors on the deformation and recrystallization behavior of duplex alloys has been investigated in the equilibrium condition. Cooke et al [73] have studied the deformation and recrystallization behavior of moderately cold rolled Fe-Cr-Ni DSS with different volume fractions of the two phases, with 50% and 75% ferrite. They have observed that the annealing behavior was affected by the relative volume fractions of the two phases, by level of imposed strain, annealing temperature and time. No substantial recovery could be observed in austenite during annealing and the chief softening process is the usual discontinuous recrystallization by movement of HAGBs. In contrast, the annealing behavior of the ferrite phase depends upon the relative volume fraction of the two phases. When the two phases are present in equal proportion, extended recovery or continuous recrystallization process is observed in the ferrite phase. A transition from continuous to discontinuous recrystallization behavior is observed in alloys where ferrite is the dominant phase (volume fraction $\sim 75\%$).

Keichel et al [74] have extended their study to understand the recrystallization behavior of heavily rolled (up to 90% reduction in thickness) high nitrogen alloyed DSS with nearly equal volume fractions of ferrite and austenite [66]. Although it is observed that during cold-rolling the strain is nearly equally partitioned between the two phases so that the two phases deform independent of each other, the recrystallization behavior of austenite is affected by the presence of the second phase. Austenite undergoes discontinuous recrystallization, although the annealing texture of austenite is characterized by the presence of deformation texture components, particularly strong Goss component ($\{011\}\langle 100 \rangle$) and twin of the

Goss component ($\{111\} \langle 442 \rangle$) (Fig.2.22(a)) [66]. The brass recrystallization component $\{236\} \langle 385 \rangle$ is not observed. On the other hand, ferrite shows strong presence of the RD-fiber in the annealing texture (Fig.2.22(b)) [66]. This is attributed to the strong recovery behavior of ferrite during annealing.

If the temperature of annealing is different from the temperature at which the alloy is initially stabilized, recrystallization and phase transformations may happen concurrently. DSS are particularly prone to precipitation of intermetallic phases if treated below 1000°C [75]. It is reported that these intermetallic phases delay the recrystallization kinetics of both ferrite and austenite [76]. This behavior is very similar to duplex brass where recrystallization and precipitation may happen simultaneously, resulting in very fine grained duplex structure [77].

Only very few studies have focused on understanding the effect of SPD processing on the recrystallization behavior of DSS. Belyakov et al [78] have studied the effect of annealing on the microstructure evolution in SPD processed duplex steel. Up on annealing, extensive recovery or continuous recrystallization is reported in the ferrite while discontinuous recrystallization is observed in austenitic. The evolution of texture during annealing has not been reported in that study.

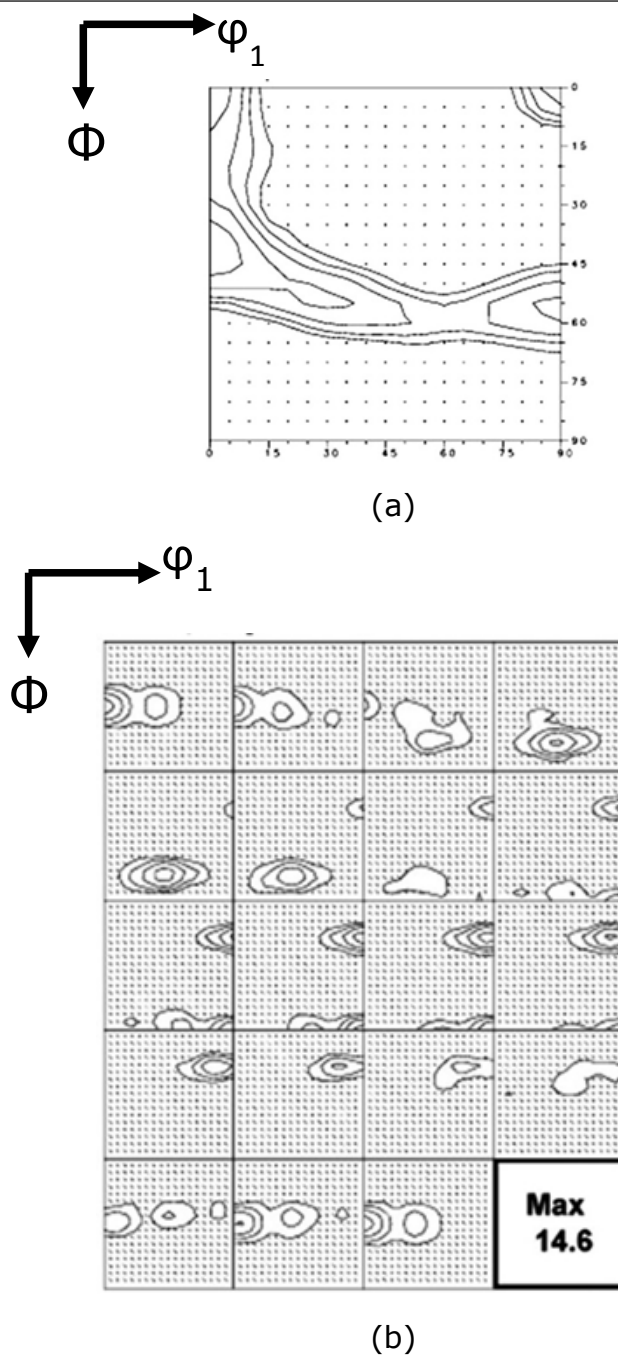


Fig.2.22: (a) $\phi_2 = 45^\circ$ section of ODF of ferrite and (b) ODF of austenite in DSS cold-rolled to 90% reduction in thickness and annealed for 2000s at 1100°C [66].

2.5 Objectives and scope of the present work

The brief yet critical literature review presented here suggests that the evolution of microstructure and texture during thermo-mechanical processing has been intensely investigated in single phase materials including ferritic and austenitic steels. However, the evolution of microstructure and texture following heavy deformation and annealing is much less investigated and understood in DSS and other duplex alloys.

The available literatures on DSS suggest that other authors have attempted to study the evolution of microstructure and texture after hot-working or cold-working followed by recrystallization. As already discussed the evolution of microstructure and texture in these materials could be affected by several factors, including starting microstructure/texture, volume fraction of phases, imposed strain and annealing temperatures.

In contrast to previous studies the present research work attempts to study the evolution of microstructure and texture in DSS during thermo-mechanical processing by warm-rolling. It may be noted that while the effect of warm-rolling has been investigated in single phase ferritic steels (interstitial free and extra low carbon steels), the effect of warm-rolling on microstructure and texture evolution in DSS alloys has not been clarified so far. This constitutes the prime novelty of the present research.

Processing by warm-rolling is considered particularly important in the present work due to several reasons. It is expected that strain induced phase transformation of austenite can be avoided during processing by warm-rolling. Therefore, microstructure and texture evolution can be studied without involving additional complexities arising out of unwanted phase transformations. From a practical standpoint warm-rolling can be particularly attractive due to lower forming loads and possibility of achieving enhanced properties in the processed alloys.

The effects of three parameters, namely, temperature, severe plastic strain and strain path change on the evolution of microstructure and texture have been investigated in the present work. The warm-rolling has been carried out over a wide temperature range and up to a very high strain in order to clarify the effect of the first two parameters. The effect of strain path change is investigated by employing cross-rolling route (to be detailed in the experimental section) in order to clarify the response of the individual phases to strain path change and consequent microstructure and texture development during deformation and annealing.

The major focus of the present work is to understand the microstructure and texture evolution in the individual phases of a DSS alloy processed by this novel thermo-mechanical processing route. The tensile properties have been studied to a limited extent primarily to have a preliminary evaluation of the effect of this novel processing route on mechanical properties. Detailed understanding of the mechanical behavior is beyond the scope of the present work. It is envisaged that the results obtained should be useful for understanding the evolution of microstructure and texture in other duplex alloys during thermo-mechanical processing by warm-rolling.

-: CHAPTER 3 :- EXPERIMENTAL

3.1 Alloy preparation

The experimental duplex stainless steel (DSS) alloy for the present study having chemical composition shown in Table 1 was prepared by induction melting using commercially available super duplex stainless steel – SAF 2507 (Sandvik, Sweden) and high purity nickel (99.9%) as the raw materials. Results obtained from the exploratory experiments on 2507 DSS alloy showed that austenite was not stable during heavy deformation and thus it was felt necessary to increase the nickel content in order to achieve stable austenite. Melting and casting operations were performed in a vacuum induction melting furnace at 1873K (1600°C). The as cast ingot was obtained in the form of a tapered cylinder with a top diameter of 72mm, bottom diameter of 62mm and height of 290mm as shown in Fig. 3.1.

3.2 Preparation of starting material for deformation processing

The starting material for deformation processing was prepared by cogging of the as-cast ingot material at 1473K (1200°C). Figure 3.2 shows the cogged billet having dimensions of 60 mm (thickness) x 55mm (width) x 300mm (length). The cogged billet was subsequently hot-rolled at 1398K (1125°C) to ~82.5% reduction in thickness to a final thickness of 10.5 mm using seven passes. Rectangular samples (30mm x 80 mm) were machined out from the hot-rolled material and subsequently homogenized at 1448K (1175°C) for 120 minutes (2 hours) in a tubular furnace in flowing argon atmosphere. The homogenization temperature was optimized for obtaining approximately equal volume fraction of austenite and ferrite. Flow chart of preparation of the starting material is summarized in Fig.3.3.

Table 3.1: Chemical composition of as-cast custom made DSS.

Element	C	S	Cr	Mn	Ni	P	Si	Mo	Fe
wt. %	0.08	0.001	24-25	0.14	10.5	0.017	0.45	3.10	balance



Fig 3.1: As cast ingot of DSS used in the present research.

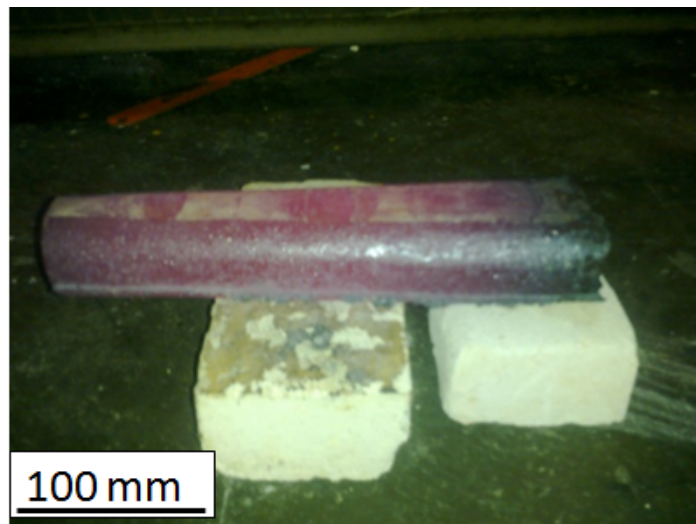


Fig 3.2: DSS billet in the hot forged condition.

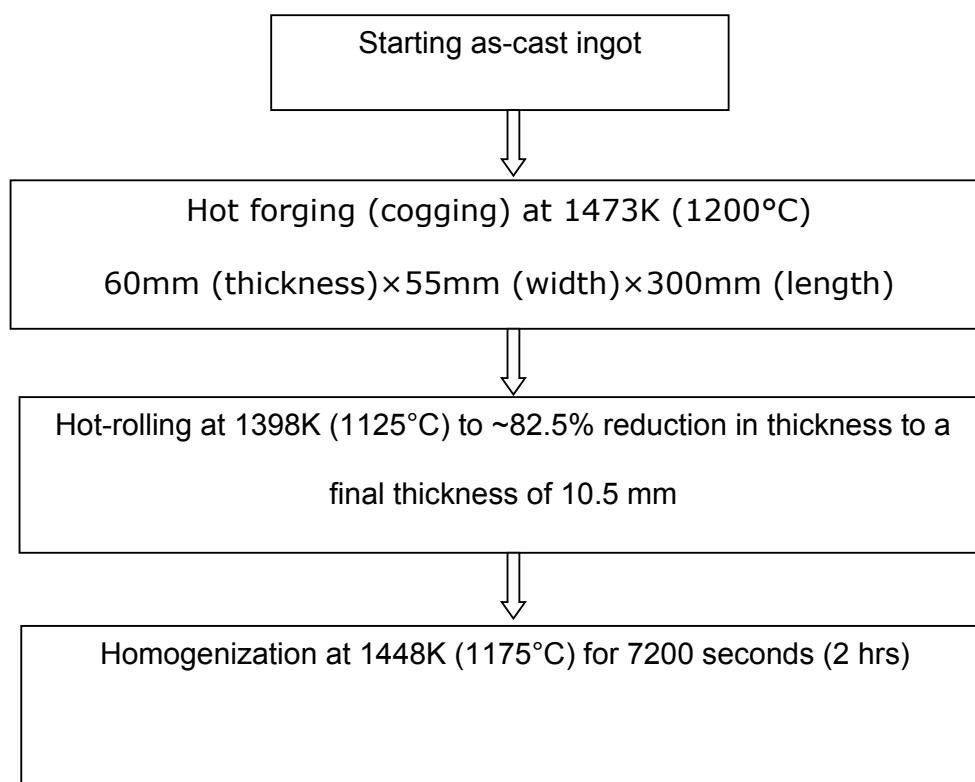


Fig.3.3: Flow diagram showing the preparation of the homogenized starting material.

3.3 Deformation processing

The starting material was initially cold-rolled up to 90% reduction in thickness. It was observed that the volume fraction of austenite decreased consistently with increasing thickness reduction. This suggested that increased nickel content was not sufficient to prevent deformation induced martensitic transformation of austenite in the DSS during heavy cold-rolling. Consequently, the concept of warm-rolling was introduced. The deformation temperature was kept above the deformation induced martensitic transformation temperature (M_d) of the experimental DSS in order to successfully retain austenite as a stable phase.

The effect of three different processing parameters was investigated as explained below:

- a) **Processing temperature:** Warm-rolling was carried out at 498K (225°C), 698K (425°C), and 898K (625°C) temperatures up to 90% reduction in thickness.
- b) **Strain:** Warm-rolling temperature of 898K (625°C) was selected to reveal the effect of strain during warm-rolling. The warm-rolling at this temperature was carried out up to 98% reduction in thickness. The reasons for selecting this specific temperature would be discussed at the appropriate place.
- c) **Strain path:** The effect of strain path change was investigated employing cross-rolling process. Warm cross-rolling at 898K (625°C) is carried out up to 90% reduction in thickness by mutually interchanging the rolling direction (RD) and transverse direction (TD) by rotation of the sample around ND by 90° in every pass.

3.4 Warm-Rolling

3.4.1 Unidirectional or straight warm-Rolling

Homogenized material with equal volume fraction of the two phases was subjected to straight or unidirectional warm-rolling (UWR). UWR was carried out at 498K (225°C), 698K (425°C) and 898K (625°C) temperatures along the prior hot-rolling direction up to 98% reduction in thickness. The thickness of the homogenized material (~10 mm) was reduced in steps of ~1 mm to a thickness of 2 mm (total 8 rolling passes). Beyond that, due to increased strain hardening the final thickness of 1 mm (corresponding to ~90% reduction in thickness) was achieved in steps of 0.5 mm using two additional passes. Thus, total reduction in thickness was achieved in 10 passes.

Further warm-rolling to 98% reduction in thickness at the three warm-rolling temperatures was achieved with rather small incremental thickness reduction in each pass. The additional number of passes used to achieve the thickness reduction varied from 10 to 12 depending on the temperature of processing.

A laboratory scale rolling mill (SPX Precision Equipment, USA) having 140mm roll diameter was used for rolling. The rolls were pre-heated to 523K (250°C) in order to minimize sudden quenching effect during warm-rolling. The specimens for warm-rolling were heated to the warm-rolling temperatures in a box furnace. The protective argon atmosphere was used during heating. Isothermal holding time 15 minutes was used before every warm-rolling pass. The samples were water quenched immediately after every warm-rolling pass.

3.4.2 Cross warm rolling

Cross warm-rolling (CWR) of the homogenized starting material was carried out at 898K (625°C). In contrast to UWR, during cross warm-rolling, RD and TD were interchanged in every pass by

rotating the sample 90° around the normal direction (ND) so that the TD of the previous pass became the RD of the current pass (Fig.3.4). The total reduction of 90% during CWR was achieved in eleven passes as illustrated in Fig.3.4.

3.5 Annealing

3.5.1 Annealing of UWR processed materials

The 90% deformed samples of all the three warm-rolled conditions (i.e. 498K (225°C), 698K (425°C), 898K (625°C) temperature) were selected for isothermal annealing experiments. Annealing experiments were carried out at 1448K (1175°C) in a tubular furnace in flowing argon atmosphere for different isothermal holding times ranging from 2 minutes to 120 minutes. The annealed samples were immediately water-quenched following the heat-treatment.

The same annealing temperature and holding times were used for DSS warm-rolled to 70%, 95% and 98% reduction in thickness at 898K (625°C).

3.5.2 Annealing of CWR processed materials

Samples obtained from DSS CWR processed to 90% reduction in thickness at 898K (625°C) were also isothermally annealed at 1448K (1175°C) in a tubular furnace in flowing argon atmosphere for different time intervals ranging from 2 minutes to 120 minutes. The annealed samples were immediately water-quenched following the heat-treatment.

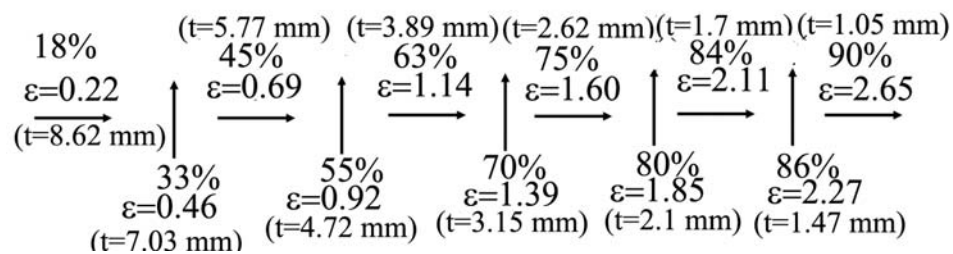


Fig.3.4: Schematic illustration of the CWR route. The RD of the current pass, thickness of the sheet at every pass, % reduction in thickness and corresponding equivalent strain ($\epsilon_{eq} = \frac{2}{\sqrt{3}} \ln(1 + e)$, where e is the engineering strain or percentage thickness reduction) are indicated.

3.6 Chemical composition, microstructural and textural Characterization

Chemical composition analysis of the two phases in the homogenized starting material was carried out by energy dispersive spectroscopy (EDS) (EDAX Inc., USA) attached to a scanning electron microscope (SEM) equipped with field emission gun (FEG) (Make: Carl Zeiss make, Germany; Model: SUPRA-40). EDS measurements were obtained using an accelerating voltage of 20 kV and working distance of 10 mm approximately. The EDS data were collected using the point scan mode. The EDS data were collected from 10 individual points from each phase from different locations of the homogenized material to determine the chemical composition and reveal partitioning of the alloying elements in the two phases. The samples for EDS measurements were prepared by careful mechanical polishing using colloidal silica as the final polishing medium. The samples prepared in this way were ultrasonically cleaned before mounting on the SEM.

The microstructure and microtexture of the homogenized starting material, deformed and annealed materials were characterized using an electron backscatter diffraction (EBSD) system (Oxford Instruments, UK) attached with FEG-SEM (Make: Carl Zeiss make, Germany; Model: SUPRA-40). The EBSD measurements were carried out using a constant 20 KV accelerating voltage and working distance approximately 20 mm for the majority of the measurements. Samples for EBSD were prepared by manual polishing followed by electro-polishing at room temperature using an applied voltage of 27 V and holding time ranging from 15 seconds to 20 seconds. A solution consisting of 700 ml ethanol, 120 ml distilled water, 100 ml glycerol and 80ml perchloric acid was used as electrolyte.

EBSD is the most preferred technique for simultaneous characterization of microstructure and texture. Due to this EBSD

was used as the major technique for microstructural and textural characterization in the present work. The principles of automated EBSD for microtexture measurement could be summarized below.

3.6.1 Measurement of microtexture using EBSD

Macrotexture or bulk texture determined by x-ray diffraction (XRD) does not give information about the spatial distribution of individual orientations, but only provides information regarding average texture present in the materials. Microtexture gives information regarding individual orientations along with their spatial distribution in polycrystalline materials. Microtexture determination by EBSD is achieved by analyzing the orientation information obtained from Kikuchi diffraction patterns.

When an electron beam enters a crystalline solid it is diffusely scattered in all directions. Electrons which satisfy the Bragg's law at every set of lattice planes will diffract at an angle θ_B (Bragg angle) and will undergo elastic scattering to give a strong reinforced beam. Since diffraction of the electrons through the Bragg angle is occurring in all directions, the locus of the diffracted radiation is the surface of a cone (Kossel cone) that extends about the normal of the reflecting atomic planes with half apex angle $90^\circ - \theta_B$. The source of electron scattering can be considered to be between lattice planes, as shown in Fig.3.5, and hence two cones of radiation result from each family of planes. Calculations using typical values of electron wavelength and lattice interplanar spacing show that θ_B is approximately 0.5° . As a result, the apex angle of a diffraction cone is close to 180° , that is, the cones are almost flat. When the phosphor screen intercepts the diffracted cones a pair of parallel conic sections thus form. These sections are nearly straight such

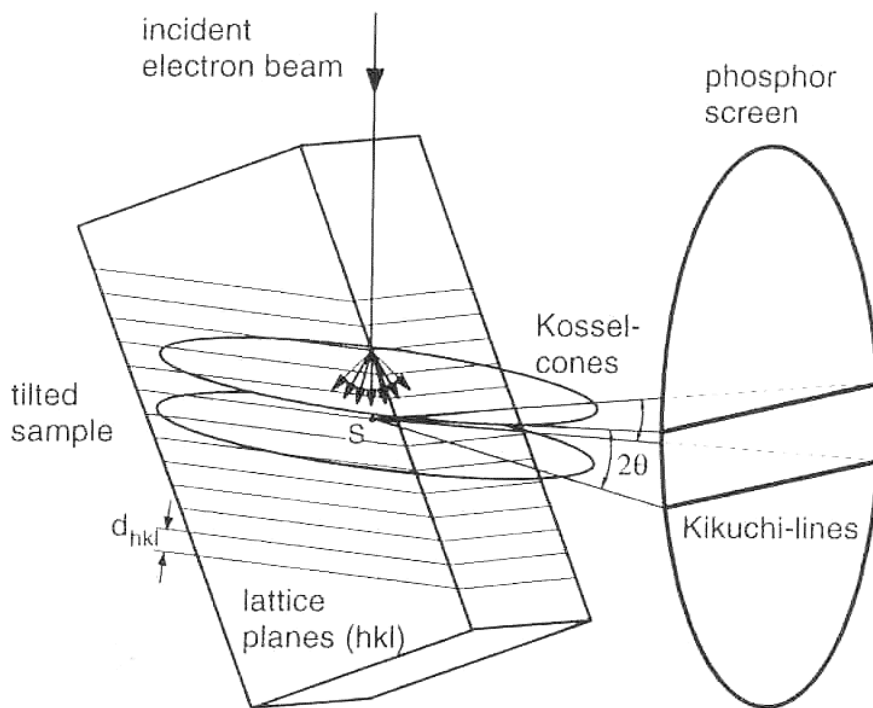


Fig. 3.5: Origin of Kikuchi lines from the EBSD perspective [8].

that they generally appear to be parallel lines. These are the so called Kikuchi lines of Kikuchi bands. Spacing between the Kikuchi bands corresponds to an angular distance of $2\theta_B$ which in turn is proportional to the interplanar spacing.

In SEM the bulk specimen is to be tilted to about 20° about the vertical in order to obtain patterns of high intensity. Fully automated EBSD systems attached to SEM acquires and index Kikuchi patterns from a large number of individual grains and allows quantitative analysis of the orientation data.

For acquisition of diffracted beam a phosphor screen is placed parallel to the incident beam, right in front of the tilted specimen. A pattern thus acquired spans over a wide angular range up to $\pm 60^\circ$ and contains several principal zones. Schematics of a commercial EBSD setup are shown in Fig.3.6.

Determination of individual orientation by fully automated EBSD system can be divided into the following steps [79]

(A) *Image Processing*: Low signal to noise ratio of patterns needs to be improved for further analysis. This is done by applying image processing techniques. Background correction is one of the most common image processing techniques used in EBSD for improving the contrast of diffraction bands.

(B) *Automatic Band detection*: Automatic indexing of Kikuchi patterns is done after the bands in the Kikuchi patterns are detected. Krieger Lassen et al [80] suggested an algorithm for the first time for detecting Kikuchi bands called Hough transformation method. During the Hough transformation each point (x_i, y_i) of the original image is transformed into a sinusoidal curve in the Hough space which is governed by the relation:

$$\rho(\varphi) = x_i \cos \varphi + y_i \sin \varphi, \rho \in (0^\circ, 180^\circ), \varphi \in (-R, R) \quad (3.1)$$

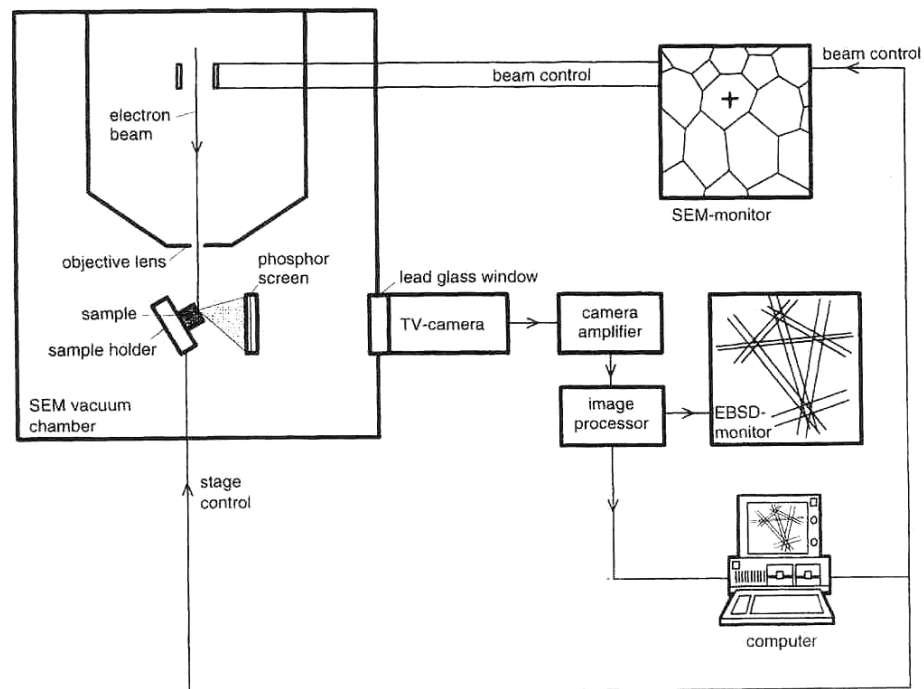


Fig: 3.6: Components of a commercial EBSD system [8].

The above relation specifies a line by the angle ϕ between its normal and the pattern x-axis and its distance p from the origin. The principle of Hough transformation has been schematically shown in Fig.3.7 for two bands which are defined by two points. Points which lie in the original image in Fig.3.7 (a) have the same distance p and angle ϕ with respect to the origin and hence, they all accumulate at the same point in the Hough space Fig.3.7 (b). Thus, by transforming an image into Hough space, lines in the image space become single points in the Hough space. This is done by first dividing Hough space into discrete bins.

Then the intensity at every (x, y) pixel in the image is added into all discrete bins on the curve defined by Eq (3.1) (where p is calculated for each discrete ϕ). The problem of finding a band in diffraction pattern is then reduced to finding a peak of high intensity in Hough space. The peak in Hough space has a characteristic butterfly shape - a peak surrounded by two valleys. In order to draw out peak of this shape, the Hough transformation is convoluted with a "butterfly mask".

(C) *Indexing of the Bands*: Automatic indexing of the bands is done by commercially available software packages and the algorithm implemented may vary depending on the system. The commercial software package HKL CHANNEL 5 (Oxford Instruments, UK) used in this work for data acquisition employs simple Hough transformation for band detection as well as an "Advance Fit" algorithm to generate a short list of possible solutions very quickly, compares the simulated EBSP for each possible solution in the shortlist very accurately against the actual acquired EBSP [81].

(D) *Orientation Determination*: After the miller indices associated with at least two bands are correctly identified the orientation (with respect to some fixed reference frame) can be calculated in the following manner (Fig.3.8).

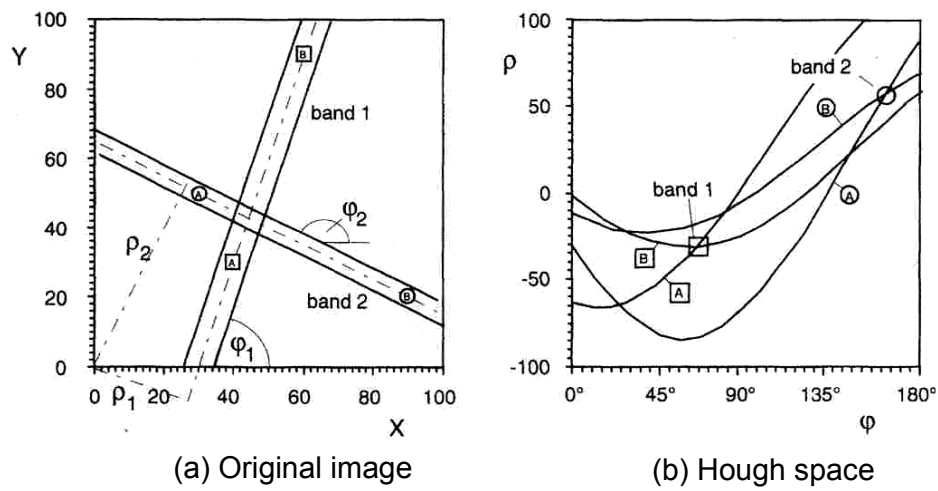


Fig.3.7: Schematic representation of the Hough transformation; (a) two bands in the real space, (b) the bands in the transformed Hough space [8].

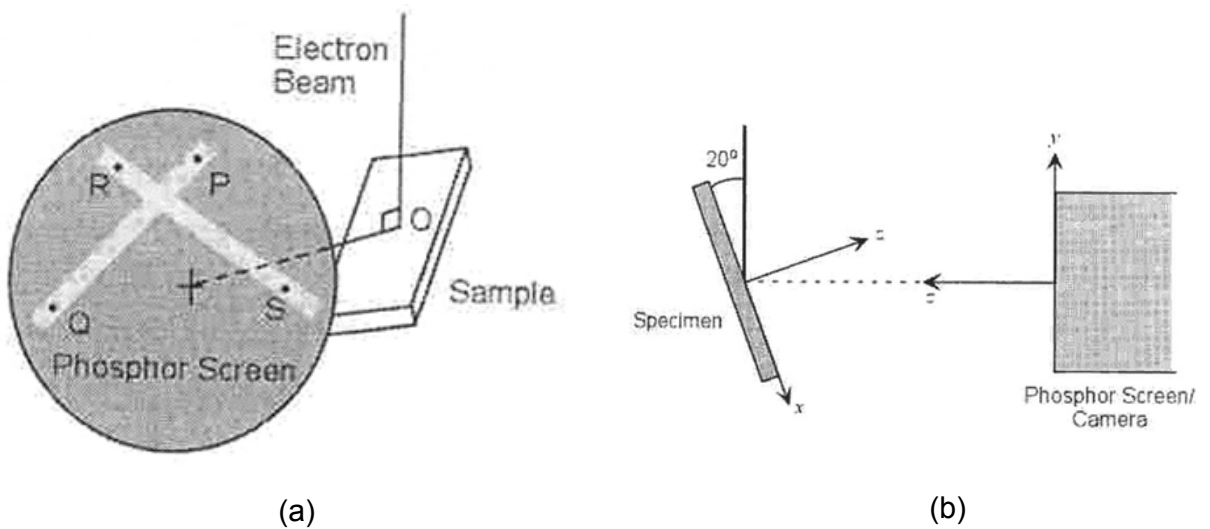


Fig.3.8: Schematic representation of the geometry of (a) diffraction and (b) EBSD [79].

Two vectors can be defined (Fig.3.8) representing two plane normal in pattern coordinates:

$$\hat{n}_1^p = \frac{\overline{OP} \times \overline{OQ}}{\|\overline{OP} \times \overline{OQ}\|} \text{ and } \hat{n}_2^p = \frac{\overline{OR} \times \overline{OS}}{\|\overline{OR} \times \overline{OS}\|} \quad (3.2)$$

($\|V\|$ denotes the magnitude of the vector V , i.e, $\|V\| = \sqrt{V \cdot V} = (V_1^2 + V_2^2 + V_3^2)^{1/2}$ and \hat{V} denotes a normalized vector, i.e, $\|V\| = 1$).

From these two normalized vectors an orthogonal frame can be constructed in the following manner:

$$\hat{e}_1^{*p} = \hat{n}_1^p, \hat{e}_2^{*p} = \frac{\hat{n}_1^p \times \hat{n}_2^p}{\|\hat{n}_1^p \times \hat{n}_2^p\|} \text{ and } \hat{e}_3^{*p} = \hat{e}_1^{*p} \times \hat{e}_2^{*p} \quad (3.3)$$

Similarly, an orthogonal frame can be constructed in the crystal frame, given the (hkl) indices associated with the bands used in the calculation of \hat{n}_1^p and \hat{n}_2^p shown previously.

This is done in the following manner:

$$\hat{e}_1^{*C} = \frac{(hkl)_1}{\|(hkl)_1\|}, \hat{e}_2^{*C} = \frac{(hkl)_1 \times (hkl)_2}{\|(hkl)_1 \times (hkl)_2\|} \text{ and } \hat{e}_3^{*C} = \hat{e}_1^{*C} \times \hat{e}_2^{*C} \quad (3.4)$$

Thereafter, two sets of direction cosines relating the new (pattern) frame to the sample and crystal frames may be given by:

$$g_{ij}^s = \hat{e}_i^{*p} \cdot \hat{e}_j^s ; g_{ij}^c = \hat{e}_i^c \cdot \hat{e}_j^{*C} \quad (3.5)$$

The vectors \hat{e}_j^s is given as:

$$\hat{e}_1^s = -\cos(20^\circ)\hat{j} - \sin(20^\circ)\hat{k}, \hat{e}_2^s = -\hat{i} \text{ and } \hat{e}_3^s = -\sin(20^\circ)\hat{j} - \cos(20^\circ)\hat{k} \quad (3.6)$$

And the vector \hat{e}_i^c is given by:

$$\hat{e}_1^c = \hat{i}, \hat{e}_2^c = \hat{j} \text{ and } \hat{e}_3^c = \hat{k} \quad (3.7)$$

The orientation matrix (i.e. the rotation required to bring the sample frame into coincidence with the crystal frame) can be calculated as follows

$$g_{ij} = g_{ik}^s \cdot g_{kj}^c \quad (3.8)$$

3.6.2 Experimental details of EBSD analysis

The EBSD measurements were obtained from the longitudinal section (ND-RD plane) of different deformed and annealed samples. Samples which are deformed to lower strains (upto 70% thickness reduction), the dimensions of the acquired EBSD maps were not less than 150x150 μm . For heavily deformed samples ($\geq 90\%$ reduction in thickness), a large number of EBSD maps of dimensions approximately 50 μm x 50 μm were acquired from different areas close to the mid-thickness regions of the sheets and merged together. At least 4000 grains of each phase in deformed specimens were considered for calculating the texture. A fine scan step size of 50nm (0.5 μm) was used for deformed specimens.

For isothermally annealed materials several large area EBSD maps of dimensions up to 1000 μm x 1000 μm were acquired from the mid-thickness regions of the sheets to get orientation information of a sufficiently large number of grains of each phase. The step size was fixed in such a manner that at least 4-5 points could be collected from each grain.

The EBSD scans acquired using the HKL EBSD (Oxford Instruments, UK) software were imported into the TSL-OIM™ (version 6.2) analysis software (EDAX Inc., USA) in channel text file format (.ctf extension) for the analysis purpose. Orthotropic sample symmetry was assumed in calculating the ODFs from the microtexture data using the series expansion method of Bunge

(series rank = 22). The volume fractions of different texture components were determined using a tolerance angle of 15°.

3.7 Mechanical Property Characterization

Tensile tests were carried out for selected deformed and annealed specimens. A schematic drawing of a typical tensile test specimen is shown in Fig.3.9. A table mounted tensile testing machine (Make: INSTRON, UK; Model: 5967) with 30KN capacity was used for tensile testing. The tensile testing was carried out using a constant strain rate of 10^{-3} sec^{-1} . The tensile load was applied along the RD.

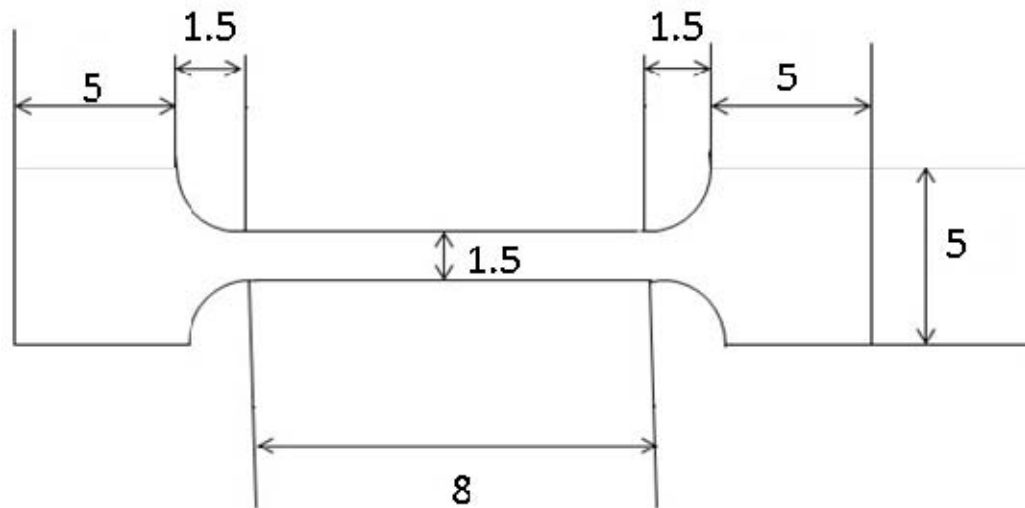


Fig.3.9: Schematic of the tensile test specimens (all dimensions shown are in mm).

-: CHAPTER 4 :-

***EFFECT OF PROCESSING TEMPERATURE ON THE
EVOLUTION OF MICROSTRUCTURE AND TEXTURE
DURING WARM-ROLLING AND RECRYSTALLIZATION***

4.1 Microstructure and texture of the homogenized starting material

The chemical composition analysis of the two constituent phases of the DSS is carried out using EDS to determine the partitioning of alloying elements. Table 4.1 summarizes the distribution of the alloying elements in the two phases. Nickel being an austenite stabilizer is partitioned more to austenite while chromium being a ferrite stabilizer is partitioned more to ferrite.

Figure 4.1 shows the phase map of the starting material homogenized at 1498K (1175°C) for 120 minutes. The phase map of the homogenized DSS shows nearly equal volume fraction (~50%) of austenite (highlighted in green) and ferrite (highlighted in red). Both the phases show elongated structure along the prior hot-rolling direction. The two phases have a similar average thickness (~6 μm) measured along the normal direction (ND). Since each phase band is one grain thick the phase band thickness and grain thickness are identical in the starting homogenized material. The austenite bands contain profuse annealing twins revealed by the presence of $\Sigma 3$ annealing twin boundaries (highlighted by yellow lines).

The texture of ferrite in the starting homogenized DSS is shown by the $\phi_2=45^\circ$ section of the ODF (Fig.4.2) which reveals the presence of the two texture fibers, namely, the RD and ND fibers. The ideal locations of different texture components along the two fibers are shown in Fig.4.2. The intensities of the contour lines in the ODF section clearly reveal the presence of a strong ND-fiber (ND//<111>) along with a minor rotated cube component ($\{001\}$ <140>). The strongest component along the ND-fiber is $\{111\}$ <112> having a fraction of ~27%. The total fraction of the ND-fiber is ~30% and that of the RD-fiber (RD//<110>) is only ~6%.

Table 4.1: Distribution of alloying elements in the two constituent phases in the starting homogenized DSS.

Element	wt. %	
	Austenite	Ferrite
Fe	61.2 ± 0.15	59.5 ± 0.31
Cr	21.9 ± 0.6	27 ± 0.6
Ni	12.9 ± 0.15	8.9 ± 0.49
Mo	2.8 ± 0.43	3.9 ± 0.19
Si	0.49 ± 0.1	0.48 ± 0.1

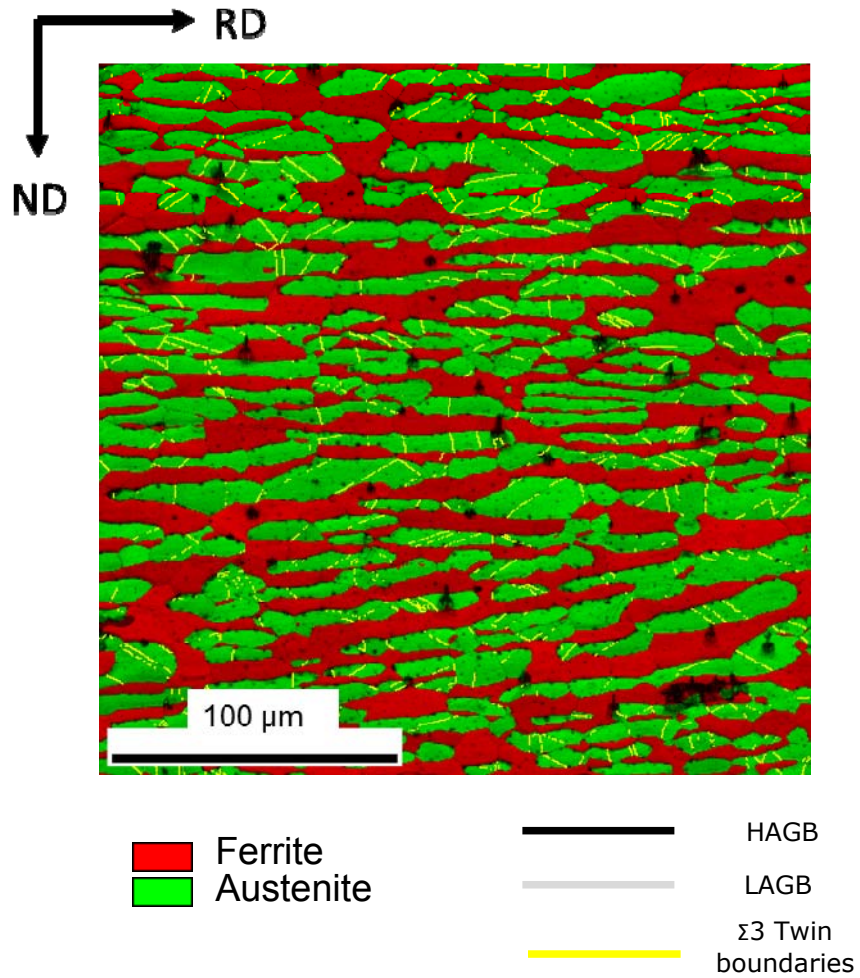


Fig.4.1: Phase map showing the distribution of ferrite and austenite in the homogenized DSS used as the starting material for subsequent warm-rolling.

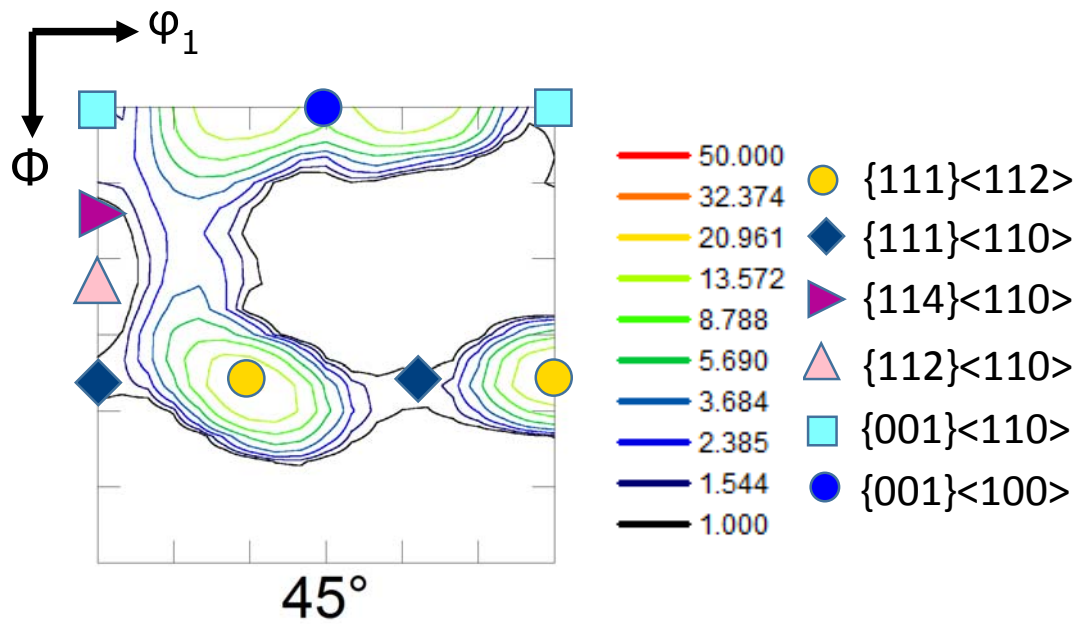


Fig.4.2: $\phi_2 = 45^\circ$ section of the ODF of ferrite in starting homogenized DSS. The ideal locations of the texture components are shown in the ODF section.

The texture of austenite in the starting homogenized DSS is represented by the (111) pole figure (PF) (Fig.4.3(a)). A (111) PF showing the ideal locations of individual texture components (Fig. 4.3(b)) is also shown for ease of understanding. The $\phi_2 = 0^\circ, 45^\circ$ and 65° sections of the ODF of austenite in starting homogenized DSS is shown in Fig.4.3(c). The locations of the ideal texture components are shown in the ODF sections. A weak copper type texture is evident in the austenite of the starting homogenized DSS.

4.2. Evolution of microstructure and texture during warm-rolling at 498K (225 °C)

4.2.1 Evolution of microstructure

Evolution of microstructure during warm-rolling at 498K (225°C) is shown in Fig.4.4 which shows the phase maps of ~20% ($\epsilon_q=0.25$) (Fig.4.4(a)), 40% ($\epsilon_q=0.58$) (Fig.4.4(b)), 70% ($\epsilon_q=1.39$) (Fig.4.4(c)) and 90% ($\epsilon_q=2.66$) (Fig.4.4(d)) warm-rolled DSS. The low angle (LAGBs; defined by $2^\circ \leq$ misorientation angle (θ_{mis}) $\leq 15^\circ$) and high angle grain boundaries (HAGBs; defined by $\theta_{\text{mis}} \geq 15^\circ$) are highlighted in gray and black lines, respectively (the same convention for representing different grain boundaries is followed throughout this work).

Gradual development of banded morphology with an alternate arrangement of deformed ferrite and austenite bands is observed with increasing deformation. This microstructural transformation is quite prominent in the 70% warm rolled material (Fig.4.4(c)) as compared to the 20% (Fig.4.4(a)) and 40% (Fig.4.4(b)) warm-rolled materials. Inside the deformed phase bands development of LAGB network could be clearly observed.

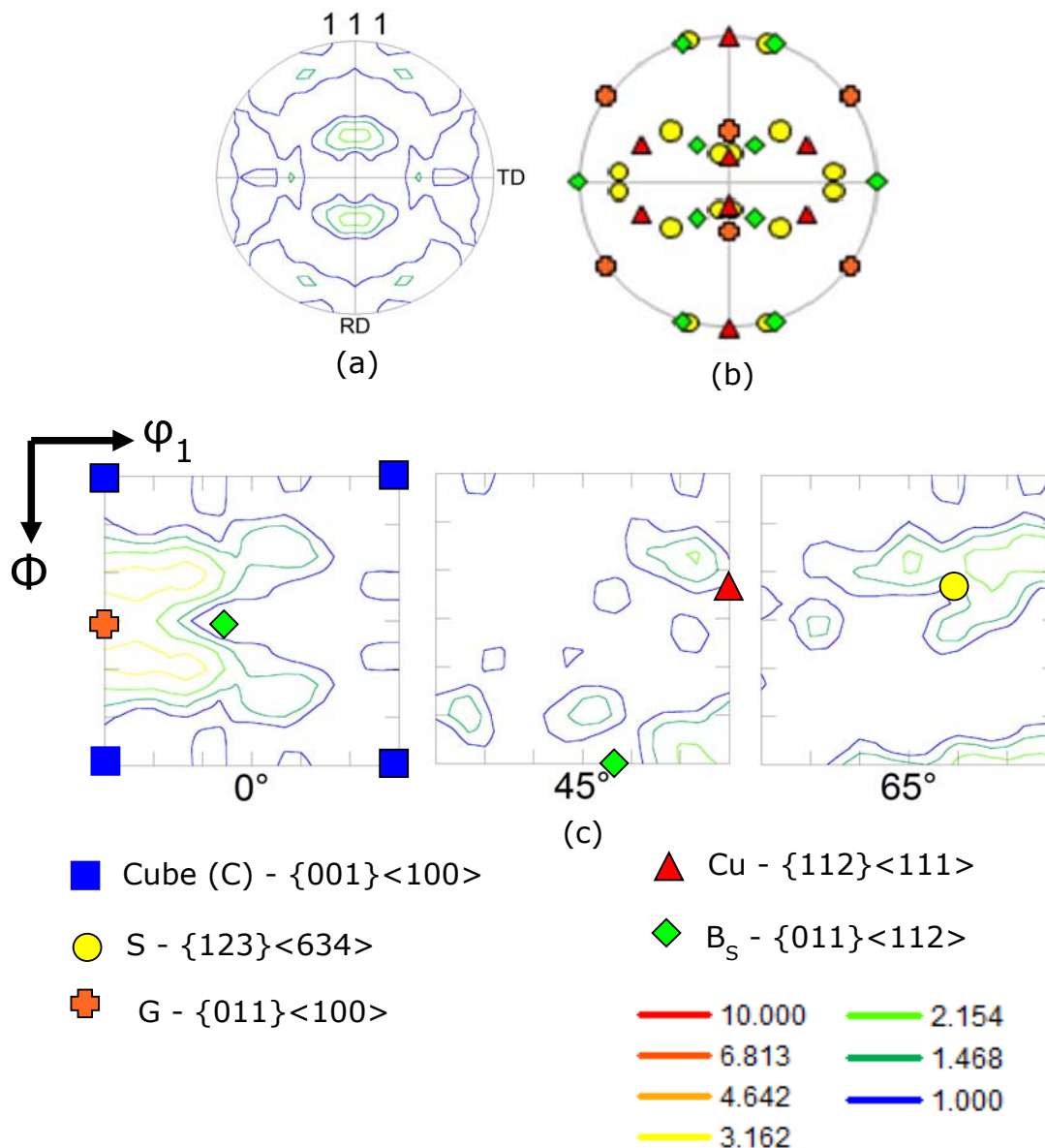


Fig.4.3: (a) shows the (111) PF of austenite in homogenized DSS, (b) shows the ideal locations of individual texture components in (111) PF. (c) shows the $\phi_2 = 0^\circ$, 45° and 65° sections of the ODF of austenite in homogenized DSS along with the ideal locations of individual texture components.

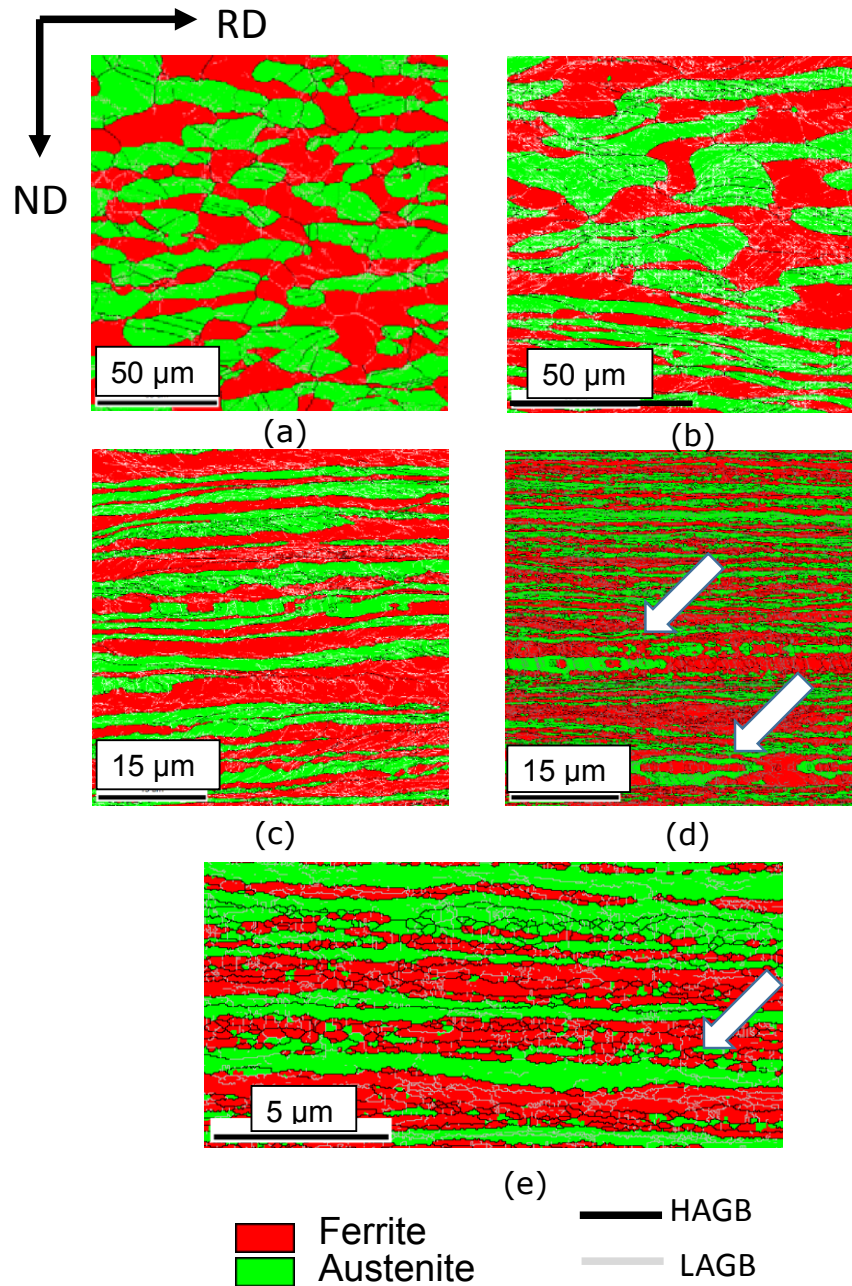


Fig 4.4: Phase maps of the DSS warm-rolled at 498K (225°C) to (a) 20%, (b) 40%, (c) 70% and (d) 90% reduction in thickness. (e) shows a region of interest cropped from the phase map of 90% warm-rolled material shown in (d).

The microstructure of the 90% warm-rolled material (Fig.4.4 (d)) shows well developed lamellar morphology with an alternate arrangement of deformed ferrite and austenite bands extended parallel to the RD. The phase map also shows the presence of locally fragmented regions within the deformed matrix (marked by an arrow in the phase map of Fig.4.4 (d)). Figure 4.4(e) is a region of interest cropped from the phase map shown in Fig.4.4(d). Figure 4.4(e) clearly shows that the individual phase bands in 90% warm-rolled material are further subdivided by HAGBs extended parallel to the RD. The deformed phase bands continue to show LAGB network. Table 4.2 shows the evolution of key microstructural parameters, such as phase fraction, phase band spacing, HAGB fraction and HAGB spacing along the ND during warm-rolling at 498K (225°C). Significant change in the austenite phase fraction as compared to that in the starting homogenized DSS is not observed even after 90% warm-rolling. The phase band thickness at different deformation level indicates the strain partitioning amongst the constituent phases. With increasing deformation average band thickness of the two phases is decreased. The average phase band thickness of austenite ($\sim 0.56 \mu\text{m}$) and ferrite ($\sim 0.61 \mu\text{m}$) is quite similar after 90% warm-rolling. This shows that the imposed strain during warm-rolling is partitioned almost equally amongst the two constituent phases.

Table 4.2 further shows that the HAGB fraction in the two phases is decreased up to 40% reduction in thickness but is increased consistently thereafter. The HAGB spacing is decreased with increasing thickness reduction. The HAGB fraction of austenite shows consistently higher average values as compared to those in ferrite so that the HAGB fractions in austenite and ferrite after 90% warm-rolling are found to be ~ 0.41 and ~ 0.25 , respectively. At the

Table.4.2: Evolution of key microstructural parameters in ferrite and austenite in DSS during warm-rolling at 498K (225°C).

% Thickness reduction	Austenite phase fraction (%)	Phase band spacing (μm)		HAGB fraction (μm)		HAGB spacing (μm)	
		Ferrite	Austenite	Ferrite	Austenite	Ferrite	Austenite
20	52 \pm 0.8	5.06	5.6	0.14 \pm 0.014	0.31 \pm 0.03	8 \pm 2	5.7 \pm 1.3
40	50	4.16	4.8	0.06 \pm 0.01	0.16 \pm 0.01	4.36 \pm 0.14	3 \pm 0.03
70	46 \pm 5	1.2	1.7	0.1 \pm 0.01	0.23 \pm 0.01	1.41 \pm 0	1.1 \pm 0.01
90	45	0.61	0.56	0.25 \pm 0.03	0.41 \pm 0.03	0.53 \pm 0.09	0.48 \pm 0.11

same time austenite shows lower average HAGB spacing along the ND as compared to that in ferrite. The HAGB spacing values in austenite and ferrite, are $\sim 0.48 \mu\text{m}$ and $\sim 0.53 \mu\text{m}$, respectively after 90% warm-rolling.

The dynamic recovery behavior of the two phases during warm-rolling is understood from the kernel average misorientation (KAM) distribution. The local misorientation within a grain can be characterized using the KAM approach [82].

Figure 4.5 shows the schematic representation of KAM approach. Here the average misorientation of a given point with all points at the perimeter of the kernel (Fig.4.5(a)) or with all points in the kernel is calculated with a provision that misorientation exceeding some tolerance value is excluded. In the present work up to the third nearest neighbor is considered for calculating KAM values and a tolerance angle of 5° is used.

To understand the recovery behavior misorientation exceeding 1° is excluded and the area fraction with less than 1° misorientation (i.e. $\text{KAM} \leq 1$) is considered. Area fraction having $\text{KAM} \leq 1$ in the two phases of DSS 90% warm-rolled at 498K (225°C) is calculated. Area fraction with $\text{KAM} \leq 1$ in ferrite is ~ 0.8 whereas for austenite it is ~ 0.25 . This indicates that during warm-rolling at 498K (225°C) ferrite shows considerably more dynamic recovery as compared to austenite.

4.2.2 Evolution of Texture

Figure 4.6 shows the texture of ferrite of DSS 90% warm rolled at 498K (225°C). Figure 4.6(a) shows the $\phi_2=45^\circ$ section of the ODF of ferrite. The spatial distribution of individual texture components belonging to the two fibers is shown in the orientation map in Fig.4.6(b). The orientation map of ferrite shown in Fig.4.6(b)

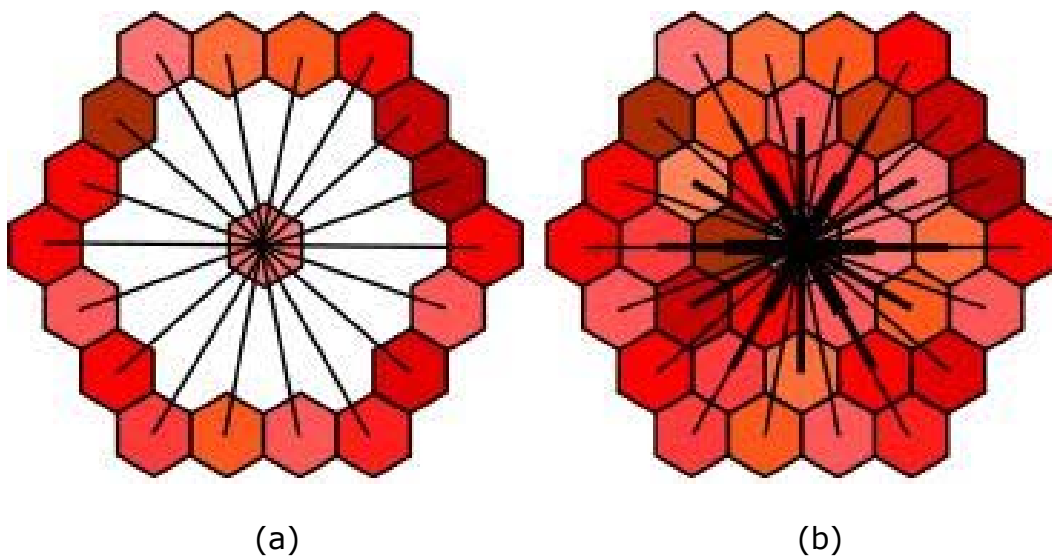


Fig.4.5: Schematic diagram showing (a) misorientation between a grain at the center and all other points at the perimeter of the kernel and (b) misorientation between a grain at the center and all points in the kernel [82].

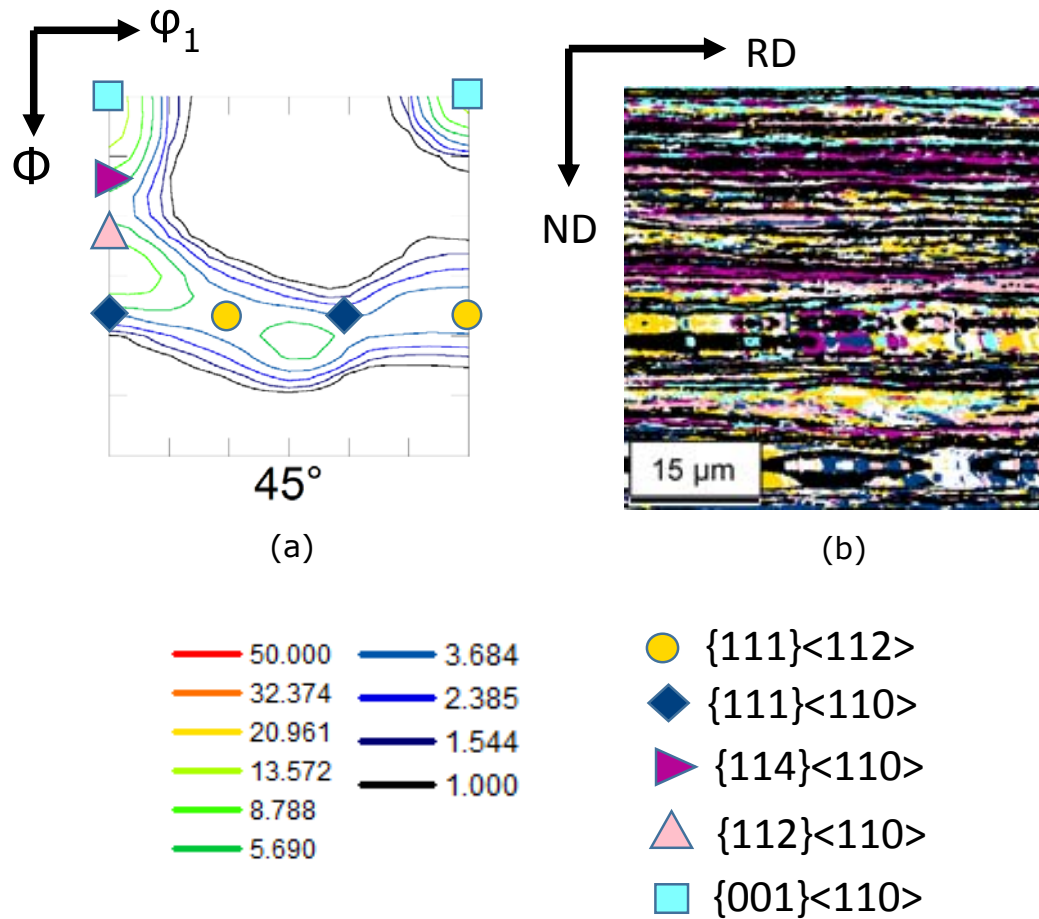


Fig.4.6: (a) shows the $\phi_2=45^\circ$ section of the ODF and (b) shows the orientation map of ferrite (austenite regions are masked) in DSS warm-rolled to 90% reduction in thickness at 498K (225°C).

corresponds to the phase map shown in Fig.4.4(d) with the austenite regions masked in black.

The ODF section (Fig.4.6(a)) clearly shows the presence of both RD and ND fibers in ferrite in contrast to the texture of ferrite the starting homogenized material, where the ND-fiber (ND//<111>) dominates the texture of ferrite (Fig.4.2). The ODF section, thus indicates that the RD-fiber is strengthened during warm-rolling. The major components along the RD-fiber are the $\{114\}<110>$ (highlighted in purple color in the orientation map in Fig.4.6(b) having volume fraction $\sim 14\%$), $\{112\}<110>$ (highlighted in pink color in the orientation map Fig.4.6(b) having volume fraction $\sim 14\%$) and $\{001\}<110>$ (highlighted in aqua color in the orientation map in Fig.4.6(b) having volume fraction $\sim 12\%$). The strongest component along the ND-fiber is $\{111\}<112>$ (highlighted in gold color in the orientation map in Fig.4.6(b) having volume fraction $\sim 17\%$). The fraction of the $\{111\}<110>$ (highlighted in deep blue color in the orientation map in Fig.4.6(b)) component is $\sim 13\%$.

The average volume fraction of the RD fiber ($\sim 43\%$) is decidedly greater than that of the ND-fiber ($\sim 23\%$). Thus, the strength of the ND-fiber is slightly reduced, whereas the strength of the RD-fiber is significantly enhanced in ferrite in DSS 90% warm-rolled at 498K (225°C) as compared ferrite in starting homogenized material.

Figure 4.7 shows the texture of austenite in DSS 90% warm-rolled at 498K (225°C). The (111) PF (Fig.4.7(a)) indicates the development of pure metal type texture which is confirmed by the presence of S ($\{123\}<634>$), brass or B_s ($\{110\}<112>$) and copper or Cu ($\{112\}<111>$) components in the respective ODF sections (Fig.4.7(b)). The orientation map of austenite is shown in Fig.4.7(c) which corresponds to the phase map shown in Fig.4.4(d)

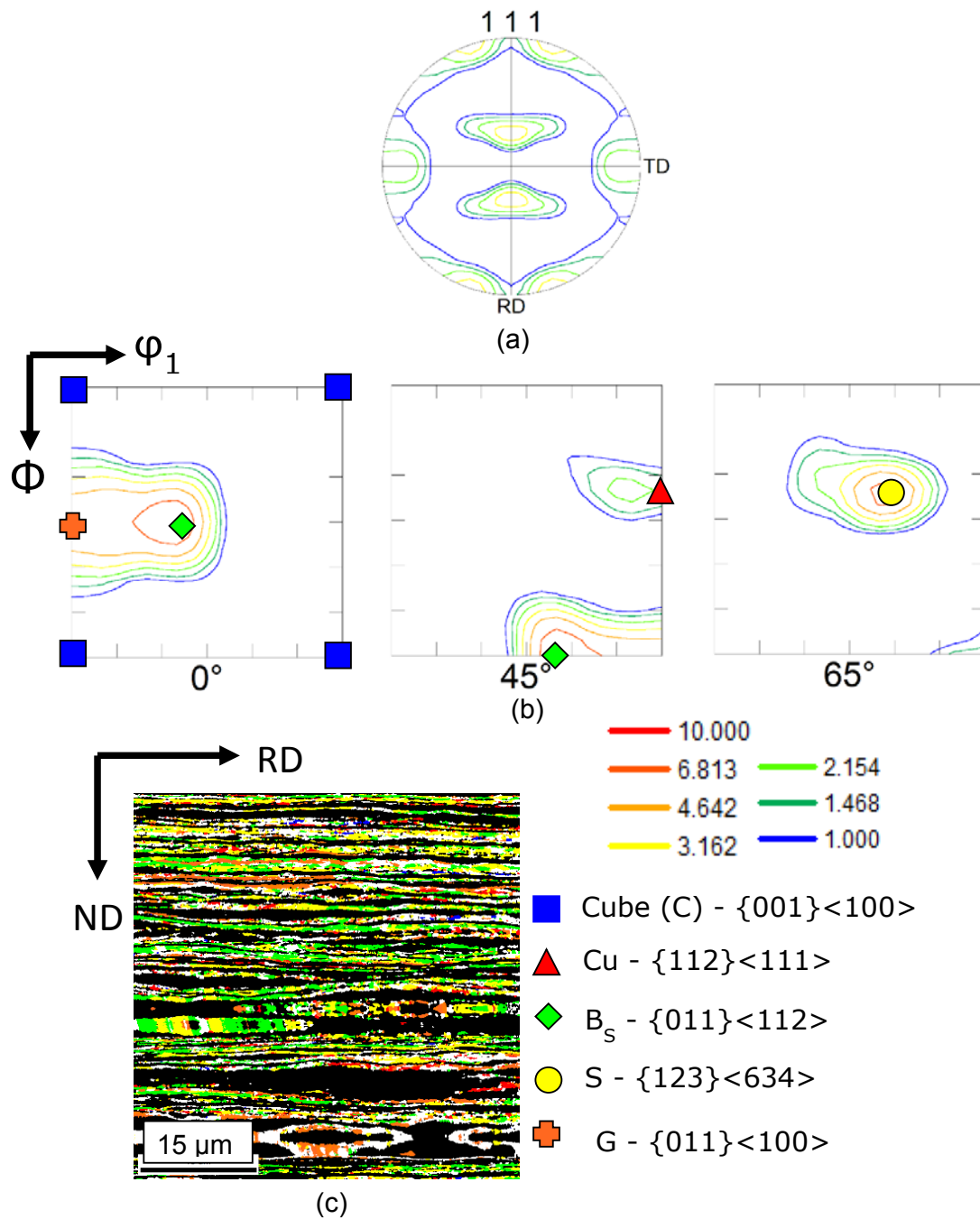


Fig.4.7: (a) shows the (111) PF, (b) shows the $\phi_2 = 0^\circ, 45^\circ$ and 65° sections of the ODF and (c) shows the orientation map of austenite (ferrite regions are masked) in DSS 90% warm-rolled at 498K (225°C).

with the ferrite regions masked in black. The orientation map of austenite clearly shows that S (highlighted in yellow) is the strongest component having volume fraction $\sim 27\%$, followed by the B_s (highlighted in green, volume fraction $\sim 20\%$), Goss or G ($\{110\}\langle 001\rangle$, highlighted in orange, volume fraction $\sim 10\%$) and Cu (highlighted in red, volume fraction $\sim 6\%$) components.

4.3. Evolution of microstructure and texture during warm-rolling at 698K (425°C)

4.3.1 Evolution of microstructure

Evolution of microstructure in DSS during warm-rolling at 698K (425°C) is shown in Fig.4.8 which shows the phase maps $\sim 20\%$ ($\epsilon_q=0.25$) (Fig.4.8(a)), 40% ($\epsilon_q=0.58$) (Fig.4.8(b)), 70% ($\epsilon_q=1.39$) (Fig.4.8(c)) and 90% ($\epsilon_q=2.66$) (Fig.4.8(d)) warm-rolled materials. Development of elongated banded morphology is observed with increasing deformation during warm-rolling at 698K (425°C). Alternate arrangement of ferrite and austenite bands start developing after 40% reduction in thickness (Fig.4.8(b)). The thickness of the ferrite bands differs significantly from one end of the bands to the other end as may be clearly observed from the phase map of the material warm-rolled to 70% reduction in thickness (Fig.4.8(c)).

The microstructure of DSS warm-rolled to 90% reduction in thickness at 698K (425°C) (Fig.4.8(d)) appears significantly different as compared to that of the material warm-rolled at 498K (225°C) (Fig.4.4(d)). The phase map of DSS 90% warm-rolled at 698K (425°C) (Fig.4.8(d)) shows remarkable fragmentation and presence of thick isolated ferrite blocks (marked by arrows in Fig.4.8(d)). Figure 4.8(e) shows a region of interest cropped from Fig.4.8(d) which clearly shows the fragmentation of microstructure.

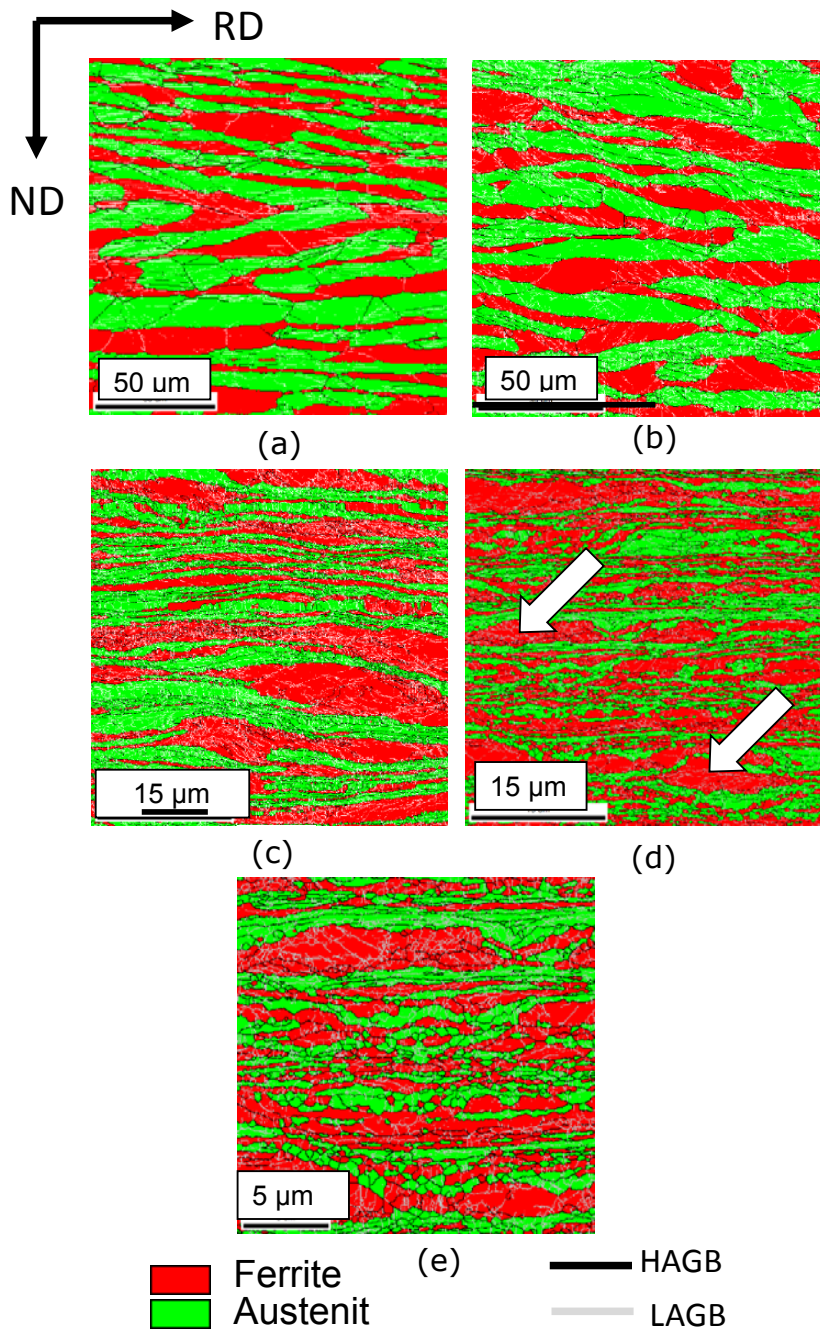


Fig.4.8: Phase maps of DSS warm-rolled at 698K (425°C) to (a) 20%, (b) 40%, (c) 70% and (d) 90% reduction in thickness. (e) shows a region of interest cropped from the map shown in (d).

Remarkably, the thick ferrite blocks do not show prominent subdivision by HAGBs. This is consistently observed throughout the microstructure of the 90% warm-rolled DSS at 698K (425°C). A number of scans have been acquired from different regions to confirm the fragmentation behavior.

A phase map from one such region of interest is shown in Fig.4.9(a). Thick ferrite blocks (indicated by arrow) and finely fragmented regions (shown with bounded circle) are observed in the phase map along with regions having a rather lamellar morphology (shown bounded by square). Extended HAGBs are not observed inside the thick ferrite blocks (marked by arrow in Fig.4.9(a)).

Table 4.3 summarizes the evolution of key microstructural parameters during warm-rolling at 698K (425°C). With increasing reduction the average phase band thickness of the two phases is decreased. Interestingly, there is a considerable difference in the average phase band thickness of austenite ($\sim 0.63\mu\text{m}$) and ferrite ($\sim 1.19\mu\text{m}$) following 90% warm-rolling. With increasing deformation beyond 40% thickness reduction, the HAGB fraction is increased. The HAGB spacing is consistently decreased during deformation. The HAGB fraction of austenite ($\sim 0.45\%$) is much higher than that of ferrite ($\sim 0.18\%$) in the 90% warm-rolled DSS. This also results in lower HAGB spacing in austenite ($\sim 0.66\mu\text{m}$) as compared to that in ferrite ($\sim 0.8\mu\text{m}$) in the 90% warm-rolled DSS.

The recovery behavior of the two phases during warm-rolling is studied using the KAM approach as already explained before. Area fraction having $\text{KAM} \leq 1$ for ferrite (~ 0.69) and austenite (~ 0.71) is found to be very similar in DSS 90% warm-rolled at 698K (425°C). Thus, the two phases show similar recovery behavior during warm-rolling at 698K (425°C).

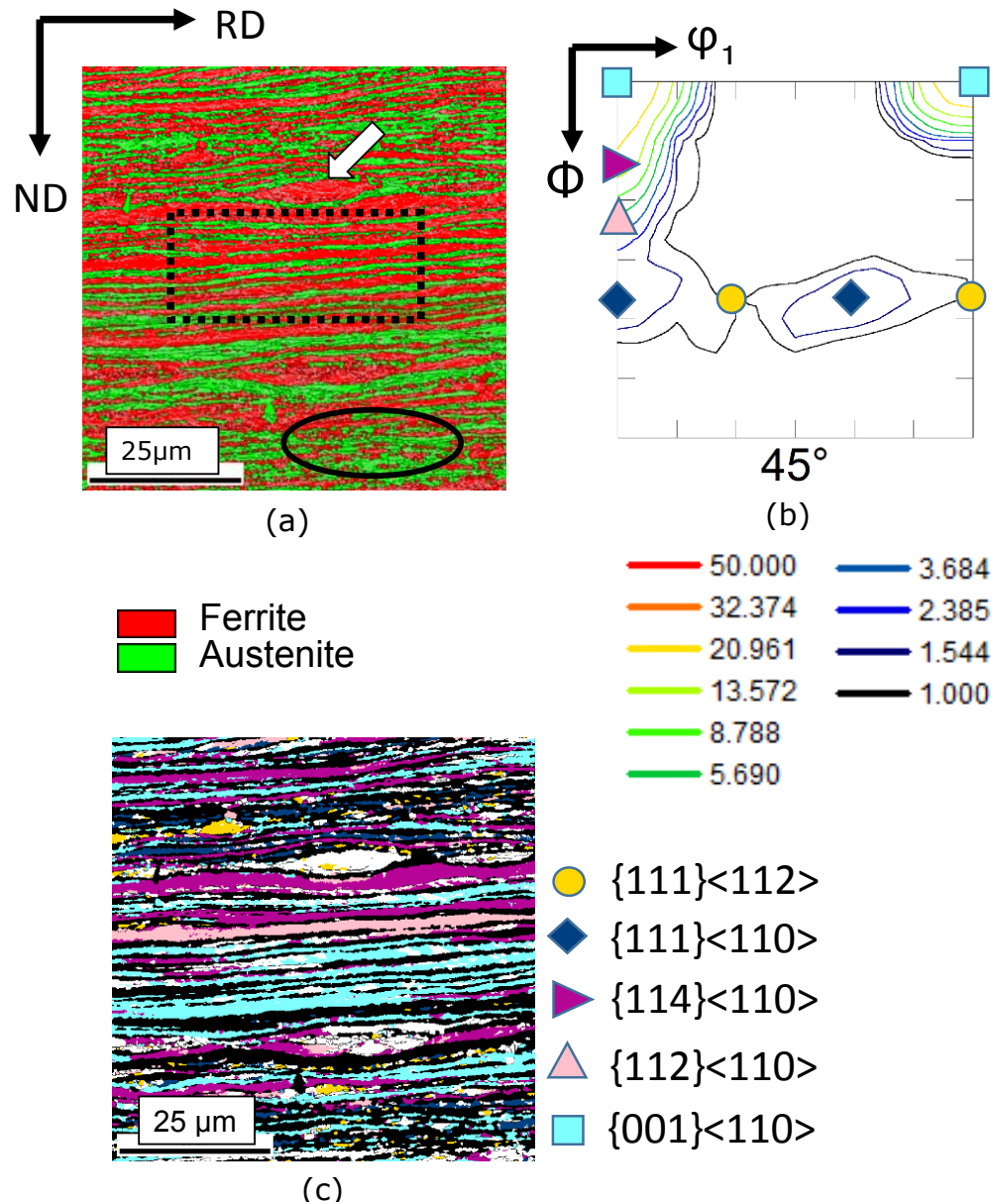


Fig.4.9: (a) shows the phase map obtained from another region of interest in DSS 90% warm-rolled to 90% reduction in thickness at 698K (425°C). (b) shows the $\phi_2 = 45^\circ$ section of ODF and (c) shows the orientation map of ferrite (austenite regions are masked)

Table.4.3: Evolution of key microstructural parameters in ferrite and austenite in DSS during warm-rolling at 698K (425°C).

% Thickness reduction	Area fraction of austenite	Phase band of spacing (μm)		HAGB fraction (%)		HAGB spacing (μm)	
		Ferrite	Austenite	Ferrite	Austenite	Ferrite	Austenite
20	50 \pm 3.9	4.1	5.1	0.09 \pm 0.01	0.24 \pm 0.021	5.37 \pm 0.19	3.86 \pm 0.01
40	57 \pm 0	3.7	5	0.08 \pm 0.017	0.19 \pm 0.017	4.73 \pm 0.53	3.32 \pm 0.24
70	48 \pm 0	2	3.5	0.15 \pm 0.045	0.27 \pm 0.038	1.68 \pm 0.1	1.22 \pm 0.08
90	45	1.19	0.63	0.18 \pm 0.023	0.45 \pm 0.016	0.8 \pm 0.07	0.66 \pm 0.01

4.3.2 Evolution of Texture

The texture of ferrite in DSS after 90% warm-rolling at 698K (425°C) is shown in Fig.4.10. The intensity distribution in the $\varphi_2 = 45^\circ$ section of ODF of ferrite (Fig.4.10(a)) in 90% warm-rolled DSS at 698K (425°C) shows remarkable strengthening of the RD-fiber at the expense of the ND-fiber. The strongest component along the RD-fiber is $\{001\}\langle 110 \rangle$. The orientation map of ferrite (Fig.4.10(b)) which corresponds to the phase map shown in Fig.4.8(d), with the austenite phase masked in black, amply supports the qualitative observations obtained from the ODF. The volume fractions of the RD-fiber components $\{001\}\langle 110 \rangle$ (highlighted in aqua in the orientation map in Fig.4.10(b)), $\{114\}\langle 110 \rangle$ (highlighted in purple in the orientation map in Fig.4.10(b)) and $\{112\}\langle 110 \rangle$ (highlighted in pink in the orientation map) are $\sim 44\%$, 18% and $\sim 5\%$, respectively. The strongest component along the ND-fiber is $\{111\}\langle 112 \rangle$ (highlighted in gold in the orientation map in Fig.4.10(b)) having volume fraction $\sim 7\%$. The fraction of the $\{111\}\langle 110 \rangle$ (highlighted in deep blue in the orientation map in Fig.4.10(b)) component is $\sim 5\%$. The presence of the much stronger RD-fiber as compared to the ND-fiber in ferrite in DSS 90% warm-rolled at 698K (425°C) is also confirmed from the scan obtained from the other region of the DSS (Fig 4.9).

The $\varphi_2 = 45^\circ$ section of the ODF (Fig.4.9(b)) and the orientation map of ferrite (Fig.4.9(c) which corresponds to the phase map shown in Fig.4.9(a) with the austenite regions masked in black) shows the presence of remarkably stronger RD-fiber as compared to the ND-fiber confirming that RD-fiber dominates the texture of ferrite in DSS warm-rolled at 698K (425°C). The strongest RD-fiber component observed in this area is $\{001\}\langle 110 \rangle$ (highlighted in aqua in the orientation map in Fig.4.9(b)) having volume fraction

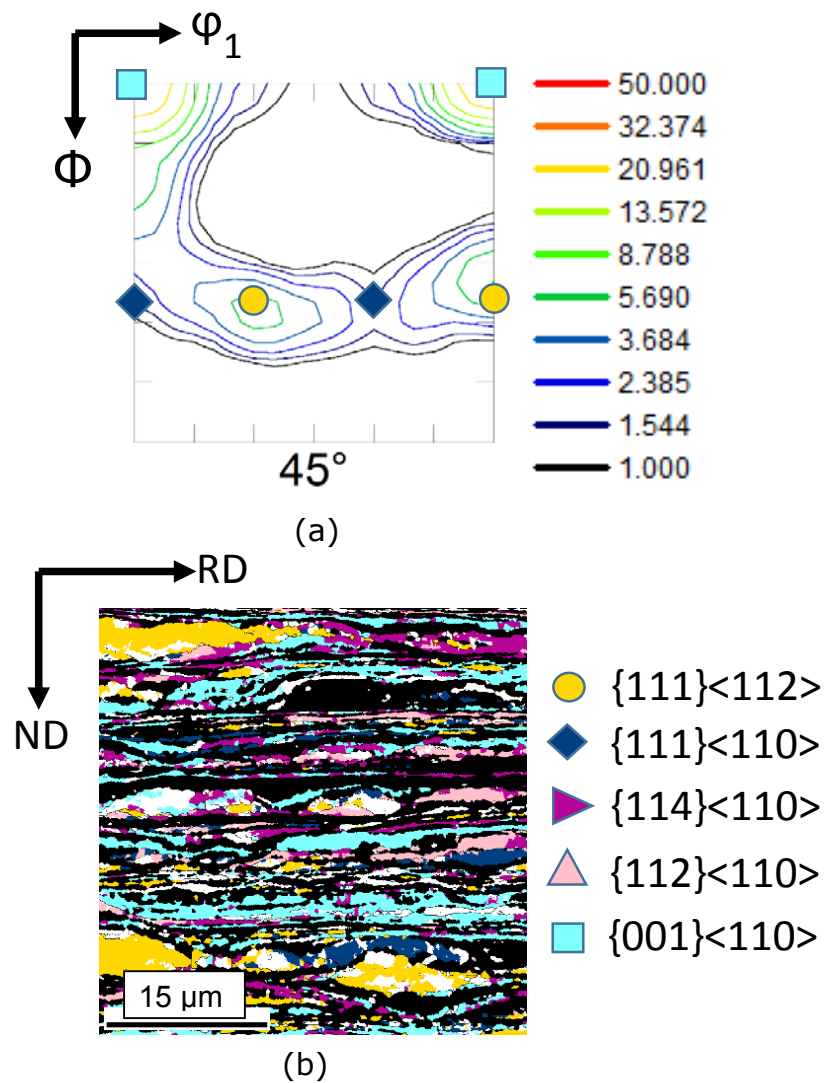


Fig.4.10: (a) shows the $\phi_2=45^\circ$ section of the ODF and (b) shows the orientation map of ferrite (austenite regions are masked) in DSS warm-rolled to 90% reduction in thickness at 698K (425°C).

~33%, followed by the $\{114\}\langle 110 \rangle$ (highlighted in purple in the orientation map in Fig.4.9 (b)) having volume fraction ~ 28%.

The total average volume fraction of the RD-fiber is ~68%, while that of the ND-fiber is ~10% in the 90% warm-rolled DSS at 698K (425°C). Thus, in comparison to the texture of ferrite in the starting homogenized DSS (Fig.4.2) and in the 90% warm-rolled DSS at 498K (225°C) (Fig.4.6), the texture of ferrite in DSS 90% warm-rolled at 698K (425°C) (Figures 4.9 and 4.10) shows the development of much stronger RD-fiber than the ND-fiber.

The texture of austenite in 90% warm-rolled DSS at 698K (425°C) is shown in Fig.4.11. The (111) PF (Fig.4.11(a)) indicates the development of pure metal type texture characterized by the presence of S, B_S and Cu components. This is also supported by the $\varphi_2 = 0^\circ, 45^\circ$ and 65° sections of the ODF (Fig.4.11 (b)) revealing the presence of the above components in the respective ODF sections.

The spatial distribution of the texture components is shown in the orientation map in Fig.4.11(c). The orientation map shown in Fig.4.11(c) corresponds to the phase map shown in Fig.4.8(d) with the ferrite regions masked. The strongest texture component is the S (highlighted in yellow in the orientation map in Fig.4.11(c) having volume fraction of ~22%), followed by the B_S (highlighted in green in the orientation map in Fig.4.11(c) having volume fraction of ~17%), Cu (highlighted in red in the orientation map in Fig.4.11(c)) having volume fraction of ~9%) and G (highlighted in orange in the orientation map in Fig.4.11(c)) having volume fraction of ~3%.

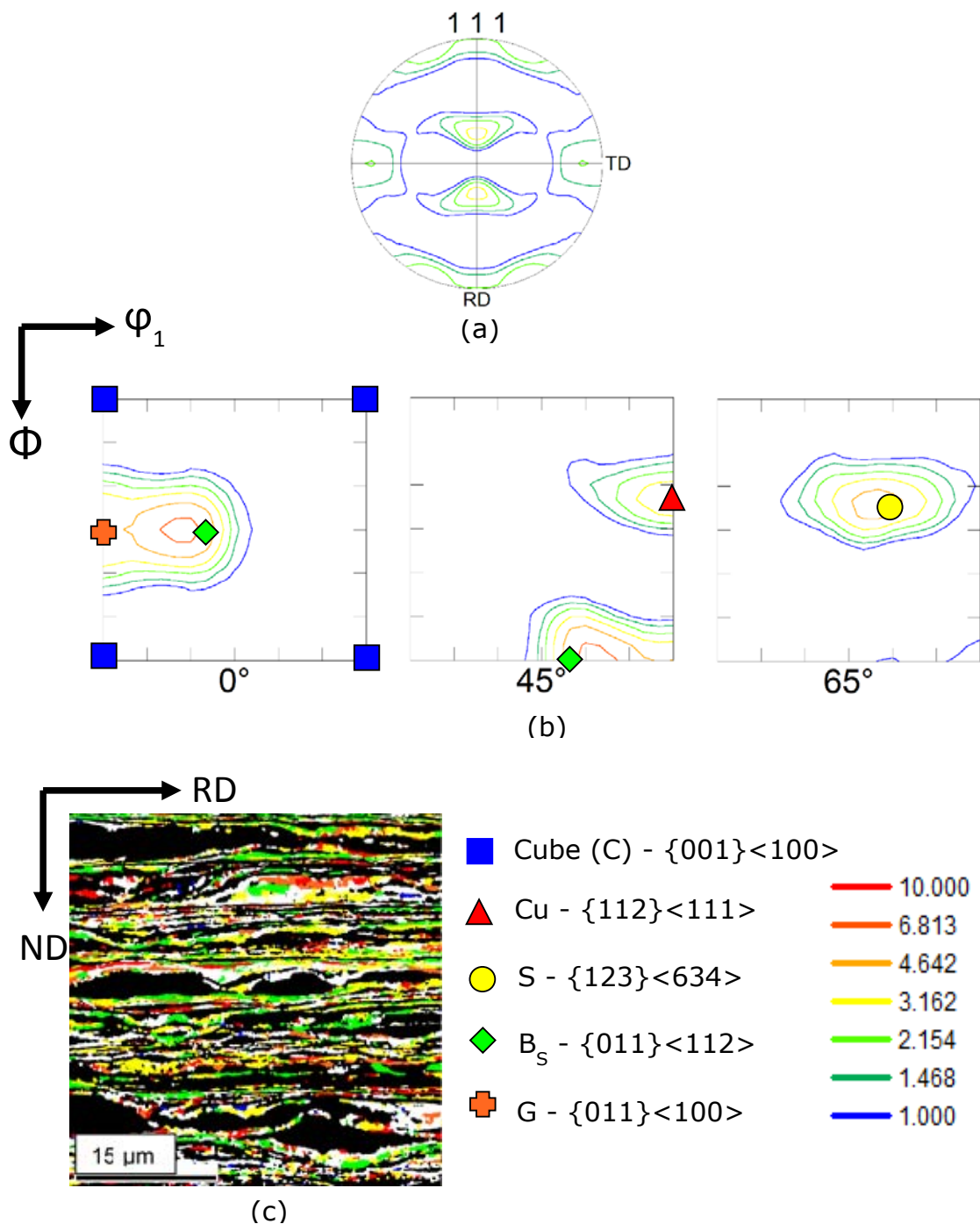


Fig.4.11: (a) shows the (111) PF, (b) shows the $\phi_2 = 0^\circ, 45^\circ$ and 65° sections of the ODF and (c) shows the orientation map of austenite (ferrite regions are masked) in DSS warm-rolled to 90% reduction in thickness at 698K (425°C).

4.4. Evolution of microstructure and texture during warm-rolling at 898K (625 °C)

4.4.1 Evolution of microstructure

Evolution of microstructure during warm-rolling at 898K (625°C) is shown in Fig.4.12 which shows the phase maps of the DSS warm-rolled to 20% ($\epsilon_q=0.25$) (Fig.4.12(a)), 40% ($\epsilon_q=0.58$) (Fig.4.12(b)), 70% ($\epsilon_q=0.1.39$) (Fig.4.12(c)) and 90% ($\epsilon_q=2.66$) (Fig.4.12(d)) reduction in thickness. With increasing deformation up to 70% reduction in thickness (Fig.4.12(a)-(c)), development of lamellar morphology with alternate arrangement of deformed ferrite and austenite bands could be observed.

The microstructure of the DSS after 90% (Fig.4.12(d)) warm-rolling shows the development of remarkably fine lamellar morphology almost free of local fragmentation throughout the thickness. This is in sharp contrast to profuse local fragmentation observed in the case of DSS 90% warm-rolled at 698K (425°C) (Figures 4.8(d) and 4.9(a)). The fine lamellar microstructure is revealed clearly in Fig.4.12(e) which is a region of interest cropped from the phase map shown in Fig.4.12(d). It is clearly observed that individual deformed bands of austenite and ferrite are finely subdivided by HAGBs extended parallel to the RD.

Table 4.4 shows the evolution of key microstructural parameters during warm-rolling at 898K (625°C). Austenite remains stable during warm-rolling at 898K (625°C) having a volume fraction $\sim 55\%$ in the 90% warm-rolled DSS. The average thickness of austenite ($\sim 0.52 \mu\text{m}$) and ferrite ($\sim 0.45 \mu\text{m}$) bands are found quite similar to the 90% warm-rolled DSS. This indicates that the imposed strain during warm-rolling at 898K (625°C) is partitioned equally amongst the two constituent phases.

The HAGB fraction increases beyond 40% warm-rolling. The HAGB spacing is decreased consistently with increasing deformation

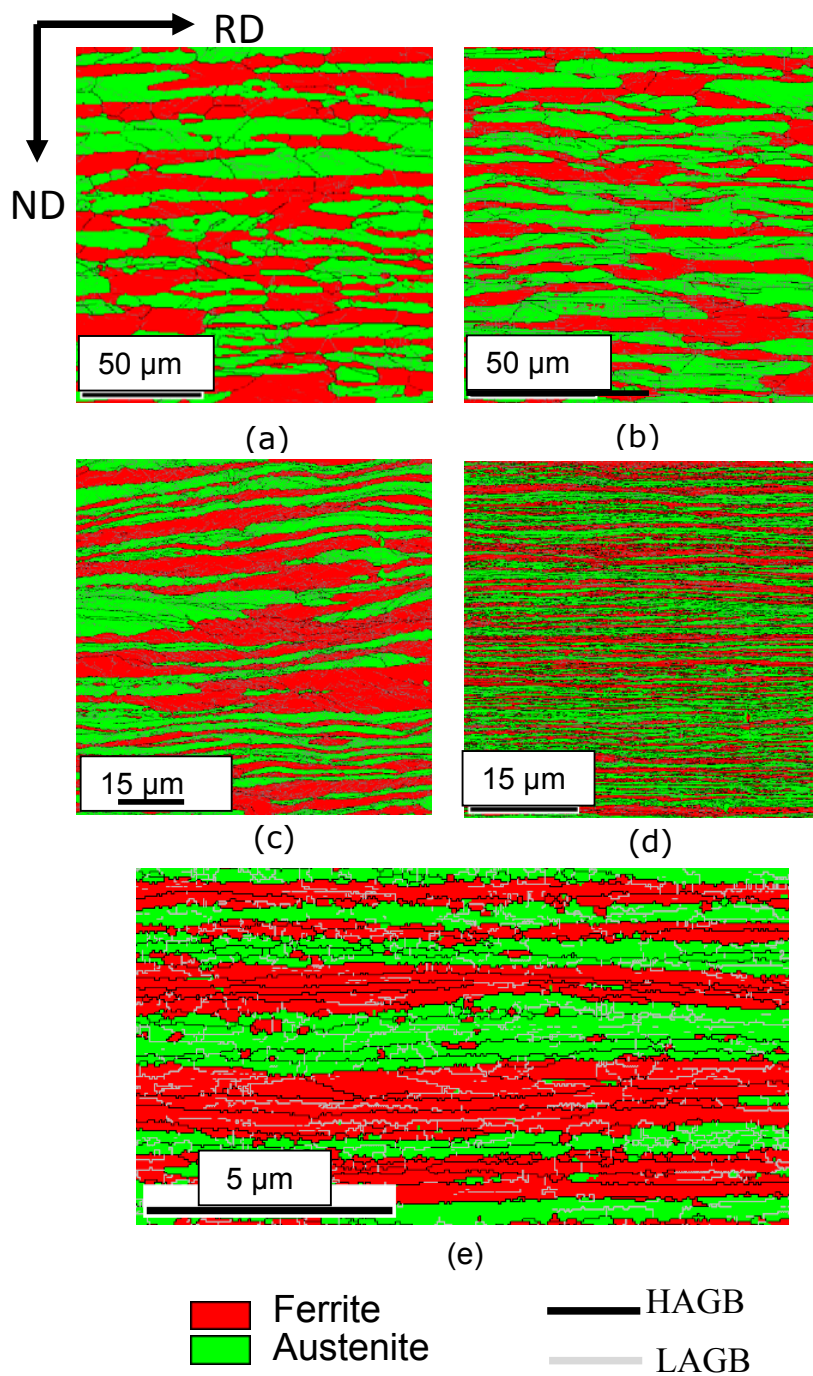


Fig.4.12: Phase maps of DSS warm-rolled at 898K (625°C) to (a) 20%, (b) 40%, (c) 70% and (d) 90% reduction in thickness. (e) shows a region of interest cropped from the phase map of 90% warm-rolled DSS shown in (d).

Table.4.4: Evolution of key microstructural parameters in ferrite and austenite in DSS during warm-rolling at 898K (625°C).

% Thickness reduction	Area fraction of austenite	Phase band spacing (μm)		HAGB fraction (%)		HAGB spacing (μm)	
		Ferrite	Austenite	Ferrite	Austenite	Ferrite	Austenite
20	53 \pm 2.5	5.75	5.7	0.17 \pm 0.019	0.37 \pm 0.031	4.2 \pm 0.14	4.8 \pm 0.25
40	55 \pm 2.5	3.8	4.6	0.07 \pm 0.012	0.21 \pm 0.016	2.13 \pm 0.48	2.8 \pm 0.6
70	60 \pm 4	1.67	1.65	0.12 \pm 0.009	0.27 \pm 0.015	2 \pm 0.1	1.52 \pm 0.17
90	55	0.52	0.45	0.38 \pm 0.08	0.56 \pm 0.032	0.39 \pm 0.07	0.31 \pm 0.06

in both the phases. However, austenite shows much finer structure as compared to ferrite. This is easily understood from significantly higher HAGB fraction and lower HAGB spacing in austenite ($\sim 0.56\%$ and $0.31\mu\text{m}$, respectively) as compared to those in ferrite ($\sim 0.38\%$ and $0.39\mu\text{m}$, respectively) in the DSS warm-rolled to 90% reduction in thickness at 898K (625°C).

The recovery behavior of the two phases during warm-rolling is studied by KAM approach as already explained before. Area fraction having $\text{KAM} < 1$ in the two phases is found to be quite similar ~ 0.87 .

4.4.2 Evolution of Texture

The texture of ferrite in DSS warm-rolled to 90% reduction in thickness at 898K (625°C) is shown in Fig.4.13. The $\phi_2 = 45^\circ$ section of ODF of ferrite (Fig.4.13(a)) reveals the presence of both RD and ND fibers. The spatial distribution of individual texture components belonging to the two fibers is shown in the orientation map in Fig.4.13(b). The orientation map shown in Fig.4.13(b) corresponds to the phase map of Fig.4.12(d) with the austenite phase masked in black. The strongest component along the RD-fiber is $\{114\}<110>$ (highlighted in purple in the orientation map in Fig. 4.13(b)) having volume fraction $\sim 15\%$, followed by the $\{001\}<110>$ (highlighted in aqua in the orientation map in Fig. 4.13(b)) having volume fraction $\sim 12\%$ and $\{112\}<110>$ (highlighted in pink in the orientation map in Fig. 4.13(b)) having volume fraction $\sim 9\%$. The strongest component along the ND-fiber is $\{111\}<112>$ (highlighted in gold in the orientation map in Fig. 4.13(b)) having volume fraction $\sim 14\%$. The fraction of the $\{111\}<011>$ component (highlighted in deep blue in the orientation map in Fig. 4.13(b)) is $\sim 12\%$. The total average volume fraction of the RD-fiber is $\sim 37\%$, while that of the ND fiber is $\sim 22\%$. Thus, the textures of ferrite in

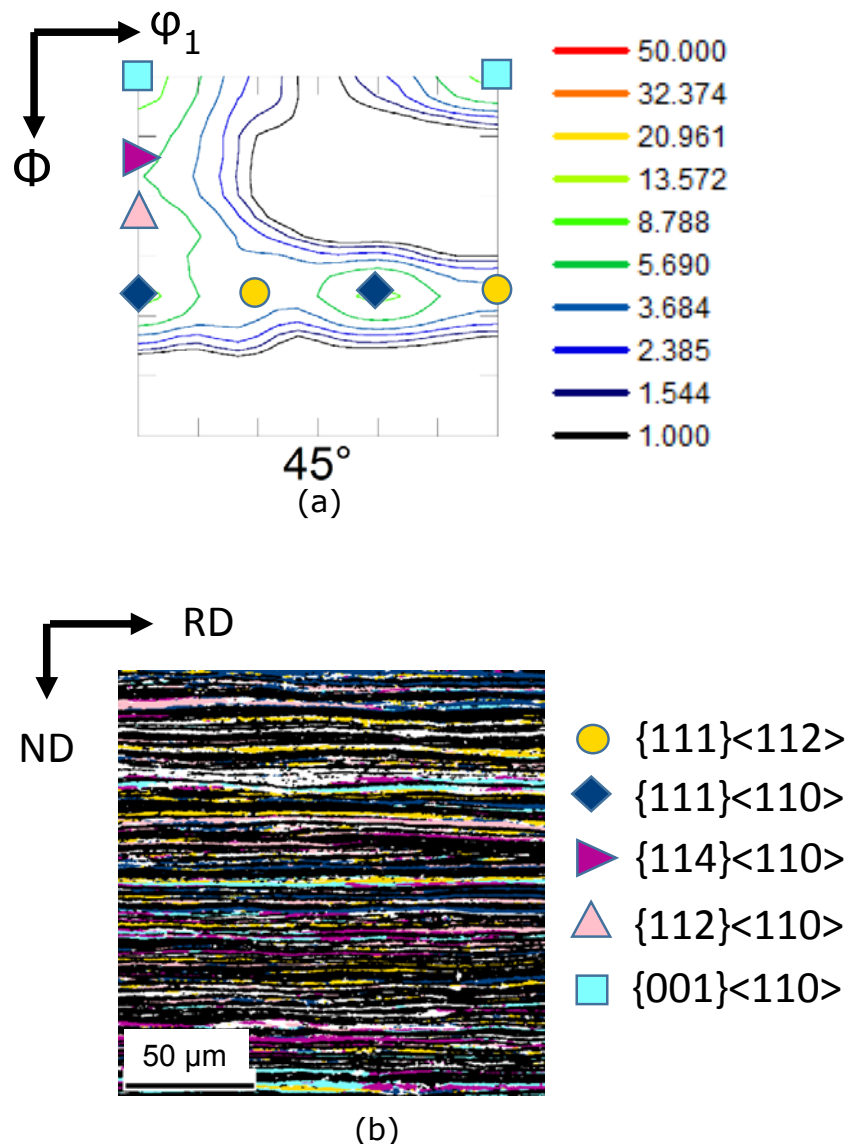


Fig.4.13: (a) shows the $\phi_2=45^\circ$ section of the ODF and (b) shows the orientation map of ferrite (austenite regions are masked) in DSS warm-rolled to 90% reduction in thickness at 898K (625°C).

DSS 90% warm-rolled at 498K (225°C) and 898K (625°C) are similar but significantly different than that of ferrite in DSS 90% warm-rolled at 698K (425°C).

The texture of austenite in 90% warm-rolled DSS at 898K (625°C) is shown in Fig.4.14. The (111) PF (Fig.4.14(a)) clearly shows the development of pure metal type texture. The $\phi_2 = 0^\circ$, 45° and 65° sections of ODF of austenite (Fig.4.14(b)) indicate the presence S, B_s and Cu components in the respective ODF sections. The spatial distribution of the texture components is shown in the orientation map in Fig.4.14(c) which corresponds to the phase map shown in Fig.4.12(d) with the ferrite regions masked. The orientation map shows that the strongest component is the S (highlighted in yellow in the orientation map of Fig.4.14(c)) having volume fraction of $\sim 25\%$, followed by the Cu (highlighted in red in the orientation map of Fig.4.14(c)) having volume fraction $\sim 14\%$, B_s (highlighted in green in the orientation map of Fig.4.14(c)) having volume fraction $\sim 9\%$ and G (highlighted in orange in the orientation map of Fig.4.14(c)) having volume fraction $\sim 4\%$.

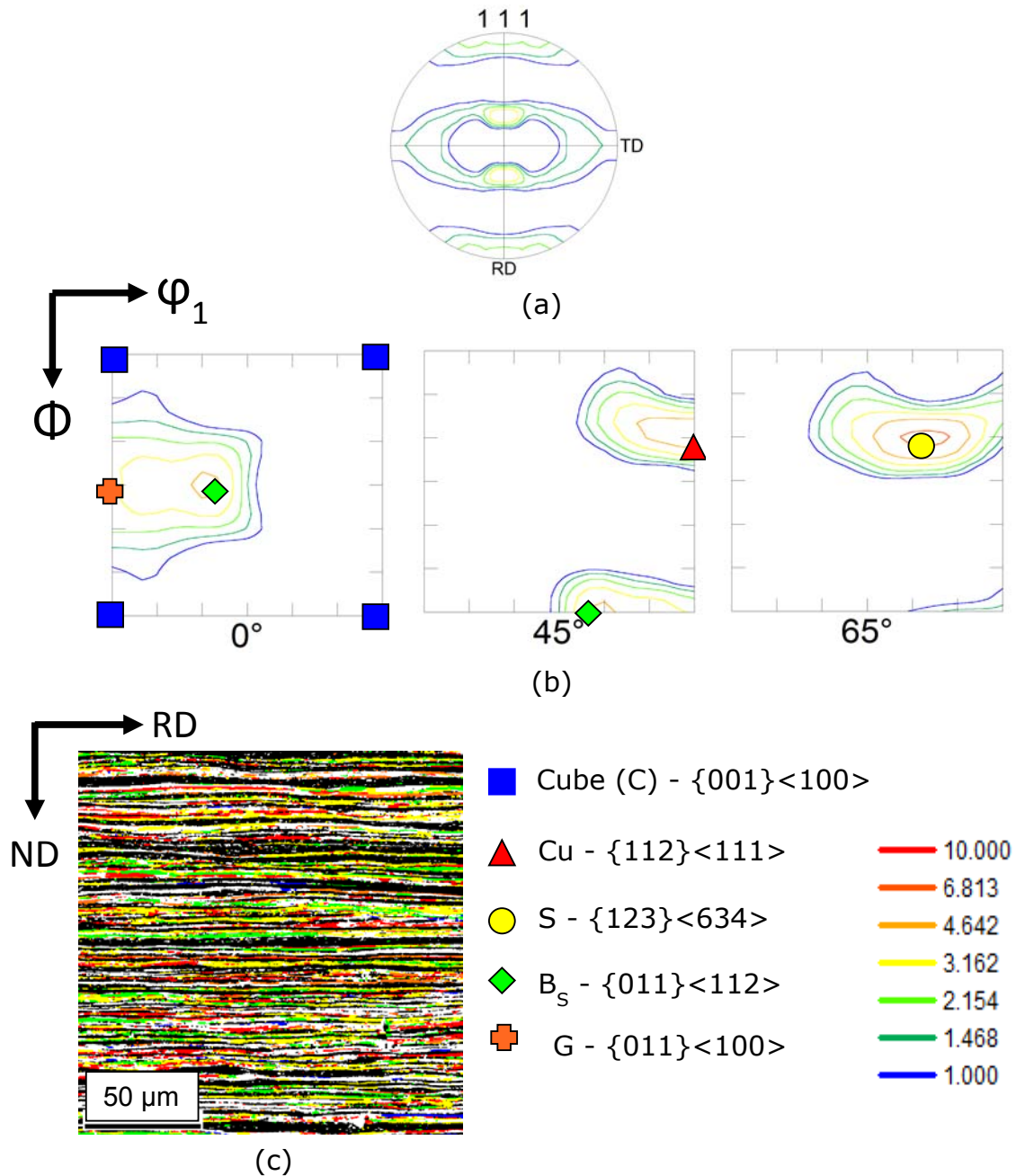


Fig.4.14: (a) shows the (111) PF and (b) shows the $\phi_2 = 0^\circ$, 45° and 65° sections of the ODF, (c) shows the orientation map of austenite (ferrite regions are masked) in DSS warm-rolled to 90% reduction in thickness at 898K (625°C).

4.5 Evolution of microstructure and texture during subsequent recrystallization

The evolution of microstructure and texture during recrystallization is investigated by studying the isothermal annealing behavior of DSS warm-rolled to 90% reduction in thickness at the three temperatures. The isothermal annealing treatments are carried out at 1448K (1175°C) i.e. at the homogenization temperature in order to avoid phase transformation during annealing.

The 90% deformation level is selected for the annealing studies as the main features of deformation microstructure are already developed in this condition. As already observed, the two phases of DSS in 90% warm-rolled DSS at different temperatures show significant variation in microstructure and texture. Therefore, isothermal annealing behavior of 90% warm-rolled DSS would be helpful to understand the effect of warm-rolling temperature on the evolution of microstructure and texture during subsequent annealing.

For effective discussion of the isothermal annealing treatments, a simple sample designation scheme is used in the present work as shown in Table 4.5. The three series of DSS warm-rolled to 90% reduction in thickness at 498K (225°C), 698K (425°C) and 898K (625°C) are designated as A, B and C series specimens, respectively. Further, a suffix is used to denote the annealing time. For easy referencing in the text, the as warm-rolled specimens are also included in the table with suffix 0 (for e.g. A0 denotes the as warm-rolled material at 498K (225°C)).

Table 4.5: Sample designation scheme used in the present work for different warm-rolled (90% reduction in thickness) and isothermally annealed specimens.

Warm-rolling temperature	Sample designation				
	As warm-rolled (90%)	Isothermal holding time (minutes) during subsequent annealing at 1448K (1175°C)			
		2	20	30	120
498K (225°C)	A0	A2	A20	A30	A120
698K (425°C)	B0	B2	B20	B30	B120
898K (625°C)	C0	C2	C20	C30	C120

4.6 Evolution of microstructure and texture during annealing of 90% warm-rolled DSS at 498K (225 °C)

4.6.1 Evolution of microstructure during annealing

Figure 4.15 shows phase maps of A2 (Fig.4.15(a)), A20 (Fig.4.15(b)), A30 (Fig.4.15(c)) and A120 (Fig.4.15(d)) specimens. The lamellar banded morphology of the as warm-rolled material (Fig.4.4(d)) is retained after isothermal annealing for 2 minutes (Fig.4.15(a)) which is evidenced by the presence of extended phase bands along RD (marked by arrows). Each phase band appears to be one grain thick when measured along the ND. LAGBs in ferrite and HAGBs in austenite are found to run perpendicular to the phase boundaries. This results in a classical 'bamboo' type morphology. Annealing twins (indicated by yellow lines) are clearly observed inside the austenite bands. However, several regions (marked by dotted circles) are observed in the phase map in Fig.4.15(a) where mutual interpenetration of phase bands along the grain boundaries quite evident.

With increasing isothermal annealing time, the lamellar morphology is broken down, resulting in the gradual evolution of a more globular morphology, which is quite evident in the phase maps of the A20 (Fig.4.15(b)) and A30 (Fig.4.15(c)) specimens. The interpenetration of phase bands is clearly observed in the phase map in Fig.4.15(b) (marked by dotted circle). Further increase in isothermal holding time does not change the morphology significantly as may be quite evident from the phase map of the A120 specimen (Fig.4.15(d)).

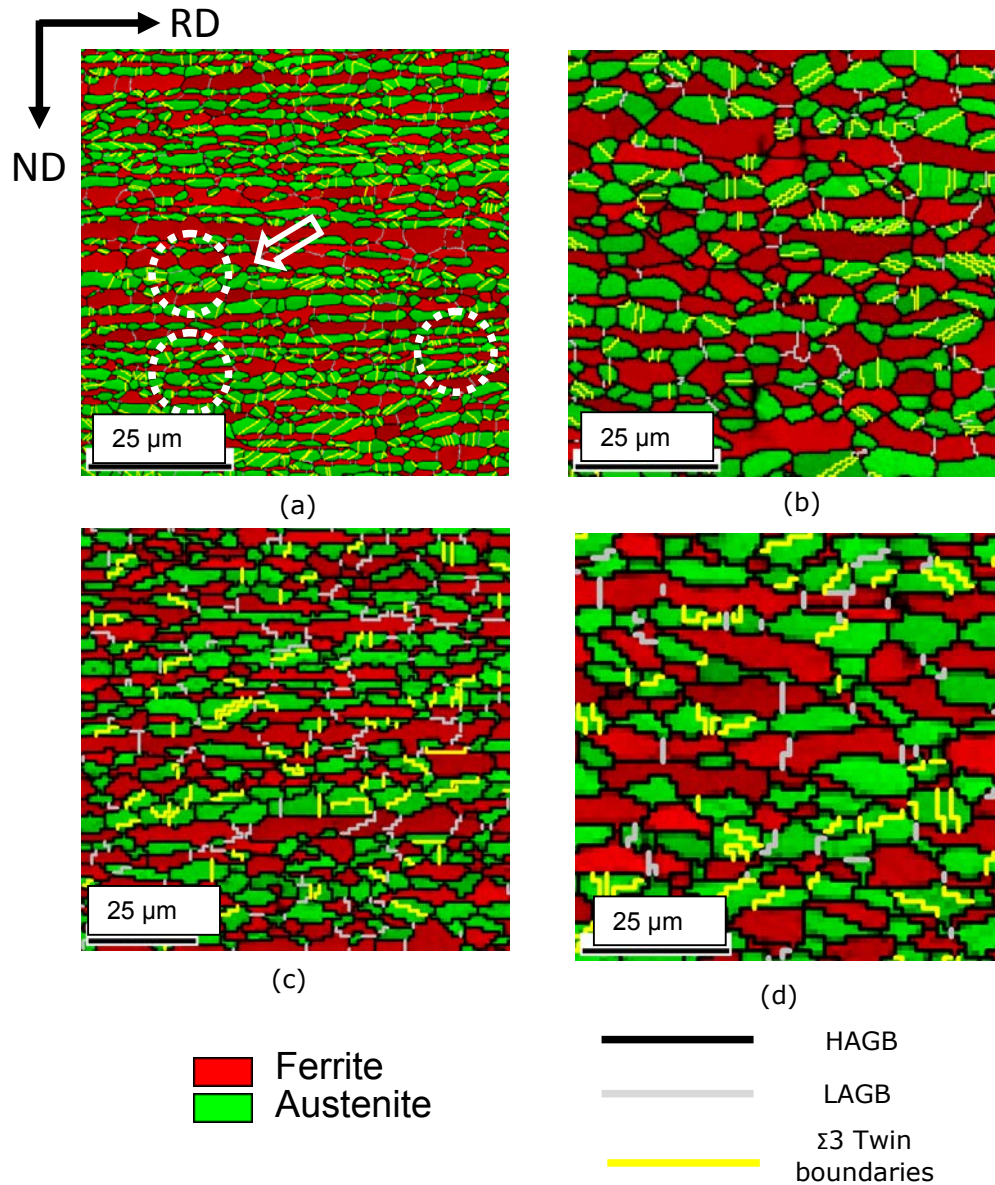


Fig.4.15: Phase maps of the (a) A2, (b) A20, (c) A30 and (d) A120 DSS specimens.

The evolution of key microstructural parameters, such as, phase fraction, grain thickness along the ND and aspect ratio is summarized in Fig. 4.16. Interestingly, the ferrite phase fraction is decreased initially, but is stabilized at $\sim 50\%$ during the prolonged isothermal holding (Fig.4.16(a)). Grain size of the two phases in different annealed conditions is determined by measuring the grain thickness along the ND. Since each phase band is one grain thick as is observed from the phase maps, the grain and phase band thickness are same. Figure 4.16(b) shows the variation of ferrite and austenite grain thickness along ND during isothermal annealing. Although, increase in grain thickness is observed during annealing up to 30 minutes, extensive grain growth is not observed even after annealing for 120 minutes. This is quite evident from similar average grain size ($\sim 5 \mu\text{m}$) of the two phases in the A120 specimen. The aspect ratio (defined by the ratio of grain thickness along the ND and the RD) of ferrite and austenite is shown in Fig.4.16(c). The aspect ratio of the two phases is decreased initially after isothermal annealing for 2 minutes. This shows that grain growth is initially higher along the RD. However, the aspect ratio is increased with increasing isothermal annealing time, however, significant variation in aspect ratio is not observed beyond annealing time of 30 minutes. The aspect ratio of austenite is found to be consistently greater than that of the ferrite in different isothermally annealed A series DSS specimens.

4.6.2 Evolution of texture during annealing

Figure 4.17 shows the $\varphi_2=45^\circ$ sections of the ODFs of ferrite in different isothermally annealed A series DSS specimens. The intensity distribution in the ODF sections clearly shows the presence of stronger RD-fiber than ND-fiber in ferrite of the annealed A series DSS specimens.

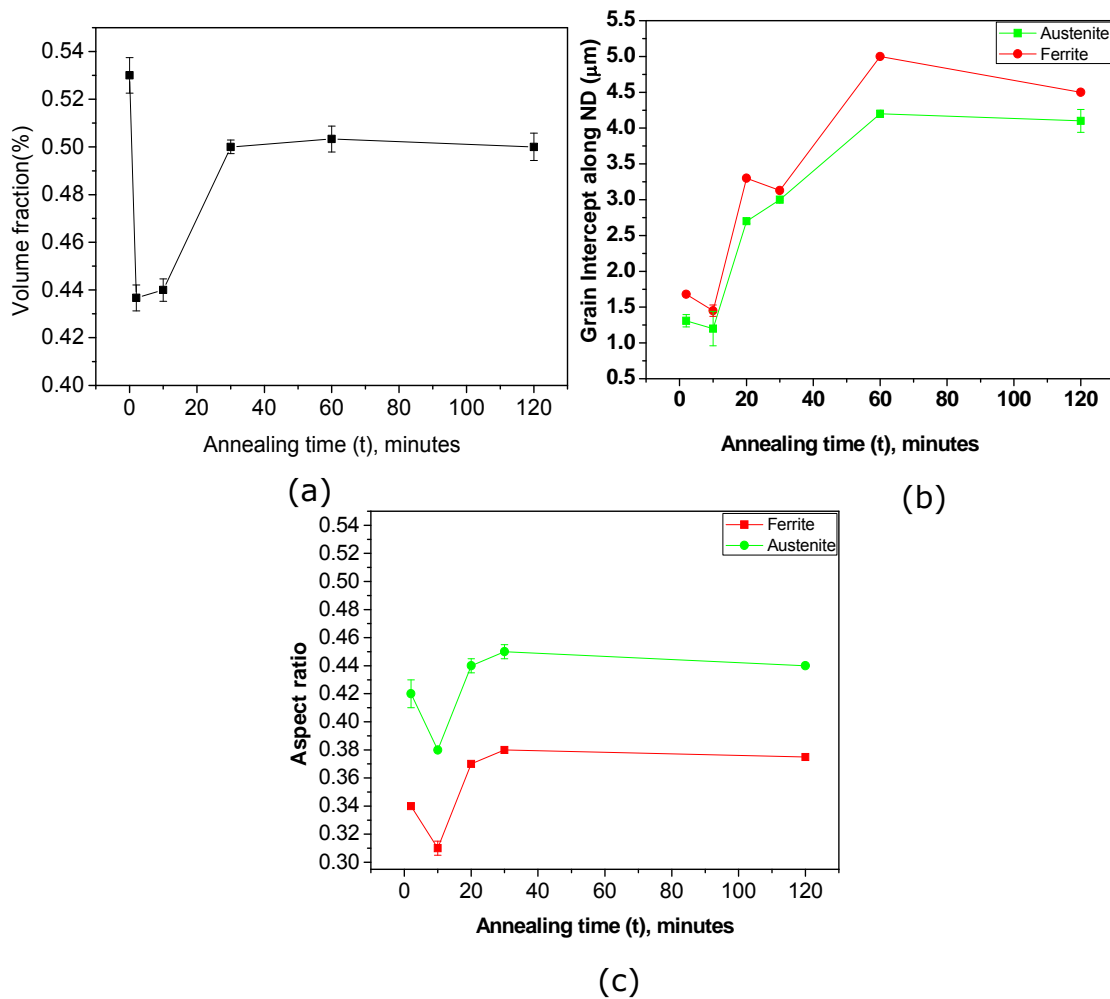


Fig.4.16: Evolution of (a) ferrite fraction, (b) grain thickness (measured along the ND) and (c) aspect ratio of the two phases in isothermally annealed A series DSS specimens.

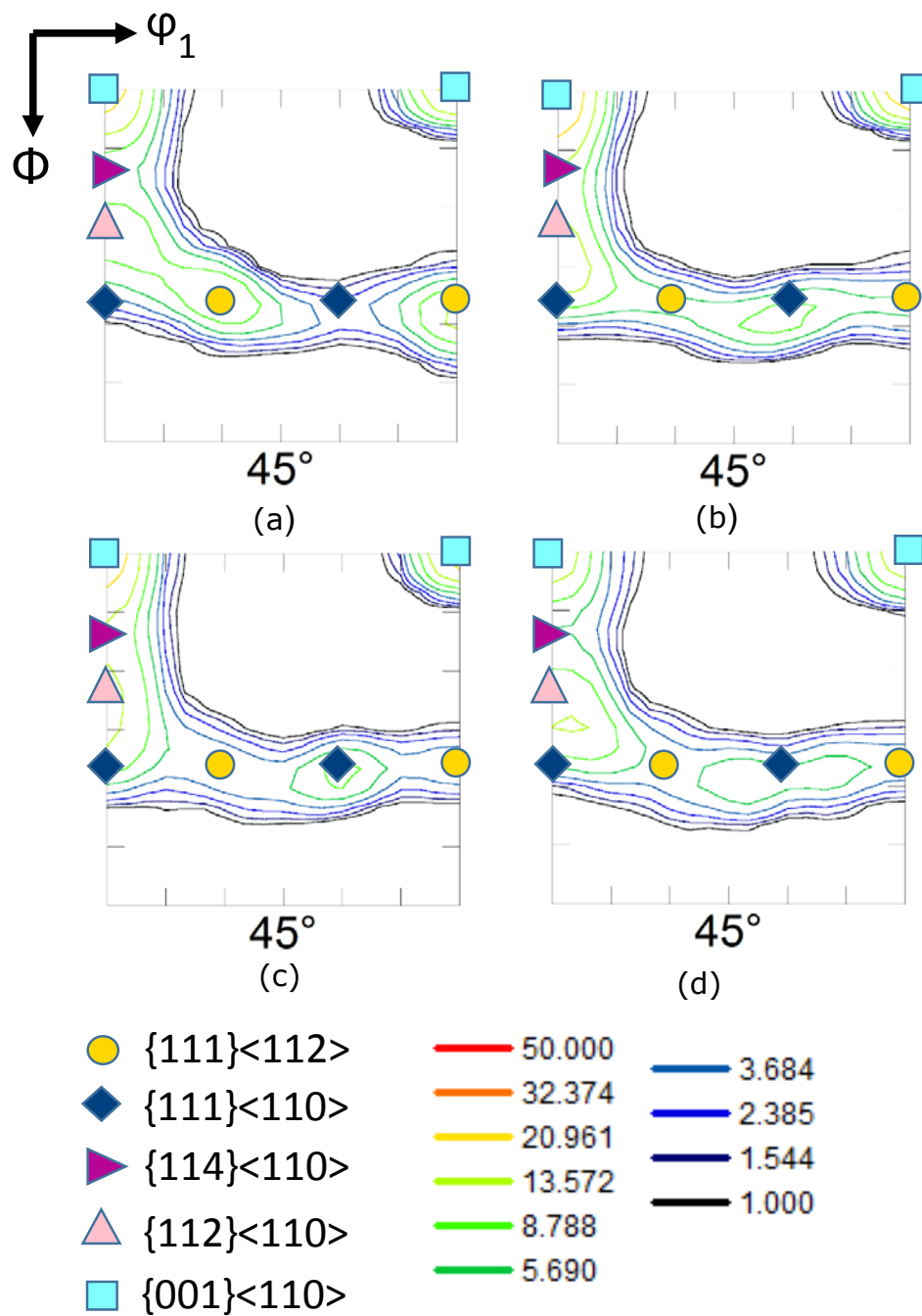


Fig.4.17: $\phi_2 = 45^\circ$ section of the ODF of ferrite in isothermally annealed (a) A2, (b) A20, (c) A30, (d) A120 DSS specimens.

The intensity peak along the RD-fiber in the A2 specimen is located at $\{112\}\langle 110\rangle$ (Fig.4.17(a)). With increasing isothermal annealing time the intensity peak along the RD-fiber is shifted to the $\{001\}\langle 110\rangle$ location which is evident from the ODF section of the A20 (Fig.4.17(b)), A30 (Fig.4.17(c)) and A120 (Fig.4.17(d)). The strongest component along the ND-fiber is $\{111\}\langle 112\rangle$ in the annealed A2 specimen. However, with increasing isothermal annealing time the intensity peak along the ND-fiber is shifted to the $\{111\}\langle 110\rangle$ location.

Evolution of the two texture fibers in ferrite of the annealed A series specimens is shown quantitatively in Fig.4.18. Figure 4.18 also includes the data for as warm-rolled condition for ease of understanding. The RD-fiber is strengthened with increasing annealing time up to 30 minutes, but no significant change is observed during further annealing. The volume fraction of the RD-fiber ($\sim 45\%$) is much higher than that of the ND-fiber ($\sim 21\%$) in the A120 specimen. Thus, the basic features of texture of ferrite in the as warm-rolled condition, i.e. stronger RD-fiber than ND-fiber is retained by ferrite in isothermally annealed A series DSS specimens.

Figure 4.19 shows the (111) PF of austenite in A2 (Fig.4.19(a)), A20 (Fig.4.19(b)), A30 (Fig.4.19(c)) and A120 (Fig.4.19(d)) specimens. The (111) PFs in different isothermally annealed DSS specimens appear quite similar to that of austenite in the as warm-rolled DSS (Fig.4.7(a)), indicating the retention of deformation texture components even after annealing. This is also amply corroborated by the appearance of the $\phi_2 = 0^\circ$, 45° and 65° sections of the ODF of austenite in different annealed A series specimens (Fig.4.20) which clearly reveal the presence of S, B_S, Cu and G components.

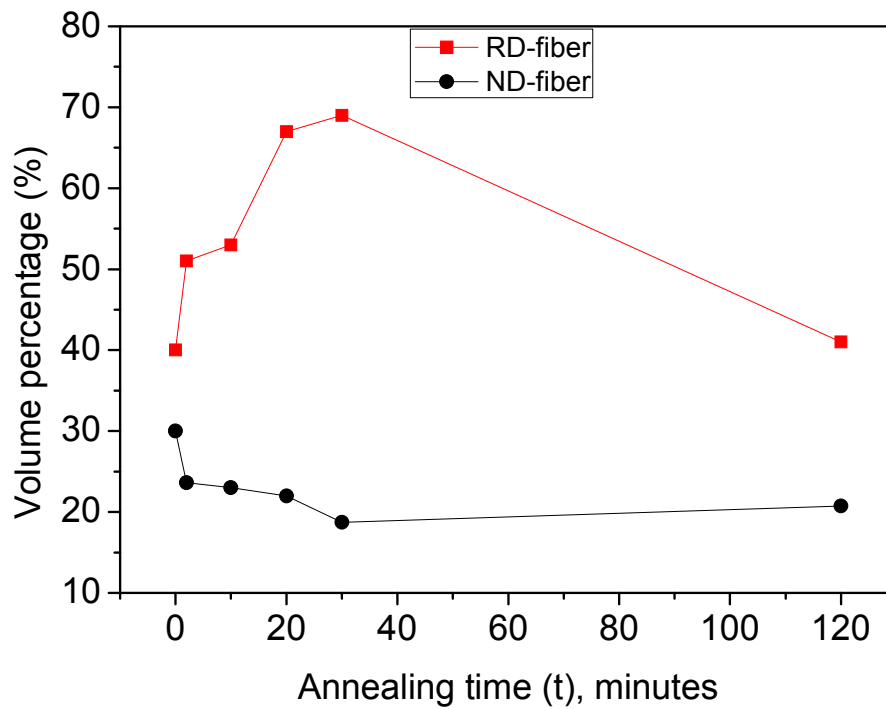


Fig.4.18: Variation of RD and ND-fiber fractions in ferrite in isothermally annealed A series DSS specimens.

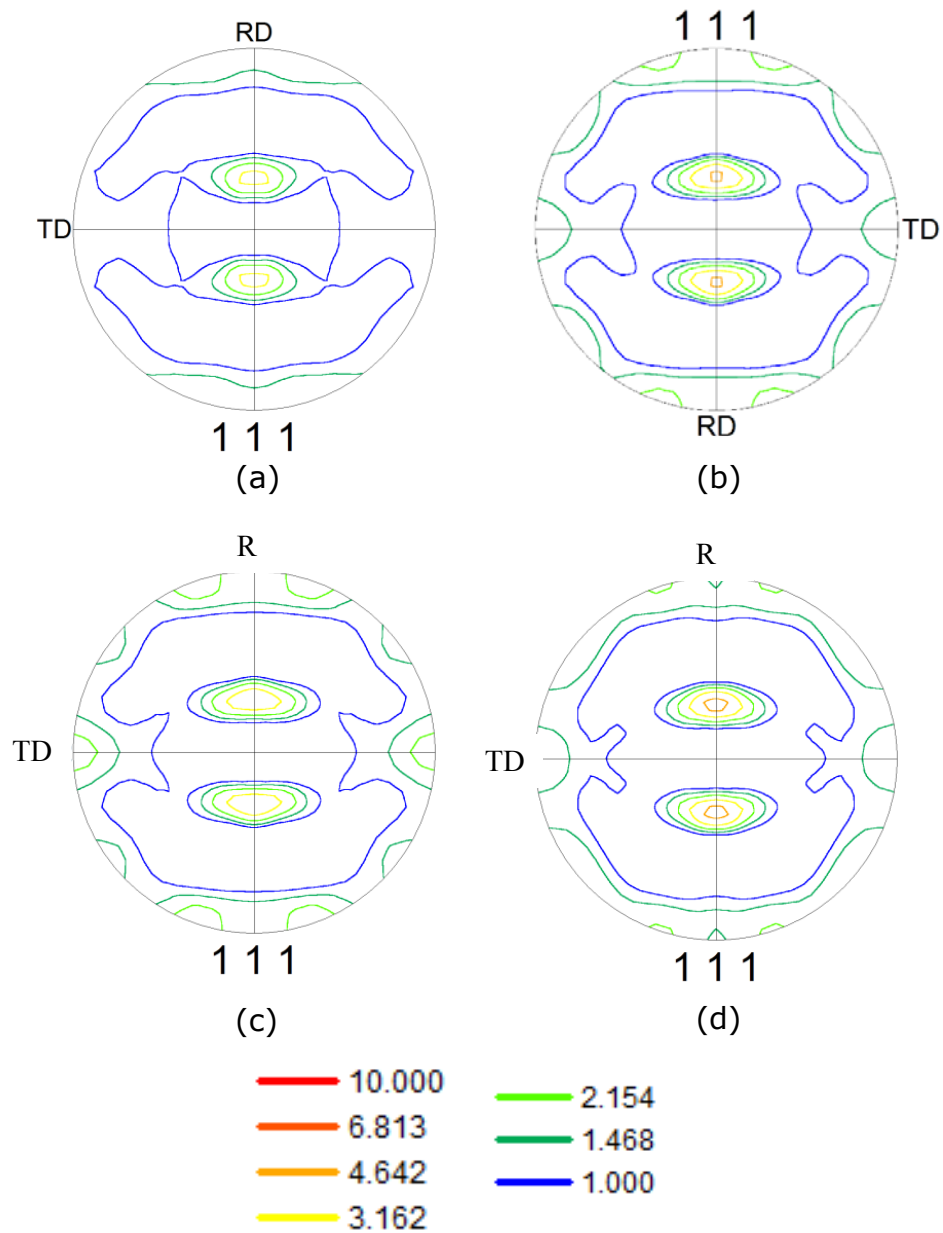


Fig.4.19: (111) PF of austenite in isothermally annealed (a) A2, (b) A20, (c) A30, (d) A120 DSS specimens.

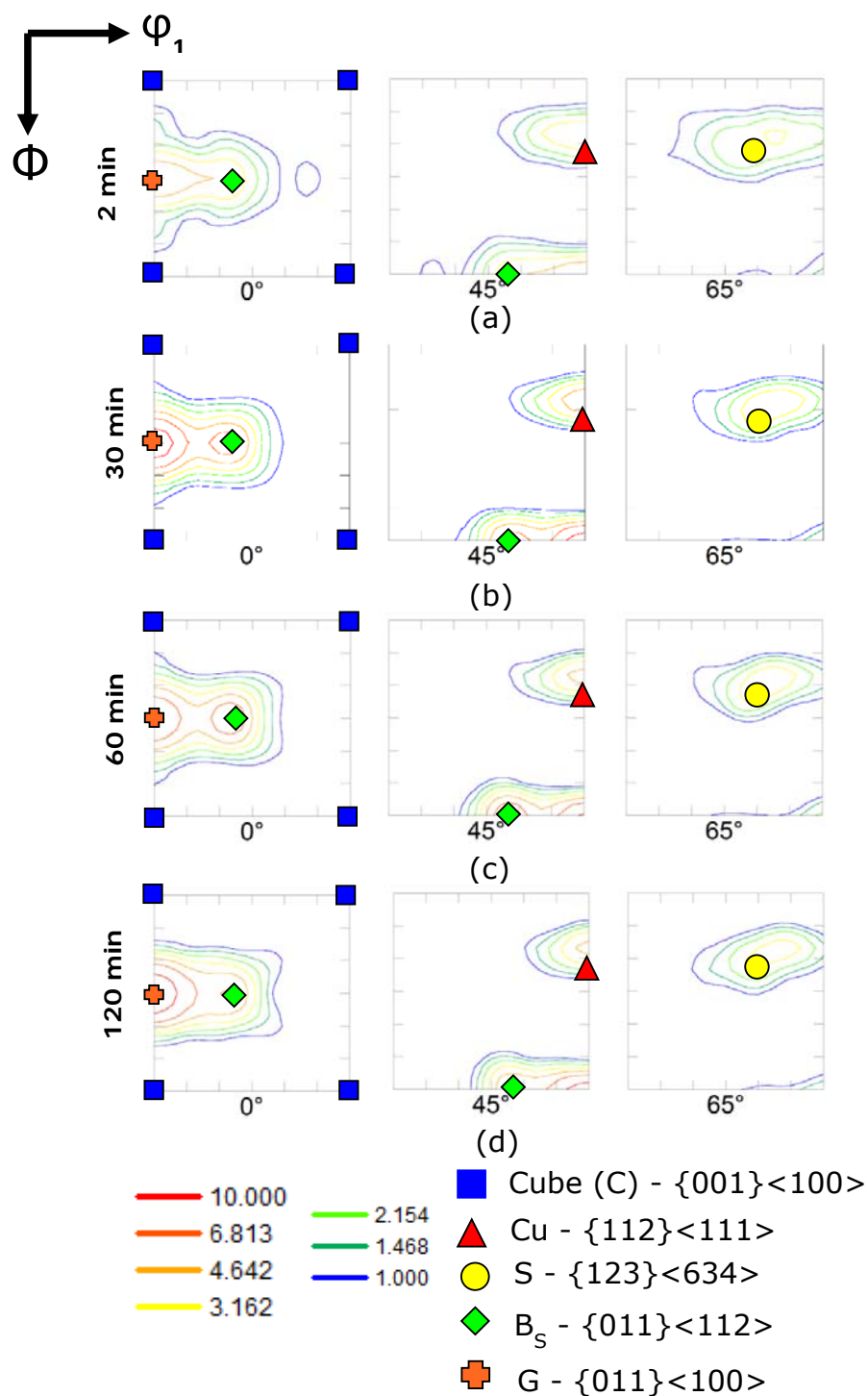


Fig.4.20: $\phi_2 = 0^\circ, 45^\circ, 65^\circ$ sections of the ODFs of austenite in isothermally annealed (a) A2, (b) A20, (c) A30, (d) A120 DSS specimens.

Figure 4.21 shows the variation of individual texture components during isothermal annealing, quantitatively. The volume fraction of the S component decreases in A0 specimen (i.e. as warm rolled DSS) ~24% to ~10% in the A120 specimen. The volume fraction of the B_s and G components are very similar ~13% in the A120 specimen.

The volume fraction of the brass recrystallization component (BR) {236}<385> which is often reported as the major component in the recrystallization texture of low SFE materials [7] is not particularly strong in the annealed A series specimens. The volume fraction of the Goss twin (G^T) component {4 4 11}<11 11 8> is ~10% in the A120 specimen. However, the volume fraction of the random components is quite high in annealed A2 and A20 specimens, but is significantly decreased in A30 and A120 specimens.

4.7 Evolution of microstructure and texture during annealing of 90% warm-rolled DSS at 698K (425 °C)

4.7.1 Evolution of microstructure during annealing

Figure 4.22 shows the phase maps of annealed B2 (Fig.4.22(a)), B20 (Fig.4.22(b)), B30 (Fig.4.22(c)) and B120 (Fig.4.22(d)) specimens. After annealing for 2 minutes, the lamellar morphology of the as warm-rolled material (Figures 4.8(d) and 4.9(a)) is still evidenced by the presence of extended phase bands along the RD (marked by arrows) in the phase maps of the B2 specimen (Figure 4.22(a)). However, at the same time the continuity of the phase bands appears to be broken locally. Mutual Interpenetration of phases along the grain boundaries is observed (indicated by dotted circles). The phase bands of the two constituent phases do not reveal LAGB network as is observed in the microstructure of the 90% warm-rolled material (Fig.4.8(d) and Fig.4.99(a)). Instead, the phase bands mostly show grain boundaries normal to the phase

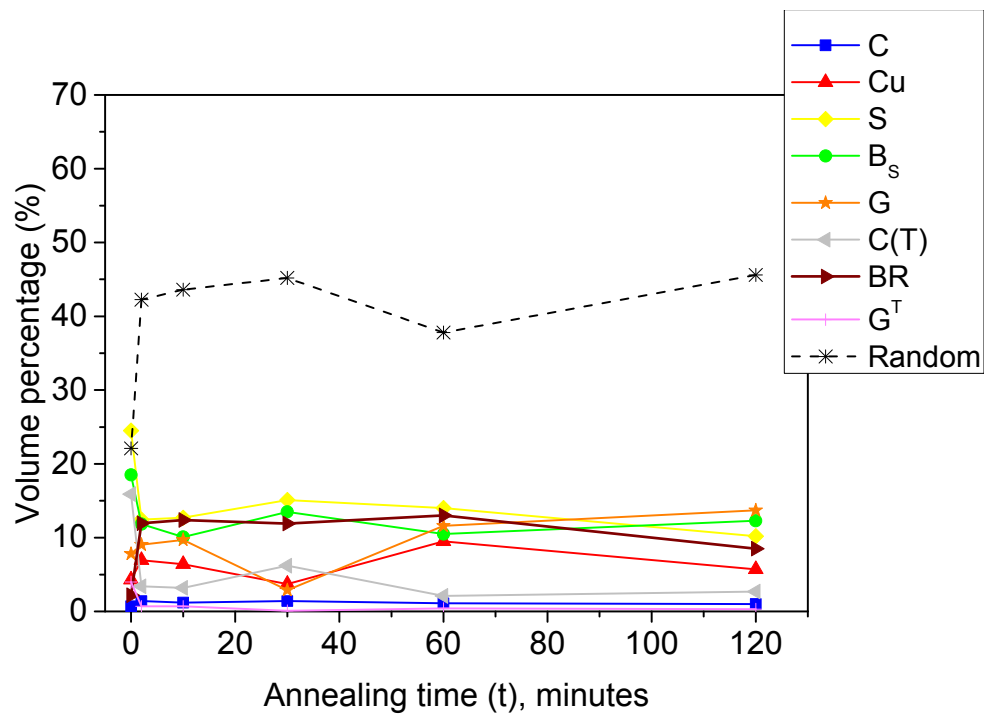


Fig.4.21: Evolution of texture components in austenite in isothermally annealed A series DSS specimens.

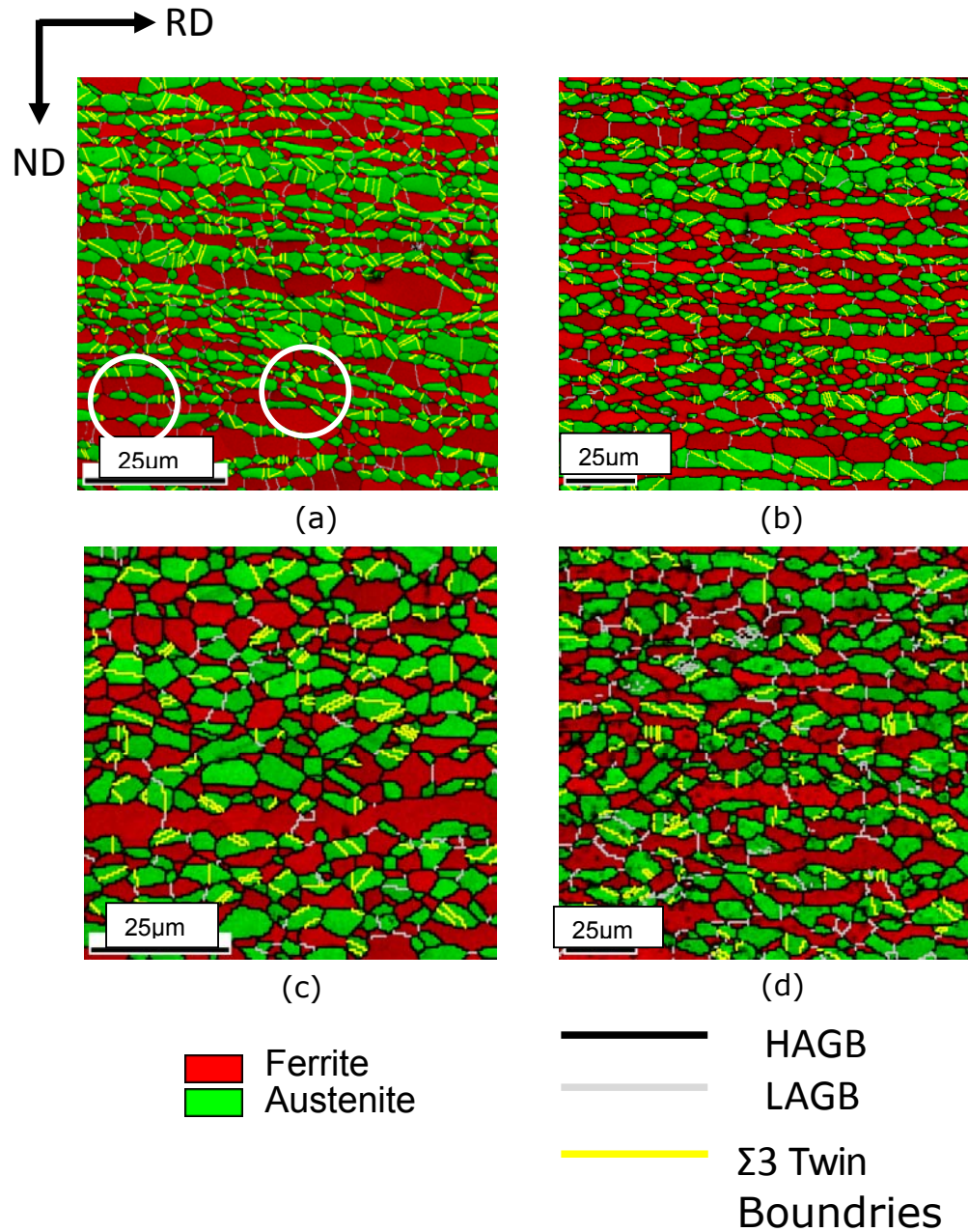


Fig.4.22: Phase maps of the (a) B2, (b) B20, (c) B30 and (d) B120 DSS specimens.

boundaries resulting in a bamboo type morphology. In case of ferrite the perpendicular phase boundaries are frequently LAGBs while in austenite those are mostly HAGBs. Profuse annealing twins (highlighted by yellow lines) are clearly observed inside the austenite bands. Each individual phase band is one grain thick when measured along the ND.

The continuity of the lamellar phase bands continues to break down with increasing annealing time. This is evidenced by the appearance of regions with comparatively more globular morphology in the microstructures of the specimen annealed for 20 minutes as shown in the phase maps of B20 (Figure 4.22(b)). Annealing for 30 minutes results in the extensive break-down of the lamellar phase bands resulting in a microstructure where the two constituent phases appear distributed throughout the matrix. Such regions are quite evident in the microstructure of the B30 specimen (Figure 4.22(c)). Further annealing, even for 120 minutes, does not change the morphology significantly (Fig. 4.22(d)).

The evolution of key microstructural parameters during isothermal annealing is summarized in Fig.4.23. The ferrite fraction plot (Fig. 4.23(a)) shows that the fraction of ferrite is decreased initially for a shorter isothermal holding time as compared to the fraction in the as warm-rolled condition. However, the ferrite fraction increases with increasing annealing time and approaches a stable value of ~ 0.50 after annealing for 20 minutes. Figure 4.23(b) shows the variation of ferrite and austenite grain thickness (measured along the ND), respectively with annealing time. Since each phase band is mostly one grain thick as observed from the phase maps already (Fig.4.22), the grain thickness is thus same as the phase band thickness for the different annealed materials.

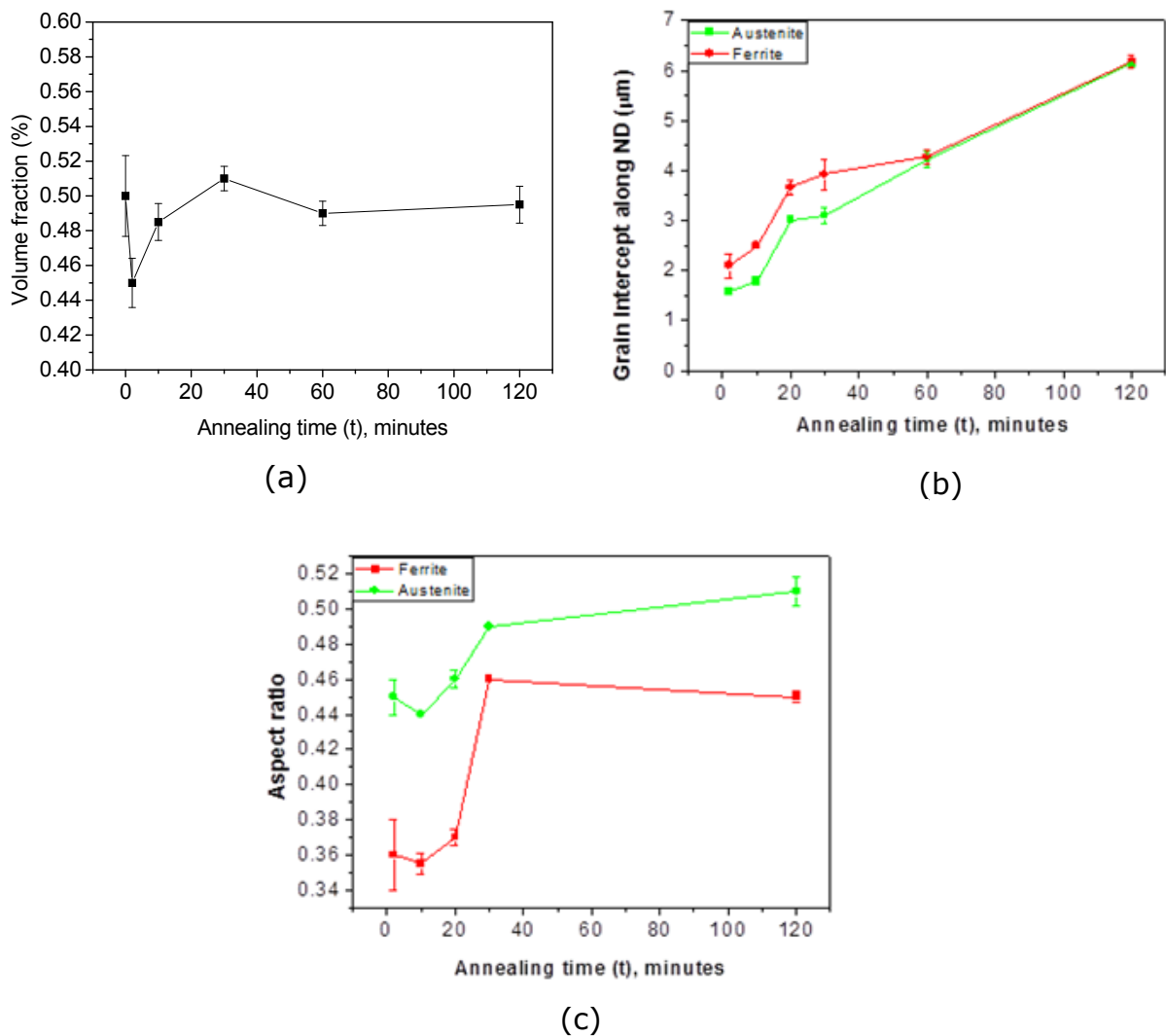


Fig.4.23: Evolution of (a) ferrite fraction, (b) grain thickness (measured along the ND) and (c) aspect ratio of the two phases in isothermally annealed B series DSS specimens.

Both ferrite and austenite grain thickness increase with increasing time, however, extensive coarsening of the microstructure is not observed even after annealing for 120 minutes, which is demonstrated by quite similar recrystallized grain thickness along ND $\sim 5\text{-}6\text{ }\mu\text{m}$ for the two phases (Fig.4.23(b)). The aspect ratio of ferrite (Fig.4.23(c)) is low ($\sim 0.34\text{-}0.35$) after annealing for 2 minutes but increases with increasing annealing time up to 30 minutes. The aspect ratio does not show any perceptible change during further isothermal holding. The aspect ratio of austenite (Fig.4.23(c)) shows a very similar trend as observed in ferrite; increasing with increasing isothermal holding time but no significant change beyond isothermal holding time of 30 minutes. The aspect ratio of austenite is found to be consistently greater than that of ferrite in different annealed materials.

4.7.2 Evolution of texture during annealing

Figure 4.24 shows the $\phi_2=45^\circ$ section of the ODFs of ferrite in annealed B series specimens. The intensities of the contour lines in the ODF sections clearly reveal the presence of stronger RD-fiber as compared to the ND-fiber. In the B2 specimen (Fig.4.24(a)) presence of the RD-fiber component $\{112\}\langle 110\rangle$ is noticed along with the $\{001\}\langle 110\rangle$ component. The $\{001\}\langle 110\rangle$ component is strengthened while the $\{112\}\langle 110\rangle$ component is significantly weakened with increasing isothermal holding time. The intensity distribution along the ND-fiber remains weak throughout the annealing process. The intensity along the ND-fiber in the B2 specimen is found closer to the $\{111\}\langle 112\rangle$ location (volume fraction $\sim 14\%$). However, slightly higher intensity is observed for $\{111\}\langle 011\rangle$ (volume fraction $\sim 7.6\%$) as compared to $\{111\}\langle 112\rangle$ (volume fraction $\sim 6.0\%$) in the B120 specimen.

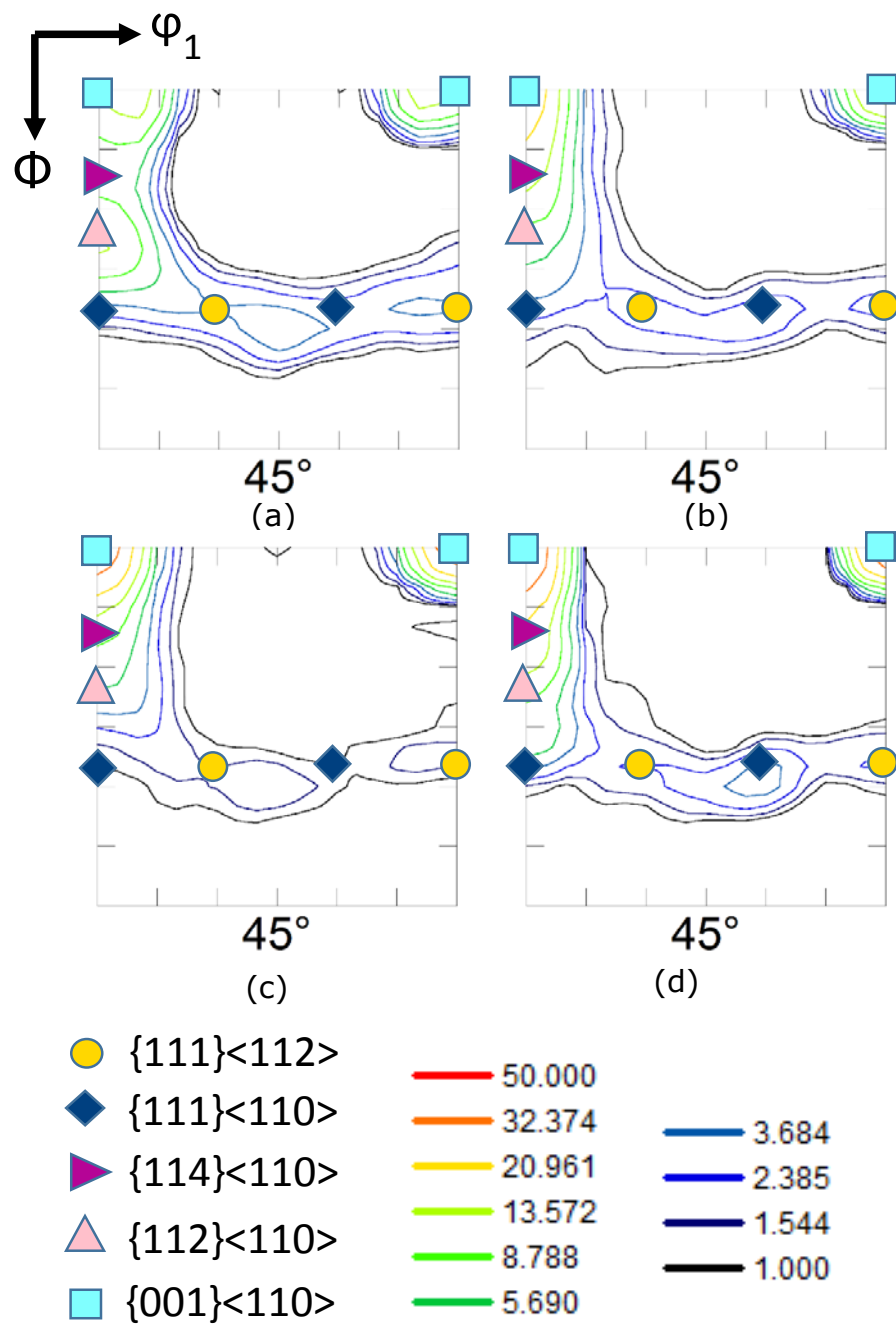


Fig.4.24: $\phi_2 = 45^\circ$ section of the ODF of ferrite in (a) B2, (b) B20, (c) B30, (d) B120 DSS specimens.

The evolution of the two prominent texture fibers during isothermal annealing of the B series specimens is shown quantitatively in Fig. 4.25. The volume fraction of the RD-fiber and ND-fiber in the B0 specimen is ~67% and 11%, respectively. In the B2 specimen the volume fractions of the two fibers are ~60% and 16%, respectively, indicating only minor changes in the volume fraction of the two fibers.

The volume fractions of the two fibers do not show any significant change even after isothermal annealing for 120 minutes, so that the volume fractions of the RD and ND fibers in the B120 specimen are found to be ~67% and 12%, respectively. Thus, the annealing textures of ferrite in the isothermally annealed B series specimens are evidently similar to that of the ferrite in the as warm-rolled condition i.e. in the B0 specimen (Fig.4.9 and Fig.4.10). Figure 4.26 shows the (111) PFs of austenite in B2 (Fig.4.26(a)), B20 (Fig.4.26(b)), B30 (Fig.4.26(c)) and B120 (Fig.4.26(d)) specimens. The (111) PFs of austenite in different isothermally annealed DSS specimens appear quite similar and also resemble the (111) PF of austenite in the as warm-rolled DSS (Fig.4.11(a)) indicating the retention of deformation texture components even after annealing. This is also amply corroborated by the appearance of the $\phi_2 = 0^\circ$, 45° and 65° sections of the ODFs of austenite in different annealed B series specimens (Fig.4.27) which clearly reveal the retention of the S, B_s , Cu and G components after annealing. However, the intensity distribution in the ODF sections of the annealed B series specimens shows stronger S and B_s components than Cu component, particularly after longer isothermal holding time.

The evolution of texture during isothermal annealing of annealed B series specimens is shown quantitatively in Fig.4.28. Importantly, the BR component is evidently not the strongest component. It is clearly observed that the volume fraction of the S component

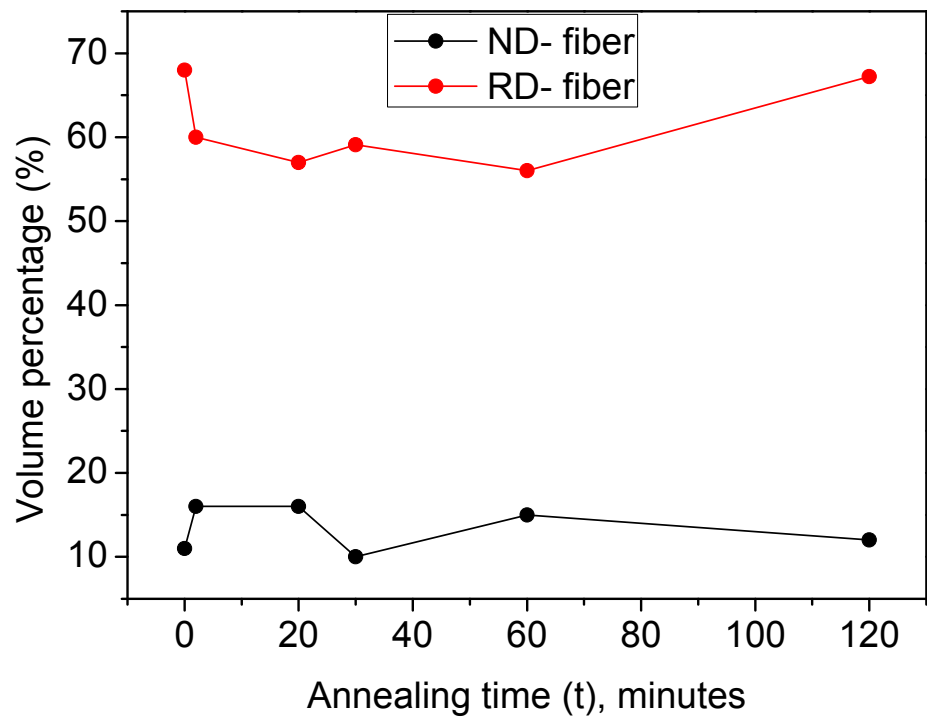


Fig.4.25: Evolution of texture components during isothermal annealing in ferrite in isothermally annealed B series DSS specimens.

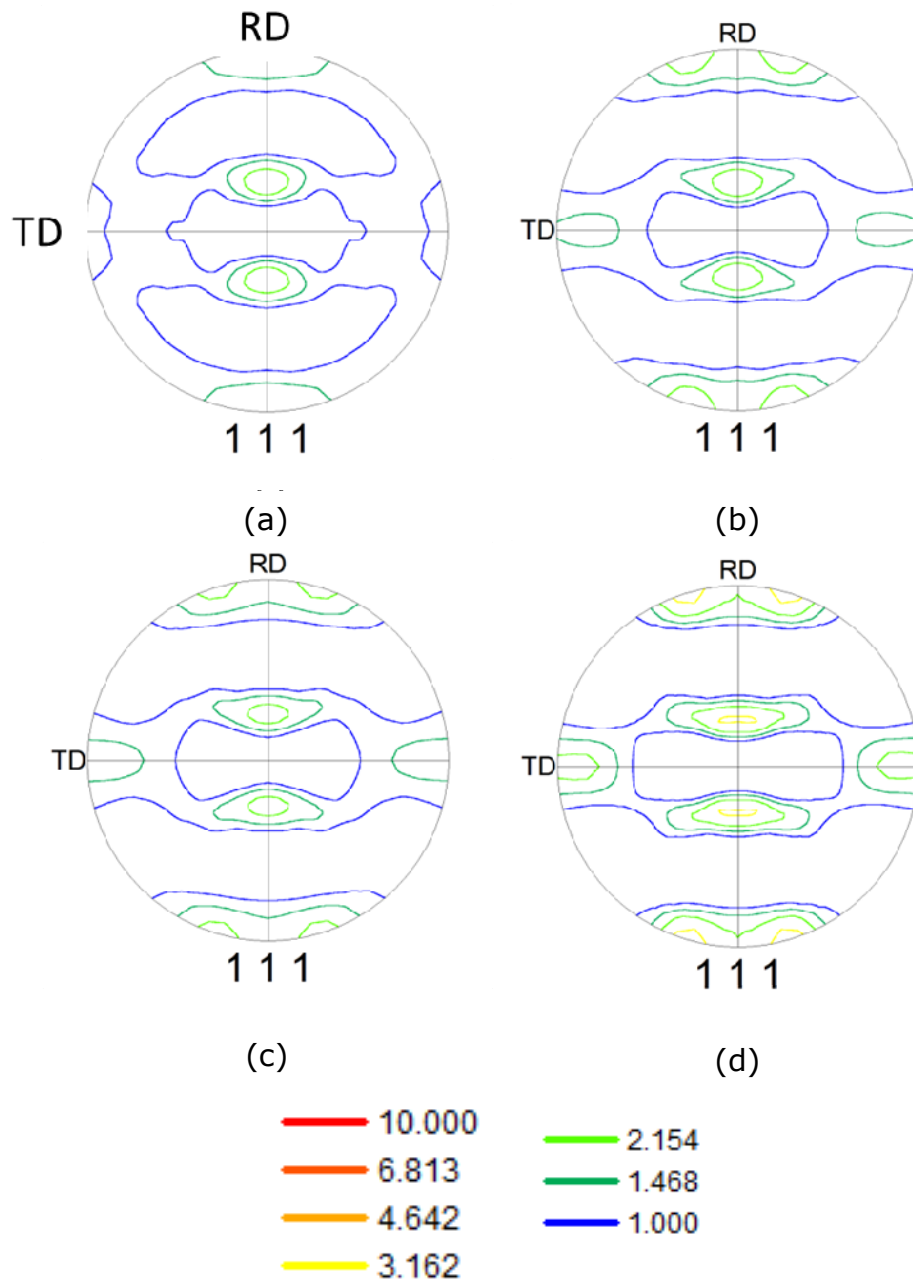


Fig.4.26: (111) PFs of austenite in isothermally annealed (a) B0, (b) B2, (c) B20, (d) B30, (e) B120 specimens.

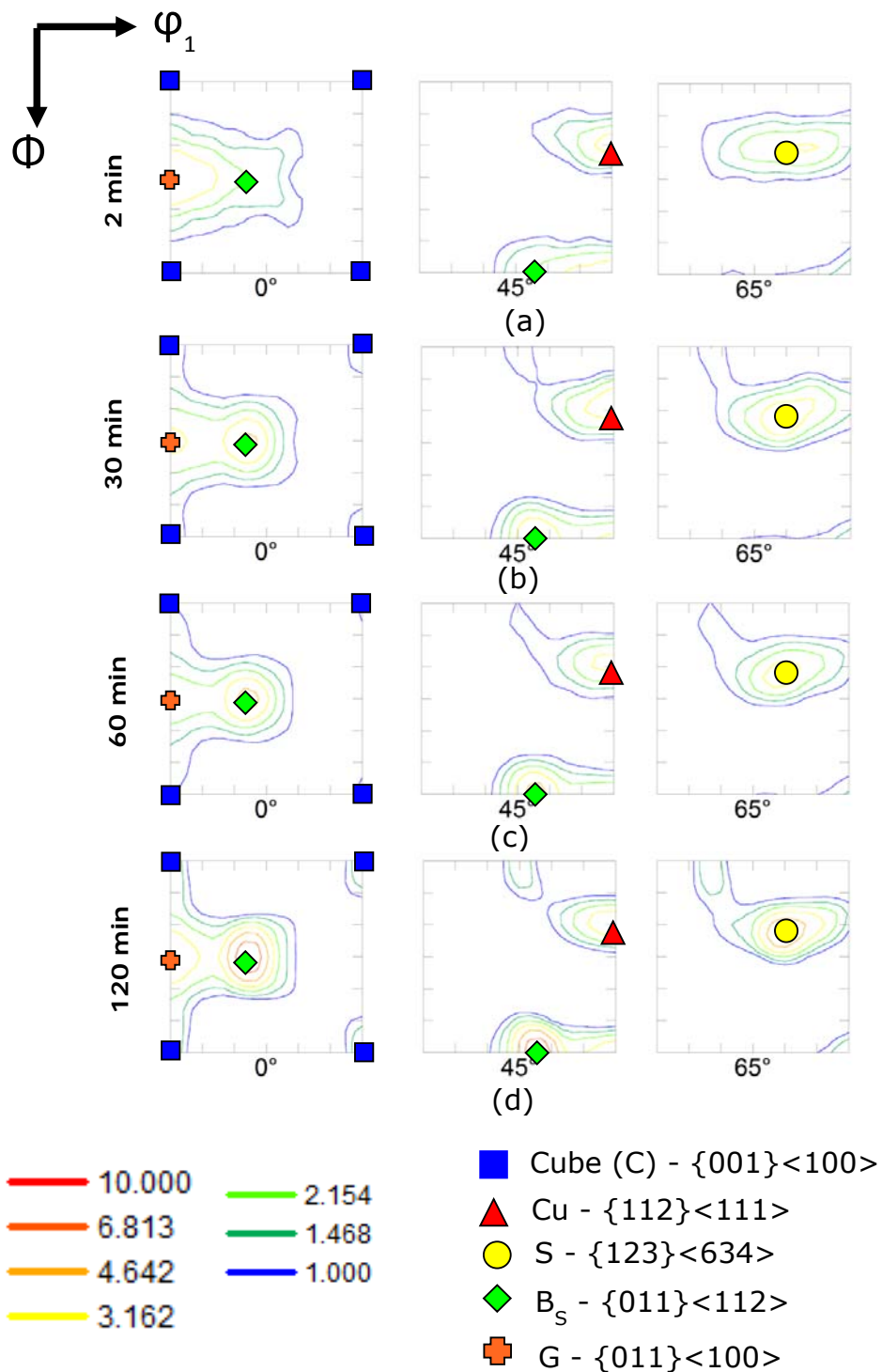


Fig.4.27: $\Phi_2 = 0^\circ, 45^\circ, 65^\circ$ sections of the ODFs of austenite in isothermally annealed (a) B2, (b) B20, (c) B30, (d) B120 specimens.

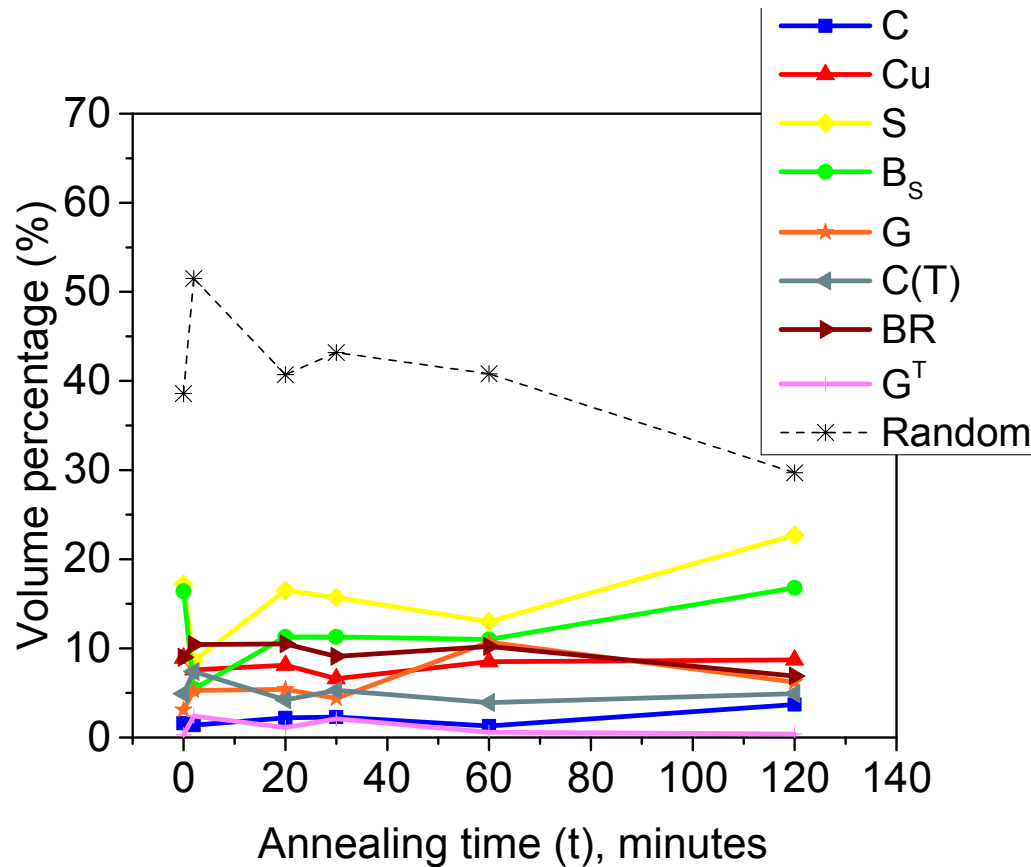


Fig.4.28: Evolution of texture components during isothermal annealing in austenite in B series DSS specimens. C (T) and G^T are the twin components of C and G, respectively.

decreases after isothermal annealing for 120 minutes as compared to that in the as warm-rolled material.

However, the S component remains as the most prominent texture component and appears particularly strong in specimens isothermally annealed for longer durations. The S component shows volume fraction $\sim 21\%$ in the B120 specimen. B_S , Cu and G components are also observed in different isothermally annealed specimens, thus, amply corroborating the qualitative assessment of the presence of pure metal type texture. In good agreement with the ODF analysis, it is further observed that the B_S component is stronger than the Cu component in the B series specimens isothermally annealed for longer durations. However, the G^T component shows negligible presence in the annealed A series specimens (volume fraction usually less than 1%). The volume fraction of the random components increase initially after isothermal annealing for 2 minutes as compared to that in the as warm-rolled DSS. However, the random fraction has decreased with increasing isothermal annealing time indicating progressive strengthening of the annealing texture.

4.8 Evolution of microstructure and texture during annealing of 90% warm-rolled DSS at 898K (625 °C)

4.8.1 Evolution of microstructure during annealing

Figure 4.29 shows the phase maps of annealed C2 (Fig.4.29(a)), C20 (Fig.4.29(b)), C30 (Fig.4.29(c)) and C120 (Fig.4.29(d)) specimens. Lamellar morphology of the as warm-rolled material characterized by the presence of extended phase bands along the RD is also observed in the phase map of the annealed C2 specimen (Fig.4.29(a)) (marked by arrow). Grain boundaries appear to be arranged normal to the phase boundaries resulting in the formation of typical bamboo type morphology. In case of ferrite the

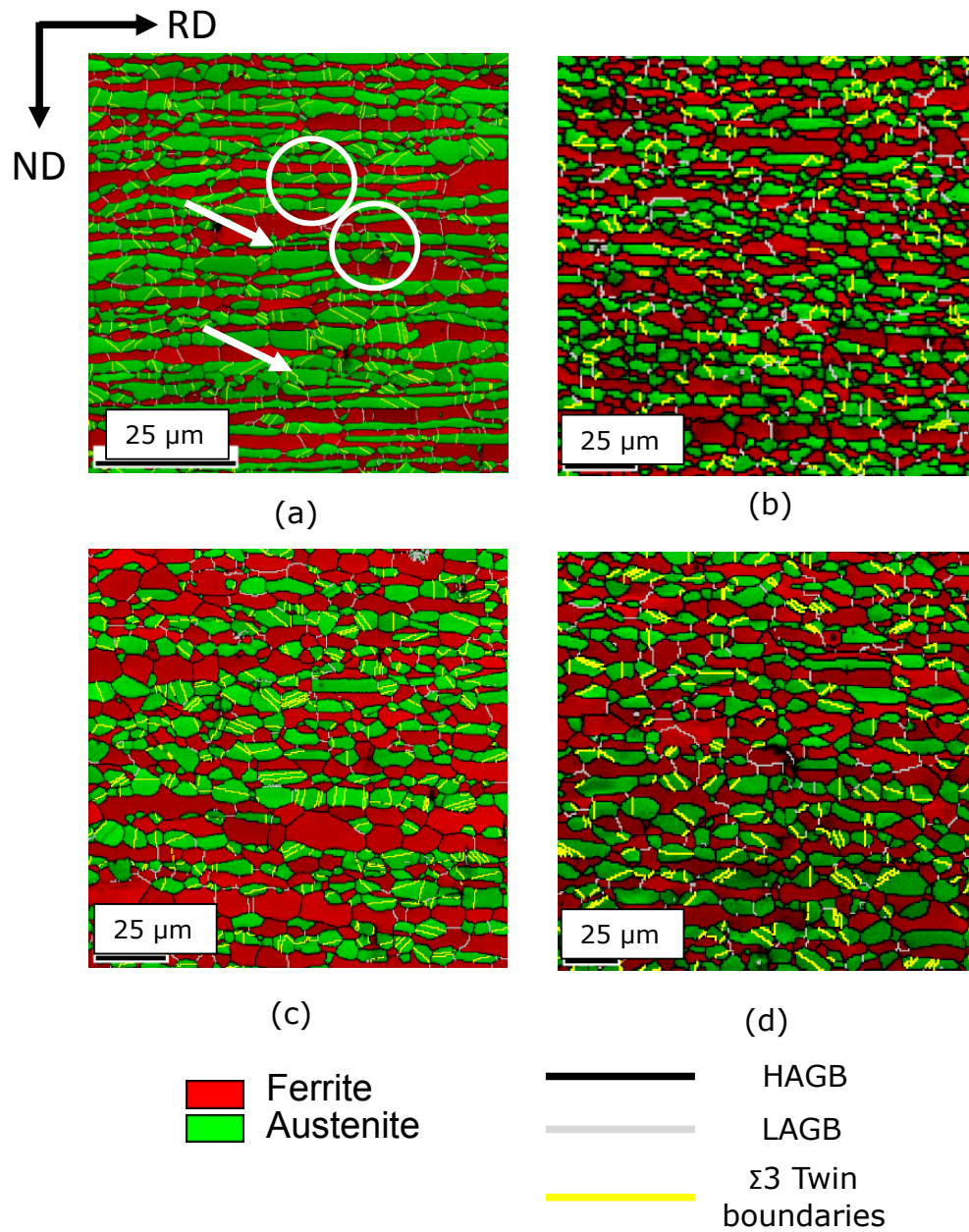


Fig.4.29: Phase maps of isothermally annealed (a) C2, (b) C20, (c) C30 and (d) C120 specimens.

perpendicular boundaries are frequently LAGBs while in austenite those are mostly HAGBs. Profuse annealing twins (indicated by yellow lines) are identified inside the austenite bands. Each individual phase band appears to be one grain thick when measured along the ND. The interpenetration of phases along the grain boundaries is also observed in this case (marked by dotted circles). During further isothermal annealing extensive break-down of the lamellar morphology is observed with the concurrent evolution of more globular morphology. This is quite evident from the phase maps of the C20 (Fig.4.29(b)) and C30 (Fig.4.29(c)) specimens. Further annealing for 120 minutes (Fig.4.29(d)) does not change the morphology significantly.

The evolution of microstructural parameters during isothermal annealing of isothermally annealed C series specimens is shown in Fig.4.30. The ferrite phase fraction (Fig.4.30(a)) is decreased initially in the C2 specimen. However, the ferrite fraction is increased with increasing isothermal holding time and approaches a stable value of ~ 0.50 .

The variation of grain thickness along the ND of the two phases during isothermal annealing is shown in Fig.4.30(b). It may be noted that grain thickness is the same as phase band thickness (along ND) in the annealed specimens as the grains extend to the full thickness of the phase bands. Both ferrite and austenite grain thickness is increased with increasing annealing time, however, extensive coarsening of the microstructure is not observed even after annealing for 120 minutes. The average grain size of the two phases measured along the ND is found to be similar ($\sim 6 \mu\text{m}$) in the annealed C120 specimen. The aspect ratio variation of the two phases during isothermal annealing is shown in Fig.4.30(c). The aspect ratio values in the two phases are low after annealing for 2 minutes, but significantly increased during isothermal annealing up

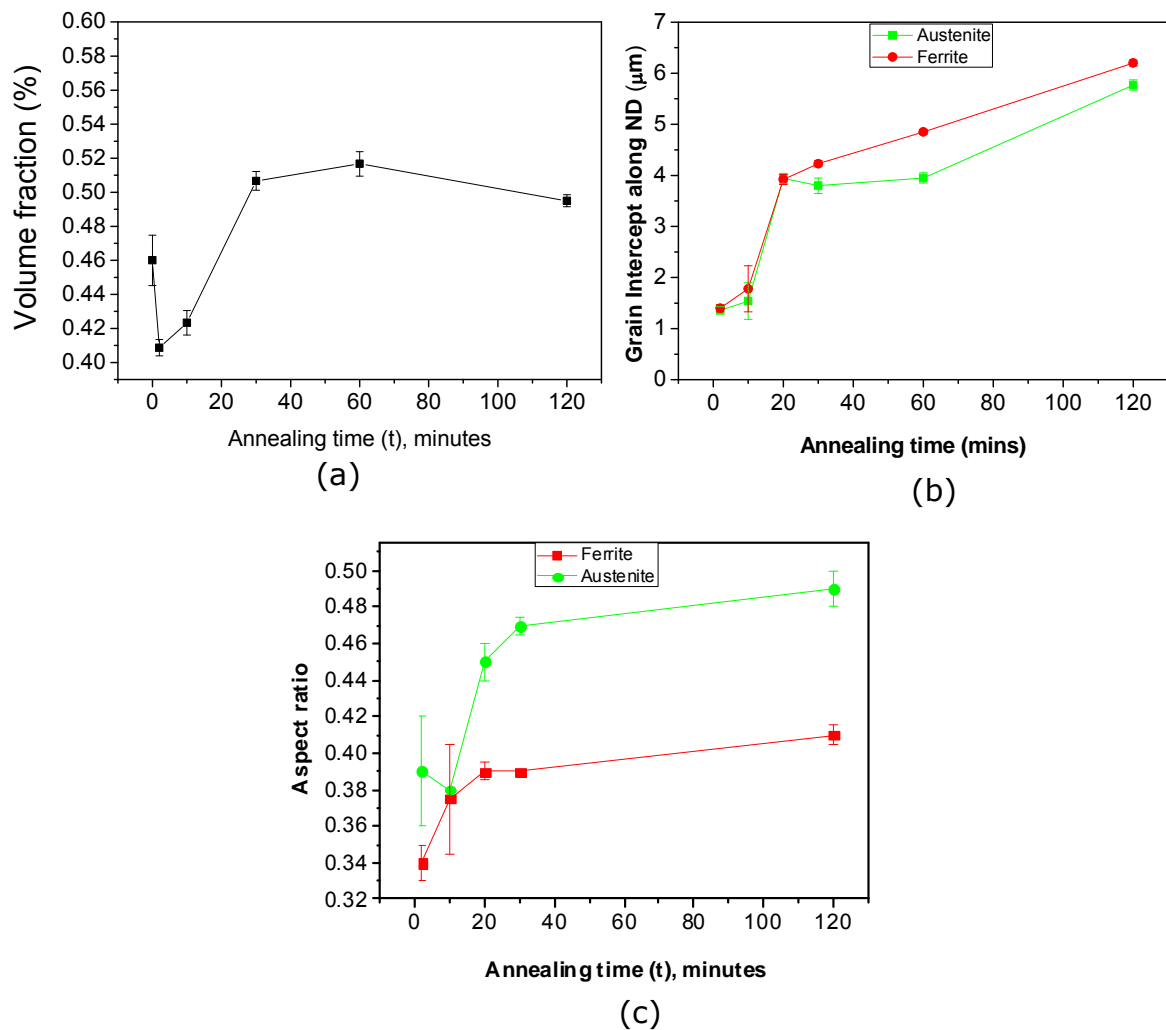


Fig.4.30: Variation of (a) ferrite fraction, (b) grain thickness (measured along the ND) and (c) aspect ratio of the two phases in isothermally annealed C series DSS specimens.

to 30 minutes. Significant variation in aspect ratio is not observed during further isothermal annealing. Ferrite in annealed C series specimens consistently shows lower average aspect ratio values as compared to those in austenite.

4.8.2 Evolution of texture during annealing

The $\varphi_2=45^\circ$ sections of the ODFs of ferrite in different isothermally annealed C series specimens (Fig.4.31) shows the presence of both RD and ND fiber components. The intensity distribution of the contour lines clearly shows the presence of much stronger RD fiber as compared to the ND fiber after different annealing treatments. It may be noted that although the RD-fiber is stronger than the ND-fiber in the as warm-rolled material (i.e. in the C0 specimen) having volume fractions $\sim 37\%$ and $\sim 23\%$, respectively, the strength of the RD-fiber is increased further after annealing. This is easily understood from the evolution of the two texture fibers with annealing time shown quantitatively in Fig.4.32. The RD-fiber is increased to 48% after annealing for 2 minutes while the fraction of the ND-fiber is decreased to 15%. The strength of the RD fiber is decidedly greater than that of the ND-fiber in different isothermally annealed specimens. The main intensity peak along the ND fiber in the C2 specimen is located close to the $\{111\}\langle 110 \rangle$ location which shows higher volume fraction ($\sim 15\%$) than $\{111\}\langle 112 \rangle$ ($\sim 10\%$). However, with increasing annealing time the intensity peak is shifted closer to the $\{111\}\langle 112 \rangle$ location. In the C2 specimen slightly higher intensity along the RD fiber is observed at the $\{112\}\langle 110 \rangle$ location than at the $\{001\}\langle 110 \rangle$ location. This is consistent with higher volume fraction of the $\{112\}\langle 110 \rangle$ component ($\sim 27\%$) as compared to the $\{001\}\langle 110 \rangle$ component ($\sim 10\%$) in the C2 specimen. The $\{001\}\langle 110 \rangle$ component is strengthened by increasing the isothermal

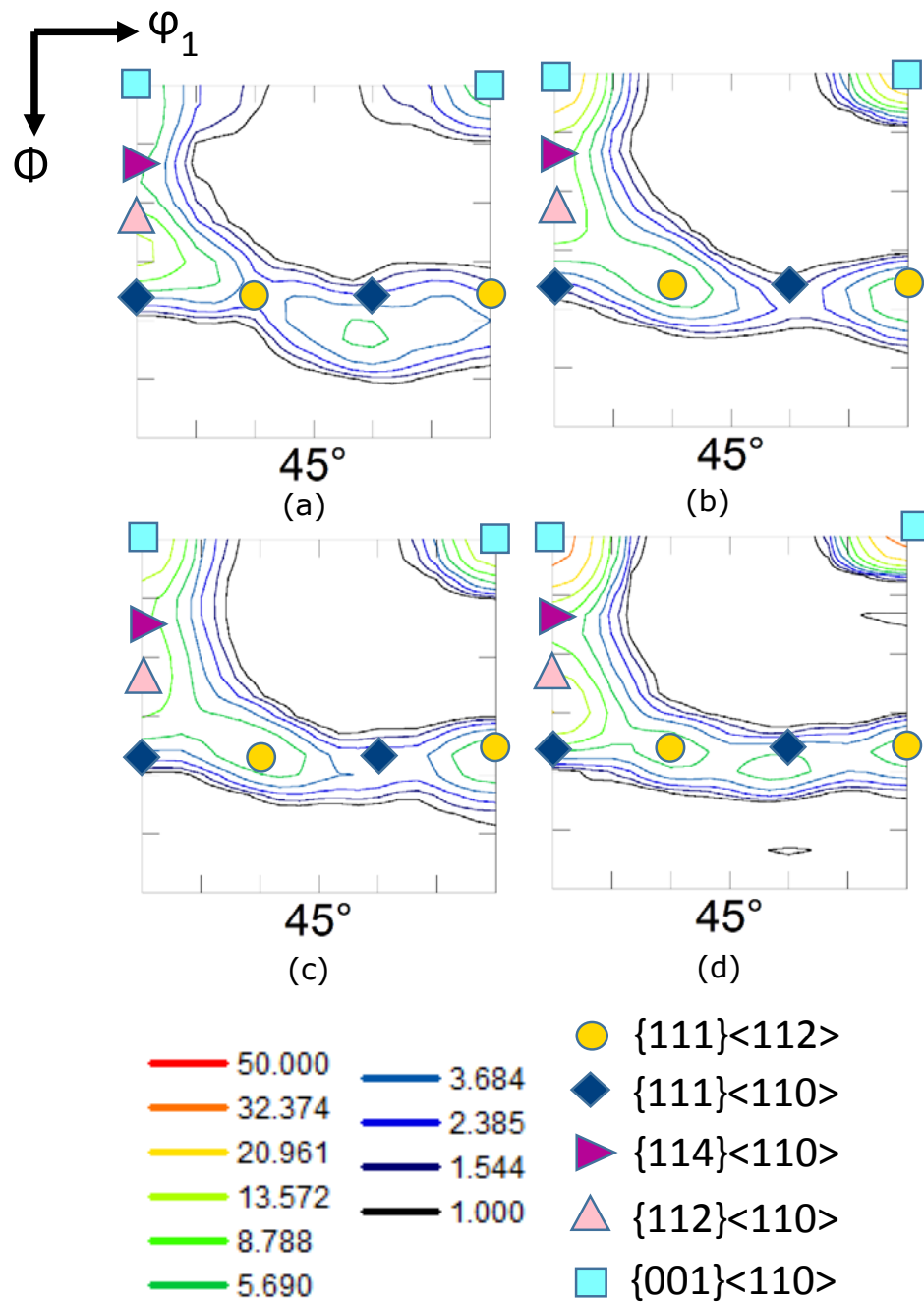


Fig.4.31: $\phi_2=45^\circ$ section of the ODF of ferrite in (a) C2, (b) C20, (c) C30, (d) C120 DSS specimens.

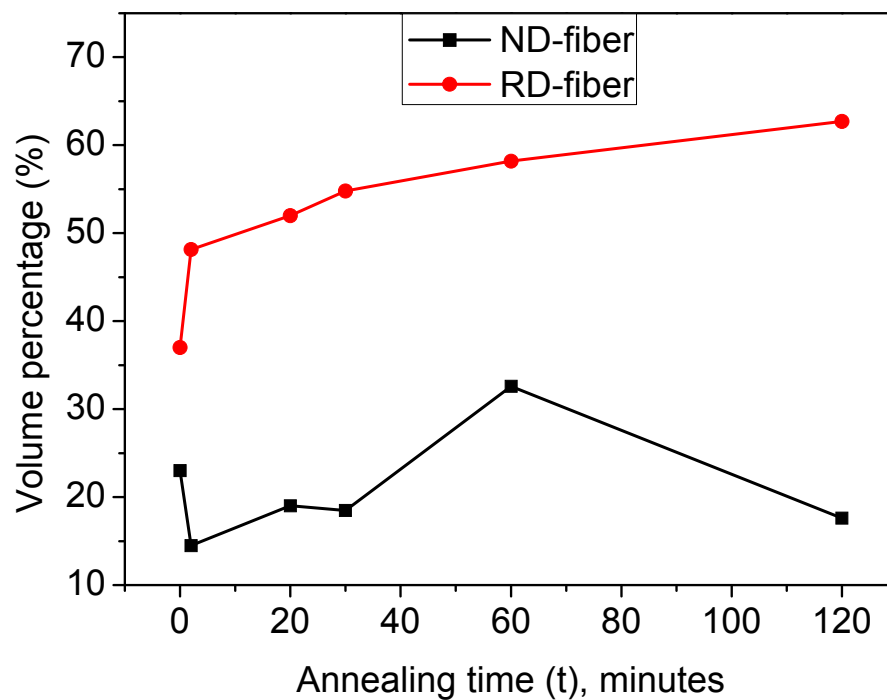


Fig.4.32: Variation of RD and ND-fiber fractions in ferrite in isothermally annealed C series DSS specimens.

holding time.

Figure 4.33 shows the (111) PF of austenite in isothermally annealed C2 (Fig.4.32(a)), C20 (Fig.4.32(b)), C30 (Fig.4.32(c)) and C120 (Fig.4.32(d)) specimens. The (111) PFs appear very similar to that of austenite in the as warm-rolled DSS i.e. in the C0 specimen (Fig.4.14(a)) indicating the retention of pure metal type texture after annealing. The $\varphi_2 = 0^\circ$, 45° and 65° section of the ODFs of austenite in isothermally annealed C series specimens are shown in Fig.4.34 for better understanding of the texture development in austenite. The intensity distribution in the ODF sections indicates strong presence of the S component. The strength of the B_s and Cu components, however, appears rather similar.

The evolution of different texture components in austenite of annealed C series specimens is shown in Fig.4.35. The S component remains as the most prominent texture component and appears particularly strong in specimens isothermally annealed for longer durations, so that the volume fraction of the S component is $\sim 23\%$ in the B120 specimen. BS, Cu and G components are also observed in different annealed specimens amply corroborating qualitative assessment of presence of pure metal type texture deduced from the ODF analysis. Further, in good agreement with ODF analysis, it is observed that the volume fractions of the B_s and Cu components are rather similar in the annealed C series specimens. The BR and G^T components are present as minor texture components in austenite of isothermally annealed C series DSS specimens.

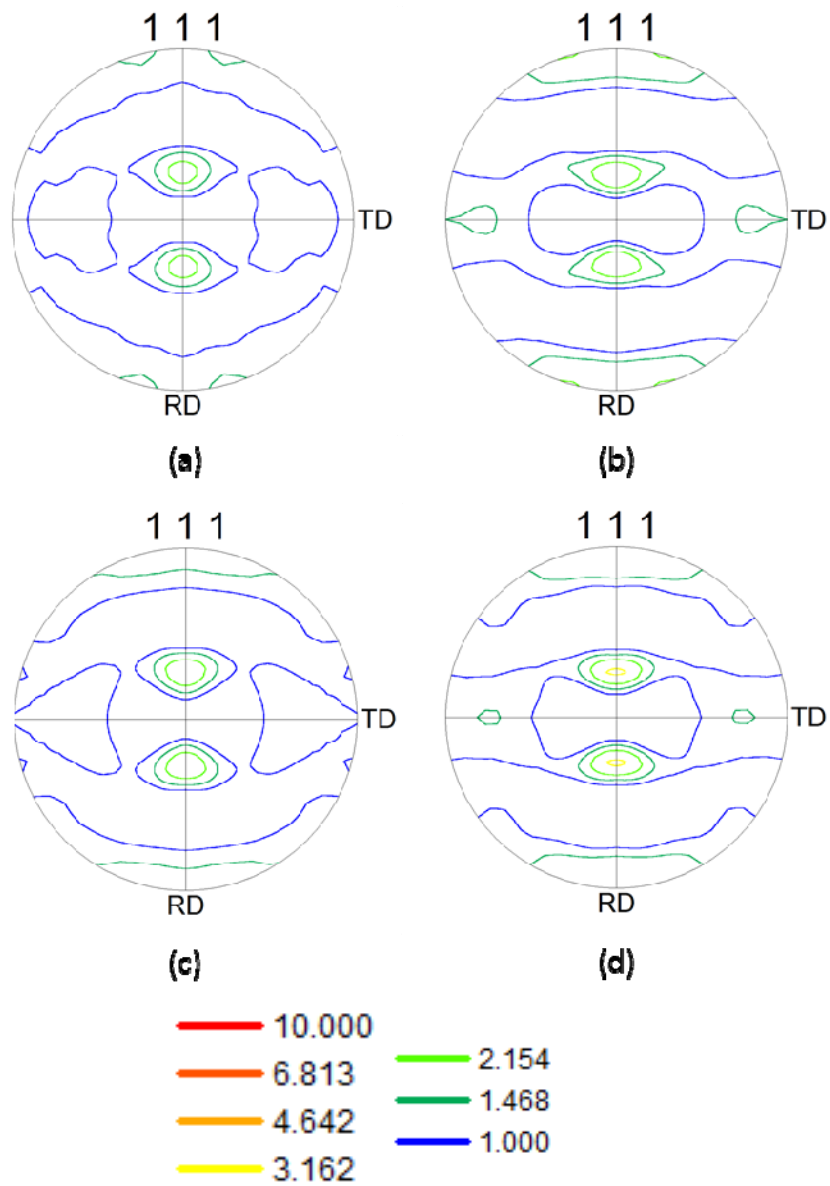


Fig.4.33: (111) PF of austenite in 90% warm-rolled and isothermally annealed (a) C2, (b) C20, (c) C30, (d) C120 DSS specimens.

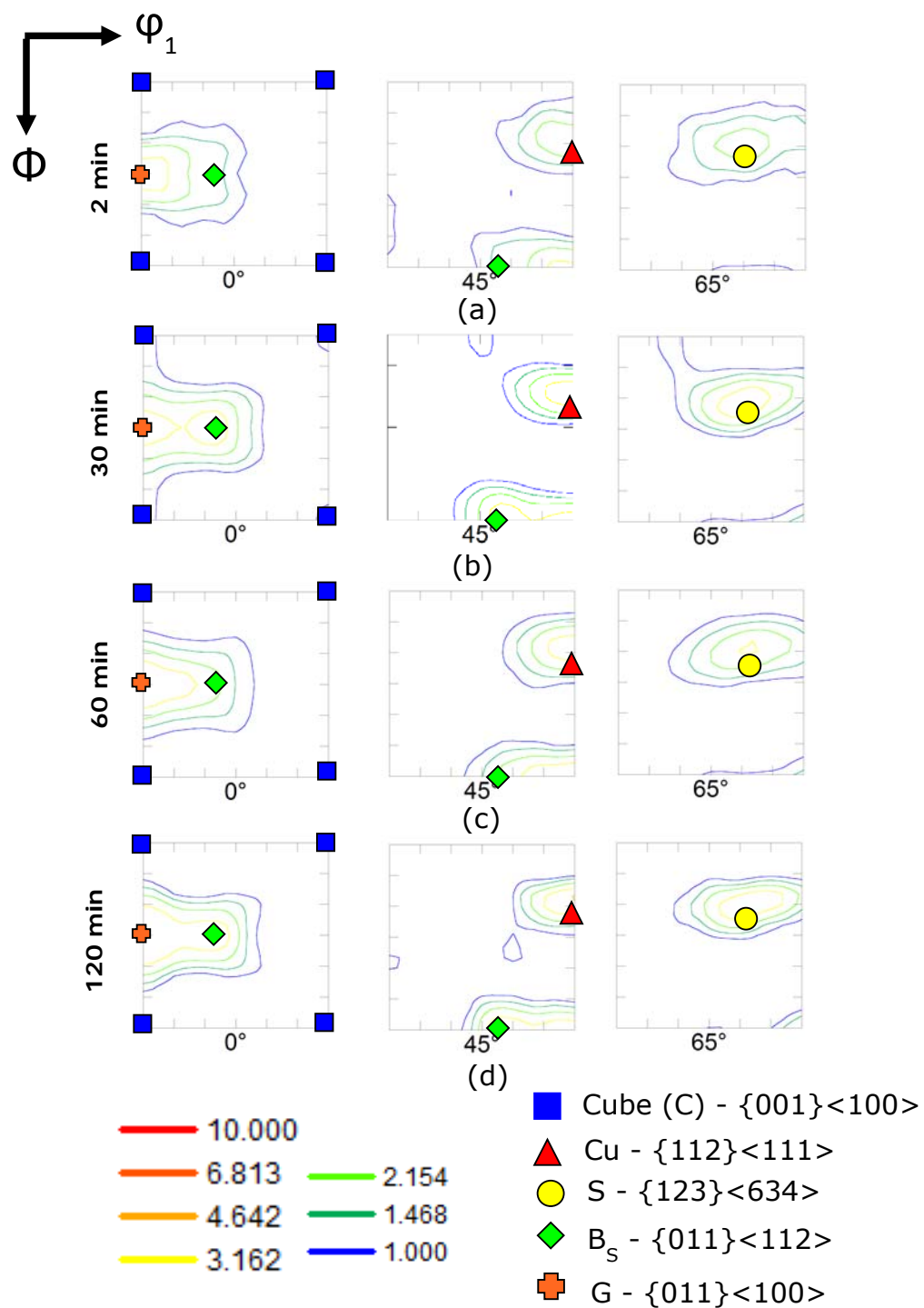


Fig.4.34: $\phi_2 = 0^\circ, 45^\circ, 65^\circ$ ODF sections of austenite in (a) C2, (b) C20, (c) C30, (d) C120 DSS specimens.

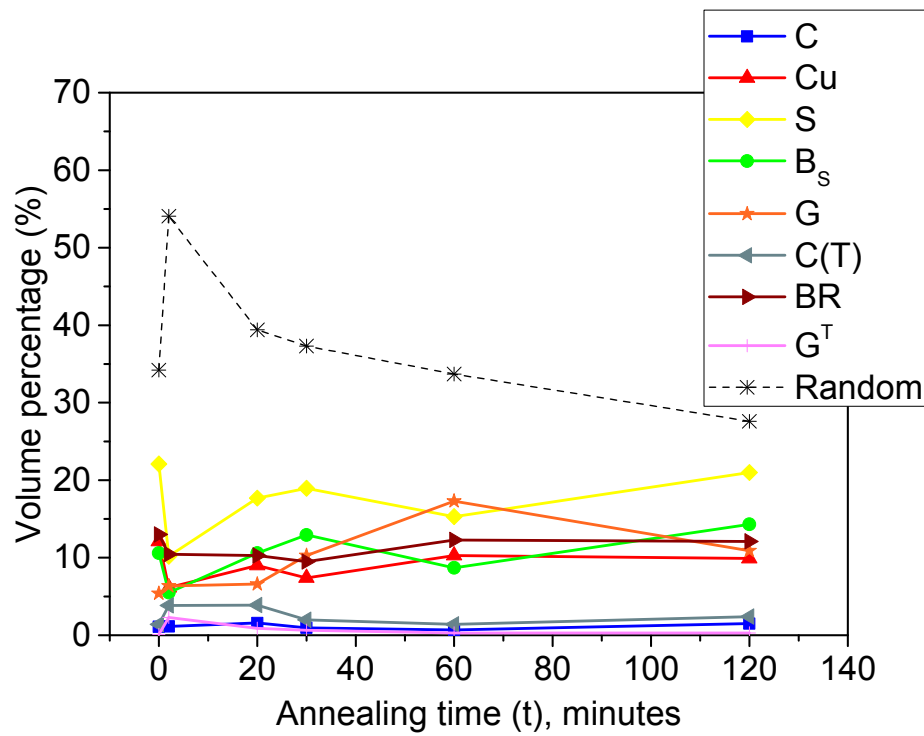


Fig.4.35: Evolution of texture components during isothermal annealing in austenite in C series DSS specimens.

4.9 Discussion

4.9.1 Evolution of microstructure and texture during warm-rolling

In order to understand the effect of warm-rolling the key microstructural parameters in DSS 90% warm-rolled at different temperatures is compared in Fig.4.36 for clarity. The volume fraction of austenite in DSS after 90% warm-rolling at different temperatures (Fig.4.36(a)) is found to vary from 45% to 55% i.e. very close to the volume fraction of austenite in the starting material (~50%) used for the warm-rolling experiments. This clearly indicates that austenite is rather stable during warm-rolling and effect of any deformation induced phase transformation on the development of microstructure and texture can be ruled out.

After 90% warm-rolling at 498K (225°C) and 898K (625°C) the thickness of the two phases are found similar (Fig.4.36(b)). Since the starting average grain size of the two phases is also quite similar (Fig.4.1) it is easily concluded that the strain is partitioned approximately equally at these two warm-rolling temperatures. Thus, strain partitioning behavior at these two warm-rolling temperatures is similar to that observed during cold-rolling of DSS [66]. However, at the intermediate warm-rolling temperature of 698K (425°C) the average thickness of the austenite bands is found to be significantly lower than that of the ferrite bands (Fig.4.36(b)). This indicates that imposed strain is partitioned more to austenite at this warm-rolling temperature, or in other words, ferrite is the harder amongst the two phases. It may be recalled that the microstructure of 90% warm-rolled DSS at this temperature (Figures 4.8(d) and 4.9(a)) is also characterized by remarkable inhomogeneity and the presence of fragmented ferrite regions.

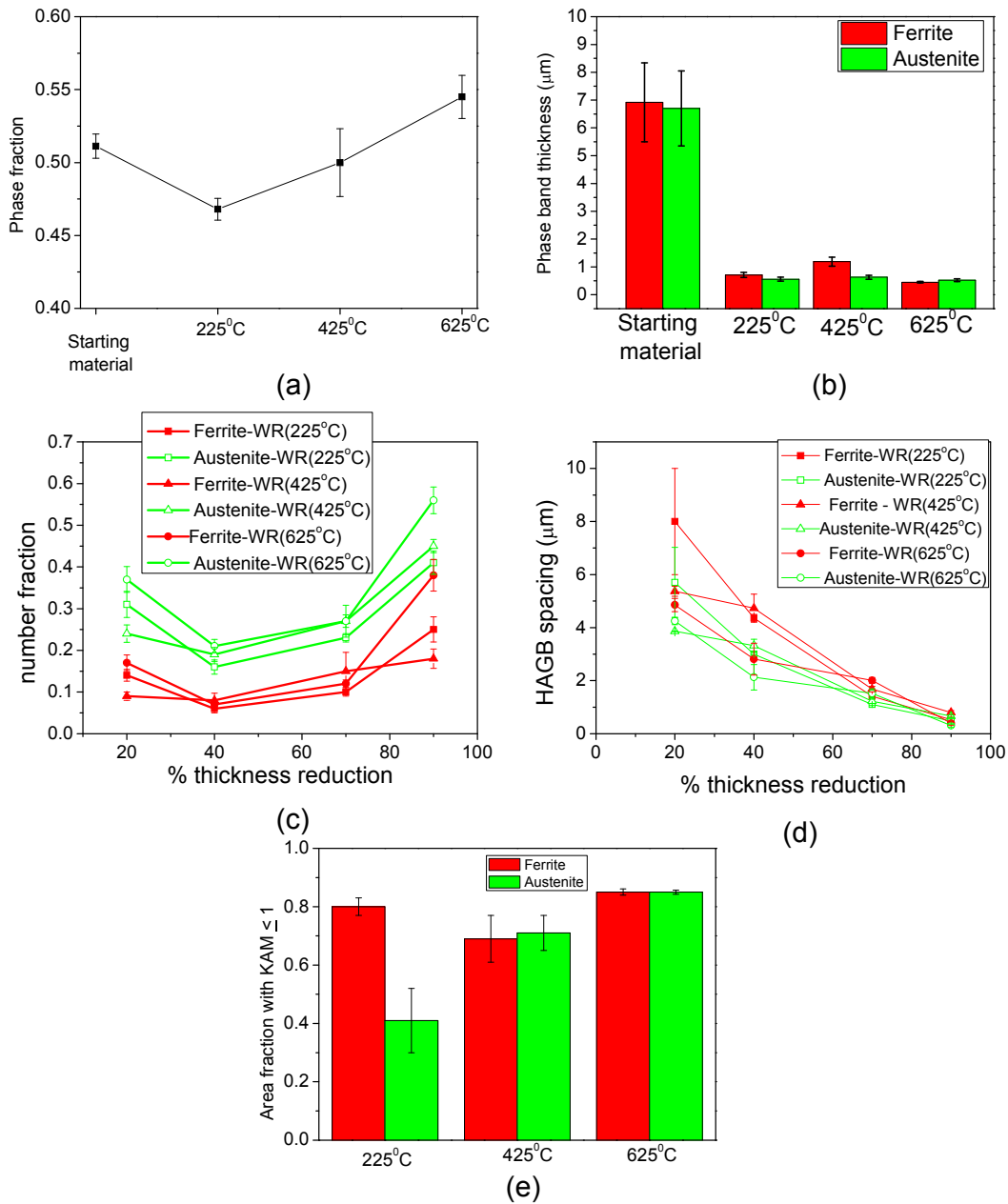


Fig.4.36: (a) shows austenite fraction, (b) shows the thickness of the phase bands, (c) and (d) show HAGB fraction and HAGB spacing of the two phases, respectively after 90% warm-rolling at different temperatures. (e) shows area fraction having $\text{KAM} \leq 1$ in the two phases in DSS 90% warm-rolled at different temperatures. The abbreviation WR is used for “Warm-Rolling” for convenience.

The observed differences in the microstructure evolution at the intermediate warm-rolling temperature of 698K (425°C) appear to be strongly affected by dynamic strain-aging also observed in single phase ferrite [83] and ferrite in DSS [84] due to which the flow stress is increased. It may be noted that the warm-rolling temperature of 698K (425°C) is well within the observed dynamic strain aging temperature range in DSS [84, 85], so that the effect will be much stronger in comparison to the two end temperatures of warm-rolling. This would lead to increased hardness of ferrite and difference in hardness of the two phases would lead to strain being partitioned more to austenite than ferrite. This would result in the average thickness of the austenite phase bands being lower than that of the ferrite bands which is also observed experimentally. The increased hardness of ferrite would lead to the suppression of grain sub-division originating from the process of slip [23,24] but an increase in mechanical fragmentation of grains at the vicinity of phase interfaces. Remarkably low HAGB fraction (Table 4.3 and Fig.4.36(c)) and fragmented microstructure observed after 90% warm-rolling at 698K (425°C) (Figures 4.8(d) and 4.9(a)) are in excellent agreement with the above observations. In contrast, the microstructures at the two end temperatures of warm-rolling show characteristics of more grain sub-division (finely sub-divided structure in both the phases) [86, 87] and much less mechanical fragmentation of grains.

It is clearly observed that austenite shows significantly higher HAGB fraction (Fig.4.36(c)) and smaller HAGB spacing (Fig.4.36(d)) as compared to ferrite in the same warm-rolled condition. Austenite in the 90% warm-rolled DSS at 498K (225°C) shows higher HAGB fraction, lower HAGB spacing and much lower area fraction with $KAM \leq 1$ (Fig.4.36(e)) as compared to ferrite. These clearly reveal that recovery is much less in austenite as compared to ferrite at this

warm-rolling temperature. The area fractions of the two phases having $KAM \leq 1$ are similar after 90% warm-rolling at 698K (425°C) and 898K (625°C). This indicates that dynamic recovery happens in both the phases at these warm-rolling temperatures and the extent of dynamic recovery is also comparable in the two phases. Therefore, dynamic recovery should affect the microstructural evolution in the two phases to a similar extent. Similar area fractions having $KAM \leq 1$ in the two phases even after 90% warm-rolling at 898K (625°C) indicates that rather than dynamic recovery greater propensity of austenite for grain sub-division is responsible for the development of finer microstructure in austenite.

The austenite in the DSS consistently shows pure metal or copper type deformation texture after warm-rolling at different temperatures (Figures 4.7, 4.11, 4.14). This is in sharp contrast to the behavior of single phase austenitic steels and also that of austenite in cold-rolled DSS, which develop predominantly brass or alloy type texture [66]. The development of brass or alloy type deformation texture in austenite during cold-rolling is attributed to the low SFE of austenite. Lowering of SFE results in the gradual transition of texture from pure metal type to predominantly brass/alloy type texture with increasing deformation [22, 29]. This phenomenon of texture transition has been attributed to the occurrence of deformation twins, which become an important deformation mode in addition to deformation by slip in low SFE materials [88].

The gradual evolution of a pure metal type texture in the austenite with increasing deformation indicates suppression of the formation of deformation twins due to the increasing SFE with increasing temperature of warm-rolling [89, 90]. Although the SFE value of austenite in the present DSS is not known precisely, however, for a Fe-10.7%Ni-18.3%Cr alloy a twofold increase in SFE

to $\sim 31 \text{ mJ/m}^2$ is noticed at 598K (325°C) from a low SFE value of $\sim 16 \text{ mJ/m}^2$ in the deformed condition at room temperature [89]. In the present case the increase in SFE is clearly evidenced by the strengthening of the pure metal type character i.e. consistent strengthening of the Cu component and weakening of the B_s component with increasing warm-rolling temperature (Fig.4.37). This is also supported by the fact that during cold-rolling of the present DSS at room temperature there is a clear transition from pure metal type texture to a predominantly brass type texture. This is clearly understood from the (111) PFs (Fig.4.38) and the relevant ODF sections of the cold-rolled materials (Fig.4.39) which reveal that strength of the B_s component increases with increasing deformation while the strength of the Cu component is diminished during cold-rolling. Although direct experimental evidence of deformation twins could not be obtained through EBSD due to the fine structure of deformation twins, but in the light of observed texture transition it is most reasonable to assume that the formation of deformation twins is prevalent in austenite of the present DSS during cold-rolling due to low SFE [10].

As already discussed before the texture of cold rolled single phase ferrite is usually described by the development of two prominent fibers, namely the RD and the ND fibers which strengthen with increasing deformation [91]. The bulk texture of the warm-rolled single phase ferrite has been studied by Barnett et al [92] who have found that the warm-rolling texture is very similar with those of the cold rolled materials characterized by the presence of the above two fibers. Increase in warm-rolling temperature further sharpens the texture, particularly for low carbon grades of steels [93, 94].

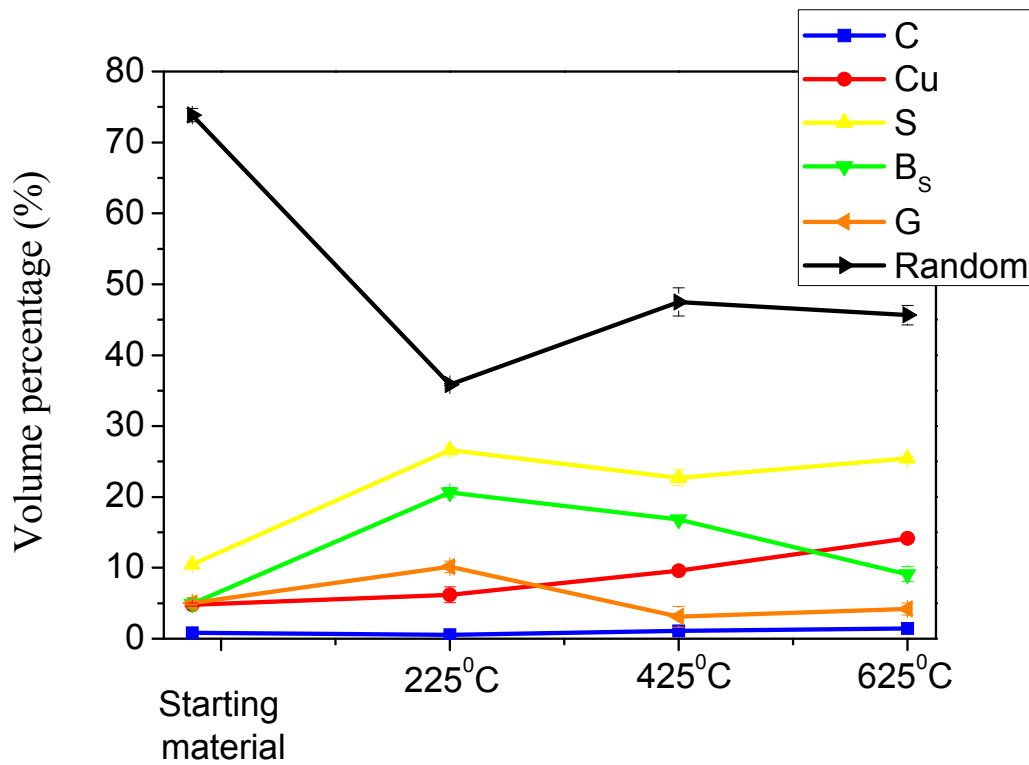


Fig.4.37: Volume percentages of different texture components in austenite in DSS warm-rolled to 90% reduction in thickness at different temperatures.

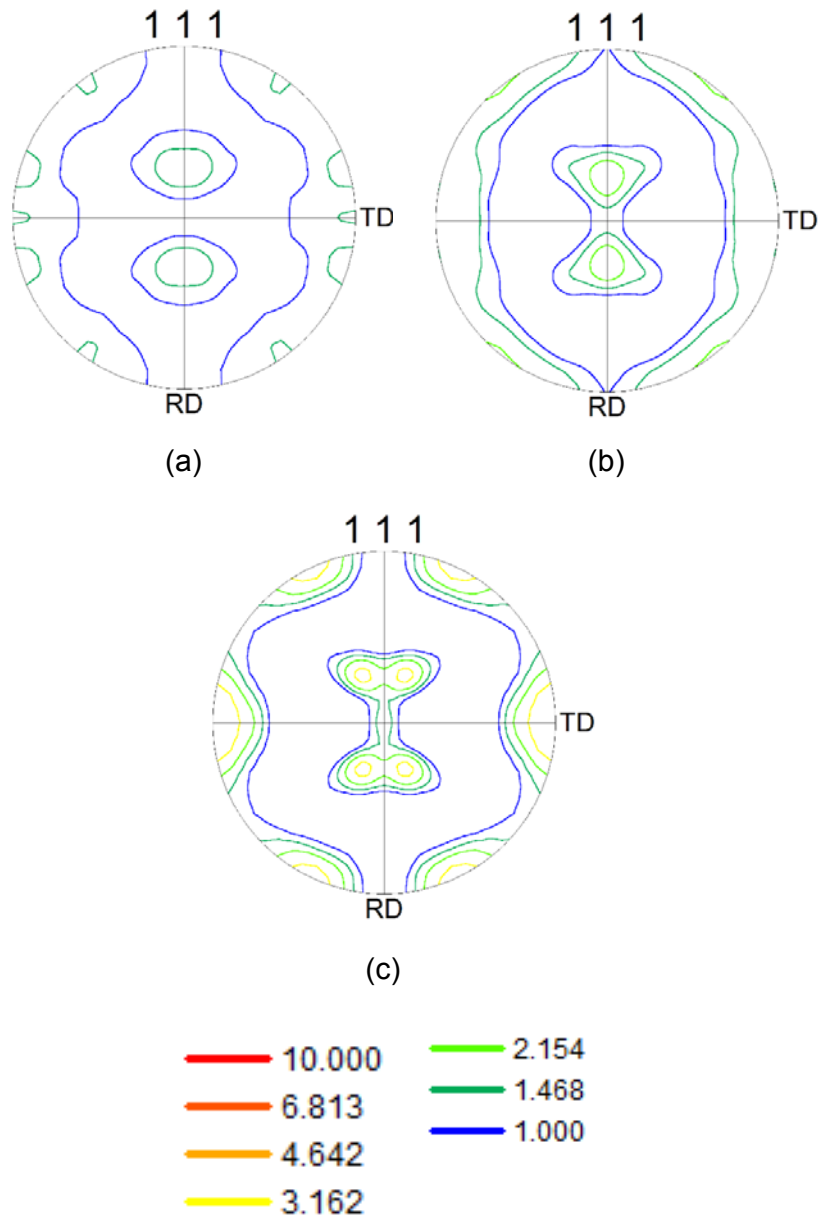


Fig.4.38: (111) pole figure of austenite in (a) 40%, (b) 70%, and (c) 90% cold-rolled DSS.

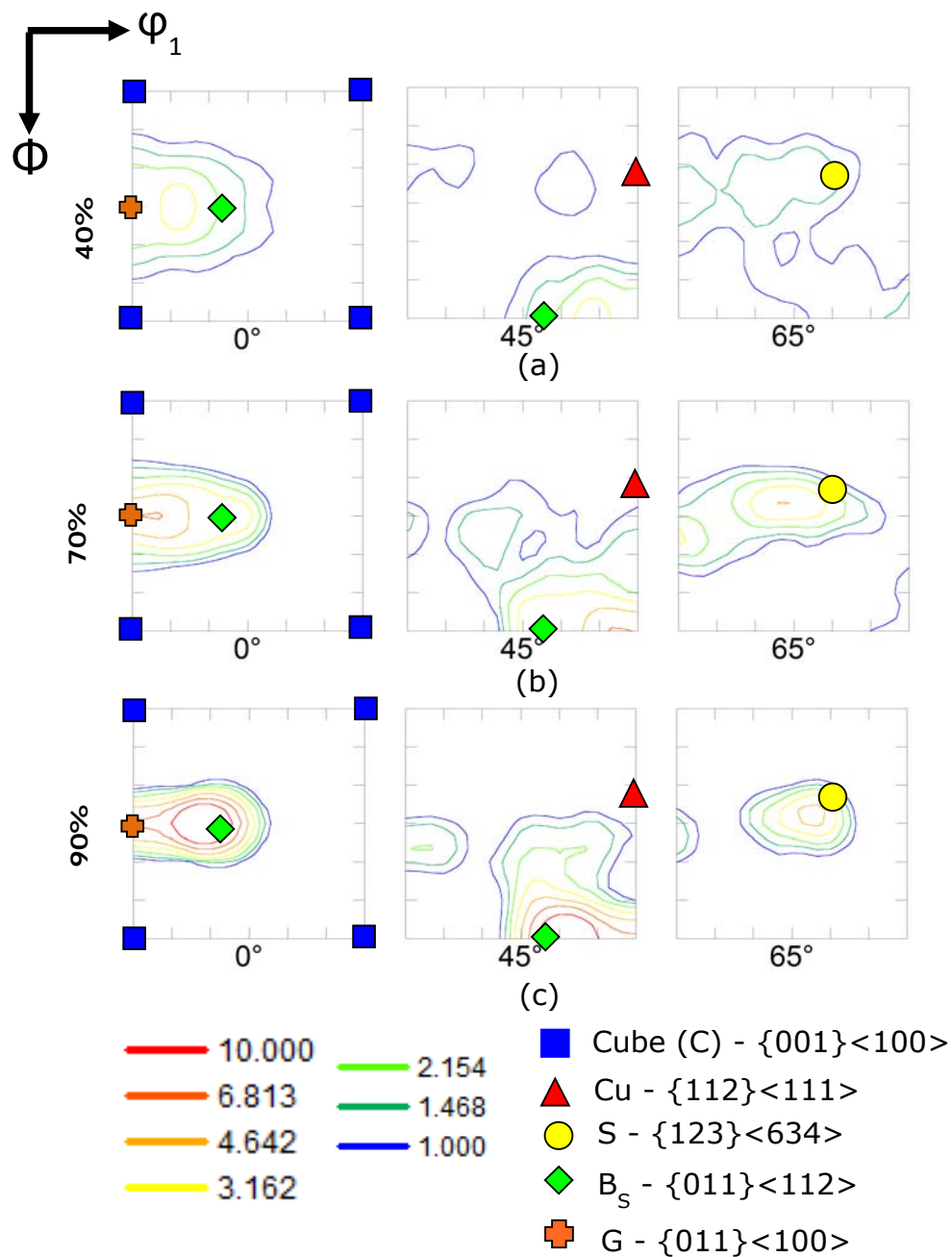


Fig.4.39: $\phi_2=0^\circ$, 45° , 65° sections of the ODFs of austenite in (a) 40%, (b) 70%, and (c) 90% cold-rolled DSS.

The texture of ferrite in experimental DSS during warm-rolling clearly shows the existence of these two major fibers (Figures 4.6, 4.10 and 4.13). However, the RD-fiber is strengthened with increasing warm-rolling temperature. The RD-fiber attains maximum strength in ferrite in DSS warm-rolled at 698K (425°C) but is diminished in strength in DSS warm-rolled at 898K (625°C). Exactly the opposite behavior is observed for the ND-fiber as quantitatively summarized in Fig.4.40.

The texture development in the present DSS is strongly affected by dynamic strain aging, which is already observed during microstructure development. The present observations concerning the texture formation can be adequately explained by the dependence of slip configuration on interaction of carbon atoms as proposed by Senuma et al [95]. It has been argued by these authors that the $\{110\}<111>$ slip is retarded preferentially at the vicinity of the grain boundaries due to the interaction of carbon atoms with dislocations piled-up against grain boundaries. The slip retardation is particularly effective for the $\{110\}<111>$ slip system due to the presence of more interstitial sites on the $\{110\}$ plane. As a result the $\{110\}<111>$ system is more work-hardened and further slip is preferred on the $\{112\}<111>$ system. The simulation of deformation texture by Raphanel et al [96] shows that the preferential retardation of $\{110\}<111>$ slip leads to an increase in the strength of the RD-fiber components $\{001\}<110>$ and $\{112\}<110>$ and decrease in the intensity of the ND-fiber component $\{111\}<112>$.

The presence of strong RD and ND fibers after warm-rolling at 498K (225°C) and 898K (625°C) is consistent with the limited dynamic strain aging effect at these two temperatures. However, the strength of the RD-fiber component is maximum while that of

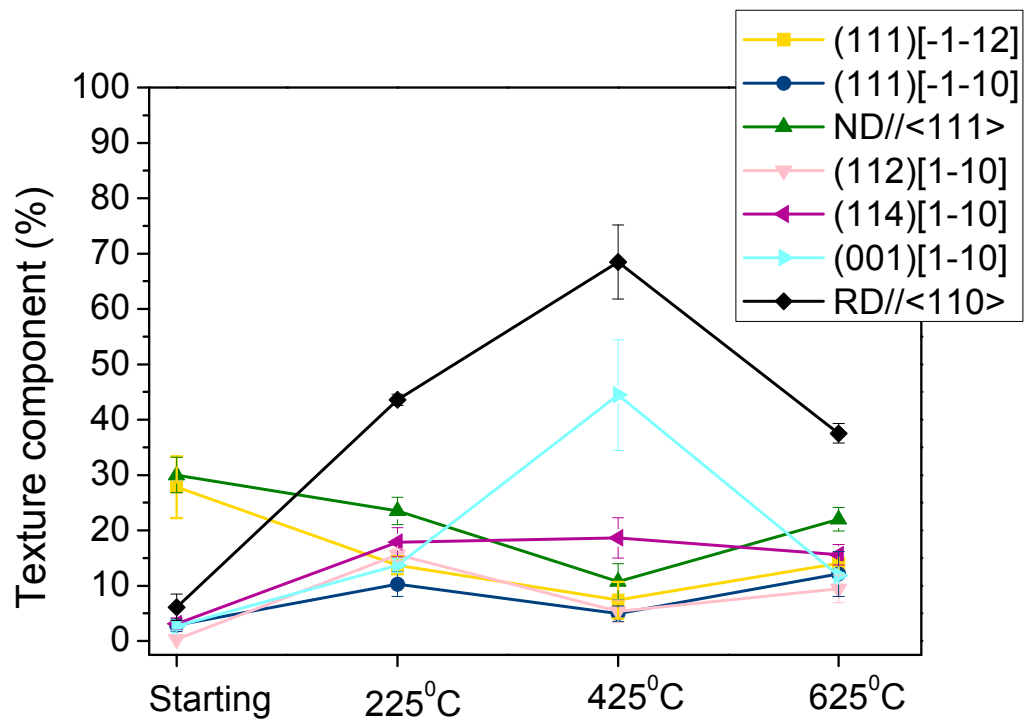


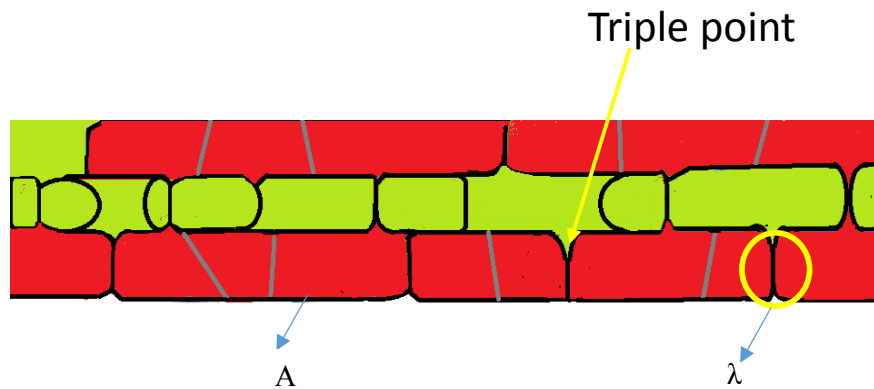
Fig.4.40: Texture components in ferrite in DSS warm-rolled to 90% reduction in thickness at different temperatures.

the ND-fiber component is minimum in ferrite in DSS 90% warm-rolled at 698K (425°C) (Fig.4.40). This is consistent with slip retardation on $\{110\}<111>$ system due to dislocation pinning resulting from a very strong dynamic strain aging effect.

Nevertheless, the main characteristics of the deformation texture of single phase materials are retained by the two constituent phases in the DSS alloy during warm-rolling. In other words the presence of the other phase does not remarkably affect the development of texture in the two phases in DSS during warm-rolling. However, the temperature of warm-rolling greatly affects the microstructure and texture development of the two phases. In effect, the two constituent phases tend to behave independently of one another. These observations are in excellent agreement with the study of Keichel et al [66] on texture evolution during cold-rolling of DSS who have argued that the major strain accommodation takes place at the phase boundaries indicated by 'λ' in Fig.4.41. Since area of these phase boundaries is much lower in comparison to the phase boundaries indicated by 'A' in Fig.4.41, the two phases are deformed independent of one another and the end texture will be similar to the respective single phase materials.

4.9.2 Evolution of microstructure and texture during isothermal annealing

It has been observed from Fig.4.16(a), Fig.4.23(a) and Fig.4.30(a) that in all the annealed DSS series specimens the ferrite phase fraction decreases initially after annealing for 2 minutes but during prolonged isothermal holding attains the value observed in the as homogenized material. Since the annealing has been carried out in a conventional furnace, ferrite to austenite conversion happens before the material is heated up to the annealing temperature of 1448K (1175°C). Therefore, for the shorter



A - Phase boundaries running parallel to the RD
 λ - Phase boundaries running perpendicular to RD



Fig.4.41: Schematic showing mutual interpretation of two phases at triple points during breakdown of the lamellar structure.

annealing duration the phase equilibrium could not be achieved. However, for longer annealing times the phase equilibrium between ferrite and austenite is re-established and volume fraction ratio of 50:50 (same as that in the as-homogenized material) is achieved.

The major point of interest, however, is the evolution of microstructure during recrystallization. The microstructural observations (Fig.4.15, Fig.4.22 and Fig.4.29) and aspect ratio variation (Fig.4.16(c), Fig.4.23(c) and Fig.4.30(c)) of the three warm-rolled and annealed DSS series specimens clearly indicate gradual transformation from a bamboo type lamellar morphology to a comparatively more globular morphology with increasing isothermal holding time. This structural evolution is indicative of the recovery process in ferrite which is also observed during annealing of cold-rolled DSS alloys [74]. In the as warm-rolled condition ferrite already has a more recovered microstructure so that the driving force for recrystallization is low. The subgrains bounded by LAGBs thus grow during subsequent annealing. Due to the lamellar morphology of the two phases more lateral growth along the RD is favored even after the ferrite grains grow along the ND to the full thickness of the phase bands. This results in lower aspect ratio of the ferrite grains after short isothermal annealing. Meanwhile, the lateral growth of the subgrains and low misorientation build-up inside the ferrite bands. In Figure 4.42 the phase maps of the DSS 90% warm-rolled at 698K (425°C) i.e. B0 (Fig.4.42(a)) and 898K (625°C) (Fig.4.42(b)) i.e. C0 specimens are reproduced. The cumulative misorientation (i.e. misorientation between the origin and any point on the arrow) along the arrow marks is shown in Fig.4.42(c) which indicates low misorientation build up inside the ferrite bands during warm-rolling. Very similar behavior is observed for ferrite in DSS 90% warm-rolled at 498K (225°C) i.e. A0 specimen, therefore, not shown here separately. This ensures that

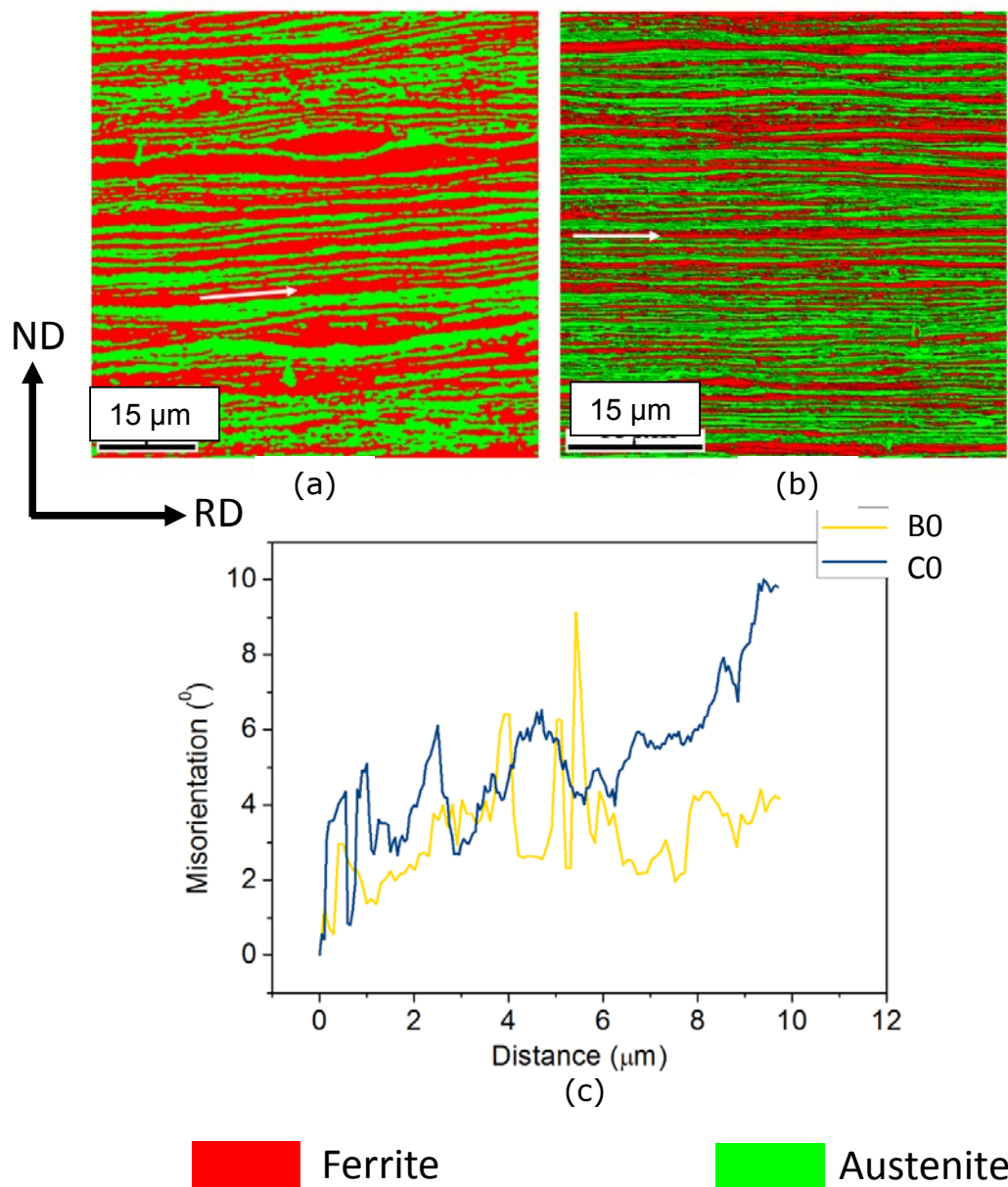


Fig.4.42: (a) and (b) show the phase maps of DSS warm-rolled to 90% reduction in thickness at 698K (425°C) and 898K (625°C) (i.e. B0 and C0 specimens), respectively. (c) shows the point to origin misorientation along the arrows inside ferrite bands in specimens B0 and C0 shown in (a) and (b), respectively.

neighboring subgrains inside the ferrite bands are separated by LAGBs after they grow and mutually impinge during annealing. This results in the well-developed bamboo type morphology observed in ferrite after short isothermal holding time.

In case of austenite the perpendicular grain boundaries are mostly HAGBs. The austenite also shows higher aspect ratio as compared to the ferrite in the same isothermally annealed condition. These microstructural observations indicate that the primary softening mechanism in austenite is discontinuous (or primary) recrystallization due to which recrystallized grains bounded by HAGBs with comparatively more globular morphology i.e. higher aspect ratio (as compared to the ferrite grains) form inside the austenite phase bands. The recrystallized austenite grains grow to cover the full thickness of the austenite bands. However, the lateral growth along the RD ensures that neighboring austenite grains are separated by HAGBs after they mutually impinge resulting in the characteristic bamboo morphology. The evolution of texture in the two phases to be discussed shortly strongly supports the proposed softening mechanisms in the two constituent phases.

Annealing beyond 20 minutes results in the gradual breakdown of the lamellar bamboo morphology and the concurrent evolution of a comparatively more globular morphology. However, extensive microstructural coarsening is not observed even during prolonged isothermal holding (Fig.4.15(d), Fig.4.22(d) and Fig.4.29(d)). These microstructural observations are consistent with a perceptible increase in the aspect ratio of both ferrite and austenite after annealing for 20 minutes, but no significant change for longer annealing times (Fig.4.16(c), Fig.4.23(c) and Fig.4.30(c)). The observed suppression of grain growth could be attributed to the hindrance to grain growth exerted by one phase on the other.

The breakdown of the lamellar structure into comparatively more globular structure with increasing annealing time has also been reported in heavily cold-rolled and annealed DSS [74]. The structural adjustment is preceded by the break-down of the bamboo morphology initiated by the mutual inter-penetration of the phases along the triple points comprising of two phase boundaries and one grain boundary as shown schematically in Fig.4.41. The patterns of microstructural evolution during annealing of the different warm-rolled DSS series specimens strongly suggest a very similar mechanism reported for cold rolled and annealed DSS [74].

The evolution of recrystallization texture in ferrite is affected by the characteristic softening process by recovery. Recovery preserves the characteristics of the deformation texture since the nucleation of strain free grains typical during discontinuous recrystallization is absent. The two fiber components also behave differently in single phase ferrite during annealing due to orientation dependent stored energy [7]. The RD fiber components such as the $\{001\}\langle 110 \rangle$ and $\{112\}\langle 110 \rangle$ would preferentially undergo recovery while the ND fiber components $\{111\}\langle 110 \rangle$ and $\{111\}\langle 112 \rangle$ due to their higher stored energy and frequency advantage tend to show a recrystallization type behavior during annealing [46, 74]). Thus, depending on which softening mechanism is predominant, stronger RD or ND fiber components will develop in the annealing texture of ferrite.

It has already been discussed that ferrite in DSS warm-rolled at different temperatures shows markedly different textures. Ferrite in the B0 specimen (Fig.4.10) shows a much higher fraction of the RD fiber than ND fiber components in sharp contrast to the rather comparative strength of the two fibers in ferrite of the A0 (Fig.4.6) and C0 specimens (Fig.4.13). Despite these apparent differences in the texture of ferrite in as warm-rolled DSS the recrystallization

texture of the three annealed DSS series specimens show much stronger RD fiber than ND fiber, though relative shift in the peak intensity along the two fibers is observed, which however, does not affect the total volume fraction of the two fibers significantly. This further indicates the dominant role of recovery on the development of annealing texture in ferrite in DSS. It might be noted that recovery of ferrite in cold-rolled and annealed DSS also leads to much stronger RD fiber than ND fiber texture [74]). Processing by warm-rolling ensures dynamic recovery and decrease in the driving force for recrystallization which is effective in suppressing recrystallization and strengthening the RD fiber components.

The austenite in cold rolled and annealed DSS shows retention of deformation texture component, particularly the G component and the G^T component [74]. However, the BR component, often reported as the major texture component in the recrystallization texture of heavily deformed low SFE materials is rather weak. The formation of strong BR component is attributed to the nucleation of this component in shear bands and subsequent growth selection due to the $40^\circ\langle 111 \rangle$ relationship with the B_s component of the deformed matrix [97]. The austenite in cold-rolled and annealed DSS does not develop strong BR component which is attributed to the absence of shear bands in the deformed matrix[74].

The austenite in warm-rolled DSS also retains the basic characteristics of the deformation texture during annealing i.e. typical pure metal type texture. These observations are similar to those reported in austenite in cold-rolled and annealed DSS [74]. This indicates very similar recrystallization mechanism i.e. nucleation of grains (discontinuous recrystallization) with orientations pre-existing in the as deformed matrix and no preferential orientation selection. Discontinuous recrystallization and growth are also supported by the presence of annealing twins inside

austenite bands (Fig.4.15, Fig.4.22 and Fig.4.29). Nucleation from pre-existing orientations in deformed matrix but no preferential orientation selection should result in a situation where the annealing texture should be a random sampling of the deformation texture [32]. Thus, observed differences in the texture of austenite should originate from the differences in texture of as warm-rolled materials i.e. the texture of austenite in A0, B0 and C0 specimens. This explains stronger S and B_s components than Cu component observed in the annealed A and B series specimens as opposed to stronger S but B_s and Cu components of similar strength in annealed C series specimens, particularly after longer isothermal holding. However, unlike austenite in cold-rolled and annealed DSS [66], the G and twin of Goss (G^T) components are not the major components. These differences may be attributed to the fact, that since the fraction of the G component is low in deformation texture upon annealing the fractions of G and G^T remain low.

In the present case a further possible reason for the absence of the BR component in the recrystallization texture of austenite appears to be the presence of a pure metal type texture instead of a dominant brass or alloy type texture in austenite in different warm-rolled DSS. Since B_s is not the dominant component in the texture of austenite in different warm-rolled DSS, the preferential growth advantage of the BR grains would be greatly reduced, preventing it from becoming the dominant texture component after recrystallization.

Thus, the two constituent phases of DSS show recrystallization process independent of each other so that the texture evolution is determined by their characteristic recrystallization behavior. However, the grain growth behavior of two phases in DSS is strongly affected by the presence of the other phase.

-: CHAPTER 5 :-
***EFFECT OF SEVERE DEFORMATION ON THE
EVOLUTION OF MICROSTRUCTURE AND TEXTURE
DURING WARM-ROLLING AND RECRYSTALLIZATION***

5.1 Severe warm-rolling of DSS

In Chapter 4 the effect of warm-rolling temperature on the evolution of deformation and recrystallization texture is clarified. In order to achieve that, the DSS is rolled at different temperatures to the same deformation level i.e. 90% reduction in thickness and then isothermally annealed for different durations. The focus of the present chapter is to clarify the effect of severe warm-rolling on the evolution of microstructure and texture.

The results obtained from warm-rolling experiments suggest that austenite is not stable in the present DSS beyond 90% reduction even at the warm-rolling temperatures of 498K (225°C) and 698K (425°C). This could be easily understood from the phase maps of DSS warm-rolled to 95% and 98% reduction in thickness at 498K (225°C) and 698K (425°C) which show that the austenite fraction is systematically reduced with increasing warm-rolling strain (Fig.5.1). This is attributed to deformation induced transformation of austenite during severe warm-rolling. The variation of austenite fraction with deformation at different warm-rolling temperatures is shown quantitatively in Fig.5.2. Figure 5.2 also includes the data on DSS warm-rolled at 898K (625°C). It is clearly established that austenite is remarkably stable at the warm-rolling temperature of 898K (625°C) even up to the highest strain level.

Since the focus of the present chapter is on the evolution of microstructure and texture during severe straining, the warm-rolling temperatures of 498K (225°C) and 698K (425°C) are not considered suitable for this purpose as austenite is not stable during warm-rolling at these two temperatures. In contrast, the warm-rolling temperature of 898K (625°C) is particularly suitable. This is due to the fact that warm-rolling can be carried out without encountering additional complexities arising from the strain induced phase transformation.

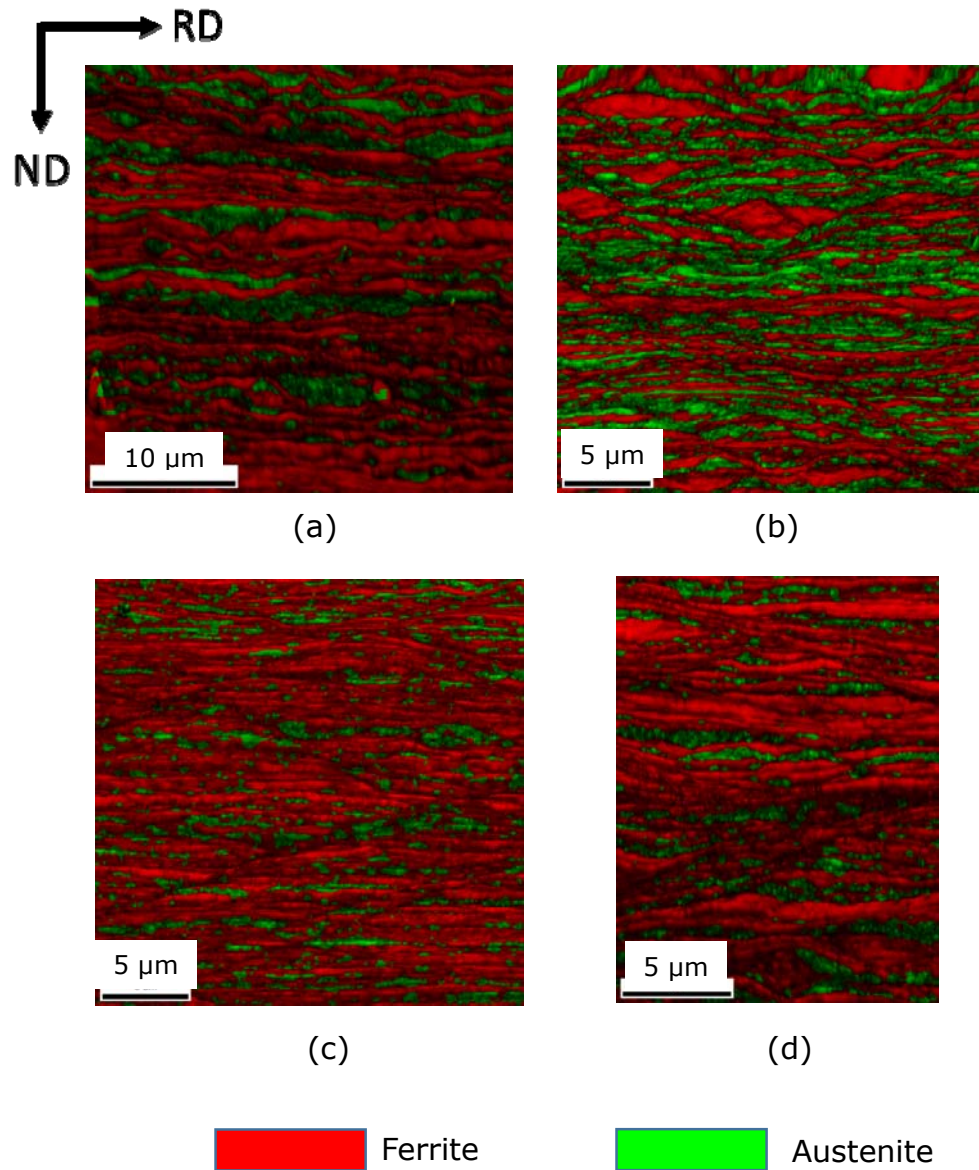


Fig.5.1: Phase maps of DSS warm-rolled to ((a),(b)) 95% and ((c),(d)) 98% reduction in thickness at ((a),(c)) 498K (225°C) and ((b),(d)) 698K (425°C).

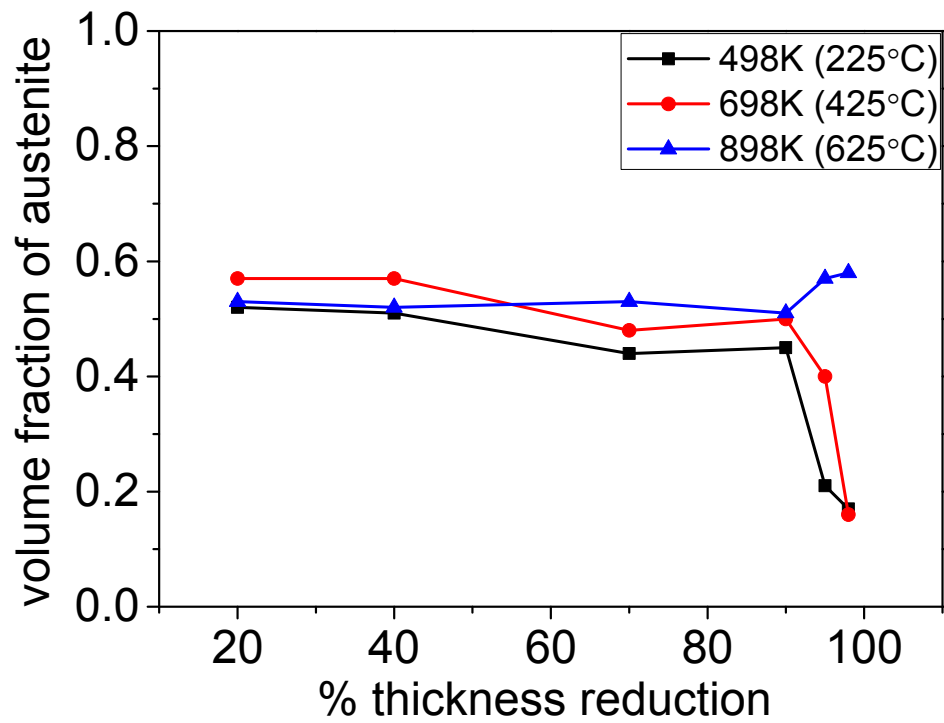


Fig.5.2: Variation of austenite fraction in DSS during warm-rolling at different temperatures.

Further, as has been already clarified in Chapter 4, the microstructure and texture evolution at the warm-rolling temperature of 898K (625°C) is not affected by dynamic strain ageing. Therefore, the effect of severe warm-rolling can be evaluated accurately without being affected by phase transformation or dynamic strain aging.

It may be noted that, although the evolution of microstructure and texture in the DSS 90% warm-rolled at 898K and isothermally annealed for different time intervals is already given in Chapter 4, however, few results are duplicated in this chapter to systematically understand the microstructure and texture evolution during severe deformation.

5.2 Evolution of microstructure and texture during severe warm-rolling of DSS at 898K (625°C)

5.2.1 Evolution of microstructure

Figure 5.3 shows the phase maps of DSS warm-rolled to 70% ($\epsilon_q=1.39$) (Fig.5.3 (a)), 90% ($\epsilon_q=2.66$) (Fig.5.3(b)), 95% ($\epsilon_q=3.45$) (Fig.5.3(c)) and 98% ($\epsilon_q=4.5$) (Fig.5.3(d)) reduction in thickness. The phase map of 70% (Fig.5.3(a)) warm-rolled DSS shows the presence of thick phase bands elongated along the RD. The thickness of the phase bands along the RD is not uniform and varies from one end of a band to the other end. The phase map of 90% warm-rolled DSS (Fig.5.3(b)) shows very fine lamellar morphology almost free of any local fragmentation. With further increase in strain to 95% (Fig.5.3(c)) and 98% (Fig.5.3(d)) reduction in thickness, local fragmentation could be easily observed in the phase maps (shown by dotted circles). It is further revealed from the phase map that ferrite bands show decidedly more fragmentation as compared to the austenite bands.

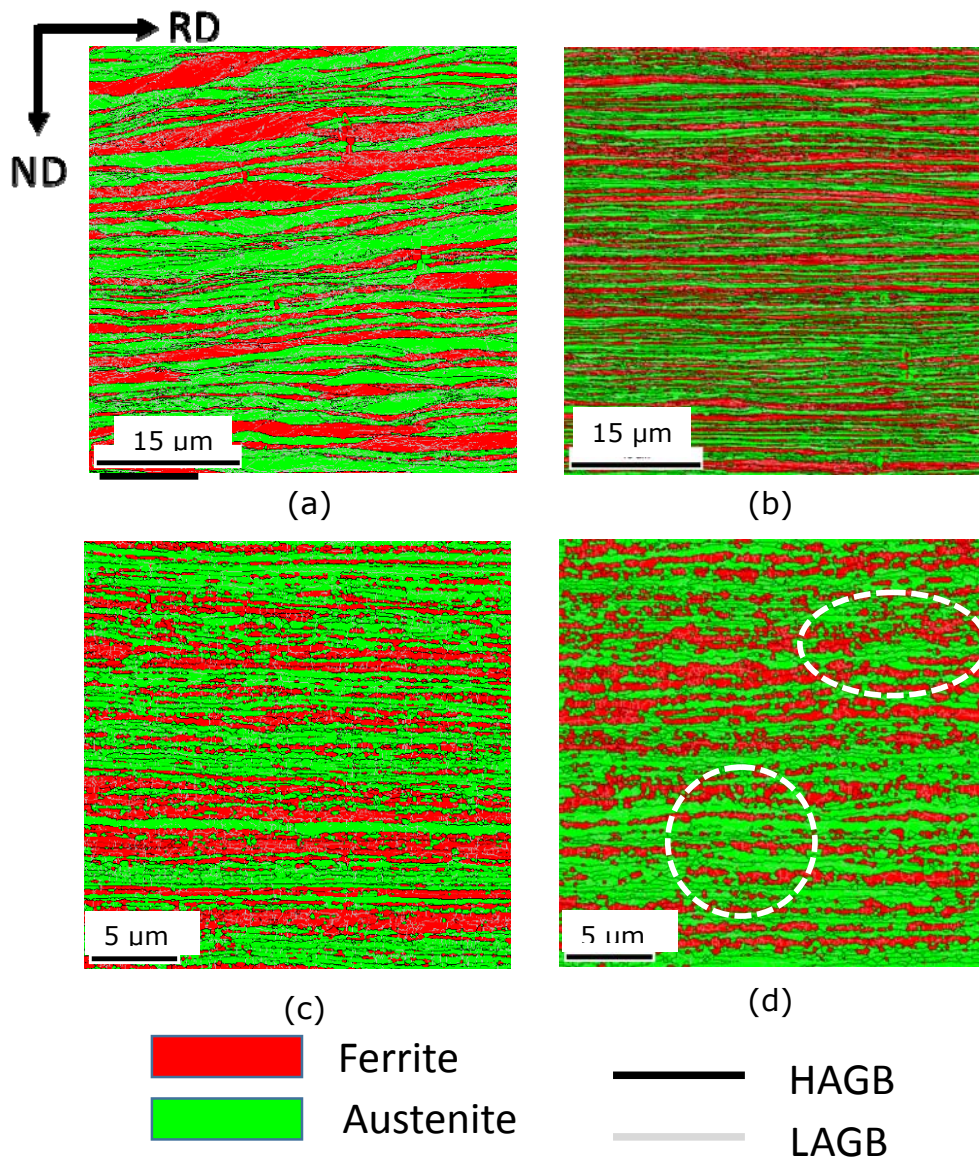


Fig.5.3: Phase maps of DSS warm-rolled at 898K (625°C) to (a) 70%, (b) 90%, (c) 95% and (d) 98% reduction in thickness.

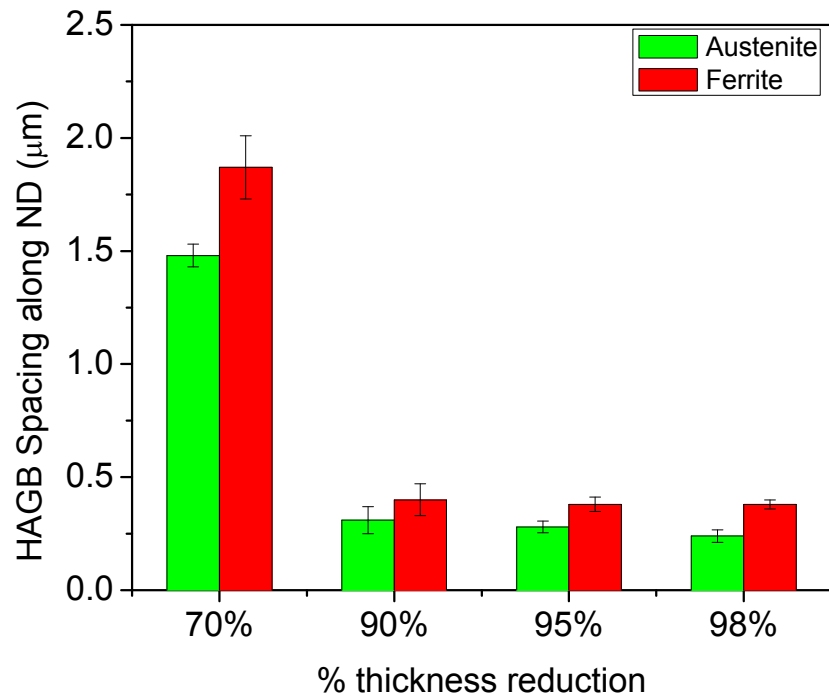


Fig.5.4: Variation of HAGB spacing along ND in the two phases of DSS warm-rolled to different reduction in thickness at 898K (625°C).

The microstructural refinement of the two phases during severe warm-rolling is shown in Fig.5.4 using the variation of HAGB spacing along the ND with thickness reduction. The HAGB spacing along the ND of austenite and ferrite is 1.87 μm and 1.48 μm , respectively in the 70% warm-rolled DSS. These HAGB spacing values are consistent with the rather coarse microstructure observed in the phase map of the 70% warm-rolled DSS (Fig.5.3(a)). The microstructure is greatly refined after 90% warm-rolling resulting in the HAGB spacing of ~ 0.31 μm and 0.4 μm for austenite ferrite, respectively. The lamellar morphology is retained up to the highest strain level. Austenite consistently shows finer microstructure than ferrite so that the HAGB spacing along ND in austenite (~ 250 nm) is lower than that of ferrite (~ 380 nm) in the 98% warm-rolled DSS (Fig.5.4). It is further observed from Fig.5.4 that the HAGB spacing along the ND in ferrite does not show any substantial change beyond 90% reduction. In contrast, the HAGB spacing in austenite is consistently decreased up to the highest strain level i.e. 98% reduction in thickness.

5.2.2 Evolution of texture

The evolution of texture in ferrite in DSS during warm-rolling is shown in Fig.5.5 by depicting the $\phi_2=45^\circ$ section of the ODFs. The $\phi_2 = 45^\circ$ section of the ODF of ferrite in 70% warm-rolled DSS (Fig.5.5(a)) shows stronger ND-fiber than RD-fiber. However, the RD-fiber is significantly strengthened during further warm-rolling as may be quite evident from the intensities of the contour lines in the $\phi_2 = 45^\circ$ sections of the ODFs of ferrite in 90% (Fig.5.5(b)), 95% (Fig.5.5(c)) and 98% (Fig.5.5(d)) warm-rolled DSS.

The evolution of the two main texture fibers in ferrite in DSS during warm-rolling is shown quantitatively in Fig.5.6. It is easily observed that, in ferrite of the starting homogenized DSS the ND-

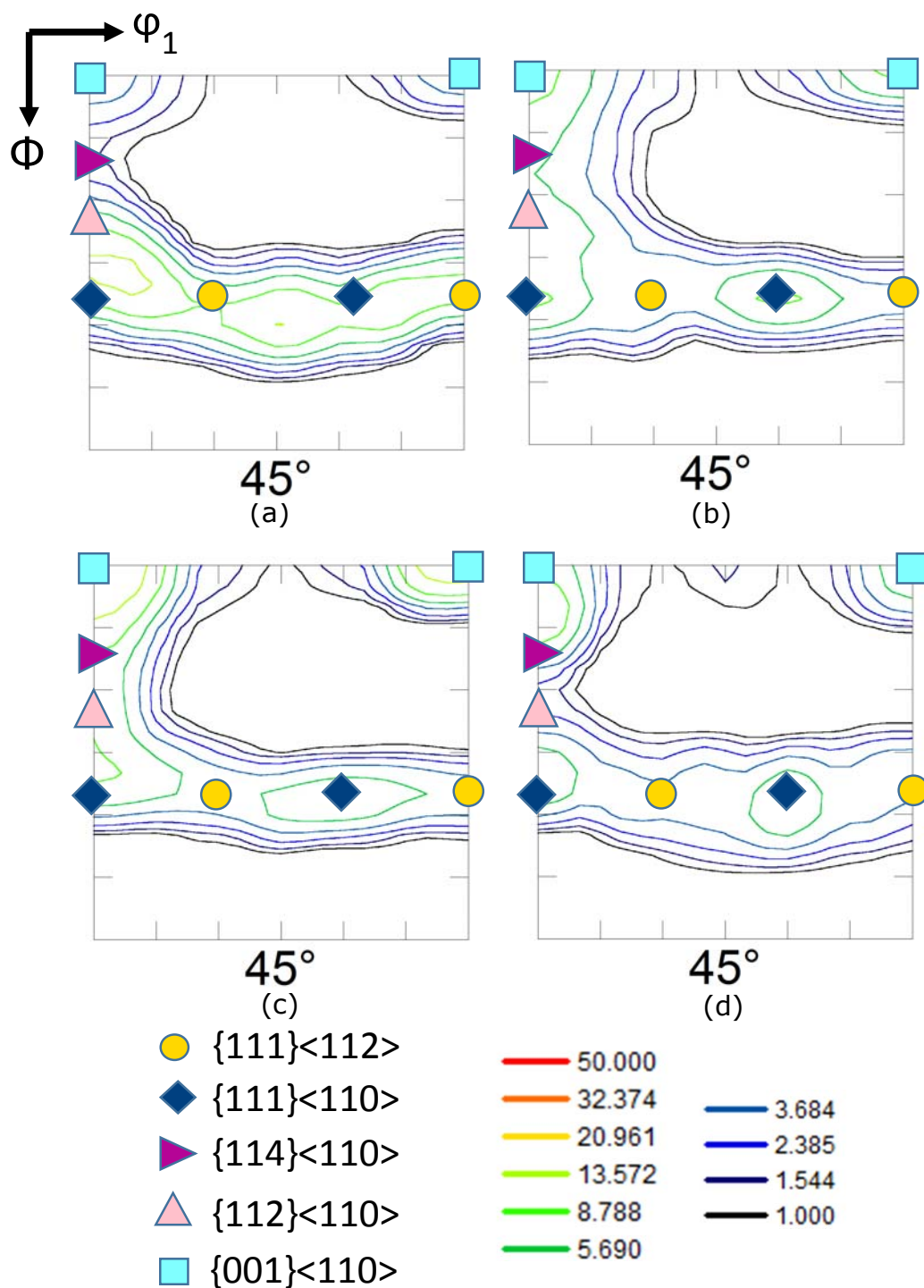


Fig.5.5: $\phi_2 = 45^\circ$ section of ODF of ferrite in DSS warm-rolled at 898K (625°C) to (a) 70%, (b) 90%, (c) 95%, (d) 98% reduction in thickness.

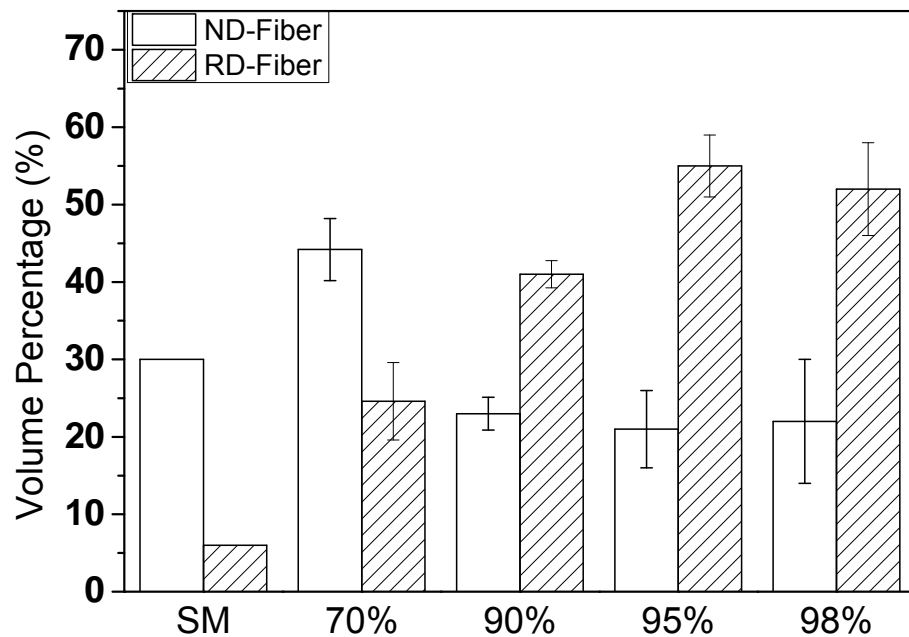


Fig.5.6: Volume fractions of RD and ND-fibers in ferrite in DSS warm-rolled at 898K (625°C) to different reduction in thickness. SM is used as an abbreviation for the homogenized starting material.

fiber (ND//<111>) is much stronger than the RD-fiber (RD//<110>). The strength of the ND-fiber is evidently greater than that of the RD fiber in ferrite in DSS warm-rolled to 70% reduction in thickness. Following 90% warm-rolling the RD-fiber is strengthened so that the volume fraction of the RD-fiber (volume fraction $\sim 41\%$) is more than that of the ND-fiber (volume fraction $\sim 23\%$). The RD-fiber in ferrite in DSS is further strengthened (volume fraction $\sim 55\%$) after 95% warm-rolling while that of the ND-fiber (volume fraction $\sim 21\%$) remains almost unchanged. However, no significant variation in the volume fraction of the RD ($\sim 52\%$) and ND ($\sim 22\%$) fibers could be observed in ferrite in 98% warm-rolled DSS.

Figure 5.7 shows the (111) PFs of austenite in DSS warm-rolled to 70% (Fig.5.7(a)), 90% (Fig.5.7(b)), 95% (Fig.5.7(c)) and 98% (Fig.5.7(d)) reduction in thickness. The PFs of austenite in 70% (Fig.5.7(a)) and 90% (Fig.5.7(b)) warm-rolled DSS clearly indicate the presence of pure metal type texture defined by the presence of prominent S ($\{123\}<634>$), brass or B_s ($\{110\}<112>$) and copper or Cu ($\{112\}<111>$) components. With increasing thickness reduction the B_s component is strengthened gradually as compared to the Cu component indicating the tendency for the development of a brass type texture in austenite. This is quite evident from the PF of austenite in 95% (Fig.5.7(c)) and 98% warm-rolled DSS (Fig.5.7(d)).

Figure 5.8 shows the $\varphi_2=0^\circ$, 45° and 65° sections of the ODF of austenite in 70% (Fig.5.8(a)), 90% (Fig.5.8(b)), 95% (Fig.5.8(c)) and 98% (Fig.5.8(d)) warm-rolled DSS. The $\varphi_2=45^\circ$ section of the ODF of austenite in 70% warm-rolled DSS shows the clear presence of typical pure metal type texture. The $\varphi_2=45^\circ$ section of the ODF of austenite in 90% warm-rolled DSS (Fig.5.8(b)) shows similar

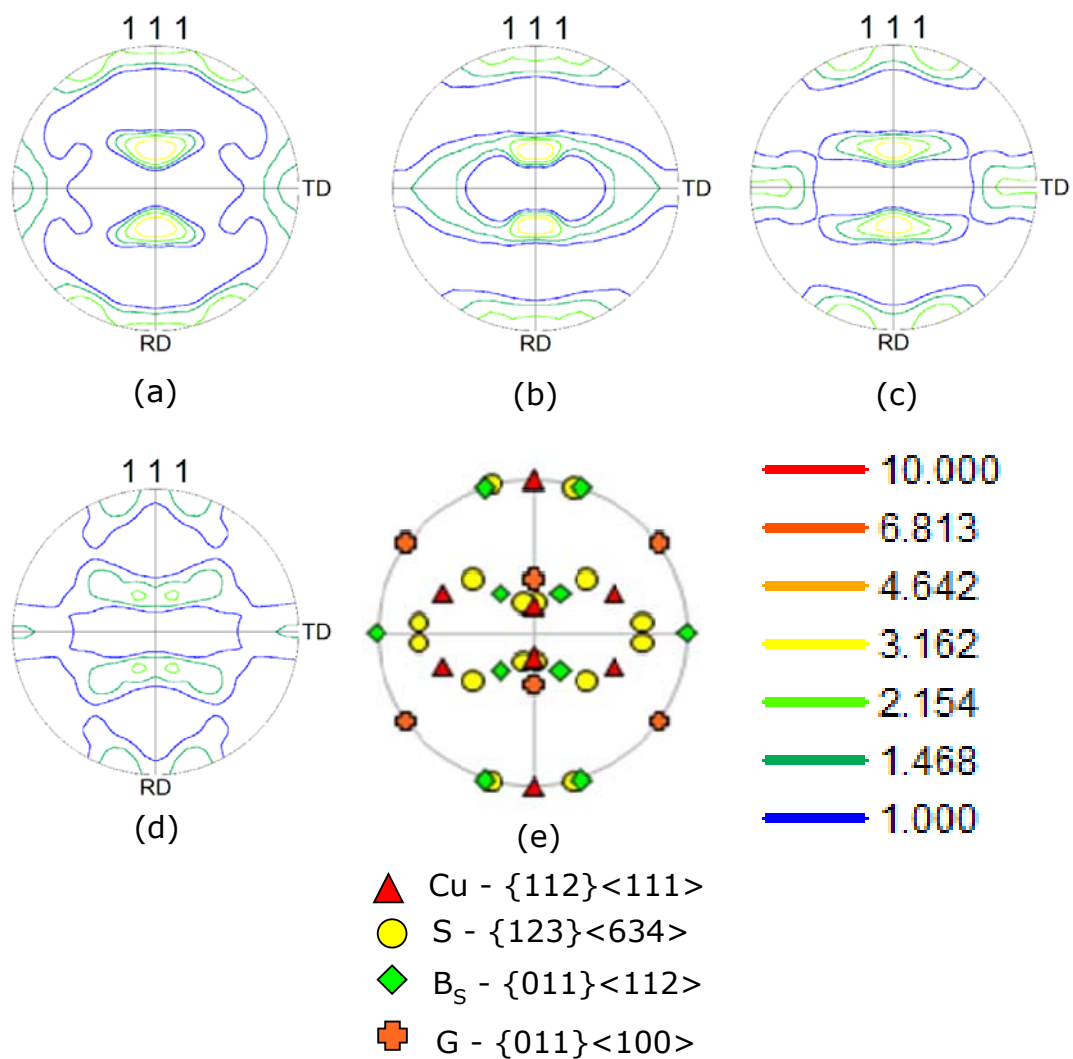


Fig.5.7: (111) PFs of austenite in DSS warm-rolled at 898K (625°C) to (a) 70%, (b) 90%, (c) 95%, (d) 98% reduction in thickness.

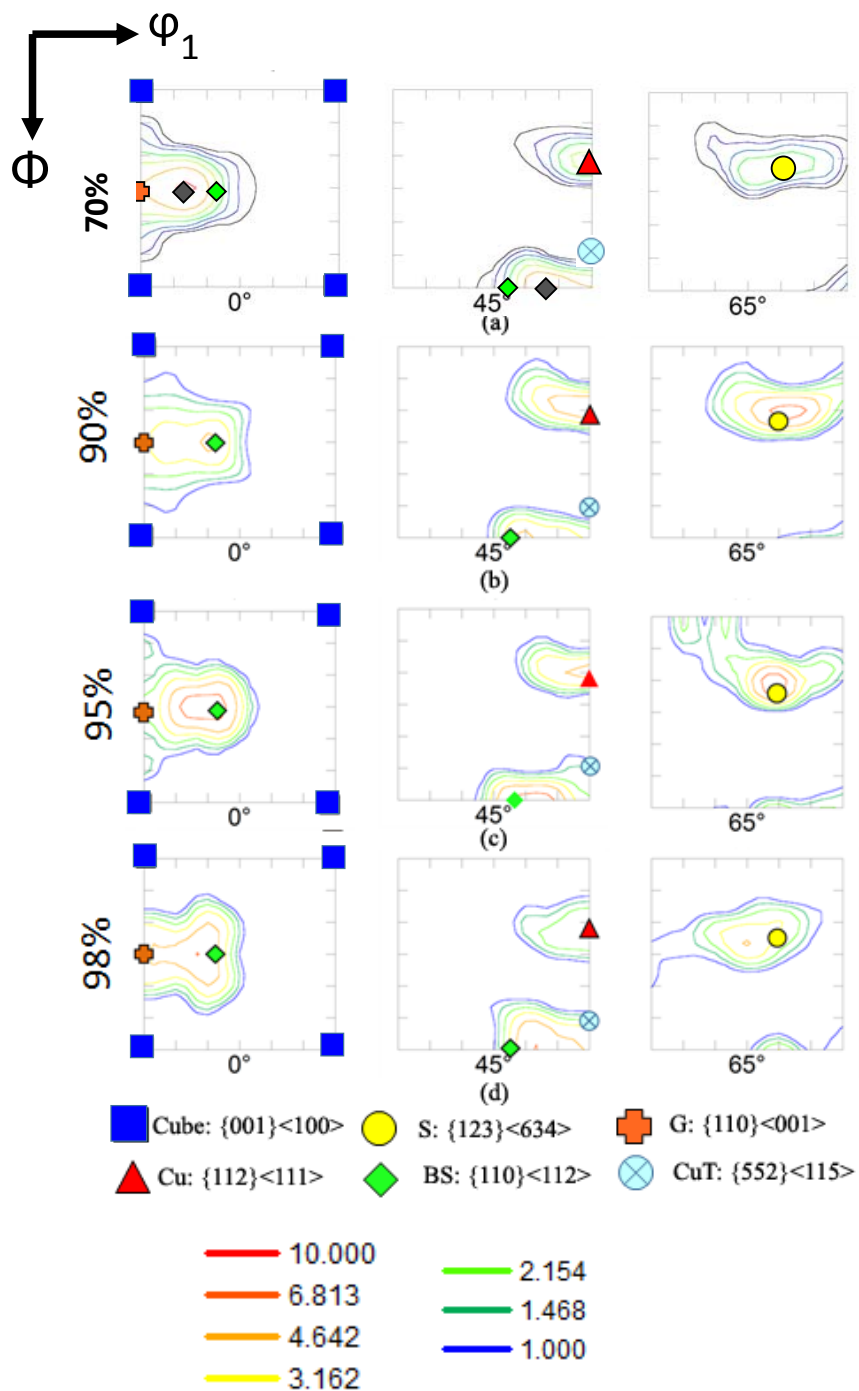


Fig.5.8: $\phi_2 = 0^\circ, 45^\circ, 65^\circ$ sections of the ODFs of austenite in DSS warm-rolled at 898K (625°C) to (a) 70%, (b) 90%, (c) 95% and (d) 98% reduction in thickness.

intensity around the Cu and B_s locations while the $\phi_2=65^\circ$ section shows slightly higher intensity around the S location.

This confirms the presence of stronger S component than B_s component or the presence of pure metal type deformation texture. Higher intensities around the B_s and S locations as compared to the Cu location could be observed in the $\phi_2=45^\circ$ section of the ODF of austenite in 95% (Fig.5.8(c)) and 98% warm-rolled DSS (Fig.5.8(d)) indicating the strengthening of the B_s component with increasing deformation. The $\phi_2=45^\circ$ sections of the ODFs of austenite in 95% and 98% warm-rolled DSS (Fig.5.8(c) and 5.8(d), respectively) show noticeable intensity at the vicinity of twin of the copper (Cu^T) ($\{552\}<115\}$) orientation, which could not be observed in the $\phi_2=45^\circ$ sections of the ODFs of austenite in the 70% (Fig.5.8(a)) and 90% (Fig.5.8 (b)) warm-rolled DSS.

The variation of texture components in austenite in DSS warm-rolled to different thickness reduction is summarized in Fig.5.9. The increase in the B_s fraction with increasing deformation is quite evident. Consistent increase in the volume fraction of the Cu^T component could be observed accompanying the gradual strengthening of the B_s component. Noticeable fraction of the Cu^T component is present in austenite in 98% warm-rolled DSS (~6%).

5.3 Evolution of microstructure and texture during annealing

5.3.1 Evolution of microstructure during annealing

The evolution of microstructure in 70% warm-rolled DSS during isothermal annealing at 1448K (1175°C) is illustrated in Fig.5.10. It is observed that the lamellar morphology consisting of elongated bands (marked by arrows) is retained after annealing for 2 minutes (Fig.5.10(a)) and 30 minutes (Fig.5.10(b)). However, the continuity of the bands is broken down locally in the specimen annealed for 30 minutes (shown enclosed by circle in Fig.5.10(b)), although few elongated bands could still be observed (marked by arrow). Each

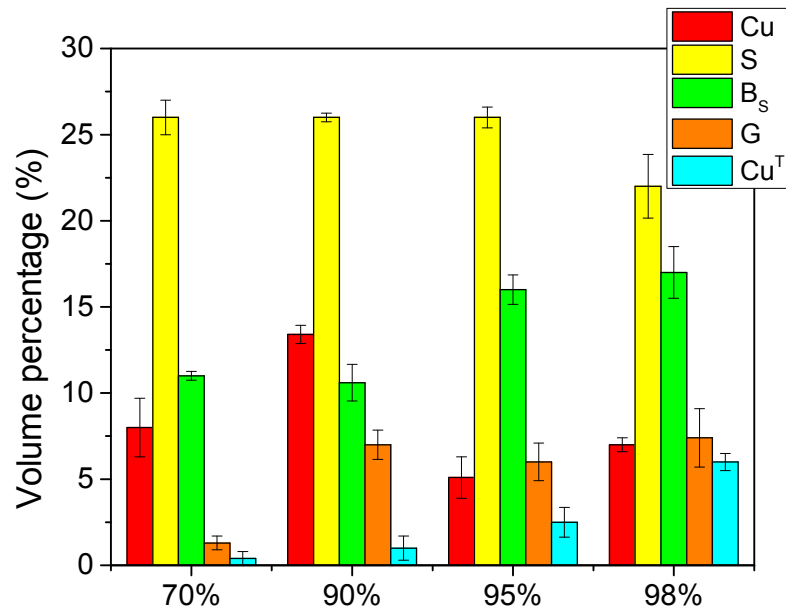


Fig.5.9: Volume fraction of texture components in austenite in DSS warm-rolled to different reduction in thickness at 898K (625°C).

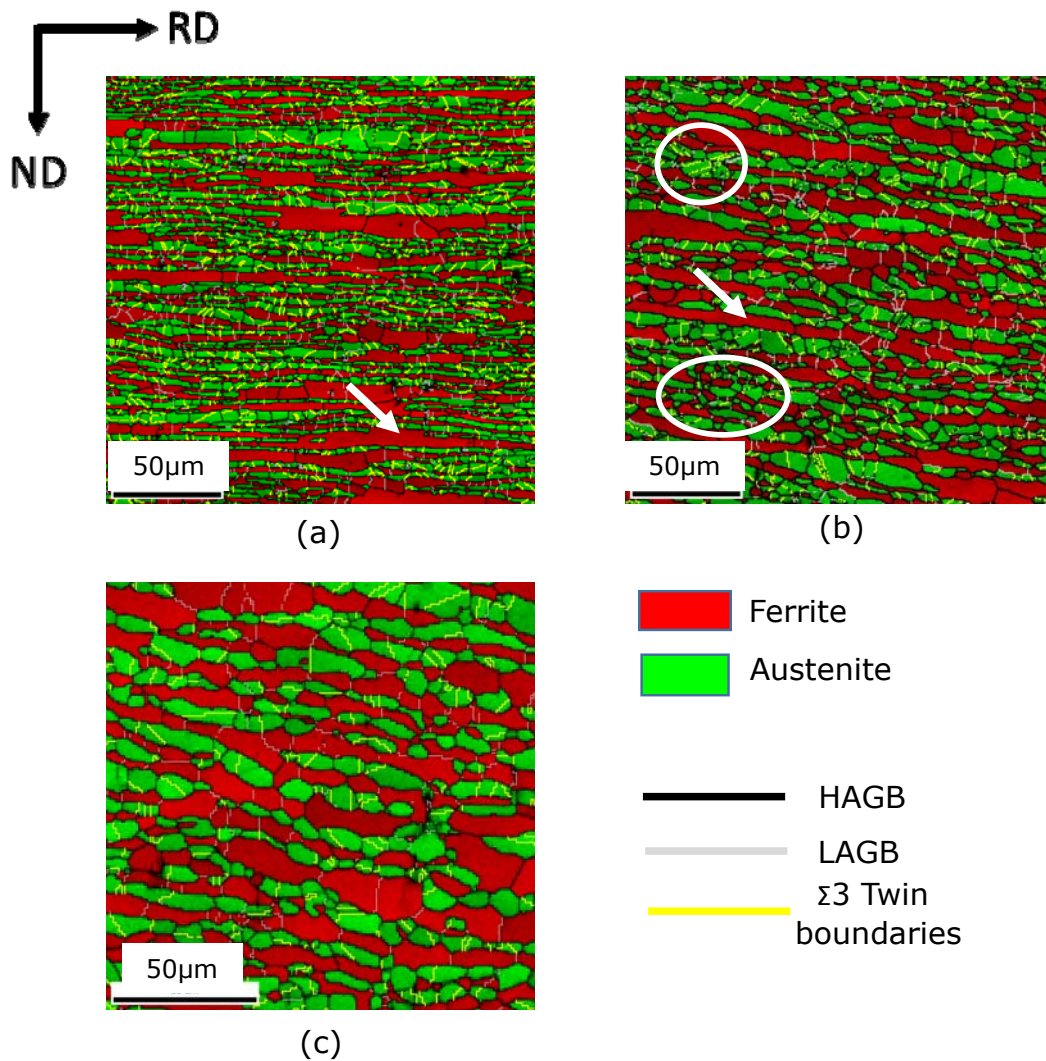


Fig.5.10: Phase maps of 70% warm-rolled DSS after isothermal annealing 1448K (1175°C) for (a) 2, (b) 30 and (c) 120 minutes.

phase band is one grain thick when measured along the ND. Inside the ferrite bands LAGBs as well as HAGBs run perpendicular to the phase boundaries. Clear presence of annealing twins (highlighted in yellow) inside the austenite bands could be easily identified. Presence of elongated bands could be clearly observed even after annealing for 120 minutes (marked by arrow in Fig.5.10(c)).

The evolution of microstructure in the 95% warm-rolled DSS during isothermal annealing is shown in Fig.5.11. The phase map of the sample isothermally annealed for 2 minutes (Fig.5.11(a)) shows the presence of elongated phase bands (marked by arrows). Each phase band is clearly one grain thick as has been observed in case of the 70% warm-rolled and annealed specimen (Fig.5.10). However, within the phase map regions could be easily identified where interpenetration or incipient interpenetration of phases could be easily observed (marked by circles). LAGBs perpendicular to the phase boundaries could be also seen within the ferrite bands. Presence of annealing twins inside the austenite bands is also quite evident in the phase map. The phase map following isothermal annealing for 30 minutes (Fig.5.11(b)) reveals pronounced breakdown of the lamellar structure due to the mutual interpenetration of the two phases (marked by circles). Significant change in microstructure or morphology is not observed during further isothermal holding for 120 (Fig.5.11(c)) minutes.

The evolution of microstructure during isothermal annealing of 98% warm-rolled DSS is shown in Fig.5.12. The microstructural evolution follows similar trend observed in case of the 95% warm-rolled and annealed DSS (Fig.5.11). The phase map after isothermal annealing for 2 minutes (Fig.5.12(a)) indicates the retention of few elongated phase bands (indicated by arrow marks) along with regions where the lamellar structure is broken down locally by interpenetration of phases (marked by circles).

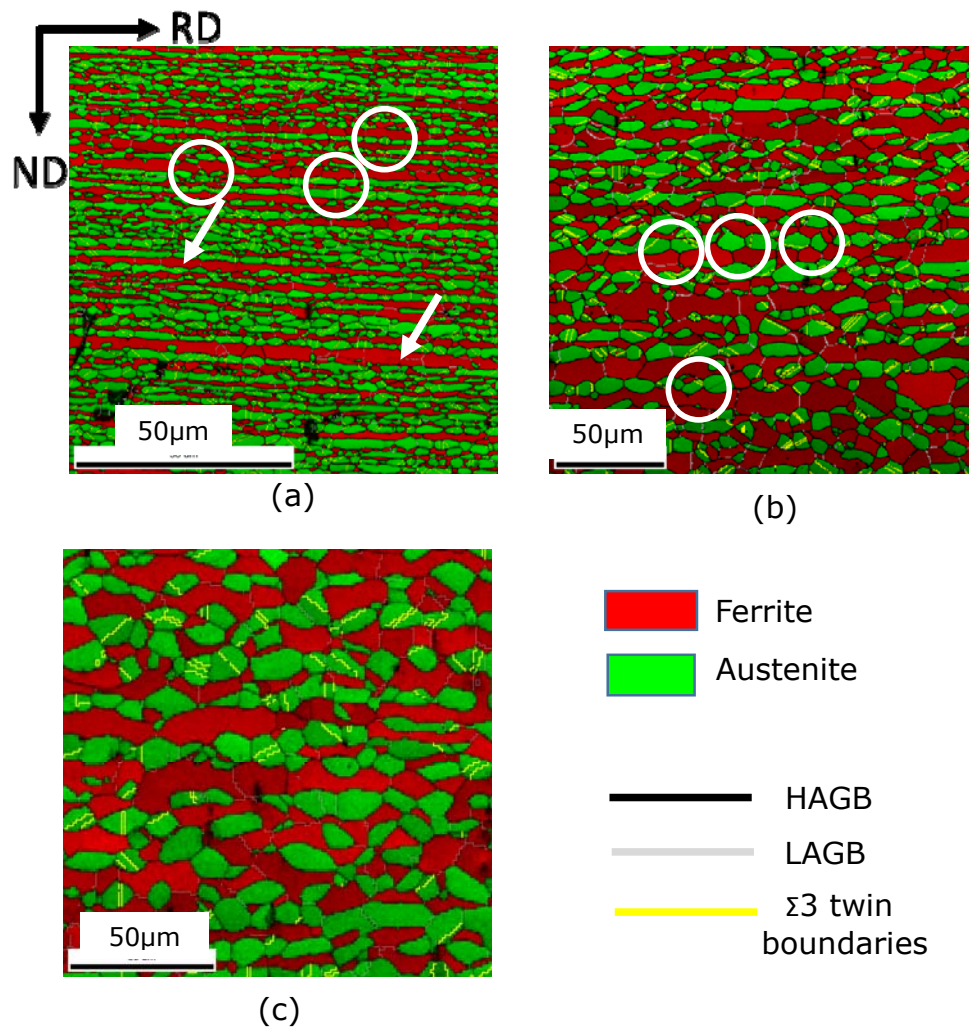


Fig.5.11: Phase maps of 95% warm-rolled DSS after isothermal annealing at 1448K (1175°C) for (a) 2, (b) 30 and (c) 120 minutes.

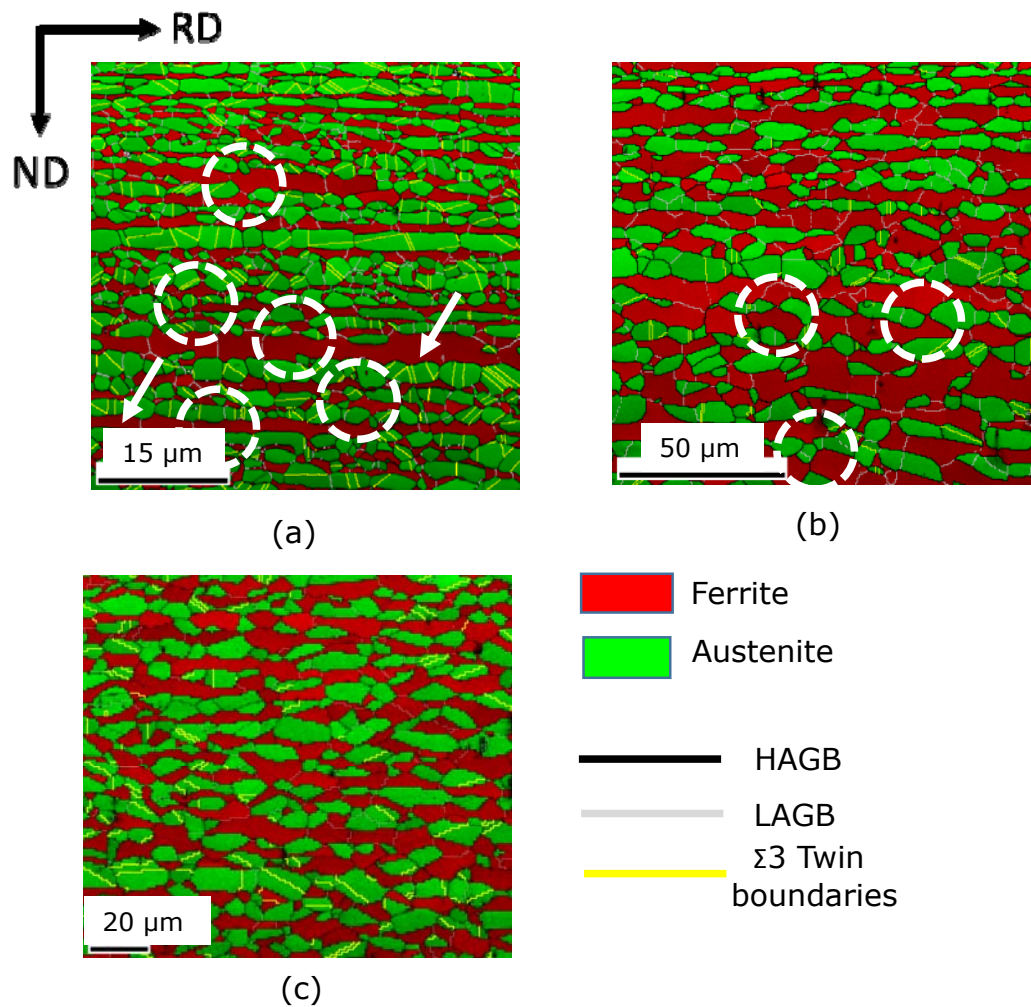


Fig.5.12: Phase maps of 98% warm-rolled DSS after isothermal annealing 1448K (1175°C) for (a) 2, (b) 30 and (c) 120 minutes.

The lamellar morphology is largely broken down after isothermal annealing for 30 minutes (Fig.5.12(b)). The fragmented microstructure continues to persist during further annealing for 120 minutes (Fig.5.12(c)).

It might be noted that the microstructural development during isothermal annealing of the DSS warm-rolled to 90% reduction in thickness at 898K (625°C) follows very similar pattern i.e. development of lamellar bamboo type morphology during annealing for short duration and gradual breakdown of the lamellar morphology with increasing isothermal holding time as already discussed in Chapter 4 (Fig. 4.29). Hence, the phase maps are not shown here separately.

The evolution of key microstructural parameters during isothermal annealing, such as HAGB spacing and aspect ratio is shown in Fig.5.13. HAGB spacing increases with increasing annealing time and upon annealing for 120 minutes the HAGB spacing of the two phases is observed to be quite similar $\sim 5 - 6 \mu\text{m}$ in 70%, 90% and 95% warm-rolled specimens ((Fig.5.13(a)) and Fig.5.13(b)). In the 98% warm-rolled specimen the HAGB spacing for both the phases is found to be slightly lower ($\sim 4 - 5 \mu\text{m}$) as compared to that in 70%, 90% and 95% warm-rolled DSS.

In order to demonstrate the effect of warm-rolling strain, the change in aspect ratio of austenite and ferrite in different warm-rolled DSS annealed for 2 minutes is shown in Fig.5.13(c). It is clearly observed that the aspect ratio of the two phases after annealing for 2 minutes is increased with increasing prior deformation. The aspect ratio of the ferrite, in particular, is found to be significantly higher in the 98% warm-rolled and annealed DSS as compared to that of ferrite in the 70% warm-rolled and annealed DSS.

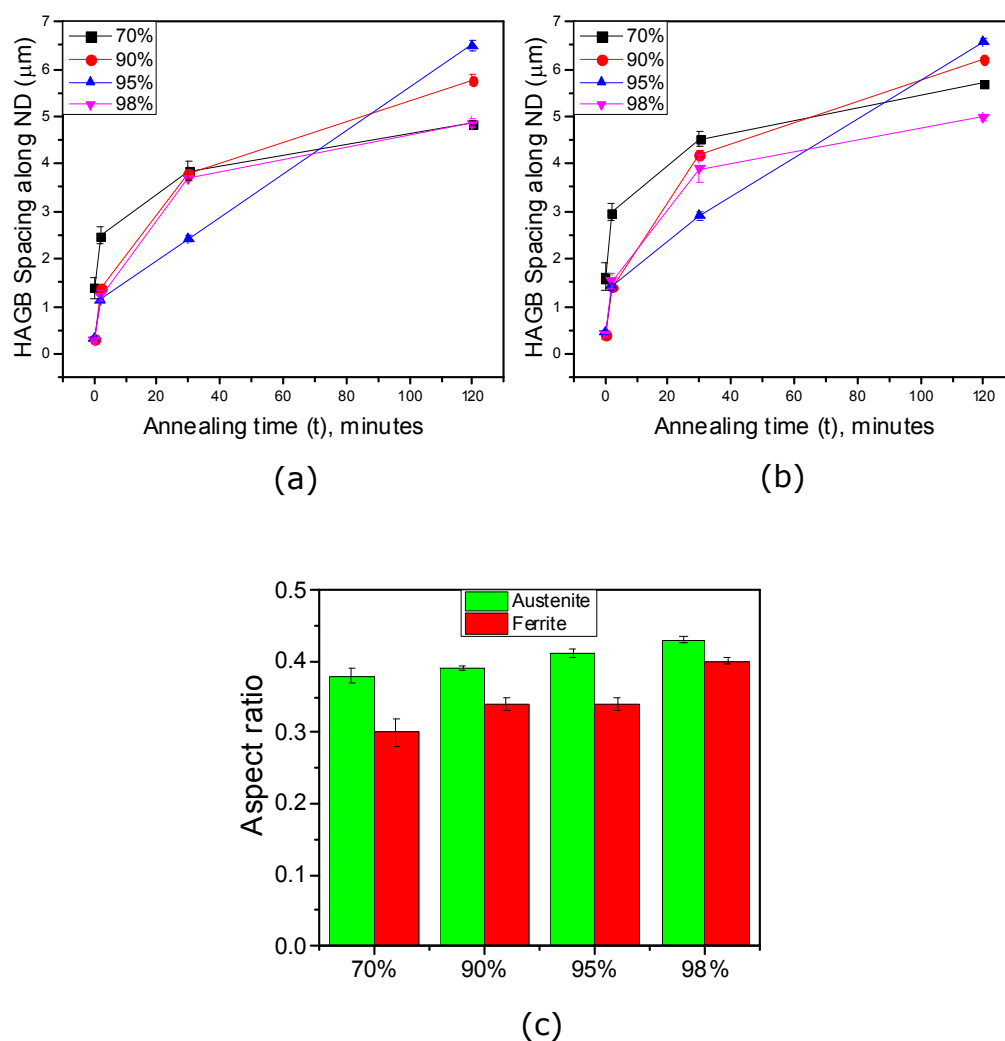


Fig.5.13: Variation of HAGB spacing in (a) austenite and (b) ferrite in DSS warm-rolled to different reduction in thickness and isothermally annealed at 1448K (1175°C). (c) shows the aspect ratio of the two phases in DSS warm-rolled to different reduction in thickness and annealed at 1448K (1175°C) for 2 minutes DSS.

5.3.2 Evolution of texture during annealing

Figure 5.14 shows the $\Phi_2=45^\circ$ sections of the ODFs of ferrite in 70% (Fig.5.14(a)-(d)), 90% (Fig.5.14(e)-(h)), 95% (Fig.5.14(i)-(l)) and 98% (Fig.5.14(m)-(p)) warm-rolled DSS following isothermal annealing treatment at 1448K (1175°C) for different time intervals. The ODF sections of 70% warm-rolled and isothermally annealed DSS specimens (Fig.5.14(a)-(d)) show the retention of the ND fiber present in the as warm-rolled material (Fig.5.5(a)). The intensity distribution of the contour lines further indicates the presence of stronger ND-fiber as compared to the RD-fiber. Presence of strong intensities around the $\{111\}\langle 110 \rangle$ and $\{111\}\langle 112 \rangle$ locations along the ND-fiber could be easily identified in the ODF sections. The evolution of the two texture fibers during isothermal annealing is shown quantitatively in Fig.5.15(a). It is clearly observed that ND-fiber is stronger than the RD-fiber in different isothermally annealed materials, although the strength of the ND-fiber is decreased significantly during isothermal annealing as compared to that in the warm-rolled condition.

The intensity distribution in the ODF sections of 90% (Fig.5.14(e)-(h)) and 95% (Fig.5.14(i)-(l)) warm-rolled and isothermally annealed DSS specimens shows the presence of much stronger RD-fiber as compared to the ND-fiber, which is also evident from the plots shown in Fig.5.15(b) and Fig.5.15(c) illustrating the evolution of the two texture fibers during isothermal annealing. The strongest component along the RD-fiber is the $\{001\}\langle 110 \rangle$ component.

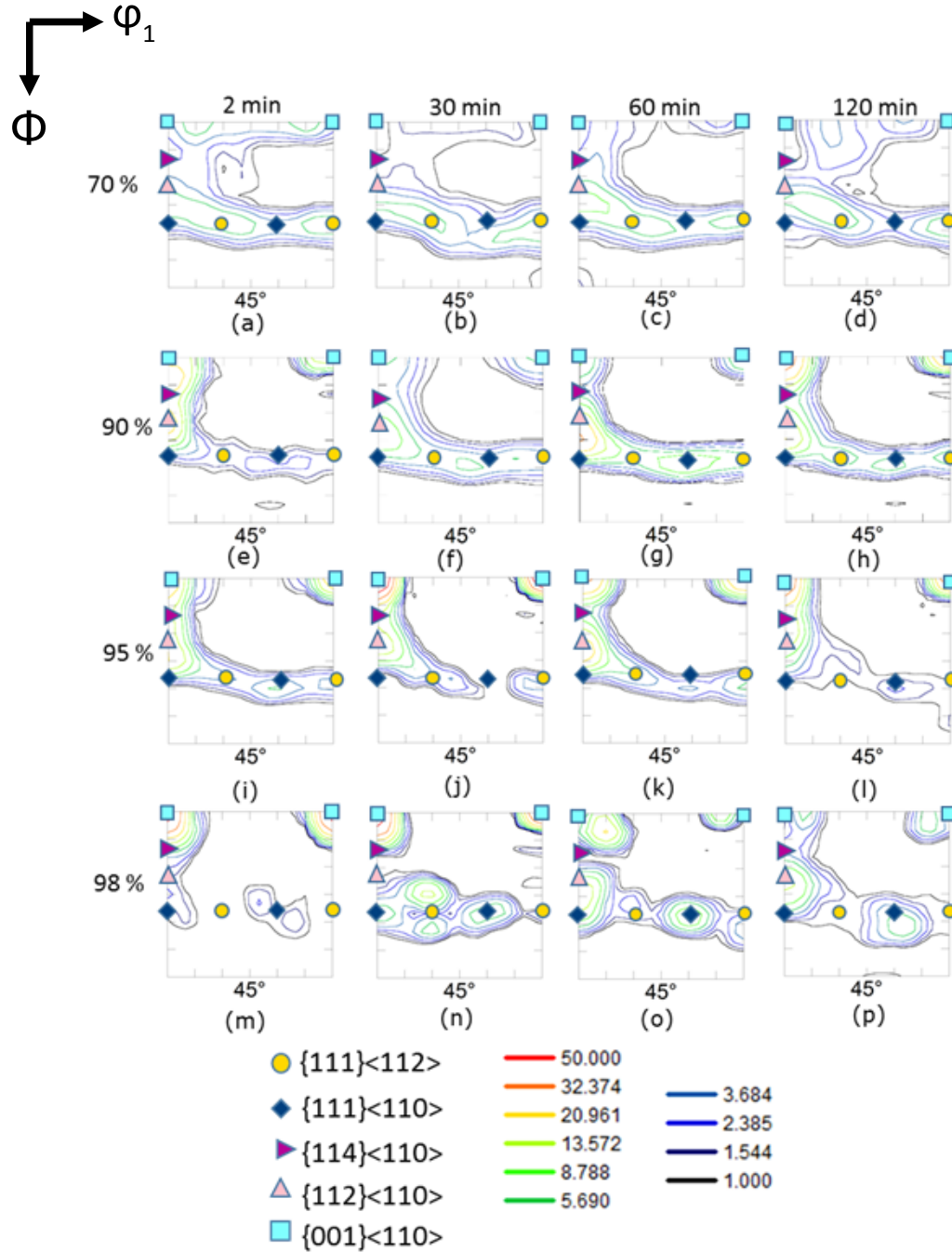


Fig.5.14: $\phi_2 = 45^\circ$ section of ODF of ferrite in DSS warm-rolled to ((a)-(d)) 70%, ((e)-(h)) 90% and ((i)-(l)) 95% and ((m)-(p)) 98% reduction in thickness and isothermally annealed at 1498K (1175°C) for 2, 30, 60 and 120 minutes.

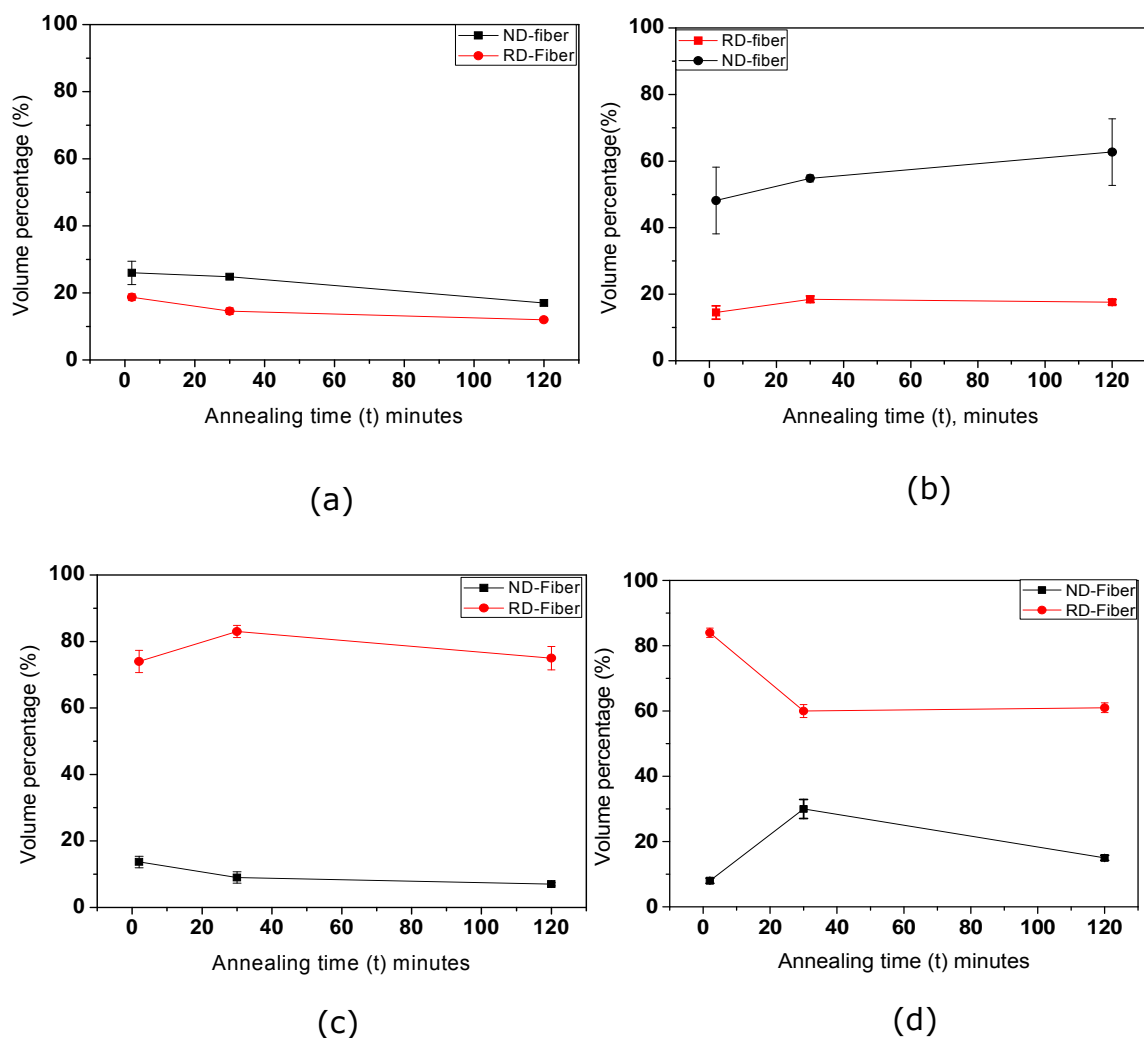


Fig.5.15: Variation in the volume fraction of RD and ND-fibers in ferrite in (a) 70%, (b) 90%, (c) 95% and (d) 98% warm-rolled DSS during isothermal annealing at 1448K (1175°C).

Stronger RD-fiber than ND-fiber is also observed during isothermal annealing of 98% warm-rolled DSS for 2 minutes (Fig.5.14(m)) and 30 minutes (Fig.5.14(n)). This is also clearly seen from the quantitative variation of the two texture fibers during isothermal annealing (Fig.5.15(d)). The RD-fiber is remarkably strengthened (volume fraction $\sim 84\%$) following isothermal annealing for 2 minutes. However, the strength of the RD-fiber is reduced during further annealing. The strongest component along the RD-fiber is $\{001\}\langle 110 \rangle$. However, $\{112\}\langle 110 \rangle$ component along the RD-fiber is strengthened while the $\{001\}\langle 110 \rangle$ component appears to be weakened in the specimens isothermally annealed for 60 (Fig.5.14(o)) and 120 (Fig.5.14(p)) minutes.

Figures 5.16((a)-(d)) show the (111) PFs of austenite in 70% warm-rolled and isothermally annealed DSS specimens. The PFs appear very similar amongst them and also resemble the PF of the as warm-rolled material (Fig.4.3(a)). This suggests the development of a pure metal type texture after different annealing treatments which is also supported by the presence of the S, Cu and B_S components in the respective ODF sections of austenite in 70% warm-rolled and isothermally annealed DSS specimens (Fig.5.17). The S component is found stronger as compared to the B_S and Cu components in austenite in 70% warm-rolled and isothermally annealed DSS specimens (Fig.5.21(a)).

The (111) PFs of austenite in 90% (Figures 5.16((e)-(h)) and 95% warm-rolled and isothermally annealed DSS specimens (Figures 5.16((i)-(l))) show the presence of pure metal type texture. This is quite clearly understood from the relevant ODF sections shown in Fig.5.18 and Fig.5.19. The evolution of texture components in austenite in 90% and 95% warm-rolled and isothermally annealed DSS is shown quantitatively in Fig.5.21(b) and Fig.5.21(c). It is clearly seen that the major component

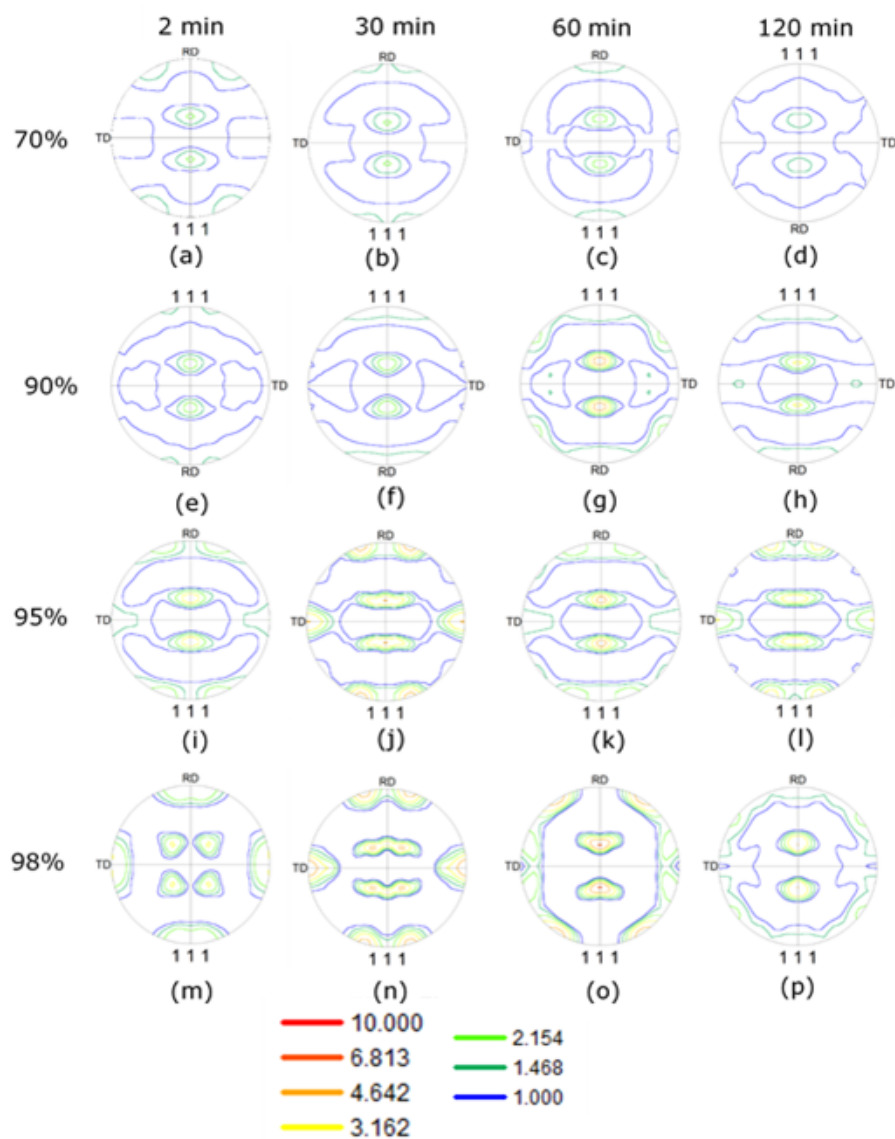


Fig.5.16: (111) PFs of austenite in DSS ((a)-(d)) 70%, ((e)-(h)) 90%, ((i)-(l)) 95% and ((m)-(p)) 98% warm-rolled and isothermally annealed at 1448K (1175°C) for 2, 30, 60 and 120 minutes.

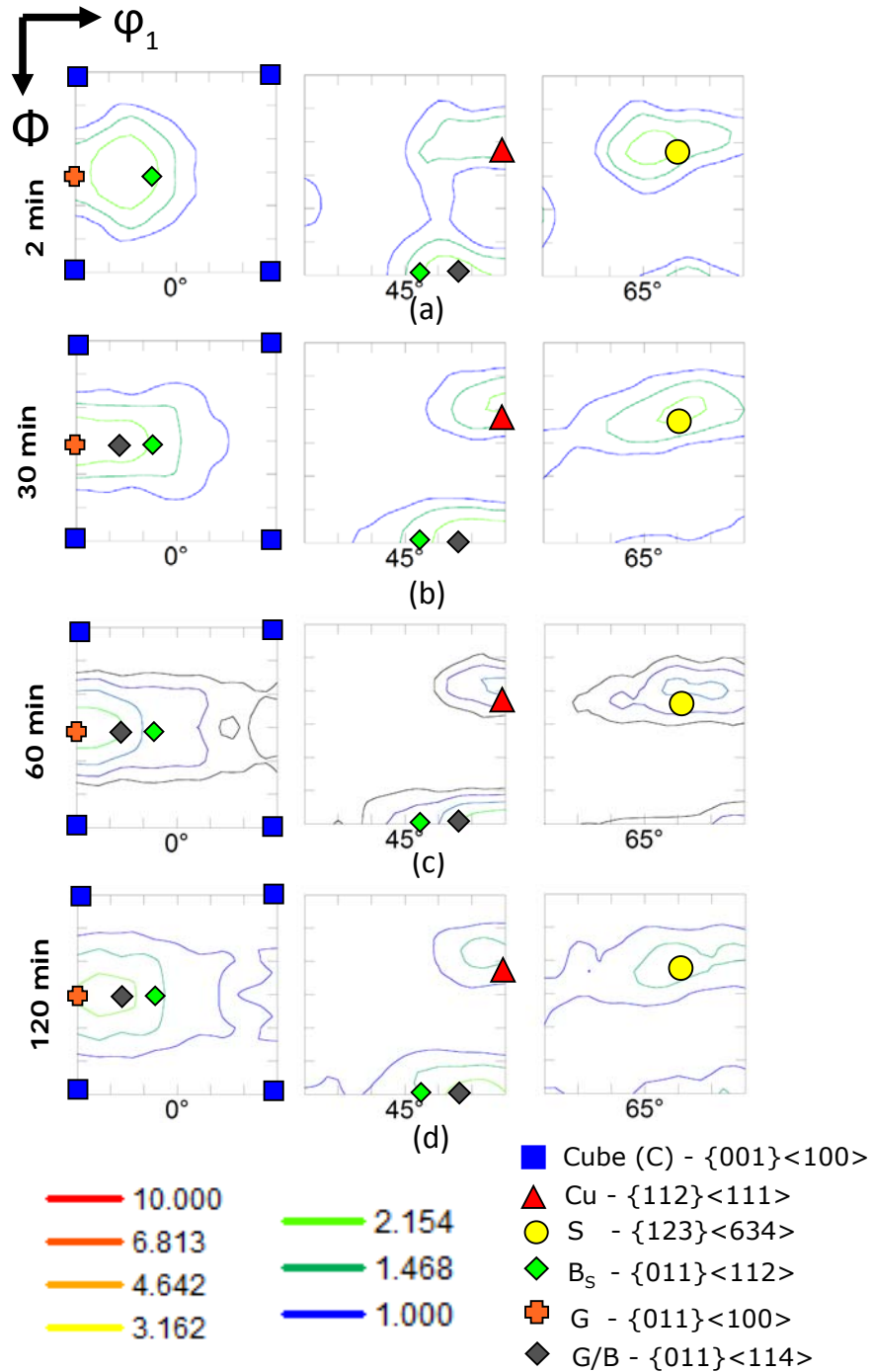


Fig.5.17: $\phi_2 = 0^\circ$, 45° and 65° sections of ODFs of austenite in DSS 70% warm-rolled and then isothermally annealed at 1448K (1175°C) for (a) 2, (b) 30, (c) 60, and (d) 120 minutes.

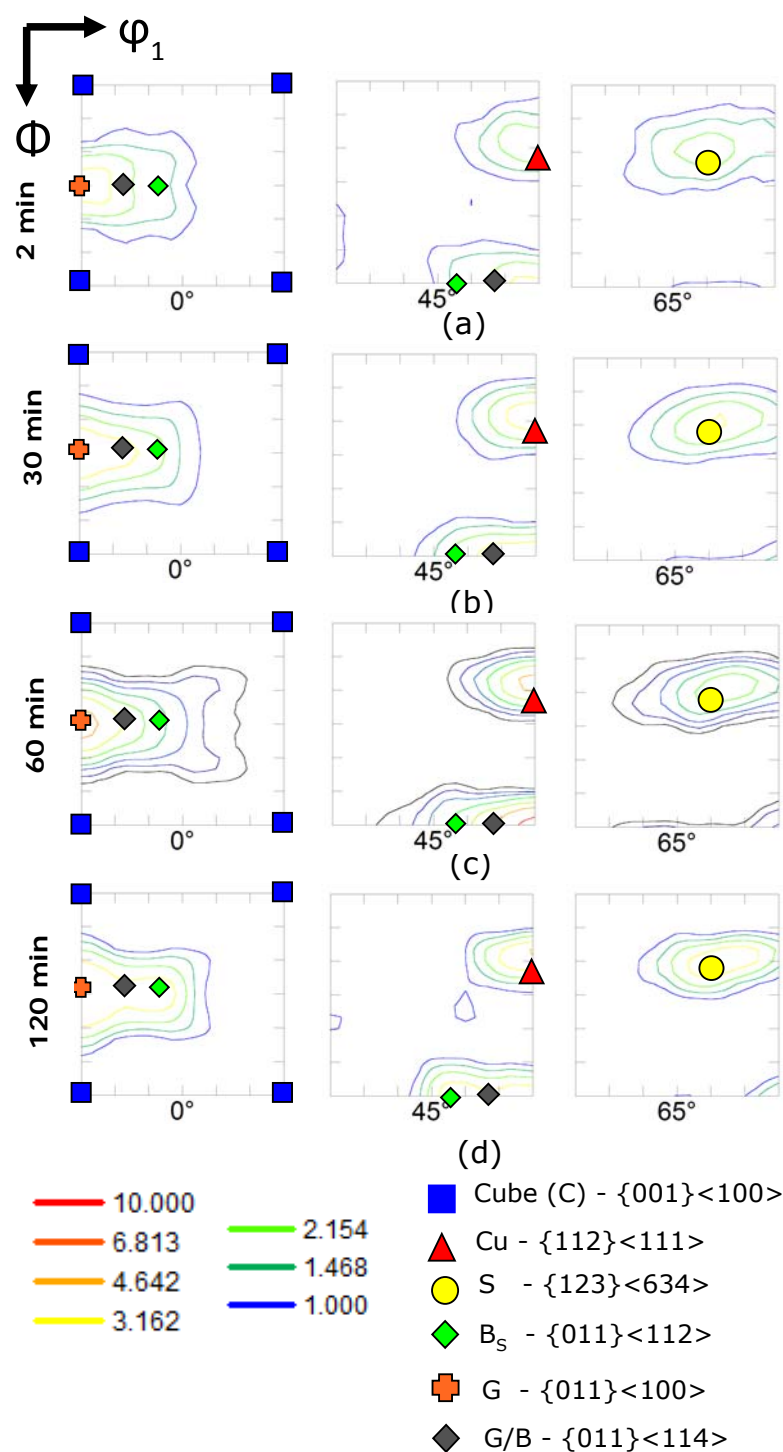


Fig.5.18: $\phi_2 = 0^\circ$, 45° and 65° sections of ODFs of austenite in DSS 90% warm-rolled and then isothermally annealed at 1448K (1175°C) for (a) 2, (b) 30, (c) 60, and (d) 120 minutes.

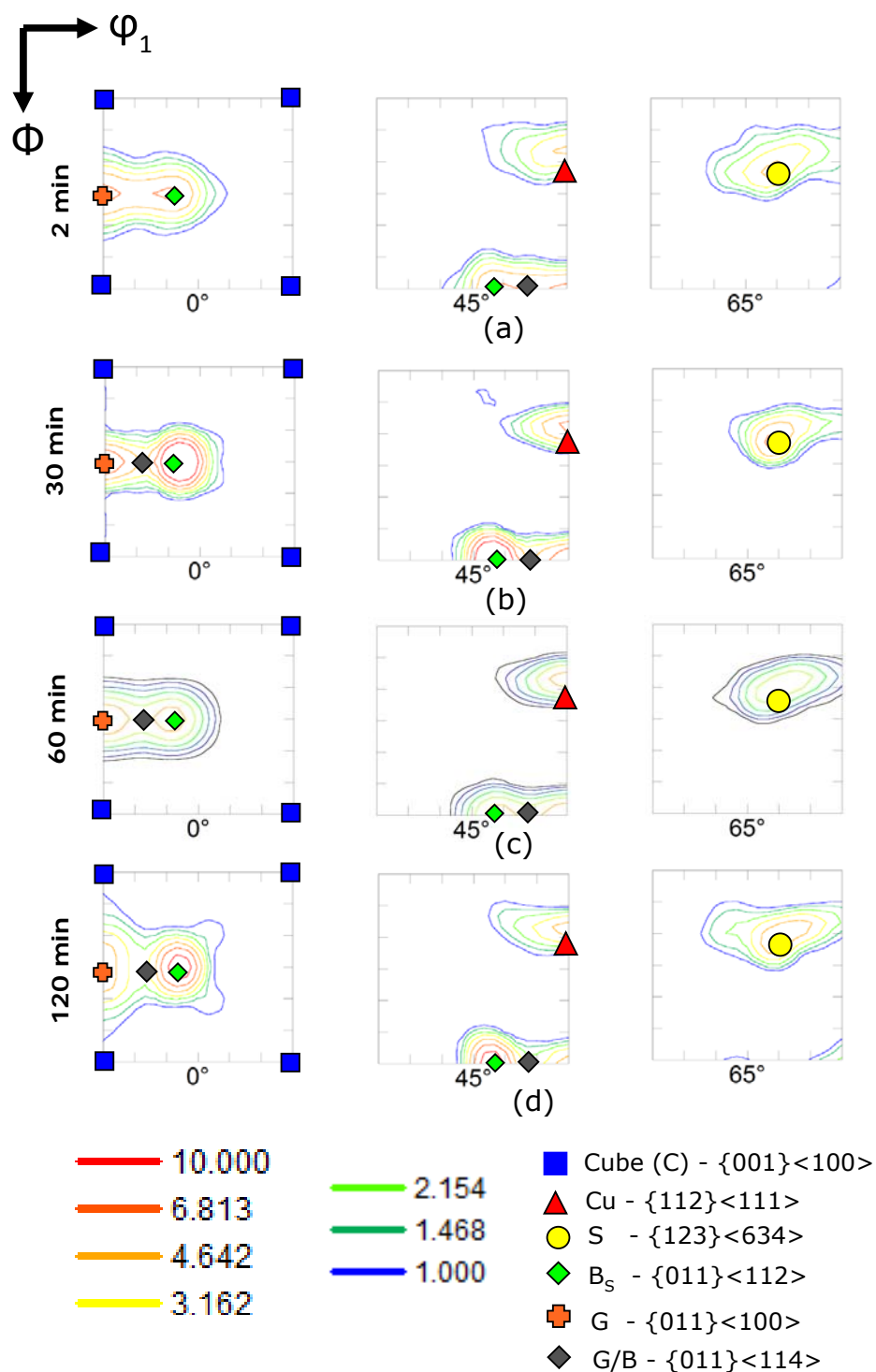


Fig.5.19: $\phi_2 = 0^\circ$, 45° and 65° sections of ODFs of austenite in DSS 95% warm-rolled and then isothermally annealed at 1448K (1175°C) for (a) 2, (b) 30, (c) 60, and (d) 120 minutes.

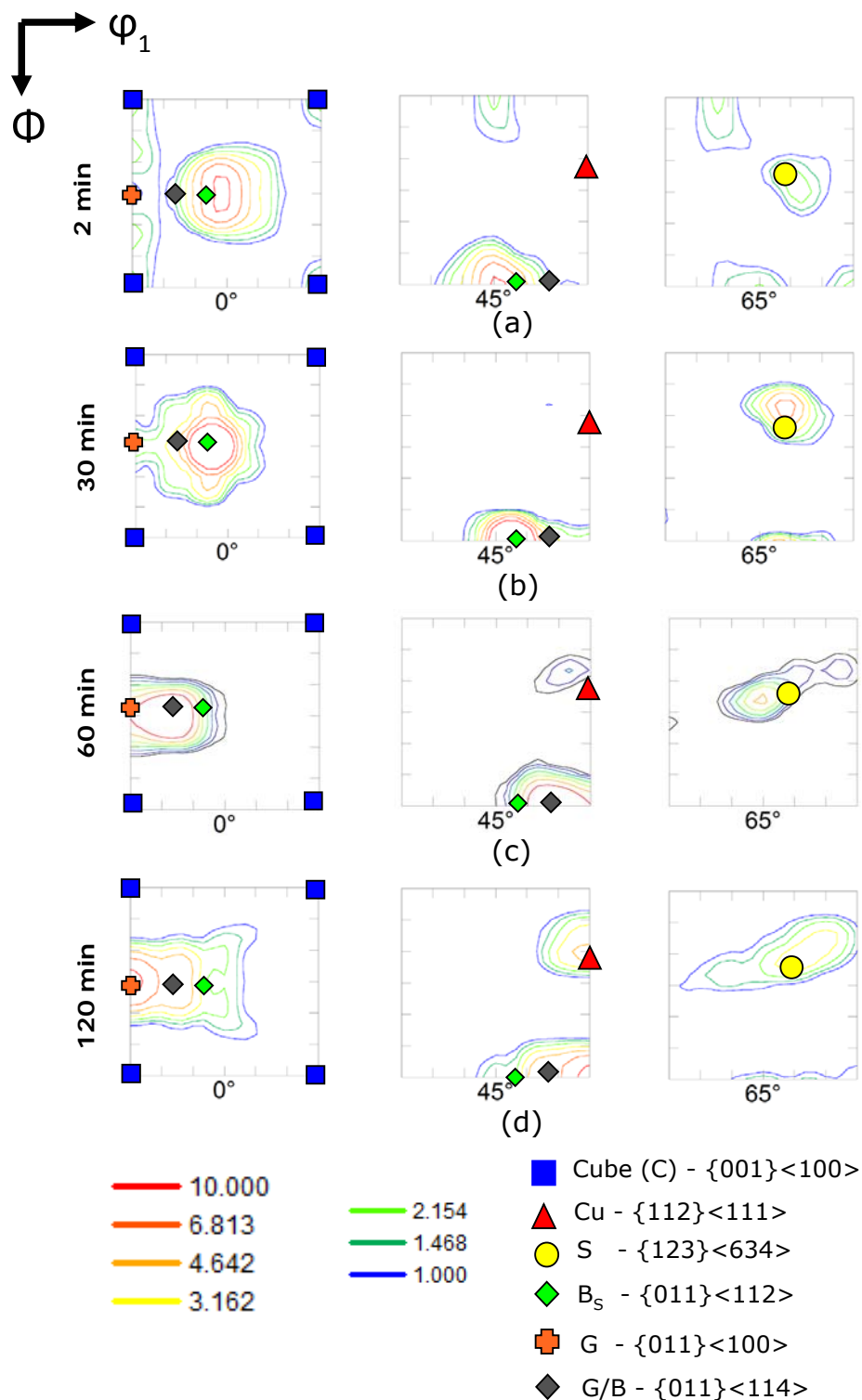


Fig.5.20: $\phi_2 = 0^\circ$, 45° and 65° sections of ODFs of austenite in DSS 98% warm-rolled and then isothermally annealed at 1448K (1175°C) for (a) 2, (b) 30, (c) 60, and (d) 120 minutes.

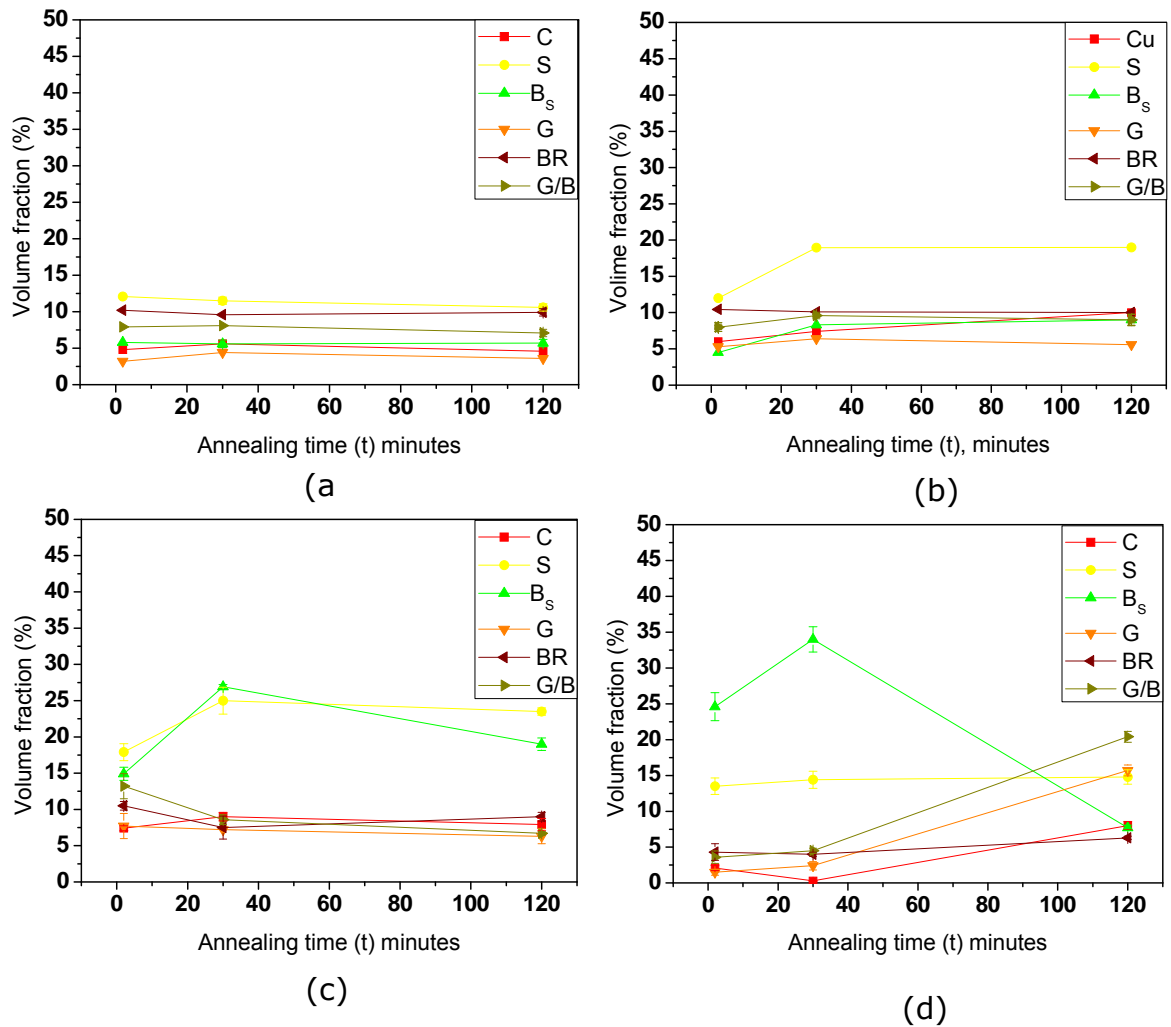


Fig.5.21: Variation of individual texture components in austenite (a) 70%, (b) 90%, (c) 95% and (d) 98% warm-rolled DSS during isothermal annealing at 1448K (1175°C).

annealing texture is the S component which amply corroborates the observations obtained from the PFs and ODFs.

The (111) PFs of austenite in 98% warm-rolled and isothermally annealed DSS specimens are shown in Figs.5.16((m)-(p)). The specimen annealed for 2 minutes (Fig.5.16(m)) shows the development of a strong B_s component which is also observed in the relevant ODF sections ($\phi_2=0^\circ$ and 45°) in Fig.5.20(a). The B_s component is further strengthened during isothermal annealing for 30 minutes, as may be clearly observed from the (111) PF (Fig.5.16(n)) and relevant ODF sections (Fig.5.20(b)). The B_s component is weakened during further isothermal annealing for 60 minutes (Fig.5.16(o)) and 120 (Fig.5.16(p)) minutes. The strongest component in the recrystallization texture of austenite in 98% warm-rolled DSS isothermally annealed for 60 minutes is shifted to an intermediate orientation $(110)[114]$ lying between the G and B_s (designated as G/B) along the α -fiber and is given by the set of Euler angles ($\phi_1, \Phi, \phi_2=20^\circ, 45^\circ, 0^\circ$). The location of this component is accordingly shown in the $\phi_2=0^\circ$ and 45° sections of the ODF of austenite in DSS isothermally annealed for 60 (Fig.5.20(c)) and 120 minutes (Fig.5.20(d)). The evolution of the texture components in austenite in 98% warm-rolled DSS during isothermal annealing is shown quantitatively in Fig.5.21(d). The strengthening of the G/B component is quite evident in austenite in 98% warm-rolled DSS during isothermal annealing beyond 60 minutes.

5.4 Evolution of mechanical properties during severe warm-rolling and isothermal annealing

Tensile tests are carried out selectively to reveal the effect of severe warm-rolling and annealing on the evolution of mechanical properties. For this purpose DSS severely warm-rolled beyond 90%

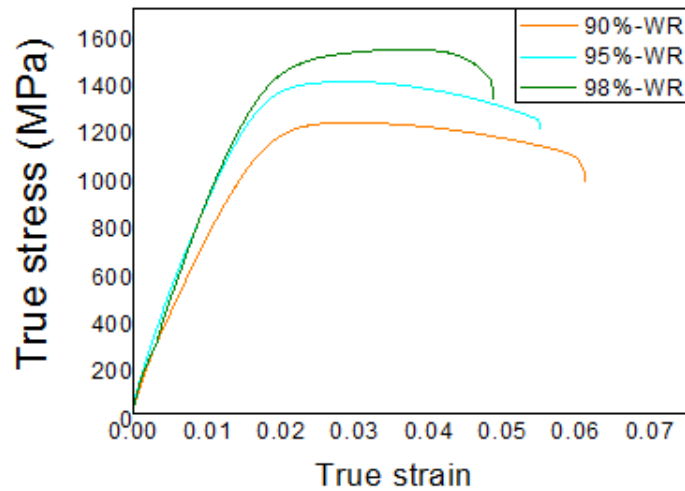


Fig.5.22: Comparison of True stress- True strain plots of severely warm-rolled DSS.

deformation and isothermally annealed for 2 minutes and 30 minutes are investigated. Figure 5.22 shows the comparison of tensile test results for 90%, 95% and 98% warm rolled DSS. The strength and elongation to failure (%) are summarized in Table 5.1. A significant increase in the ultimate tensile strength (UTS) is observed with increasing deformation. For the three severely warm-rolled materials the UTS are found to be greater than 1000 MPa i.e. in the ultrahigh strength regime. After 90%, 95% and 98% reduction the UTS values are ~ 1220 MPa, ~ 1380 MPa and 1525 MPa, respectively. However, the elongation to failure in all cases is less than 6%.

The effect of annealing on the strength and ductility of warm rolled material is shown in Figures 5.23, 5.24 and 5.25, respectively, for the 90%, 95% and 98% warm-rolled and annealed materials. Drastic decrease in strength, but significant increase in ductility is observed in all the three warm-rolled materials after annealing for 2 minutes. No significant change in strength or ductility is observed upon further isothermal annealing for 30 minutes.

5.5 Discussion

5.5.1 Evolution of microstructure and texture during severe warm-rolling

The stability of austenite in DSS during warm-rolling rules out any significant effect of phase change on the evolution of microstructure and texture. The development of lamellar ultrafine microstructure subdivided by deformation induced HAGBs in DSS after 90% warm-rolling indicates pronounced grain subdivision which is typically observed in heavily deformed metals and alloys [98]. The origin of the deformation induced HAGBs during the

Table 5.1: Summary of the mechanical properties of warm rolled and subsequently annealed material

WR (%)	0-minutes			2-minutes		30-minutes		
	YS (MPa)	Elongation to failure (%)	UTS (MPa)	YS (MPa)	Elongation to failure (%)	UTS (MPa)	YS (MPa)	Elongation to failure (%)
90	1140	6	1220	588	25	910	515	26
95	1320	5.5	1380	575	22	845	525	20
98	1390	5	1525	580	19	860	540	20.5
								805

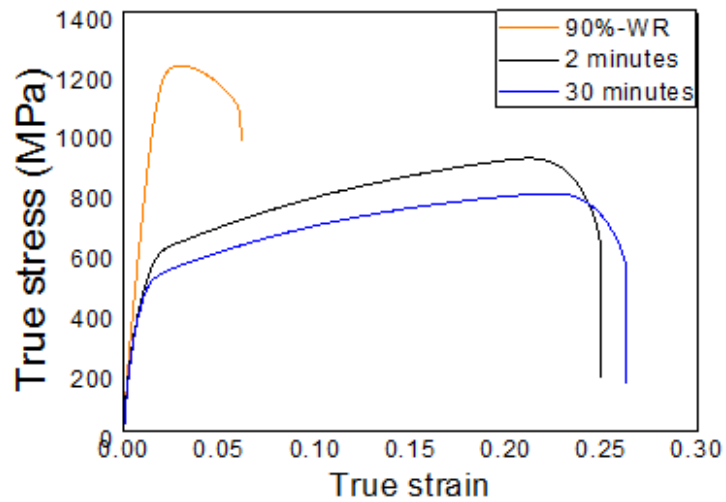


Fig.5.23: True stress - True strain plots of 90% warm-rolled and isothermally annealed DSS.

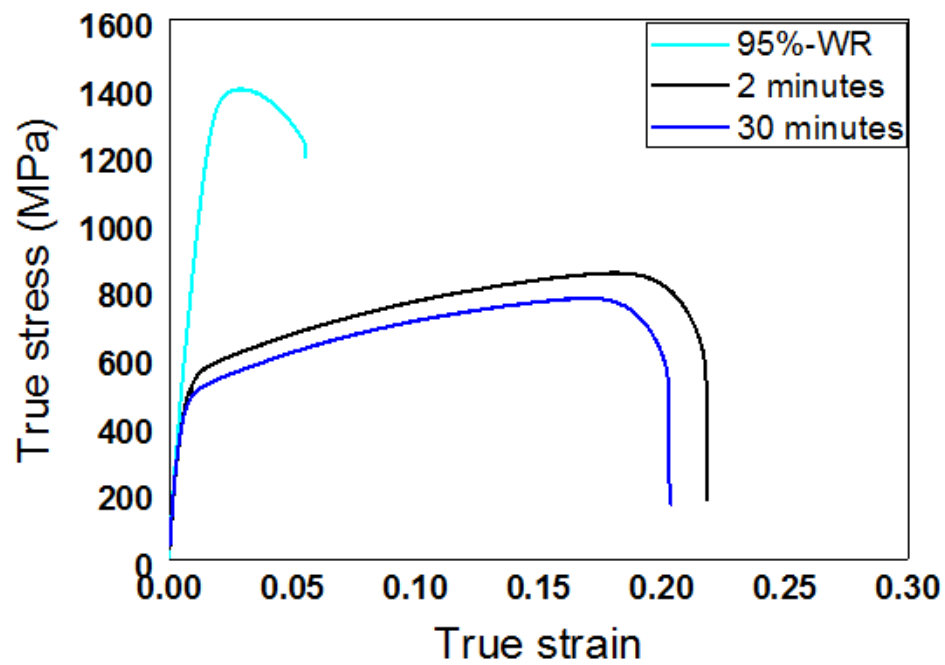


Fig.5.24: True stress - True strain plots of 95% warm-rolled and isothermally annealed DSS.

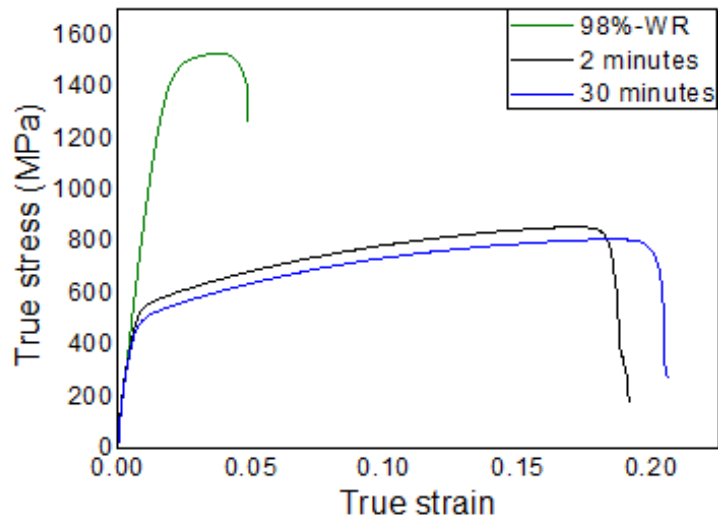


Fig.5.25: True stress - True strain plots of 98% warm-rolled and isothermally annealed DSS.

grain subdivision process is explained by different microstructural or textural mechanisms.

The microstructural mechanisms may involve evolution of cell block structure dominated by long boundaries (microbands and dense dislocation walls) and further increase in misorientation with increasing deformation due to accumulation of dislocations, formation of deformation heterogeneities such as shear bands which result in large orientation gradient in a small volume and coalescence of boundaries at large strains. The textural mechanisms on the other hand, involve relative rotation between different parts of a grain to different end orientations due to the difference in choice of slip systems [87].

However, there are certain differences in the grain subdivision process in the two phases. The most striking difference is that the average HAGB spacing of ferrite is not substantially reduced beyond 90% reduction while that of the austenite is decreased consistently up to the highest strain level i.e. up to 98% reduction in thickness (Fig.5.4). This indicates that a near saturation in ultrafine grain size is reached in ferrite in DSS within this strain regime, but additional grain refinement process must be operative in austenite in DSS.

The deformation texture of ferrite in warm-rolled DSS is dominated by the two well-known fibers and strongly resembles the texture of ferrite in cold-rolled DSS [66], cold and warm-rolled single phase ferrite. However, no fundamental change in deformation texture in ferrite is observed beyond 90% deformation (Fig.5.5((c)-(d)) and Fig.5.6) which appears to be consistent with the near saturation in the grain subdivision process in ferrite in this strain regime as revealed by the variation in HAGB spacing (Fig.5.4). This is consistent with the idea that a large change in HAGB fraction or grain refinement should also be accompanied by rapid evolution of texture.

It might be noted that the austenite in the present DSS during cold-rolling shows a strong texture transition from copper to predominantly brass type texture with increasing cold-rolling reduction typical of low stacking fault energy (SFE) materials [22]. This texture transition during cold-rolling occurs at a much lower deformation level i.e. even after 70% reduction (Fig.4.38). The texture transition during cold-rolling has been explained by the volume effect of deformation twins following a sequence of complex crystal rotation path involving twinning of the copper oriented grains to the Cu^T orientation ($\{552\}\langle 115 \rangle$), shear band formation and homogenous slip. Other researchers have negated the volume effect of in favor of the latent hardening effect of deformation twins. In any case the role of deformation twins in transition of texture from pure metal to brass type has been established [22]. In contrast to the prominent brass texture of austenite in cold-rolled DSS [11], the deformation texture of austenite in 70% and 90% warm-rolled DSS is a pure metal type (Fig.5.7((a),(b)) and Fig.5.8(a),(b)). Beyond this deformation level the gradual transition to brass type texture is evident (Fig.5.7((c)-(d)) and Fig.5.8((c)-(d)). It is, thus, amply clear that the onset of brass transition is effectively delayed during warm-rolling. This could be adequately explained by the increase in the SFE due to the increase in the deformation temperature so that deformation by slip is preferred over the formation of deformation twins. Very similar pattern of texture development during warm-rolling has been reported in other low SFE alloys. However, the strength of the B_s component is increased beyond 90% warm-rolling. The role of deformation twins in the course of this texture transition is amply made clear by the presence of the Cu^T component in the ODF sections of 95% and 98% deformed samples (Fig.5.8(c) and 5.8(d), respectively).

The possible origin of additional or continued grain refinement in austenite in DSS can be understood from the role of deformation TBs on grain refinement [99]. In low stacking fault energy (SFE) FCC materials deformation twinning is an important deformation mechanism in addition to dislocation slip. It is proposed that the deformation twin boundaries (TBs) are effective barriers to dislocation motion so that the glide dislocations are piled up against the TBs. The accumulation of dislocation at TBs increases the misorientation at the TBs finally converting the TBs into new random HAGBs resulting in further refinement of microstructure [99]. In the present case, although direct experimental support of the role of TBs on microstructural refinement could not be obtained due to the fine structure of TBs, support for the possible role of TBs in microstructure refinement in austenite of DSS is obtained from the pattern of texture evolution in the two phases as discussed below.

The propensity for the formation of deformation twins beyond 90% deformation is expected to be enhanced by the strain-hardening of austenite so that the flow stress is increased and the formation of deformation twins is once again favored even during warm-rolling. This results in the observed texture transition accompanied by the formation of TBs. Importantly, formation of deformation twins is particularly preferred in bulk ultrafine grained and nanostructured materials [100, 101]. It has been argued that Shockley partial dislocations can be emitted from non-equilibrium GBs in such ultrafine grained materials resulting in the nucleation of deformation twins. Since the grain size of austenite after 90% deformation is only $\sim 250\text{nm}$ i.e. well into the ultrafine regime, formation of deformation twins should be enhanced. The newly formed TBs should further enhance the grain refinement process in austenite as observed experimentally and the mechanisms have

been discussed already. The absence of such a mechanism in ferrite evidently results in no significant grain refinement beyond 90% reduction. Instead, mechanical fragmentation of ferrite regions readily occurs which is clearly seen in the phase maps of 95% (Fig.5.3(c)) and 98% (Fig.5.3(d)) warm-rolled DSS.

It may be noted that the evolution of the microstructure and texture in the two phases of DSS can be well explained from the knowledge of the behavior of the respective single phase materials, thus, significant effect of phase interaction during warm-rolling is ruled out. This agrees well with the behavior observed experimentally in cold-rolled DSS and amply corroborated by the simulation results [66]. The limited interaction between the two phases may be understood from the lamellar morphology with an alternate arrangement of the two phase bands developed during rolling. Major strain accommodation in this case should take place at the phase boundaries separating the two phases in the principal direction of working i.e. RD. However, since the majority of the phase boundaries is parallel to the sheet plane or RD (Fig.5.3) strong interaction is not expected. The two constituent phases should undergo deformation independent of one another, so that the evolution of deformation texture should follow the characteristics of the respective single phase materials.

5.5.2 Evolution of microstructure and texture during annealing

The microstructural evolution during isothermal annealing of severely warm-rolled DSS specimens shows the development of a lamellar morphology having an alternate arrangement of bands of the two constituent phases for the short holding duration. The lamellar morphology breaks down during further isothermal holding with the concurrent evolution of a more globular morphology.

The microstructural transformation during isothermal annealing of 90%, 95% and 98% warm-rolled specimens shows similar behavior. Therefore, a similar mechanism of microstructural evolution should be effective during isothermal annealing of these warm-rolled DSS series. As already explained in Chapter 4 the two phases of warm-rolled DSS during isothermal annealing show different softening behavior. Ferrite and austenite undergo recovery and discontinuous recrystallization, respectively. The growth of ferrite subgrains inside the ferrite bands ensures that the subgrains are separated by LAGBs after they impinge on the neighboring subgrains. The discontinuous recrystallization in austenite which is supported by the presence of annealing twins inside the austenite bands, results in the recrystallized austenite grains being separated by HAGBs after they impinge on each other. These processes result in the evolution of bamboo type morphology during short isothermal holding. The breakdown of the bamboo morphology during further isothermal holding is due to the mechanism of mutual interpenetration of the two phases along the triple points. Such regions are highlighted in the phase maps of 95% (Fig.5.11(b)) and 98% ((Fig.5.12(b)) warm-rolled specimens annealed for 30 minutes. These regions have already been observed and identified in the 90% warm-rolled DSS after annealing (Fig.4.15).

However, the microstructural transformation process is evidently slower in the 70% warm-rolled material. As a result the lamellar structure is more pronounced in 70% warm-rolled material after annealing for 2 minutes (Fig.5.10(a)) resulting in the aspect ratio of the two phases being lower than the corresponding values severely deformed material for e.g. the 98% warm-rolled and annealed DSS.

The slow structural evolution in the 70% warm-rolled DSS during isothermal annealing as compared to the other warm-rolled

conditions is quite interesting. The slower kinetics of microstructural transformation has also been observed in cold-rolled and annealed DSS [74] may be attributed to much finer deformation microstructure observed in DSS warm-rolled beyond 90% reduction in thickness which is understood from the HAGB spacing in the two phases (Fig.5.4). It may be noted that the process of microstructural transformation as outlined above is evidently controlled by diffusion. The much finer microstructure achieved during severe warm-rolling yields faster diffusion paths (i.e. grain boundaries and phase boundaries) and reduced diffusion length, resulting in faster microstructural evolution.

The evolution of texture in the two phases in severely warm-rolled and isothermally annealed DSS is affected by their characteristic softening processes. As already discussed, ferrite undergoes recovery while austenite undergoes discontinuous recrystallization. The recovery in ferrite results in the retention of the deformation texture components. This is clearly visible in the texture of ferrite in 70% warm-rolled DSS after different isothermal annealing treatments (Fig.5.14(a)-(d) and Fig.5.15(a)) which shows stronger ND-fiber as compared to the RD-fiber. This results from the stronger ND-fiber present in ferrite in the as warm-rolled condition (Fig.5.5(a)). With further deformation the RD-fiber in ferrite of DSS is strengthened (Fig.5.5(b)-(d)). This results in the presence of very similar texture characterized by stronger RD-fiber as compared to the ND-fiber in ferrite in 90% (Fig.5.14(e)-(h) and Fig.5.15(b)), 95% (Fig.5.14(i)-(l) and Fig.5.15(c)) and 98% (Fig.5.14(m)-(p) and Fig.5.15(d)) warm-rolled and isothermally annealed DSS.

The evolution of texture in austenite is affected by discontinuous recrystallization without preferential orientation selection as already explained in detail in Chapter 4. The pure metal type texture of

austenite 70%, 90% and 95% warm-rolled and isothermally annealed DSS results from the presence of predominant pure metal type texture of austenite in the as warm-rolled condition (Fig.5.7((a)-(c)) and Fig.5.8((a)-(c)). In contrast, austenite in DSS 98% warm-rolled and isothermally annealed for 2 and 30 minutes shows stronger B_s texture. This clearly results from the presence of stronger B_s component in austenite in 98% warm-rolled DSS. The increase in the intensity of the G/B component at the expense of the B_s component is attributed to the growth of this component during prolonged annealing.

5.6 Evolution of mechanical properties during severe warm-rolling and annealing

The significant increase in strength in DSS during warm-rolling is attributed to the formation of ultrafine structure. The increase in strength with increasing warm-rolling deformation is in conformity with typical strain-hardening behavior. However, the ultrahigh strength achieved during warm-rolling cannot be retained after annealing. The diminished strength of DSS after annealing appears to be due to the rapid removal of deformation structure due to annealing carried out at a rather high temperature. The significant difference in strength between the deformed and annealed materials can be explained by the fact that in the warm-rolled condition the strength is enhanced by the HAGBs and phase boundaries. However, the rapid removal of the deformation structure renders the phase boundaries as the main obstacles to dislocation motion.

It might be noted that in the case of brass significant enhancement in mechanical properties is achieved by controlled thermo-mechanical treatment involving precipitation of the second phase [7]. However, in the present work the annealing has been

carried purposefully at the temperature of homogenization to avoid significant effect of phase transformation. Therefore, it is envisaged that significant potential exists for tailoring the strength-ductility combination in DSS by warm-rolling and controlled annealing treatments. However, this is beyond the stated objectives and scope of the present work and should be a topic for further study.

-: CHAPTER 6 :-

***EFFECT OF CHANGE IN STRAIN PATH ON THE
EVOLUTION OF MICROSTRUCTURE AND TEXTURE
DURING WARM-ROLLING AND
RECRYSTALLIZATION***

6.1 Cross warm-rolling (CWR)

The effect of change in strain path during warm-rolling in DSS is investigated in this chapter. In order to achieve that cross warm-rolling (CWR) has been used. The experimental details of the CWR processing route are already given in Chapter 3. The CWR processing of DSS has been carried out at 898K (625°C) temperature. The selection of this specific temperature is due to the facts that at this temperature austenite remains stable and microstructure and texture evolution is not affected by dynamic strain aging as already clarified in chapter 4.

As already shown in the previous chapter, the two constituent phases in the present DSS behave independently of one another during straight or unidirectional warm-rolling (UWR). Thus, the microstructure and texture development in the two phases appears very similar to that of the respective single phase materials. However, processing by cross-rolling results in different microstructure and texture due to deformation along two different directions, as already demonstrated in single phase materials. This process should be particularly interesting in duplex alloys where the presence of the other phase can resist the structural adjustments and therefore affect the texture development. Thus, the major point of interest here is to clarify whether strain path change can affect the microstructure and texture development in DSS significantly.

The starting material for the CWR processing is the same homogenized DSS that has been used for UWR experiments (Fig.4.1). As a result the microstructure and texture of the starting material are not shown here separately.

6.2 Evolution of microstructure and texture during cross warm-rolling (CWR) of duplex stainless steel

6.2.1 Evolution of microstructure

Figure 6.1 shows the phase maps of cross warm rolled (CWR) material deformed to 18% ($\epsilon_{eq}=0.22$) (Fig.6.1(a)), 33% ($\epsilon_{eq}=0.46$) (Fig.6.1(b)), 45% ($\epsilon_{eq}=0.69$) (Fig.6.1(c)), 55% ($\epsilon_{eq}=0.92$) (Fig.6.1(d)), 63% ($\epsilon_{eq}=1.14$) (Fig.6.1(e)), 70% ($\epsilon_{eq}=1.19$) (Fig.6.1(f)), 75% ($\epsilon_{eq}=1.39$) (Fig.6.1(g)), 80% ($\epsilon_{eq}=1.85$) (Fig.6.1(h)), 84% ($\epsilon_{eq}=2.11$) (Fig.6.1(i)), 86% ($\epsilon_{eq}=2.27$) (Fig.6.1(j)) and 90% ($\epsilon_{eq}=2.65$) (Fig.6.1(k)) reduction in thickness. The RD indicated in Fig.6.1 is the current RD for each deformation stage.

The Austenite phase fraction is observed to vary from 45% to 55% during deformation and does not show significant difference with that in the starting homogenized DSS. The gradual evolution of lamellar morphology with an alternate arrangement of bands of the two phases is quite evident. Interestingly, at each deformation stage the deformed phase bands are found elongated parallel to the RD of that pass. Significant variation in thickness is observed from one end of a band to the other end. The phase maps also show locally sheared regions (indicated by dotted lines in Fig.6.1) distinguished by their characteristic wavy appearance.

The development of microstructure following CWR processing to 90% reduction in thickness is shown in Fig.6.2. The phase map (Fig.6.2(a)) after 90% CWR processing shows an elongated morphology along the RD with alternate arrangement of deformed bands of the two phases. The RD shown in the phase map is for the current pass which is parallel to the RD for the first pass, and in turn is parallel to the prior hot-rolling direction (Fig.3.4).

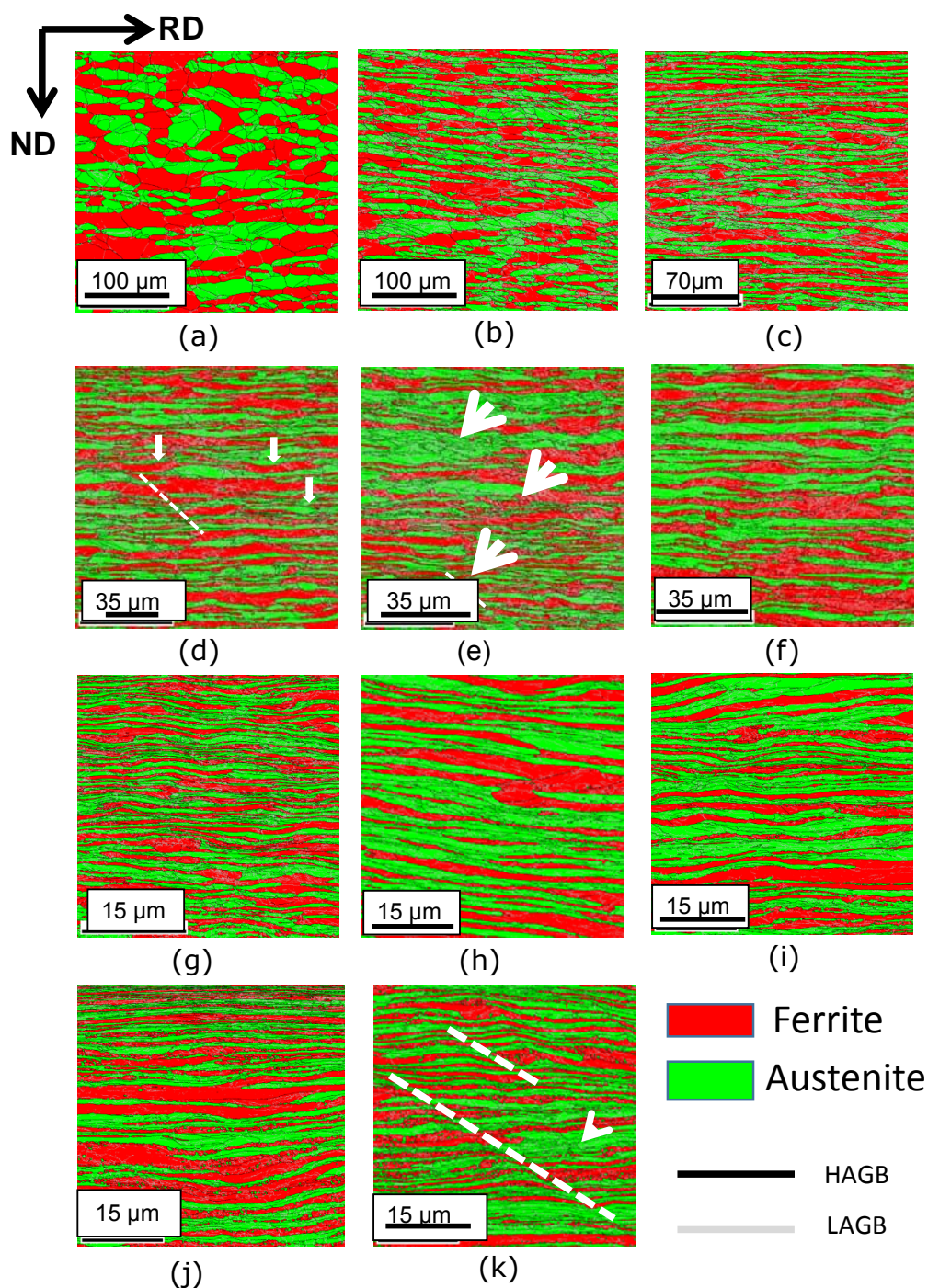


Fig.6.1: Phase maps of homogenized DSS processed by CWR at 898K (625°C) to (a) 18%, (b) 33%, (c) 45%, (d) 55%, (e) 63%, (f) 70% (g) 75%, (h) 80%, (i) 84%, (j) 86% and (k) 90% reduction in thickness.

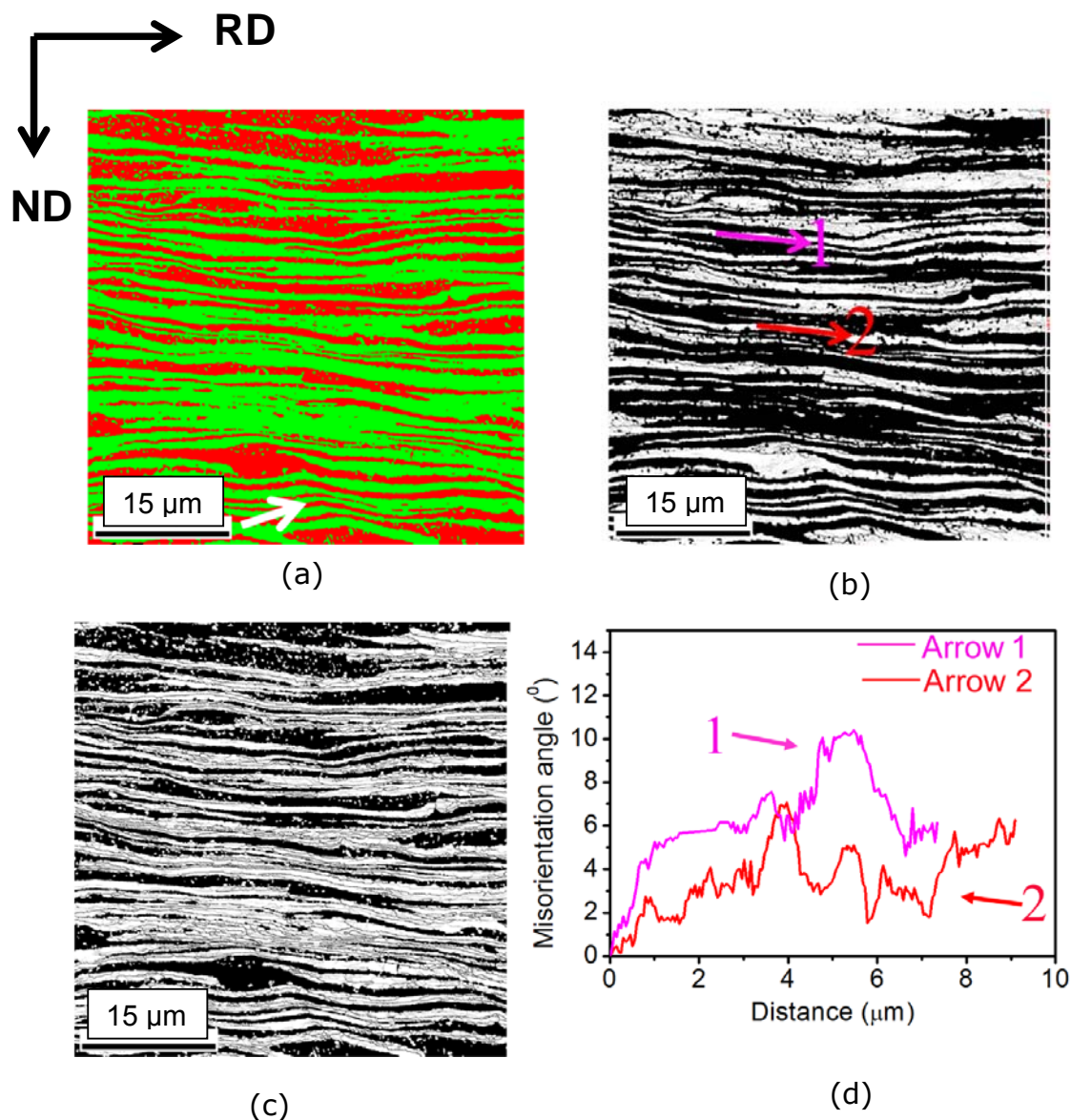
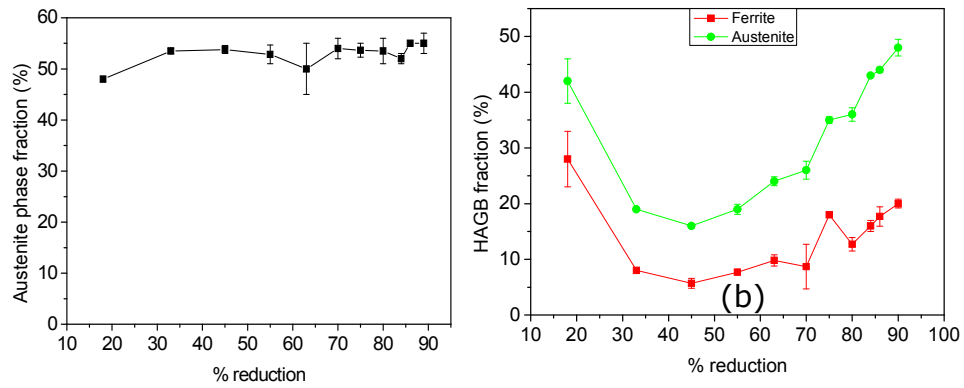


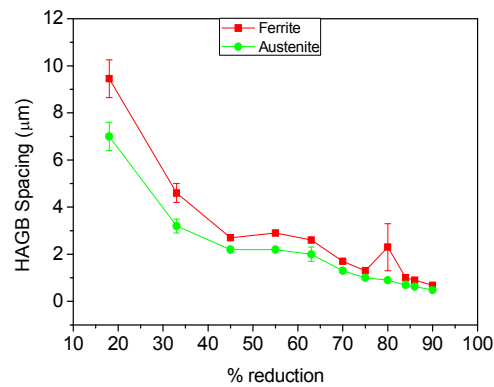
Fig.6.2: (a) shows the phase map, (b) and (c) show the GB maps of ferrite (austenite regions are masked) and austenite (ferrite regions are masked), respectively in the 90% CWR processed DSS, (d) shows the accumulated misorientation inside the ferrite bands along the arrow marks shown in (b).

It may be noted that structural rotation is observed throughout the CWR processing so that the microstructure appears elongated along the principal direction of working i.e. RD for the current pass. The phase map also shows the presence of wavy shear bands (indicated by arrow marks in the phase map in Fig.6.2 (a)) cutting through the phase bands. The phase band spacing of austenite ($\sim 0.74 \mu\text{m}$) and ferrite ($\sim 0.66 \mu\text{m}$) is comparable and close to the value expected from simple geometrical consideration of compression of phase bands with starting average thickness $\sim 6 \mu\text{m}$ in the homogenized starting material. Figure 6.2(b) and 6.2(c) show the GB maps of ferrite and austenite, respectively, in the 90% CWR processed material. The phase maps reveal the internal structure of the deformed phase bands. The presence of LAGB network (highlighted in gray) is noticed inside the deformed bands. The individual phase bands are further subdivided by HAGBs (highlighted in black). The typical accumulated misorientation inside the ferrite bands along the arrow marks 1 and 2 (i.e. misorientation between origin/starting point and any point along the arrow mark) in Fig.6.2(b) is shown in Fig. 6.2(d). It is clearly understood that the deformed ferrite bands usually have low accumulated misorientation.

Figure 6.3 shows the evolution of key microstructural parameters during CWR processing. The austenite phase fraction doesn't show any significant variation as compared to the starting homogenized material (Fig.6.3(a)). The austenite bands, however, consistently show much finer subdivision by HAGBs as compared to the ferrite bands during deformation. This results in a higher HAGB fraction ($\sim 50\%$) and lower HAGB spacing ($\sim 0.45 \mu\text{m}$) in austenite as compared to those in ferrite, $\sim 20\%$ and $0.66 \mu\text{m}$, respectively (Fig.6.3(b) and Fig.6.3(c)) after 90% CWR processing. Development



(a)



(c)

Fig.6.3: Variation of (a) phase fraction, (b) HAGB fraction and (c) HAGB spacing in DSS during processing by CWR.

of ultrafine lamellar structure is thus quite evident in both the phases after CWR processing.

6.2.2 Evolution of texture

The evolution of texture in ferrite in DSS during warm-rolling is shown in Fig. 6.4. The $\phi_2=45^\circ$ section of the ODF of ferrite (Fig.6.4(a)) shows very strong presence of the RD-fiber component $\{001\} \langle 110 \rangle$. Remarkably, the other components along the RD-fiber are virtually absent. The intensities of the contour lines reveal the presence of much weaker ND-fiber as compared to the RD-fiber component $\{001\} \langle 110 \rangle$. The orientation map of ferrite in 90% CWR processed DSS is shown in Fig.6.4(b). Figure 6.4(b) corresponds to the GB map of ferrite shown in Fig.6.2(b). Figure 6.4(b) also reveals much stronger RD-fiber (average fraction $\sim 54\%$) dominated by the $\{001\} \langle 110 \rangle$ component (highlighted in aqua in Fig.6.4(b); average fraction ($\sim 49\%$)). The fraction of ND-fiber is only $\sim 17\%$, which amply corroborates the qualitative information obtained from the ODF (Fig.6.4(a)). Figure 6.5(a) shows the (111) PF of austenite in the 90% CWR processed DSS. (111) PF showing the ideal locations of the texture components is shown in Fig.6.5(b). The appearance of the PF suggests the development of a predominantly brass (B_s) type texture. The $\phi_2=0^\circ$, 45° and 65° sections of the ODF of austenite in the 90% CWR processed DSS is shown in Fig.6.5(c). The $\phi_2=0^\circ$ section of the ODF of austenite further shows that the actual intensity maxima is shifted from the ideal brass or B_s ($\{110\} \langle 112 \rangle$) location ($35^\circ, 45^\circ, 0^\circ$) (indicated by green diamond) along the ϕ_1 to ($43^\circ, 45^\circ, 0^\circ$) location corresponding to the ND-rotated B_s orientation (B_s^{ND}) (011)[3-22] (indicated by olive circle). This shift in the B_s component is also quite evident in the $\phi_2=45^\circ$ section of the ODF. Consequently, the orientation map of austenite (Fig.6.5(d)) which corresponds to the GB map shown in Fig.6.2(c) shows that the $\{011\} \langle 322 \rangle$ (highlighted in olive in the orientation

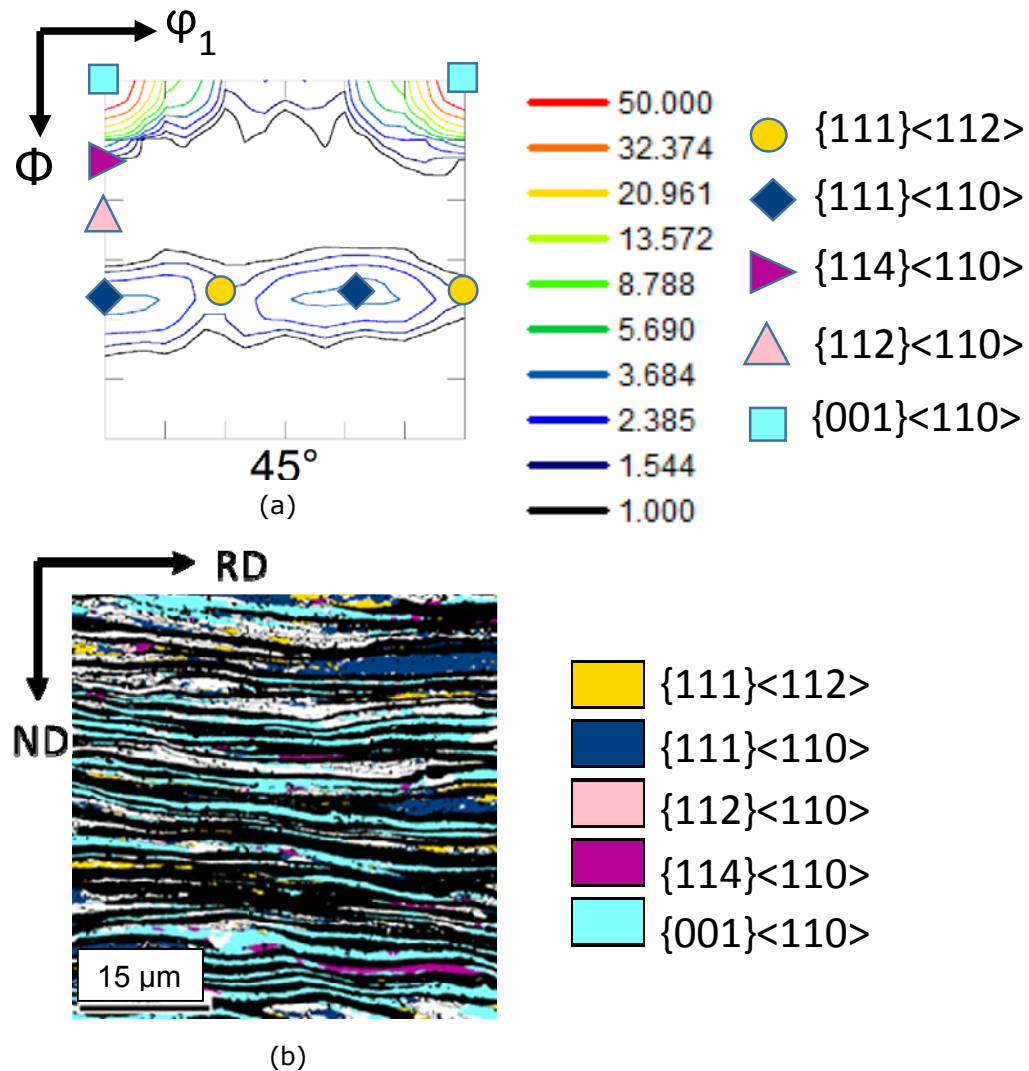


Fig.6.4: (a) shows the $\phi_2 = 45^\circ$ section and (b) shows the orientation map of ferrite (austenite regions are masked) in 90% CWR processed DSS.

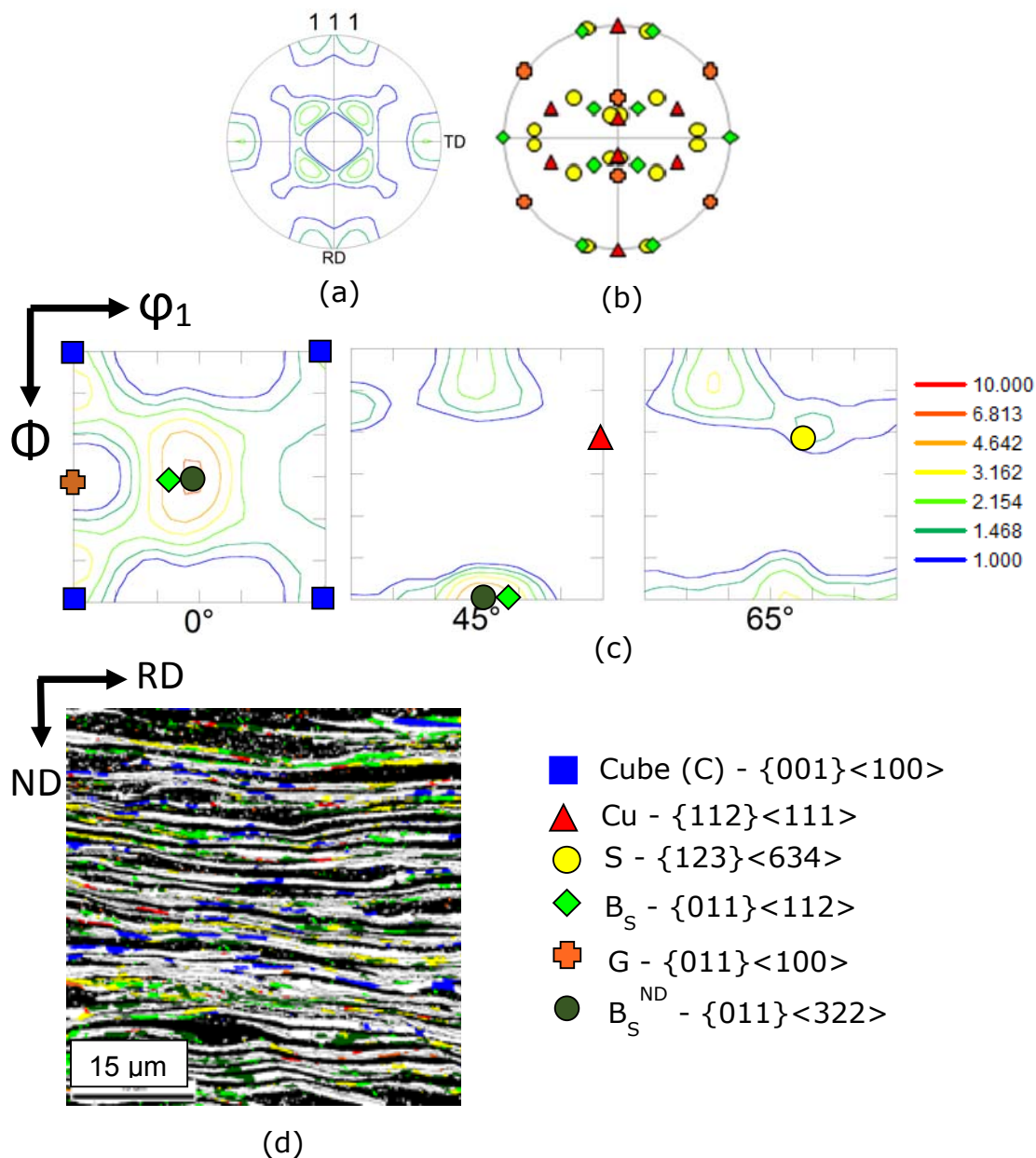


Fig.6.5: (a) shows the (111) PF of austenite in 90% CWR processed DSS and (b) shows the ideal locations of the components in the (111) PF. (c) shows the $\phi_2 = 0^\circ$, 45° and 65° sections and (d) shows the orientation map of austenite (ferrite regions are masked) in the 90% CWR processed DSS.

map in Fig.6.5(d)) is the strongest component having fraction $\sim 10\%$. The B_s (highlighted in green in Fig.6.5(d)) and S ($\{123\}\langle 634\rangle$; highlighted in yellow in Fig.6.5(d)) have very similar volume fractions, $\sim 6\%$ and 7% , respectively. The cube component (C) ($\{001\}\langle 100\rangle$; highlighted in blue in Fig.6.5(d)) shows noticeable presence having fraction $\sim 5\%$. Other components such as the copper or Cu ($\{112\}\langle 111\rangle$; highlighted in red in Fig.6.5(d); fraction $\sim 1.6\%$), and Goss or G ($\{110\}\langle 001\rangle$; highlighted in orange in Fig.6.5(d); $\sim 0.6\%$) are present in negligible proportions.

6.3 Evolution of microstructure and texture during annealing of CWR material

6.3.1 Evolution of microstructure during annealing

The 90% CWR processed DSS has been subjected to isothermal annealing treatment at 1448 K (1175°C). This allows comparison with the annealing behavior of the 90% UWR processed DSS (Section 4.8 in chapter 4) to clarify the effect of CWR processing on microstructure and texture development during annealing. As already clarified, the isothermal annealing temperature is purposefully kept same as that of the homogenization treatment to achieve equilibrium in the phase fraction.

Figure 6.6 shows the phase maps of the 90% CWR processed DSS following isothermal annealing for 2 minutes (Fig.6.6(a)), 30 minutes (Fig.6.6(b)), 60 minutes (Fig.6.6(c)) and 120 minutes (Fig.6.6(d)). The phase map after annealing for 2 minutes (Fig.6.6(a)) shows the presence of elongated ferrite bands extending parallel to the RD having length more than $50\text{ }\mu\text{m}$ (marked by arrow). Each phase band is one grain thick when measured along the ND.

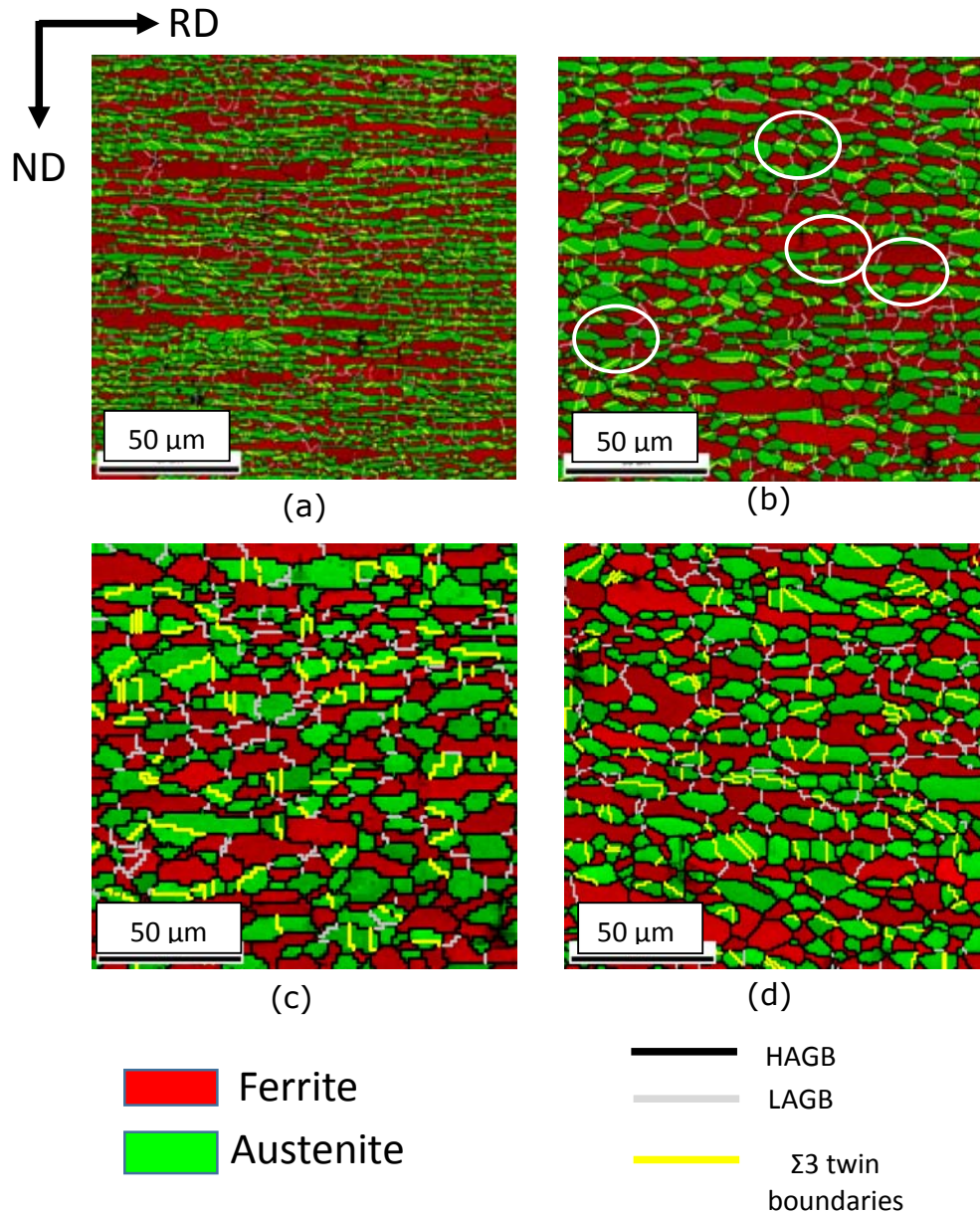


Fig.6.6: Phase maps of 90% CWR processed DSS isothermally annealed at 1448K (1175°C) for (a) 2 minutes, (b) 30 minutes, (c) 60 minutes and (d) 120 minutes.

The ferrite bands show LAGBs perpendicular or slightly inclined to the phase boundaries. In contrast, the austenite bands mostly show HAGBs perpendicular to the phase boundaries. Profuse annealing twin formation in austenite is evidence by the presence of the $\Sigma 3$ annealing twin boundaries (highlighted in yellow). Annealing for 30 minutes brings perceptible change in the microstructure (Fig.6.6(b)). The lamellar structure observed after annealing for 2 minutes (Fig.6.6(a)) is broken down and grains with more globular morphology are visible in the microstructure. The interpenetration of phases along the phase boundaries could be easily observed. Further isothermal annealing for 60 minutes (Fig.6.6(c)) and 120 minutes (Fig.6.6(d)) do not result in any significant change in the morphology of the two phases.

Figure 6.7 shows the evolution of key structural parameters during annealing. Slight decrease in the phase fraction is observed initially, but for the longer isothermal holding time a stable value of $\sim 50\%$ is achieved. The average grain thickness of the two phases measured along the ND increases with increasing temperature, but remains similar in the same annealed material (Fig.6.7(a)). The final average grain thickness for the two phases even after annealing for 120 minutes is only $\sim 6 \mu\text{m}$ which indicates very limited grain growth during annealing. Figure 6.7(b) shows the variation in aspect ratio with isothermal annealing time. It is clearly observed that for the two phases the fractional aspect ratio increases with increasing annealing time up to 60 minutes, which indicates the evolution of comparatively more globular morphology. Thereafter, the aspect ratio remains almost unchanged.

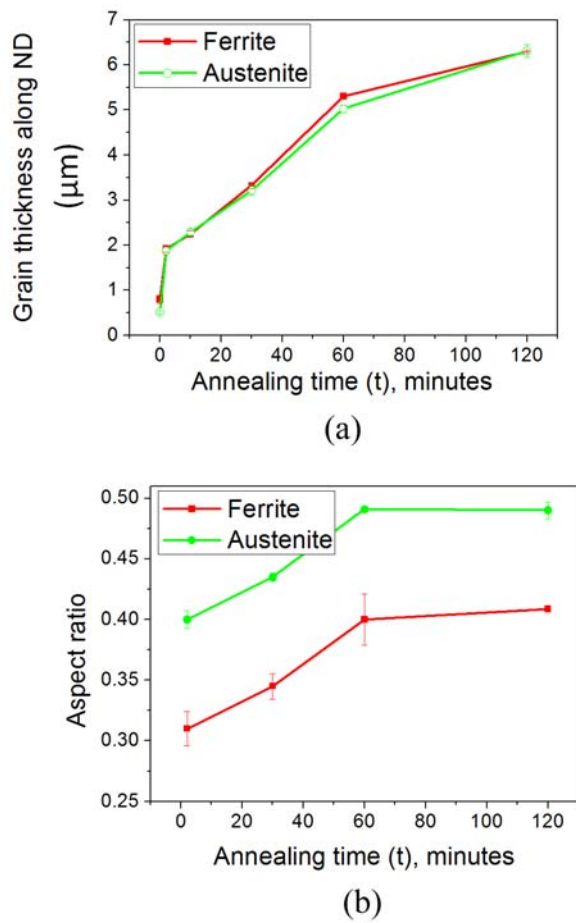


Fig.6.7: Variation of (a) grain thickness along ND and (b) aspect ratio of the two phases in 90% CWR processed DSS during isothermal annealing at 1448K (1175°C).

The aspect ratio of austenite consistently shows higher values as compared to ferrite. It might be noted that the microstructural observation of breakdown of the lamellar bamboo structure after isothermal annealing for 30 minutes with the concurrent evolution of more globular structure, but no significant change thereafter (Fig.6.6) is consistent with the variation in grain thickness (Fig.6.7(a)) and aspect ratio (Fig.6.7 (b)) during isothermal annealing.

6.3.2 Evolution of texture during annealing

The evolution of texture in ferrite of isothermally annealed DSS is shown in Fig.6.8. The appearance of the $\phi_2=45^\circ$ sections of the ODFs of ferrite in annealed DSS (Fig.6.8) greatly resembles that of the $\phi_2=45^\circ$ section of the ODF of ferrite in CWR processed DSS (Fig.6.4(a)) and thus clearly indicates the retention of a rather strong $\{001\}<110>$ RD-fiber component in different annealed conditions. The presence of other RD-fiber components in the ODFs of ferrite in isothermally annealed DSS is almost negligible (Fig.6.8). The ND-fiber, although present, is much weaker in comparison to the RD-fiber component $\{001\}<110>$.

The orientation maps depicting the spatial distribution of ferrite in annealed DSS are shown in Fig.6.9. The orientation maps shown in Fig.6.9 correspond to the phase maps shown in Fig.6.6 with the austenite regions masked in black. The orientation maps clearly reveal much higher volume fraction of the RD-fiber component $\{001\}<110>$ (highlighted in aqua in the orientation maps in Fig.6.9) in different isothermally annealed conditions amply corroborating the qualitative information obtained from the ODF. The quantitative analysis of variation of texture components with isothermal holding time (Fig.6.10) shows that the volume fraction RD-fiber component $\{001\}<110>$ increases with increase annealing

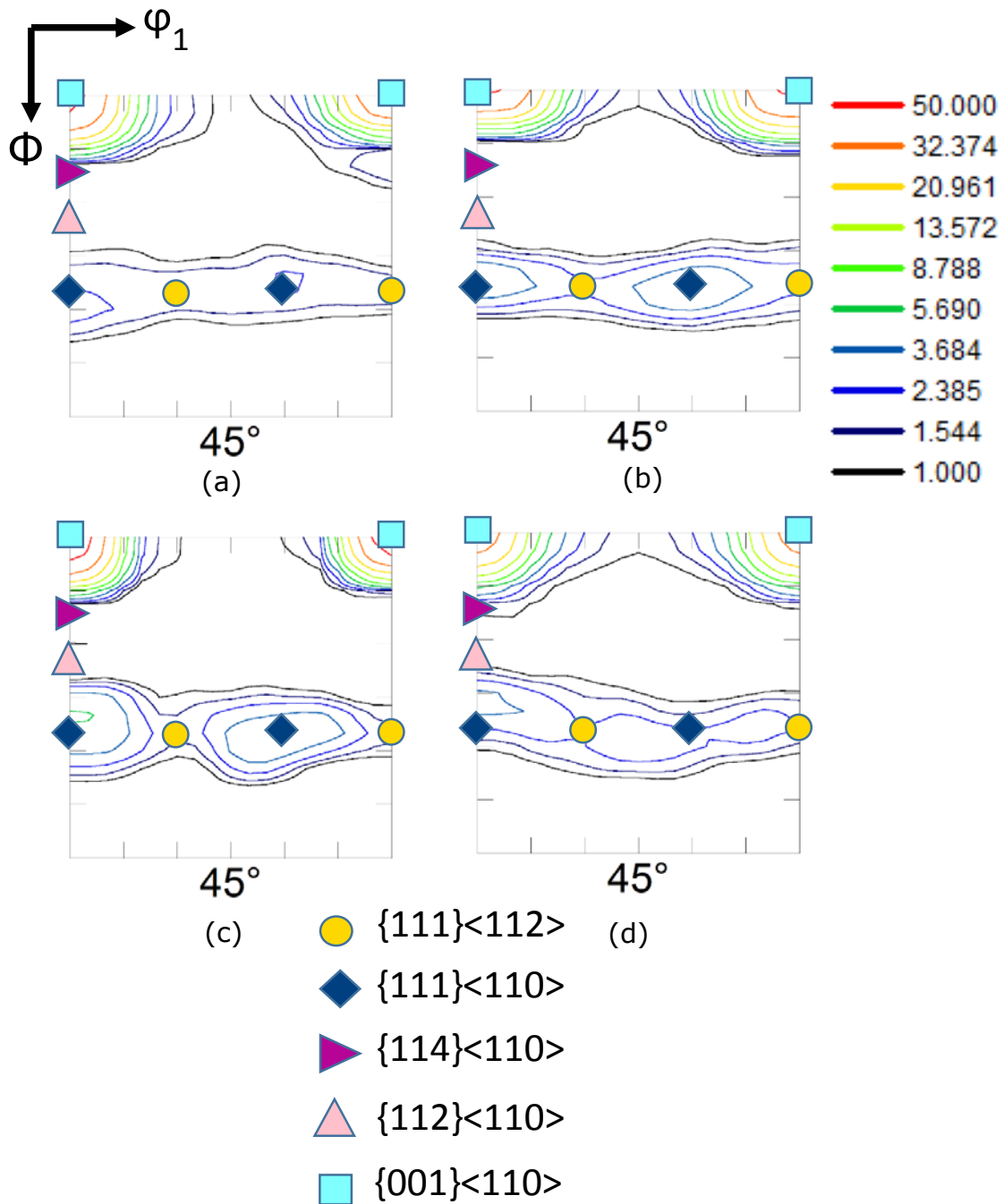


Fig.6.8: $\phi_2 = 45^\circ$ sections of ODFs of ferrite in 90% CWR processed DSS isothermally annealed at 1448K (1175°C) for (a) 2 minutes, (b) 30 minutes, (c) 60 minutes and (d) 120 minutes.

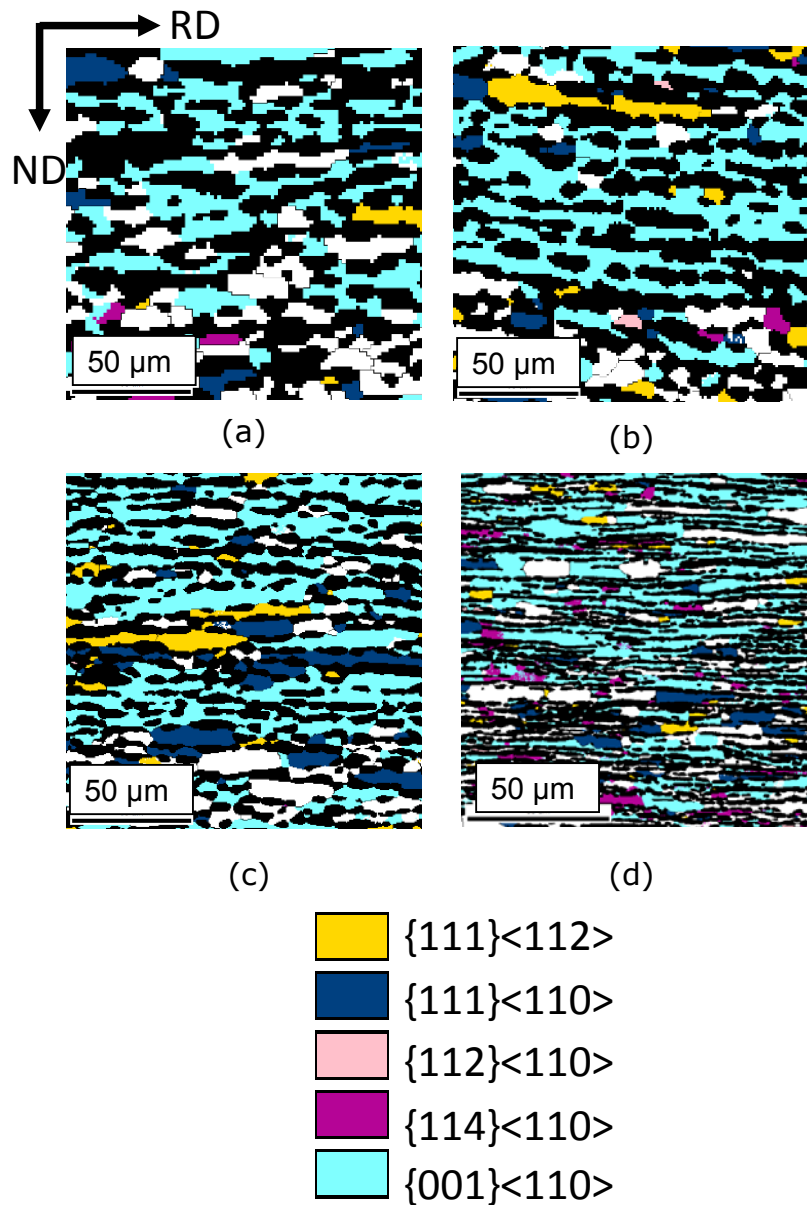


Fig.6.9: Orientation maps of ferrite (austenite regions are masked) in 90% CWR processed DSS isothermally annealed at 1448K (1175°C) for (a) 2 minutes, (b) 30 minutes, (c) 60 minutes and (d) 120 minutes.

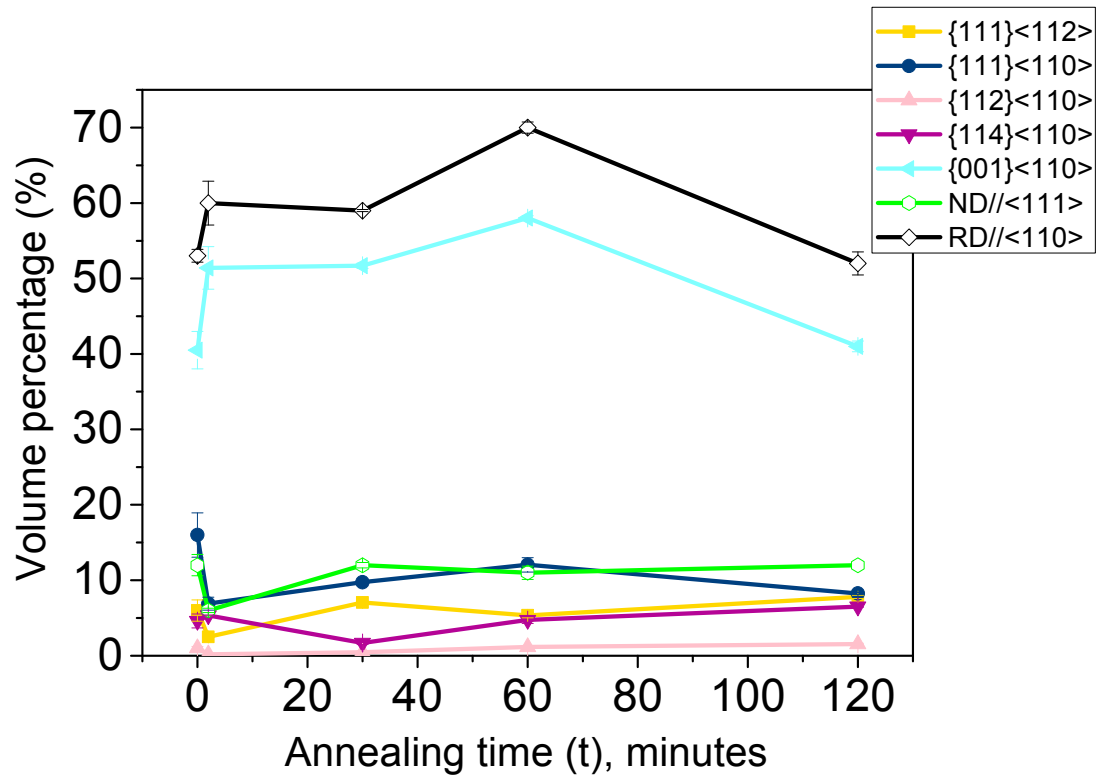


Fig.6.10: Variation of volume fraction of texture components in ferrite in 90% CWR processed DSS during isothermal annealing at 1448K (1175°C).

time up to 30 minutes (volume fraction of $\sim 70\%$) but decreases beyond that, although, shows a high volume fraction $\sim 50\%$. These observations are consistent with the decrease in intensity at the vicinity of the $\{001\}\langle 110 \rangle$ orientation in the ODF of ferrite in DSS annealed for 120 minutes (Fig.6.8(d)) and appearance of regions with random orientations (white regions in the orientation map (Fig.6.9(d))).

The appearance of the (111) pole figures of austenite in different isothermally annealed DSS samples (Fig.6.11) closely resembles that of the austenite in the CWR processed DSS (Fig.6.5(a)) and thus indicates the retention of deformation texture even after annealing. The $\phi_2=0^\circ$, 45° and 65° sections of austenite in different annealed DSS specimens is shown in Fig.6.12 which also supports the PF observations.

The spatial distribution of texture components in austenite in annealed DSS samples is shown in Fig.6.13. The orientation maps in Fig.6.13 correspond to the phase maps shown in Fig.6.7 with the ferrite regions masked in black. The orientation maps clearly reveal the presence of much stronger B_s^{ND} component (highlighted in olive) in different annealed conditions as compared to the B_s (highlighted in green) and S (highlighted in yellow) components. The quantitative analysis of texture components in austenite in different isothermally annealed conditions is given in Fig.6.14. Figure 6.14 shows that the fraction of the B_s^{ND} increases to $\sim 25\%$ after annealing for 30 minutes, but does not show significant change during further annealing. Other texture components, including Cu (highlighted in red), G (highlighted in orange) and twin of the G (G^T ; $\{11\ 11\ 8\} \langle 4\ 4\ -11 \rangle$; highlighted in pink) show only a weak presence as may be evident from the orientation maps (Fig.6.13) and the texture components plot (Fig.6.14).

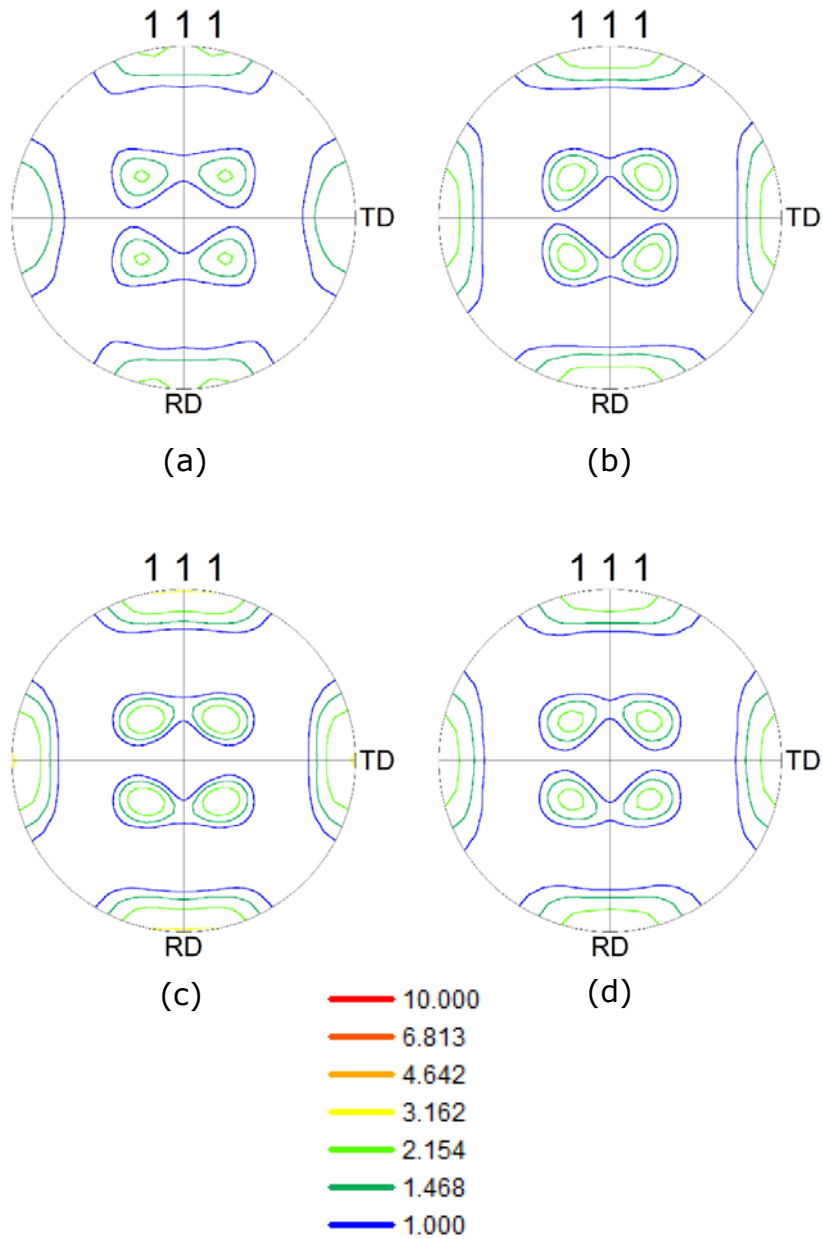


Fig.6.11: (111) PFs of austenite in 90% CWR processed DSS isothermally annealed at 1448K (1175°C) for (a) 2 minutes, (b) 30 minutes, (c) 60 minutes and (d) 120 minutes.

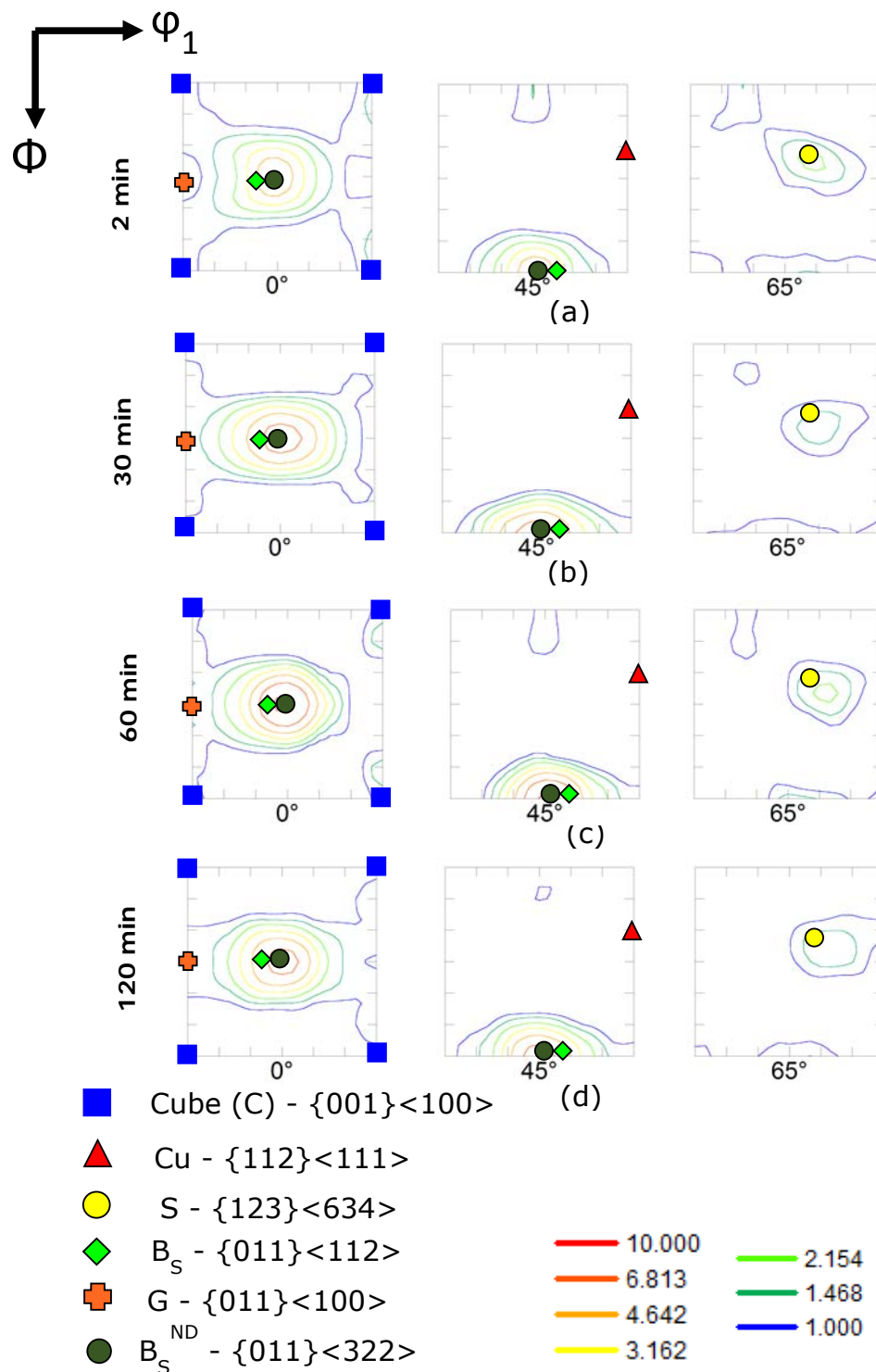


Fig.6.12: $\phi_2 = 0^\circ$, 45° and 65° sections of the ODFs of austenite in 90% CWR processed DSS isothermally annealed at 1448K (1175°C) for (a) 2 minutes, (b) 30 minutes, (c) 60 minutes and (d) 120 minutes.

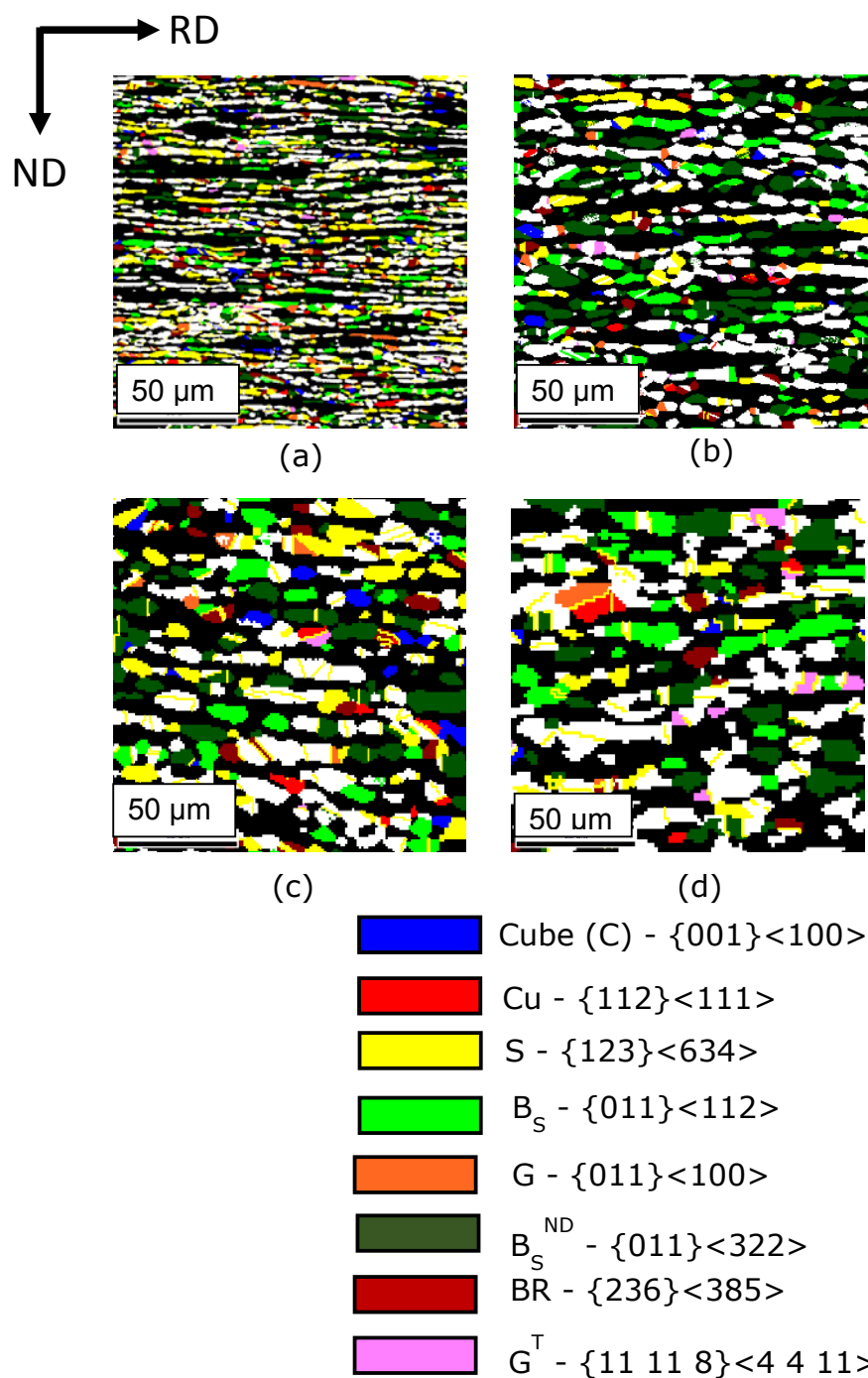


Fig.6.13: Orientation maps of austenite (ferrite regions are masked) in 90% CWR processed DSS isothermally annealed at 1448K (1175°C) for (a) 2 minutes, (b) 30 minutes, (c) 60 minutes and (d) 120 minutes.

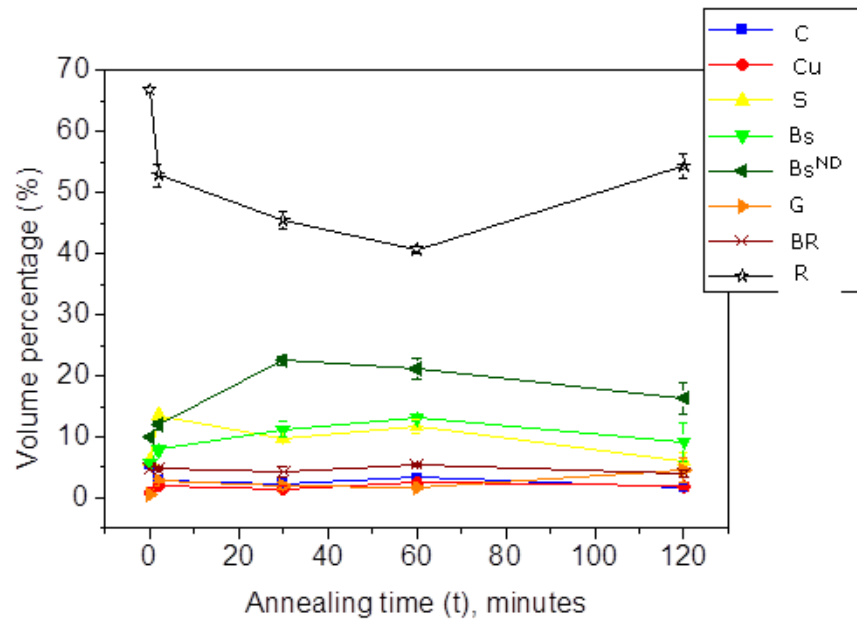


Fig.6.14: Variation of volume fraction of texture components in austenite in 90% CWR processed DSS during isothermal annealing.

Notably, the usual brass recrystallization texture component (BR) ($\{236\}\langle 385 \rangle$; highlighted in dark brown) is rather weak having a volume fraction of less than 5%. The orientation maps (Fig.6.13) and the texture component plot (Fig.6.14) reveal that the total fraction of random components decreases during annealing, but still reveals a rather high value (>50%).

6.4 Discussion

6.4.1 Texture evolution during processing by CWR

The volume fraction of austenite during CWR processing is found to be between ~45-55% as already stated. Further, the average phase band thickness values of the two phases at different stages of CWR processing indicate that the strain is partitioned approximately equally between the two phases. Therefore, the microstructure and texture evolution during CWR processing is not greatly affected either by strain-induced phase transformation of austenite or unequal strain-partitioning. It might be recalled that austenite in DSS warm-rolled to 90% reduction in thickness at 898K (625°C) by UWR develops a pure metal type texture (Fig.4.33 and Fig.4.34). The transition to a brass texture during cross-rolling from a pure metal type texture during straight rolling in austenite of DSS is explained by the relative stability of texture components [102, 103] during deformation which depends on the rotation field $\dot{R}(\phi_1, \Phi, \phi_2)$ and the divergence of the rotation field $\left(\text{div } \dot{R} = \frac{\partial \phi_1}{\partial \phi_1} + \frac{\partial \Phi}{\partial \Phi} + \frac{\partial \phi_2}{\partial \phi_2} \right)$. Stability criteria for any orientation are given by: $\dot{R} = 0$ and $\text{div } (\dot{R}) = 0$. Hong et al [104] have analyzed the stability of different texture components under cross-rolling and showed that the $(110)[111]$ orientation has the highest stability due to its higher inversion rate and large negative divergence. Therefore, the orientations during unidirectional rolling will first rotate towards the stable B_s orientation with Euler angles $(\phi_1, \Phi, \phi_2 = 35^\circ, 45^\circ, 0^\circ)$

and then would further rotate away to the $(110)[1\bar{1}1]$ orientation with $(\varphi_1, \Phi, \varphi_2 = 55^\circ, 45^\circ, 0^\circ)$ when the direction of rolling is changed. Thus, the texture components in straight-rolling with a set of Euler angles $\varphi_1, \Phi, \varphi_2$ will correspond to the cross-rolling components with a set of Euler angles $(90^\circ - \varphi_1, \Phi, 90^\circ - \varphi_2)$ due to the presence of tetragonal sample symmetry around the ND. As a result the orientations would oscillate between the two dynamically stable end orientations B_S and B_S^{ND} resulting in the build-up of orientations exactly midway between the two end orientations i.e. at $\varphi_1, \Phi, \varphi_2 = 45^\circ, 45^\circ, 0^\circ$ location. The analytical findings of Hong et al [104] is confirmed by the presence of the component $\{011\} \langle 755 \rangle$ in the measured texture of cross-rolled Cu and $\{011\} \langle 744 \rangle$ in cross-rolled Ni [105] which are very close to the predicted orientation of Hong et al [104]. In the present case the B_S^{ND} component $(011) [3\bar{2}2]$ of austenite in CWR processed DSS having set of Euler angles $(\varphi_1, \Phi, \varphi_2 = 43^\circ, 45^\circ, 0^\circ)$ is in excellent agreement with the predicted orientation of Hong et al and thus indicates very similar mechanism of texture development.

It may be noted that cold-rolling of the same DSS results in the gradual transformation to a brass-texture (Fig.4.38) in austenite typical of low SFE FCC materials [106]. This can be attributed to the crucial role played by mechanical or deformation twins [22]. Processing by UWR at 625°C results in an increase of SFE of austenite [89] so that formation of deformation twinning is suppressed and a pure metal or copper type texture instead of brass texture is developed[46]. Thus, the austenite in DSS during UWR processing behaves very similar to the single phase high to medium SFE materials where cross-rolling results in the transformation from pure metal or copper type to brass texture. This shows that the origin of brass texture in austenite during CWR is not due to mechanical twinning, instead very similar mechanisms

for texture development in cross-rolled high to medium SFE materials are responsible for the development of B_s texture.

The textures of cold-rolled single phase ferrite and BCC materials in general are conveniently described by the presence of the RD and ND fibers. However, the texture evolution due to cross-rolling in ferrite reported in the literature is contradictory. Huh et al [107] have carried out the cross-rolling along a new RD maintaining a constant angle with respect to the original RD of a 30% cold-rolled sheet. Detailed analysis of the bulk texture establishes that, irrespective of the angle of rolling the intensity of the RD-fiber and the $\{001\}\langle 110 \rangle$ component in particular, is diminished. However, the strength of the ND-fiber remains largely unaffected. In the heavy deformation regime the effect of cross-rolling is found to be less pronounced. These observations are supported by the cross-rolling results of Lee et al [108] in ferritic stainless steels. In contrast, Wronski et al [109] have carried out two stage cross-rolling imposing equivalent strain of ~ 1.34 and 1.56 , respectively, along two mutually perpendicular directions and shown that the $\{001\}\langle 110 \rangle$ component dominates the cross-rolling texture of low carbon ferritic steels along with the $\{111\}\langle 101 \rangle$ and $\{111\}\langle 112 \rangle$ components. These components in the cross-rolled texture could be related to their counterparts in the straight rolling texture by simple rotation of $\mp 90^\circ$ around the ND. Strengthening of the $\{001\}\langle 110 \rangle$ component has also been reported in cross-rolling texture of BCC molybdenum sheets [110] .

In the present work the ferrite in the CWR processed DSS shows a much stronger RD-fiber component $\{001\}\langle 110 \rangle$ as compared to that in the UWR processed material (Fig.4.13). This convincingly shows that the $\{001\}\langle 110 \rangle$ component is strengthened due to processing by CWR. As like in the case of austenite in DSS, texture component in ferrite with a set of Euler angles ϕ_1, Φ, ϕ_2 in straight-

rolling should be related to the texture component in the CWR processed material with a set of Euler angles ($90^\circ \mp \phi_1, \phi, 90^\circ \mp \phi_2$). Within this simple geometrical framework the equivalent component of $\{001\} \langle 110 \rangle$ ($\phi_1=0^\circ, \Phi=0^\circ, \phi_2=45^\circ$) in the CWR processed sample should be $\phi_1=90^\circ, \Phi=0^\circ, \phi_2=45^\circ$ or the $\{001\} \langle 110 \rangle$ component itself. The stability of the $\{001\} \langle 110 \rangle$ component is also in excellent agreement with the zero rotation rate for this component [109]. However, the other components observed in cross-rolled ferrite by Wronski et al [109], such as $\{111\} \langle 101 \rangle$ and $\{111\} \langle 112 \rangle$, are not observed in the ferrite of CWR processed DSS in the present work. This could be due to the difference in the multi-step cross-rolling process adopted in the present work with the two-step cross-rolling process adopted by Wronski et al [109]. The change of RD in every pass with small imparted strain in the multi-step cross-rolling process will make the other orientations unstable even though the rotation rates are small in a typical two step cross-rolling process [109]. It thus appears that the differences reported in literature for cross-rolling texture of ferrite and other BCC materials are largely due to the differences in the cross-rolling process and the textures present in the starting materials.

It is noted that the development of texture in the two constituent phases during CWR processing is independent of the presence of the other phases, unlike duplex ($\alpha+\beta$) brass [111]. Very similar observations are also reported concerning texture development during UWR processing (Section 4.9) and cold-rolling [66] which amply substantiate the present findings. It can thus be concluded that the textures of the two phases are significantly affected by the change in strain path, but not by the presence of the other phase. This is in good agreement with the explanation put forward by Keichel et al [66] and already explained in Fig.4.41 in Chapter 4. This aspect of deformation behavior in the present work is at

variance with that of duplex ($\alpha+\beta$) brass where the deformation behavior of the two phases are mutually affected by the presence of the other phase. It appears that different starting microstructure and morphology in the duplex ($\alpha+\beta$) brass having a large fraction of transformed Widmanstätten α phase inside the β grains [111] as opposed to the rather lamellar microstructure in the starting homogenized DSS (Fig.4.1) are the reasons for the observed differences.

6.4.2 Texture evolution during annealing

The lamellar microstructure of the CWR processed material transforms to a typical lamellar bamboo type morphology for a short isothermal holding time before the lamellar structure finally collapses. The overall microstructural transformation is indicative of the characteristic softening processes in the two phases.

In case of ferrite in the CWR processed DSS, the development of bamboo morphology during isothermal annealing indicates strong recovery, which is also reported during annealing of cold-rolled DSS [66]. In the present case the deformation has been carried out by CWR at an elevated temperature (i.e. 898K (625°C)) which favors dynamic recovery and thus further lowers the driving force for recrystallization. During recrystallization the subgrains grow to occupy the full thickness of the phase bands along the ND. However, due to the lamellar morphology with an alternate arrangement of the two phase bands, growing subgrains experience resistance to further growth along the ND but can grow laterally along the RD. Due to the low accumulated misorientation along the ferrite bands (Fig.6.2(d)) the growing subgrains will mostly be separated from neighboring subgrains by LAGBs after they mutually impinge.

A primary difference between the bamboo type austenite morphology with that of ferrite in the DSS is that the austenite grains are separated by HAGBs and shows significantly higher aspect ratio. This shows that the softening mechanism in austenite in DSS is discontinuous (primary) recrystallization with typical nucleation and growth stages which is also supported by frequent annealing or growth twins present in the austenite bands. During recrystallization the austenite grains can nucleate discontinuously fully bounded by HAGBs. This results in a higher aspect ratio or more globular morphology compared to ferrite. The austenite grains grow subsequently to extend over the full thickness of the phase bands while the lateral growth along the RD results in neighboring austenite grains along the same phase bands are separated by HAGBs.

The gradual transformation from a lamellar bamboo type morphology to a final breakdown of the lamellar structure with increasing isothermal holding time, as evidenced by the increased aspect ratio, is also observed in isothermally annealed UWR processed DSS (Fig.4.29(c) and Fig.4.30(c)) and cold-rolled and annealed DSS [66]. Keichel et al [92] have shown that for heavily cold-rolled DSS this process of evolution of globular morphology is due to Ostwald ripening which will be preceded by the break-down of the lamellar structure driven by mutual interpenetration of the phase bands at the triple points where grain boundaries meet the phase boundaries. Few representative regions are identified in Fig.6.6 (marked in white circles) in the different isothermally annealed specimens where mutual interpenetration of phase bands from opposite sides appears to have taken place during the breakdown or imminent breakdown of the intermediate bands of the other phase.

The evolution of recrystallization texture in the two phases is determined by the characteristic softening processes during annealing. Recovery in ferrite only involves subgrain growth, which leads to the deformation texture components being largely preserved in the recrystallization texture. In cold-rolled single phase ferrite the two fiber components show different behavior during annealing due to differences in the stored energy. The prominent RD-fiber components, such as $\{001\}\langle 110 \rangle$ and $\{112\}\langle 110 \rangle$ show preferential recovery. In contrast, ND-fiber components $\{111\}\langle 110 \rangle$ and $\{111\}\langle 112 \rangle$ show recrystallization type behavior due to their higher stored energy. In the present case, due to the elevated temperature of warm-rolling, the driving force for recrystallization is reduced as already discussed. As a result, the RD-fiber component $\{001\}\langle 110 \rangle$ which dominates the deformation texture of the CWR processed material obviously becomes the strongest component in different isothermally annealed specimens. This is rather similar to the origin of the recrystallization texture of ferrite in the UWR processed DSS. Limited grain growth even after annealing for a very long time results in no significant change in the recrystallization texture which is amply corroborated by the ODF sections (Fig.6.8), orientation maps (Fig.6.9) and texture component analysis (Fig.6.10).

Single phase austenite [32, 34], austenite of cold-rolled and annealed DSS [66] and austenite of UWR processed DSS (Fig.4.35) show the retention of rolling texture components during annealing, such as, B_s , G and first order twins of these orientations, in particular, G^T . The retention of deformation components in single phase austenite is explained based on the nucleation in an energetically homogenous matrix in a random manner without any preferential orientation selection [32]. The recrystallization texture is thus a random sampling of the deformation texture [21]. Very

similar pattern of texture development is observed for austenite in different isothermally annealed CWR processed DSS, which show a strong BSND component (dominant component in deformation texture). This indicates very similar mechanism of formation of recrystallization texture in austenite in CWR processed DSS. The decrease in the volume fraction of random components is nearly exactly compensated by the increase in the volume fraction of the B_S^{ND} component (Fig.6.15). However, increase in random fraction is observed after annealing for 120 minutes. The increase in the random fraction is compensated by the decrease in the total volume fraction of the S, B_S and B_S^{ND} components. Since grain growth is limited along the ND due to the resistance to growth exerted by one phase on the other, the change in volume fraction is mostly due to lateral growth along the RD of regions with random orientations inside the austenite bands.

The retention of deformation texture components is at variance with previous studies in low SFE materials such as 70:30 brass where the BR component ($\{236\}<385>$) is found dominating the recrystallization texture [97]. This is attributed to a sequential mechanism involving nucleation at shear bands, formation of annealing twins and subsequent growth of the orientation due to high mobility $40^\circ<111>$ misorientation relationship with the brass dominated deformed matrix [97]. The $\{236\}<385>$ component is not found strong in annealed single phase austenite [21], austenite in UWR processed DSS (Fig.4.35) and austenite of CWR processed DSS alloy in the present case. This is quite consistent with the recrystallization process involving nucleation without orientation selection and limited grain growth.

-: CHAPTER 7 :-
SUMMARY AND CONCLUSIONS

Summary and Conclusions

The present research work makes an attempt to understand the evolution of microstructure and texture during thermo-mechanical processing of a DSS alloy with composition 24%Cr-10.5%Ni-3%Mo-0.08%C. Warm-rolling is used as the preferred thermo-mechanical processing route in order to avoid deformation induced phase transformation of austenite. The effects of three major parameters, namely, warm-rolling temperature, strain and change in strain path are investigated in the present work.

The major conclusions that may be drawn concerning the effect of warm-rolling temperature are:

- (i) Alternate arrangement of ferrite and austenite bands is observed during warm-rolling of DSS at different temperatures.
- (ii) Inhomogeneous microstructure consisting of thick ferrite bands and fragmented ferrite regions is observed after 90% warm-rolling at 698K (425°C). In contrast, the microstructures of DSS 90% warm-rolled at the two end temperatures of warm-rolling, namely 498K (225°C) and 898K (625°C) show much less fragmentation.
- (iii) Texture of ferrite in DSS 90% warm-rolled at 698K (425°C) shows much stronger RD-fiber than ND-fiber.
- (iv) The differences in microstructure and texture of ferrite in DSS warm-rolled at 698K (425°C) are attributed to dynamic strain aging i.e. strong interaction of carbon atoms with dislocations.

- (v) Austenite in DSS develops a pure metal type texture due to increased SFE.
- (vi) Transformation from bamboo type morphology to a globular morphology is observed due to the interpenetration of the phases along the triple points.
- (vii) Much stronger RD-fiber than ND-fiber is observed in ferrite in DSS after isothermal annealing which is attributed to recovery in ferrite.
- (viii) Austenite retains the characteristics of the deformation texture due to discontinuous recrystallization without preferential orientation selection.
- (ix) The grain growth is suppressed due to the hindrance to growth exerted by one phase on the other.

In order to study the effect of severe deformation, the warm-rolling is carried out up to 98% reduction in thickness at 898K (625°C) and annealing is carried out at 1175°C for time intervals varying from 2 minutes to 120 minutes. The major conclusions that may be drawn are:

- (i) Ferrite shows fragmentation and near saturation in HAGB spacing. However, grain refinement process is continued in austenite beyond 90% reduction in thickness.
- (ii) The continued grain refinement in austenite in DSS with increasing thickness reduction indicates subdivision of grains in increasingly finer scales.

- (iii) Ferrite consistently shows texture characterized by ND and RD fibers, similar to single phase ferrite.
- (iv) The strengthening of the brass component in austenite beyond 90% warm-rolling is accompanied by the formation of deformation twins.
- (v) Microstructural break down and the concurrent evolution of a globular morphology due to the interpenetration of phases is observed during isothermal annealing.
- (vi) Kinetics of microstructural evolution during isothermal annealing is enhanced by increasing deformation.
- (vii) Ferrite in DSS shows strong recovery behavior during isothermal annealing leading to the retention of the characteristic of deformation texture after annealing.
- (viii) Austenite in different warm-rolled DSS shows discontinuous recrystallization without preferential orientation selection during isothermal annealing.

The effect of change in strain path on the evolution of microstructure and texture is studied by cross warm-rolling (CWR) at 898K (625°C) to 90% reduction in thickness followed by annealing at 1448 K (1175°C) for time intervals varying from 2 minutes to 120 minutes. The major conclusions that may be drawn are:

- (i) Austenite in DSS shows brass and ND-rotated brass component $\{011\} < 3\bar{2}2 >$ after processing by CWR. However, mechanical twinning has no role in developing brass texture.

(ii) Strong RD-fiber component $\{001\}\langle 110 \rangle$ is developed in ferrite due to the stability of this component during processing by CWR.

(iii) During annealing the lamellar structure is gradually broken down due to the mutual interpenetration of the two phases.

(iv) The RD-fiber component $\{001\}\langle 110 \rangle$ is retained in ferrite during annealing due to recovery behavior of ferrite.

(v) Retention of deformation texture in austenite due to primary recrystallization without preferential orientation selection.

An important outcome of this research work is that, although the evolution of microstructure and texture of the two phases in DSS is affected by warm-rolling temperature, severe strain and change in strain path, it is not affected by the presence of the other phase. In other words, the microstructure and texture of the two phases during deformation and annealing can be explained on the basis of characteristic deformation and recrystallization behavior of the respective single phase materials.

References

References

1. Koo, J.Y. and Thomas, G., *Design of duplex Fe/X/0.1C steels for improved mechanical properties*. Metallurgical Transactions A, 1977. **8**: p. 525-528.
2. Lai, J.K.L., Shek. C.H. and Lo K.H., *Stainless steels: An introduction and their recent developments*. 2012: Bentham Science Publishers.
3. Alvarez-Armas, I. and Degallaix-Moreuil S., *Duplex Stainless Steels*. 2013: Wiley.
4. Charles, J., *Duplex stainless steels, a review after DSS'07 in Grado*. Metallurgical Research & Technology, 2008. **105**: p. 155-171.
5. TMR stainless, Pittsburgh, PA, USA, *Practical guidelines for the fabrication of duplex stainless steel*, 2009, International Molybdenum Association (IMOA): London,UK.
6. Gunn, R., *Duplex Stainless steels: Microstructure, properties and applications*. 1997: Elsevier Science.
7. Humphreys, F.J. and Hatherly M., *Recrystallization and related annealing phenomena (second edition)*. 2004: Elsevier, Oxford.
8. Engler, O. and Randle, V., *Introduction to texture analysis: Macrotexture, microtexture, and orientation mapping, Second Edition*. 2009: Taylor & Francis, UK.
9. Bunge H.J., Z. Metallkunde 1965. **56**.
10. Roe R.J., J.Appl. Phys, 1965. **36**.
11. Hansen, J., Pośpiech, J., and Lücke, K. *Tables for texture analysis of cubic crystals*. 1978: Springer-Verlag GmbH.
12. Ray, R.K., Butron-Guillen, M.P., Jonas, J.J. and Savoie, J., *Transformation textures in steels*. ISIJ International, 1994. **34**: p. 927-942.

13. Bunge H.J., *Mathematische methoden der texturanalyse*. 1969: Academic Verlag, Berlin, Germany.
14. Bunge, H.J., *Texture analysis in materials science: Mathematical methods*. 1982: Butterworths, London, UK.
15. Hirsch, J. and Lücke, K., Overview no. 76: *Mechanism of deformation and development of rolling textures in polycrystalline f.c.c. metals—i. Description of rolling texture development in homogeneous cuzn alloys*. Acta Metallurgica, 1988. **36**: p. 2863-2882.
16. Raabe, D. and Lücke, K., *Rolling and annealing textures of bcc metals* Materials Science Forum, 1994. **157**: p. 597-610.
17. Dillamore, I.L. and Roberts, W.T., *Preferred orientation in wrought and annealed metals*. Metallurgical Reviews, 1965. **10**: p. 271-380.
18. Smallman, R.E. and Green, D., *The dependence of rolling texture on stacking fault energy*. Acta Metallurgica, 1964. **12**: p. 145-154.
19. Dillamore, I.L. and Roberts, W.T., *Rolling textures in f.c.c. and b.c.c. metals*. Acta Metallurgica, 1964. **12**: p. 281-293.
20. Hirsch, J., Lücke, K. and Hatherly, M., Overview no. 76: *mechanism of deformation and development of rolling textures in polycrystalline f.c.c. metals—iii. The influence of slip inhomogeneities and twinning*. Acta Metallurgica, 1988. **36**: p. 2905-2927.
21. El-Danaf, E., Kalidindi, S.R., Doherty, R.D. and Necker, C., *Deformation texture transition in brass: critical role of micro-scale shear bands*. Acta Materialia, 2000. **48**: p. 2665-2673.
22. Leffers, T. and Ray, R.K., *The brass-type texture and its deviation from the copper-type texture*. Progress in Materials Science, 2009. **54**: p. 351-396.

23. Hutchinson, W.B., Duggan, B.J. and Hatherly, M., *Development of deformation texture and microstructure in cold-rolled cu-30zn*. Metals Technology, 1979. **6**: p. 398-403.
24. Humphreys, F.J., *A unified theory of recovery, recrystallization and grain growth, based on the stability and growth of cellular microstructures—I. The basic model*. Acta Materialia, 1997. **45**: p. 4231-4240.
25. Engler, O. and Huh, M. Y., *Evolution of the cube texture in high purity aluminum capacitor foils by continuous recrystallization and subsequent grain growth*. Materials Science and Engineering: A, 1999. **271**: p. 371-381.
26. Bhattacharjee, P.P. and Tsuji, N., *Development of highly cube textured nickel superconductor substrate tapes by Accumulative Roll Bonding (ARB)*. International Journal of Materials Research, 2011. **102**: p. 173-182.
27. Engler, O. and Hirsch, J., *Polycrystal-plasticity simulation of six and eight ears in deep-drawn aluminum cups*. Materials Science and Engineering: A, 2007. **452–453**: p. 640-651.
28. Dillamore, I.L., Katoh, H. and Haslam, K., *The Nucleation of Recrystallisation and the Development of Textures in Heavily Compressed Iron-Carbon Alloys*. Texture, 1974. **1**: p. 151-156.
29. Ray, R.K., *Rolling textures of pure nickel, nickel-iron and nickel-cobalt alloys*. Acta Metallurgica et Materialia, 1995. **43**: p. 3861-3872.
30. Chowdhury, S.G., Sahu, P., Mahato, B. and De, P. K., *Evolution of recrystallization texture in AISI300 series austenitic stainless steels after cold rolling to large strain*, in *Microstructure and Texture in Steels*, A. Haldar, S. Suwas, and D. Bhattacharjee (editors). 2009, Springer London. p. 361-378.

31. Bracke, L., Verbeken, K. and Kestens L.A.I., *Texture generation and implications in TWIP steels*. Scripta Materialia, 2012. **66**: p. 1007-1011.
32. Bracke, L., Verbeken, K., Kestens, L. and Penning, J., *Microstructure and texture evolution during cold rolling and annealing of a high Mn TWIP steel*. Acta Materialia, 2009. **57**: p. 1512-1524.
33. Saleh, A.A., Pereloma, E.V. and Gazder, A.A., *Texture evolution of cold rolled and annealed Fe-24Mn-3Al-2Si-1Ni-0.06C TWIP steel*. Materials Science and Engineering A, 2011. **528**: p. 4537-4549.
34. Donadille, C., Valle, R., Dervin, P. and Penelle, R., *Overview .82. Development of texture and microstructure during cold-rolling and annealing of fcc alloys - example of an austenitic stainless-steel*. Acta Metallurgica, 1989. **37**: p. 1547-1571.
35. Bhattacharjee, P.P., Sathiaraj, G.D., Zaid, M., Gatti, J.R., Chi Lee., Che-Wei Tsai. and Jien-Wei Yeh., *Microstructure and texture evolution during annealing of equiatomic CoCrFeMnNi high-entropy alloy*. Journal of Alloys and Compounds, 2014. **587**: p. 544-552.
36. Barrales-Mora, L.A., Lü, Y. and Molodov, D.A., *Experimental determination and simulation of annealing textures in cold rolled twip and trip steels*. Steel Research International, 2011. **82**: p. 119-126.
37. Lü, Y., Molodov D.A., and Gottstein G., *Recrystallization kinetics and texture evolution during annealing of Fe-23.2Mn-0.57C alloy*. Materials Science Forum, **702-703**: 2012. p. 443-448.
38. Lu, Y.P., Molodov, D.A. and Gottstein, G., *Correlation between microstructure and texture development in a cold-rolled twip steel*. ISIJ International, 2011. **51**: p. 812-817.

39. Chowdhury, S.G., Sudarsan Datta., Ravi Kumar, B., De, P.K. and Ghosh, R.N., *Randomization of texture during recrystallization of austenite in a cold rolled metastable austenitic stainless steel*. Materials Science and Engineering A-Structural Materials Properties Microstructure and Processing, 2007. **443**: p. 114-119.
40. Ray, R.K., Jonas, J.J. and Hook, R.E., *Cold rolling and annealing textures in low carbon and extra low carbon steels*. International Materials Reviews, 1994. **39**: p. 129-172.
41. Hutchinson, W.B., *Development and control of annealing textures in low-carbon steels*. International Metals Reviews, 1984. **29**: p. 25-42.
42. Raabe, D., *On the influence of the chromium content on the evolution of rolling textures in ferritic stainless steels*. Journal of Materials Science, 1996. **31**: p. 3839-3845.
43. Engler, O., Tomé, C.N. and Huh, M.Y., *A study of through-thickness texture gradients in rolled sheets*. Metallurgical and Materials Transactions A, 2000. **31**: p. 2299-2315.
44. Raabe, D. and Lücke, K. *Annealing textures of BCC metals*. Scripta Metallurgica et Materialia, 1992. **27**: p. 1533-1538.
45. Raabe, D. and Lücke, K. *Texture and microstructure of hot rolled steel*. Scripta Metallurgica et Materialia, 1992. **26**: p. 1221-1226.
46. Samajdar, I., Verlinden, B., Van Houtte, P. and Vanderschueren, D., *[gamma]-Fibre recrystallization texture in IF-steel: an investigation on the recrystallization mechanisms*. Materials Science and Engineering A, 1997. **238**: p. 343-350.
47. Emren, F., Von Schlippenbach, U., and Lücke, K., *Investigation of the development of the recrystallization textures in deep drawing steels by ODF analysis*. Acta Metallurgica, 1986. **34**: p. 2105-2117.

48. Ray, R.K., Jonas, J.J. and R.E. Hook, *Cold rolling and annealing textures in low carbon and extra low carbon steels*, International Materials Reviews, 1994. **39**: p. 129-172.
49. Hutchinson, W.B., *Recrystallisation textures in iron resulting from nucleation at grain boundaries*. Acta Metallurgica, 1989. **37**: p. 1047-1056.
50. Huh, M.Y. and Engler, O. *Effect of intermediate annealing on texture, formability and ridging of 17%Cr ferritic stainless steel sheet*. Materials Science and Engineering: A, 2001. **308**: p. 74-87.
51. Vandermeer, R.A. and Snyder, W.B. *Recovery and recrystallization in rolled tantalum single crystals*. Metallurgical Transactions A, 1979. **10**: p. 1031-1044.
52. Dehghan-Manshadi, A., Barnett, M.R. and Hodgson, P. D., *Microstructural evolution during hot deformation of duplex stainless steel*. Materials Science and Technology, 2007. **23**: p. 1478-1484.
53. Fan, G.W., Liu, J., Han, P.D. and Qiao, G.J., *Hot ductility and microstructure in casted 2205 duplex stainless steels*. Materials Science and Engineering: A, 2009. **515**: p. 108-112.
54. Iza-Mendia, A., Piñol-Juez, A., Urcola, J. J. and Gutiérrez, I., *Microstructural and mechanical behavior of a duplex stainless steel under hot working conditions*. Metallurgical and Materials Transactions A, 1998. **29**: p. 2975-2986.
55. Balancin, O., Hoffmann, W.A.M. and Jonas, J.J., *Influence of microstructure on the flow behavior of duplex stainless steels at high temperatures*. Metallurgical and Materials Transactions A, 2000. **31**: p. 1353-1364.
56. Cizek, P. and Wynne, B.P., *A mechanism of ferrite softening in a duplex stainless steel deformed in hot torsion*. Materials Science and Engineering: A, 1997. **230**: p. 88-94.

57. Solomon, H.D. and Devine, T.M., *Duplex stainless steels: A tale of two phases*. 1982: American Society for Metals.
58. Johansson, J. and Odén, M. *Load sharing between austenite and ferrite in a duplex stainless steel during cyclic loading*. Metallurgical and Materials Transactions A, 2000. **31**: p. 1557-1570.
59. Chandra, T., Bendeich, D. and Dunne D.P., *Hot working of duplex stainless steels*. in *Proc. ICSMA 6*. 1982. Melbourne Australia: Gifkins RC (editor).
60. Duprez, L., De Cooman, B.C. and Akdut, N., *Deformation behaviour of duplex stainless steel during industrial hot rolling*. Steel Research, 2002. **73**: p. 531-538.
61. A Ul-Haq, H.W. and Bunge, H.J., *Textures and microstructures in duplex stainless steel*. Material Science and Technology, 1994. **10**: p. 289-298.
62. C. Herrera, D.P. and Raabe, D., *Microstructure and texture of hot-rolled duplex stainless steel*. 2009. (<http://www.mpie.de>).
63. Ryś, J. and Zielinska-Lipiec, A., *Deformation of Ferrite-Austenite Banded Structure in Cold-Rolled Duplex Steel*. Archives of Metallurgy and Materials, 2012. **57**: p. 1041-1053.
64. Ryś, J. and Zielinska-Lipiec, A., *Structural aspects of ferrite and austenite co-deformation in duplex stainless steel*. Solid State Phenomena, 2013. **203-204**: p. 28-33.
65. Rys, J. and Witkowska, M., *Influence of Band-Like Morphology on Microstructure and Texture Evolution in Rolled Super-Duplex Steel*. Archives of Metallurgy and Materials, 2010. **55**: p. 733-747.
66. Keichel, J., Foct, J. and Gottstein, G., *Deformation and annealing behavior of nitrogen alloyed duplex stainless steels. Part I: Rolling*. ISIJ International, 2003. **43**: p. 1781-1787.

67. Rys, J., Ratuszek, W. and Witkowska, M., *Rolling texture development in duplex type steel with strong initial texture*. Archives of Metallurgy and Materials, 2005. **50**: p. 857-870.
68. Ryś, J., Ratuszek, W. and Witkowska, M., *Rolling texture differences in duplex steels with strong and random initial orientations*, in *Diffusion and Defect Data Pt.B: Solid State Phenomena*, 2007. **130**: p. 57-62.
69. Hamada, J.I. and Ono, N., *Effect of microstructure before cold rolling on texture and formability of duplex stainless steel sheet*. Materials Transactions, 2010. **51**: p. 635-643.
70. Belyakov, A., Kimura, Y. and Tsuzaki, K., *Microstructure evolution in dual-phase stainless steel during severe deformation*. Acta Materialia, 2006. **54**: p. 2521-2532.
71. Chen, L., Yuan, F. P., Jiang, P. and Wu, X.L., *Mechanical properties and nanostructures in a duplex stainless steel subjected to equal channel angular pressing*. Materials Science and Engineering A, 2012. **551**: p. 154-159.
72. Cao, Y., Wang, Y.B., An, X.H., Liao, X.Z., Kawasaki, M., Ringer, S.P., Langdon, T.G. and Zhu, Y.T., *Concurrent microstructural evolution of ferrite and austenite in a duplex stainless steel processed by high-pressure torsion*. Acta Materialia, 2014. **63**: p. 16-29.
73. Cooke, B.A., Jones, A.R. and Ralph, B., *Recrystallization of microduplex steels*. Metal Science, 1978. **13**: p. 179-186.
74. Keichel, J., Foct, J. and Gottstein, G., *Deformation and annealing behavior of nitrogen alloyed duplex stainless steels. Part II: Annealing*. ISIJ International, 2003. **43**: p. 1788-1794.
75. Zucato, I., Moreira, M. C., Machado, I. F. and Giampietri Lebrão, S. M., *Microstructural characterization and the effect of phase transformations on toughness of the uns s31803*

- duplex stainless steel aged treated at 850°C*. Materials Research, 2002. **5**: p. 385-389.
76. Reick, W., Pohl, M. and Padilha, A.F., *Recrystallization-transformation combined reactions during annealing of a cold rolled ferritic-austenitic duplex stainless steel*. ISI International, 1998. **38**: p. 567-571.
77. Mäder, K. and Hornbogen, E., *Systematics of recrystallisation micromechanisms in $\alpha+\beta$ brass*. Scripta Metallurgica, 1974. **8**: p. 979-983.
78. Belyakov, A., Rustam Kaibyshev., Yuuji Kimura. and Kaneaki Tsuzaki., *Recrystallization mechanisms in severely deformed dual-phase stainless steel*. Materials Science Forum, 2010. **638-642**: p. 1905-1910.
79. Schwartz, A.J., Kumar, M. and Adams, B.L., *Electron Backscatter Diffraction in Materials Science*. 2000: Kluwer Academic.
80. Lassen, N.C.K., *Scanning Microscopy* 1992. **6**: p. 115-121.
81. Mesquita, T.J., Eric Chauveau., Marc Mantel. and Nogueirab, Ricardo P., *XPS study of the Mo effect on passivation behaviors for highly controlled stainless steels in neutral and alkaline conditions*. Applied Surface Science, 2013. **270**: p. 90-97.
82. Schwartz, A.J., Mukul Kumar., Adams, Brent L. and David Field., *Electron Backscatter Diffraction in Materials Science*. 2010: Springer Science+Business Media.
83. Dieter, G.E., *Mechanical metallurgy*. 1976: McGraw-Hill.
84. Hereñú, S., Alvarez-Armas, I. and Armas, A.F., *The influence of dynamic strain aging on the low cycle fatigue of duplex stainless steel*. Scripta Materialia, 2001. **45**: p. 739-745.
85. Kolmorgen, R. and Biermann, H., *Thermo-mechanical fatigue behaviour of a duplex stainless steel*. International Journal of Fatigue, 2012. **37**: p. 86-91.

86. Hughes, D.A. and Hansen, N., *Deformation structures developing on fine scales*. Philosophical Magazine, 2003. **83**: p. 3871-3893.
87. Hughes, D.A. and Hansen, N., *High angle boundaries formed by grain subdivision mechanisms*. Acta Materialia, 1997. **45**: p. 3871-3886.
88. Serdar, M., Zulj, L.V. and Bjegovic, D., *Long-term corrosion behaviour of stainless reinforcing steel in mortar exposed to chloride environment*. Corrosion Science, 2013. **69**: p. 149-157.
89. Latanision, R.M. and Ruff, A.W., *The temperature dependence of stacking fault energy in Fe-Cr-Ni alloys*. Metallurgical Transactions, 1971. **2**: p. 505-509.
90. Gallagher, P.C.J., *The influence of alloying, temperature, and related effects on the stacking fault energy*. Metallurgical Transactions, 1970. **1**: p. 2429-2461.
91. Park, H. and Lee, D.N., *Deformation and annealing textures of drawn Al-Mg-Si alloy tubes*. Journal of Materials Processing Technology, 2001. **113**: p. 551-555.
92. Barnett, M.R. and Jonas, J.J., *Distinctive aspects of the physical metallurgy of warm rolling*. Isij International, 1999. **39**: p. 856-873.
93. Eardley, E.S., Soulet, A., Court, S.A., Humphreys, John F. and Bate, Pete S., *Microstructure and plastic anisotropy in rolled Al-Mg alloys*. Thermec'2003, 2003. **426-432**: p. 363-368.
94. Barnett, M.R. and Jonas, J.J., *Influence of ferrite rolling temperature on microstructure and texture in deformed low C and IF steels*. ISIJ International, 1997. **37**: p. 697-705.
95. Senuma, T., Yada, H., Shimizu, R. and Harase, J., *Textures of low carbon and titanium bearing extra low carbon steel sheets hot rolled below their AR3 temperatures*. Acta Metallurgica et Materialia, 1990. **38**: p. 2673-2681.

96. Raphanel, J.L. and Van Houtte, P., *Simulation of the rolling textures of b.c.c. metals by means of the relaxed taylor theory*. Acta Metallurgica, 1985. **33**: p. 1481-1488.
97. Beck, P.A. and Hu, H., *Annealing Textures in Rolled Face-Centered Cubic Metals*. Trans. AIME, 1952. **194**: p. 83-90.
98. Hansen, N. and Jensen, D.J., *Development of microstructure in FCC metals during cold work*. Philosophical Transactions of the Royal Society of London. Series A: Mathematical, Physical and Engineering Sciences, 1999. **357**: p. 1447-1469.
99. Wang, Y.B., Wang, Y.B., Liao, X.Z., Zhao, Y.H., Lavernia, E.J., Ringer, S.P., Horita, Z., Langdon, T.G. and Zhu, Y.T., *The role of stacking faults and twin boundaries in grain refinement of a Cu-Zn alloy processed by high-pressure torsion*. Materials Science and Engineering: A, 2010. **527**: p. 4959-4966.
100. Meyers, M.A., Mishra, A. and Benson, D.J., *Mechanical properties of nanocrystalline materials*. Progress in Materials Science, 2006. **51**: p. 427-556.
101. Zhu, Y.T., Liao, X.Z. and Wu, X.L., *Deformation twinning in nanocrystalline materials*. Progress in Materials Science, 2012. **57**: p. 1-62.
102. Savoie, J. and Jonas, J.J., *Simulation of the deformation textures induced by deep drawing in extra low carbon steel sheets*. Acta Metallurgica et Materialia, 1994. **42**: p. 4101-4116.
103. Toth, L.S., Jonas, J. J., Daniel, D. and Ray, R. K., *Development of Ferrite Rolling Textures in Low-Carbon and Extra Low-Carbon Steels*. Metallurgical Transactions A-Physical Metallurgy and Materials Science, 1990. **21**: p. 2985-3000.
104. Hong, S.H. and Lee D.N., *Deformation and recrystallization textures in cross-rolled copper sheet*. Journal of Engineering

- Materials and Technology, Transactions of the ASME, 2002. **124**: p. 13-22.
105. Bhattacharjee, P.P., Joshi, M., Chaudhary, V. P., Gatti, J. R. and Zaid, M., *Texture Evolution During Cross Rolling and Annealing of High-Purity Nickel*. Metallurgical and Materials Transactions A-Physical Metallurgy and Materials Science, 2013. **44A**: p. 2707-2716.
106. Bhattacharjee, P.P. and Zaid, M., *Effect of Warm-Rolling on the Formation of Microstructure and Microtexture of the Constituent Phases in a Duplex Steel*. Materials Science Forum, 2014, **783-786**: 2555-2560.
107. Huh, M.Y., Engler, O. and Raabe, D., *On the Influence of Cross-Rolling on Shear Band Formation and Texture Evolution in Low Carbon Steel Sheets*. Textures and Microstructures, 1995. **24**: p. 225-237.
108. Lee, J.H., Park, S.H. and Huh, M.Y., *Modification of the recrystallization texture by means of cross rolling in ferritic stainless steel sheets*. Materials Science Forum, 2004. **449 – 452**: p. 113-116.
109. Wronski, S., Wrobelb, M, Baczmanskia, A. and Wierzbanowski, K., *Effects of cross-rolling on residual stress, texture and plastic anisotropy in f.c.c. and b.c.c. metals*. Materials Characterization, 2013. **77**: p. 116-126.
110. Doherty, R.D., *Recrystallization and texture*. Progress in Materials Science, 1997. **42**: p. 39-58.
111. Garg, R., Gurao, N.P., Ranganathan, S. and Satyam Suwas., *Evolution of texture and grain boundary microstructure in two-phase (alpha plus beta) brass during recrystallization*. Philosophical Magazine, 2011. **91**: p. 4089-4108.